

Aluminium Foam Production using Calcium Carbonate as a Foaming Agent

David C. Curran, St. John's College

A dissertation submitted for the Degree of
Doctor of Philosophy in the University of Cambridge

University of Cambridge
Department of Materials Science and Metallurgy



Preface

This dissertation is submitted for the degree of Doctor of Philosophy in the University of Cambridge. The research described herein was carried out by myself in the period October 2000 to December 2003, under the supervision of Professor T.W. Clyne, in the Department of Materials Science and Metallurgy at the University of Cambridge.

To the best of my knowledge, the work described in this dissertation is original except where due reference has been made to the work of others, and nothing is included which is the outcome of work done in collaboration, except where noted. No part of this dissertation, or any similar to it, has been, or is currently being submitted for any degree, or other qualification, at any other university. It is less than 60,000 words in length.

David C. Curran
Cambridge
December 2003

Abstract

The current state of the art with regards to the production of metallic foams is reviewed, with melt-based processes identified as the most promising for cost-effective large-scale production. The potential for metal carbonates as an alternative to currently-used titanium hydride foaming agents is explored, with calcium carbonate identified as the most suitable. The influence of a range of material and processing parameters on the stability of metallic foams in the molten state is discussed, and current methods of controlling melt viscosity and surface tension are reviewed. Characteristic features of the compressive deformation of metallic foams are described in the context of use as an impact-absorbing material, with a review of work in the literature linking the bulk mechanical properties to details of the cell structure.

Calcium carbonate is found to be a highly effective foaming agent for aluminium. The foams obtained have notably finer cell structures than can be achieved in foams produced with titanium hydride, coupled with enhanced stability in the molten state. This is attributed to the presence of a thin continuous surface film of metallic oxide that counteracts the effect of surface tension. This film, combined with the finer cell structure of the calcium carbonate-based foams, is found to significantly reduce the rate of gravity drainage of the melt. The formation of the thin oxide film during foaming gives rise to a number of artefacts on the cell surface, including stretch marks and tear bands. A range of chemical and surface analysis techniques are used to identify the chemical composition and thickness of the oxide film. The distribution of refractory particles in the cell faces, which are commonly employed to stabilise molten foam structures, is found to be highly non-uniform in foams which undergo significant gravity drainage of liquid metal during the foaming process. Experiments in which the concentration of particles is varied demonstrate the importance of their effect on the melt viscosity in addition to their known role as a surface stabilising phase. The effect of alloy content and foaming gas on the stability of standing molten foams is also investigated in the context of other foaming processes.

The formation of an oxide film on the surface of the cells is shown thermodynamically to be a necessary step in the production of low-density aluminium foams with a calcium carbonate foaming agent. A temperature-dependent upper limit on porosity is observed. It is established that this is the result of inhibition of the calcium carbonate decomposition reaction by its products as the thickness of the surface oxide film increases. The effect of varying cell size, porosity and chemical composition on the thickness of the surface oxide film is derived. The rate of thermal decomposition of calcium carbonate is found to be dominated by the partial pressure of carbon dioxide, with particle size and small impurity contents having only a small effect.

Compressive mechanical properties of the foams produced are compared with those of foams produced with a titanium hydride foaming agent and theoretical predictions. A reduced cell size apparently minimises the influence of point defects on the properties of specimens of finite dimensions. A significant difference in the shape of the stress-strain curves of calcium carbonate- and titanium hydride-based foams is noted, with the latter marked by extensive serrations. This difference is demonstrated to be independent of differences in cell size. Microstructural analysis of foams in various stages of failure suggests that this is due to differences in the distribution of refractory particles in the two foams, which is in turn a consequence of the reduced extent of gravity drainage of liquid metal in the calcium carbonate-based foams.

Acknowledgements

I gratefully acknowledge the provision of funding for the research described in this dissertation by the Engineering and Physical Sciences Research Council, and by Cymat Corporation. Thanks are also due to Professor Derek Fray for the use of office, laboratory and workshop facilities at the Department of Materials Science and Metallurgy.

I would like to thank my supervisor, Professor T.W. Clyne for his encouragement, advice and support throughout my time here. I have been very fortunate to work with a supervisor who is both knowledgeable and approachable, and has made the Gordon laboratory such a pleasant environment to work in. His ability to generate a plausible acronym for anything has also been useful. Thanks also to Vlado Gergely, for collaboration, technical assistance and useful discussions throughout the course of this project.

Thanks are also due to Kevin Roberts, for assistance in my invariably smoky and messy foaming experiments and maintaining a steady supply of replacement thermocouples, Paul Stokes and John Carter, for transforming my back-of-an-envelope sketches into sophisticated pieces of scientific apparatus, Brian Whitmore and Andrew Rayment, for assistance whenever the compression testing rig started to misbehave, and Brian Barber and Carol Best their patience while developing a mountain of rather similar-looking photographs. Thanks also to Heiko Stanzick at the Fraunhofer Institute for Advanced Materials for conducting X-ray radiography experiments on specimens of foamable materials in Grenoble. Special thanks also go to Professor John Watts and Andy Brown at the Surface Analysis Laboratory at the University of Surrey for invaluable assistance with understanding spectroscopic techniques, and applying them to odd-shaped specimens they probably weren't designed for.

Thanks also go to the members of the Gordon laboratory, without whom the past three years would have been a lot less interesting: Andrew (for being good company in Stuttgart, not colonising my desk, and generally adding a northern feel to the lab), James (for maintaining the Top Secret office biscuit supply), Sofia (for good company, and unlimited enthusiasm for organising lab events), Tom (for introducing me to the dark art of the Microsoft Word Master Document, and keeping the computers running despite my unparalleled ability to make absolutely anything crash), Debu (for keeping the Mafia under control, and some serious curries), Athina (for introducing me to the exciting sciences of metallographic preparation and mechanical testing), Jin (for preventing floods in the office, and a successful campaign to improve the air quality of the lab), Katerina (for inheriting the plants - don't forget to water them!), Martin (for keeping me up to date on what's happening in Switzerland), Russell (for an explosive cook-up in Villars, and lots of trips to Sainsbury's), Shiladitya (beware desk floods...), and Chris (keep up that enthusiasm factor!). Thanks also to Bill Clegg, Tomi, Helen, Igor, Steve, Luc, Alison, Jamie, Derek, Stefan and Alex Diehl, who all made the lab a pleasant place to work in. My parting gifts to you all are an organised and heavily labelled metallography lab, a complicated website to maintain, a box of 216 specimens of aluminium foam, and an office in which plants outnumber people.

Thanks also go to my friends in Cambridge, who kept me sane and hopefully won't be reading this. Last, but by no means least, thanks to my parents for all their support and encouragement over the last three years.

Table of Contents

1	Introduction	1
1.1	Cellular materials.....	1
1.2	Development of metallic foams.....	1
1.3	Uses of metallic foams	2
1.4	Structure of this thesis	3
2	Types of Metallic Foam & Overview of their Production	4
2.1	Key features of metallic foam production	4
2.2	Production of open-cell foams.....	4
2.2.1	Processes based on sintering	4
2.2.2	Investment casting.....	8
2.2.3	Exploiting chemical characteristics.....	12
2.3	Production of closed-cell Foams	14
2.3.1	Exploiting chemical characteristics.....	14
2.3.2	Direct addition of gas to metals.....	15
2.3.3	Use of foaming agents.....	17
2.4	Summary of production methods	23
3	Production of Closed-Cell Foams using Gas Generating Agents	25
3.1	Gas generating agents.....	25
3.1.1	The use of gas generating agents.....	25
3.1.2	Requirements for a gas generating agent	25
3.1.3	Current gas generating agents	26
3.1.4	Metal carbonates as gas generating agents.....	28
3.2	Stages in the evolution of a foam structure	32
3.2.1	Cell growth.....	32
3.2.2	Drainage and collapse	33
3.3	Metallic and aqueous foams	34
3.4	Factors affecting the stability of foam structure.....	34
3.4.1	Gas diffusion	34
3.4.2	Cell rearrangement	35
3.4.3	Viscosity.....	35
3.4.4	Methods of generating a solid-liquid system	38
3.4.5	Surface tension	40
3.4.6	Surfactants.....	41
3.4.7	Oxidation of aluminium	45
3.4.8	The influence of the cell structure on stability.....	48
3.4.9	Modelling of drainage	48
3.5	Components of the Duralcan™ metal-matrix composite	52
3.5.1	Silicon.....	52
3.5.2	Magnesium.....	53
3.5.3	Strontium.....	53
3.5.4	Silicon carbide.....	53
3.6	Processing phenomena	54
3.6.1	Formation of aluminium carbide.....	54
3.6.2	Gravity settling of particles	55
3.6.3	Particle pushing during solidification	56
4	Mechanical Properties of Closed-cell Aluminium Foams	58
4.1	Levels of scale	58
4.2	Tensile, compressive and shear deformation.....	58
4.3	Deformation of metallic foams in compression	59

4.3.1	Low-strain behaviour	59
4.3.2	Yielding & Plastic collapse	61
4.4	Brittle and ductile collapse modes.....	62
4.5	Relating bulk mechanical properties to cell structure	65
4.6	Modelling elastic deformation.....	66
4.6.1	Dimensional Analysis of elastic deformation	66
4.6.2	Analytical modelling of elastic deformation.....	68
4.6.3	Finite element modelling of elastic deformation.....	70
4.6.4	Upper bound models	71
4.7	Comparing the predictions.....	71
4.8	Modelling plastic yielding	72
4.8.1	Dimensional analysis.....	72
4.8.2	Other approaches.....	74
4.9	Accounting for non ideality	76
4.9.1	The effect of generalised irregularity in cellular structure	76
4.9.2	The effect of missing cell faces.....	77
4.9.3	The effect of uniform cell size anisotropy	77
4.9.4	The effect of density gradients	78
4.9.5	The effect of local variations in density	79
4.9.6	The effect of waviness and curvature of cell faces	79
4.10	Strain rate effects	80
4.11	Cell size, specimen size & boundary conditions	81
5	Experimental Procedures	86
5.1	Production of foams.....	86
5.2	Analysis of the materials used	91
5.2.1	Particle size measurement	91
5.2.2	Scanning electron microscopy	92
5.2.3	Thermal analysis	92
5.3	Microscopy	92
5.3.1	Specimen preparation.....	92
5.3.2	Image analysis	92
5.3.3	Optical microscopy	93
5.3.4	Scanning microscopy: Planar samples	93
5.3.5	Scanning microscopy: Three dimensional samples	93
5.4	Spectroscopy.....	94
5.4.1	X ray diffraction	94
5.4.2	X-ray photoelectron spectroscopy.....	94
5.4.3	Auger electron spectroscopy	95
5.5	Mechanical testing.....	95
5.5.1	Sample preparation.....	95
5.5.2	Equipment parameters.....	96
5.6	Drainage.....	96
5.7	Cell coalescence	96
6	Structural & Microstructural Features of the Foams Produced	97
6.1	Performance of CaCO ₃ as a foaming agent	97
6.2	Features of carbonate-based foams.....	98
6.2.1	Cell structure	98
6.2.2	Cell faces	100
6.2.3	Bulk porosity	102
6.3	Calcium carbonate as a foaming agent.....	103
6.3.1	Distribution of foaming agents in the foamable precursor.....	103
6.3.2	Distribution of foaming agents in the foams produced	104
6.4	Silicon carbide particles.....	105

6.4.1	Surface distribution	105
6.4.2	Bulk distribution.....	107
6.5	The oxide film	110
6.5.1	Surface features	110
6.5.2	Characterisation of the oxide film.....	113
6.6	Internal microstructure	120
6.7	Factors affecting structure and stability of standing foams.....	121
6.7.1	The effect of foaming agent & foaming gas	121
6.7.2	The effect of melt drainage in carbonate-based foams	124
6.7.3	The effect of silicon carbide content.....	127
6.7.4	The effect of magnesium content.....	131
6.8	Extension to other methods of foaming.....	132
6.8.1	Direct foaming of the melt	132
6.8.2	Foaming by induction heating.....	133
6.9	Consistency with other work.....	134
7	Mechanisms and Characteristics of Foam Production with Calcium Carbonate	135
7.1	CaCO ₃ : Measured properties.....	135
7.1.1	Characterisation of the powders.....	135
7.1.2	The effect of purity and particle size.....	137
7.1.3	Inhibition of thermal decomposition by carbon dioxide	140
7.2	Gas requirements for foaming	141
7.3	Thermodynamics of foaming with calcium carbonate	143
7.3.1	Inhibition of thermal decomposition	143
7.3.2	Reactions of the foaming gas	143
7.3.3	Formation of the oxide film	145
7.3.4	Limiting of the reaction.....	146
7.4	Estimation of surface oxide thickness	147
8	Mechanical behaviour of Fine, Closed Cell Foams	151
8.1	Measured elastic properties	151
8.2	Plastic yielding mechanisms.....	153
8.3	Plastic failure of carbonate- and hydride-based foams.....	154
8.4	Plastic collapse of FORMGRIP and FOAMCARP foams	156
8.5	Serrations in the stress-strain curve	158
8.5.1	The origin of serrations	158
8.5.2	The effect of uniformity in the cell structure on serrations.....	161
8.5.3	The effect of cell size on serrations.....	161
8.6	The effect of cell size on plastic collapse	162
8.6.1	Comparison of hydride- and carbonate-based foams	162
8.6.2	Lower limit of specimen size for carbonate-based foams.....	164
8.7	Local yielding mechanisms.....	165
8.7.1	Distribution of SiC particulate	165
8.7.2	Stages of plastic yielding.....	165
8.7.3	Cell face ductility in compression.....	168
8.7.4	Cell face ductility in tension.....	169
8.7.5	The link between foaming agent and stress-strain properties	171
9	Conclusions	173
10	References	176

Nomenclature

Greek Symbols

α	Measured cross deflection of a cell face cross section	m
χ	Aspect ratio of cells in a non-isotropic cellular structure	-
δ	Deflection of a beam at its midpoint	m
ε	Engineering strain	-
ε_{yield}	Yield strain	-
ε_d	Engineering strain at densification	-
$\dot{\varepsilon}$	Strain rate	s ⁻¹
ϕ	Fraction of solid material in a foam found in the cell edges	-
γ_{liquid}	Surface energy/tension of a liquid	N m ⁻¹ (J m ⁻²)
γ_{solid}	Surface energy of a solid	N m ⁻¹ (J m ⁻²)
$\gamma_{solid/liquid}$	Surface energy of a solid-liquid interface	N m ⁻¹ (J m ⁻²)
λ	Wavelength (1/frequency) of corrugations in a cell face	-
η	Viscosity of a liquid	Pa s (N m ⁻² s)
η_o	Reference viscosity of a liquid	Pa s (N m ⁻² s)
$\eta_{apparent}$	Measured viscosity of a liquid	Pa s (N m ⁻² s)
θ	Contact angle, diffraction angle	°, rad
ρ	Density	kg m ⁻³
ρ_{liquid}	Liquid density	kg m ⁻³
ρ_{solid}	Solid density	kg m ⁻³
ρ_X	Density of phase X	kg m ⁻³
σ	Engineering stress	Pa (N m ⁻²)
σ_{ys}	Yield stress	Pa (N m ⁻²)
$\sigma_{yield, upper}$	Upper yield stress	Pa (N m ⁻²)
$\sigma_{plateau}$	Plateau stress	Pa (N m ⁻²)
σ_{pl}	Plastic yield stress	Pa (N m ⁻²)
σ_c	Critical stress limit	Pa (N m ⁻²)
τ	Shear stress	Pa (N m ⁻²)
ν	Poisson's ratio	-

Roman Symbols

$a_{(X)}$	Activity of phase X	-
A_{PB}	Area of a Plateau border in cross section	m ²
C_x	Various numerical constants	-
d	Cell diameter	m
$d_{intercept}$	Intercept cell diameter in cross section	m
d_{CF}	Diameter of a circular cell face	m
D	Specimen size	m
E	Elastic modulus	Pa (N m ⁻²)
F	Force	N
$F_{buoyancy}$	Force acting on a bubble due to buoyancy	N
F_{drag}	Force acting on a bubble due to viscous drag	N
f	Volume fraction of solid phase dispersed in a liquid	-
f_{dec}	Fraction of foaming agent which has decomposed	-
f_{solid}	Volume fraction of fully dense solid at the base of a foam	-
f_{SiC}	Volume fraction of SiC in the foaming metal	-

Roman symbols, continued

$f_{\text{SiC,foam}}$	Volume fraction of SiC in the foam	-
f_{oxide}	Volume fraction of oxidised metal	-
f_{CaCO_3}	Volume fraction of calcium carbonate in the metal	-
$f_{\text{decomposed}}$	Fraction which has undergone thermal decomposition	-
f_G	Volume fraction of gas in a liquid foam	-
$f_{G,\text{max}}$	Upper bound limit on gas volume fraction in a liquid foam	-
f_L	Volume fraction of liquid in a liquid foam	-
g	Acceleration due to gravity, 9.81	m s^{-2}
ΔG^0	Standard free energy change	kJ mol^{-1}
I	Second moment of area of a cell edge	m^4
j	Aspect ratio (length/width) of a fibre between fibre junctions	-
L	Length of a cell strut	m
L_{PD}	Edge length of a pentagonal dodecahedron	m
l	Measured length of a cell face in cross section	m
m_X	Mass of phase X	kg
M_X	Relative molar mass of phase X	kg mol^{-1}
$n_{O(X)}$	Number of reacting oxygen atoms per formula unit of phase X	-
n_{CF}	Number of cell faces in a pentagonal dodecahedral unit cell	-
n_{PB}	Number of Plateau borders in a pentagonal dodecahedral unit cell	-
P	Total pressure	atm
pX	Partial pressure of phase X	atm
Q	Energy	J mol^{-1}
R	Universal gas constant, 8.3144	$\text{J K}^{-1} \text{mol}^{-1}$
r	Radius of curvature	m
r_{PB}	Radius of curvature of a Plateau border	m
S_{PD}	Surface area of a pentagonal dodecahedron	m^2
$S_{PD,\text{inner}}$	Inner surface area of a hollow pentagonal dodecahedron	m^2
t	Time	s
t_f	Foaming time	s, min, h
T	Temperature	$^{\circ}\text{C, K}$
T_m	Metal melting temperature	$^{\circ}\text{C, K}$
T_f	Foaming temperature	$^{\circ}\text{C, K}$
u_y	Flow speed in y direction	m s^{-1}
v	Velocity	m s^{-1}
v_{terminal}	Terminal velocity	m s^{-1}
V_{PD}	Volume of a pentagonal dodecahedron	m^3
V_X	Volume of phase X	m^3
w	Width of a cell face	m
w_X	Width of a surface film of phase X	m
$w_{\text{intercept}}$	Intercept width of a cell face in cross section	m
X_{phase}	Mole fraction of a phase	-
x,y,z	Cartesian coordinates	-

Subscripts & Superscripts

<input type="checkbox"/> <i>(s)</i>	Solid phase
<input type="checkbox"/> <i>(l)</i>	Liquid phase
<input type="checkbox"/> <i>(g)</i>	Gas phase
<input type="checkbox"/> <i>p</i>	Particulate phase
<input type="checkbox"/> <i>s</i>	Bulk property of the solid phase
<input type="checkbox"/> *	Property of the porous material
<input type="checkbox"/> <i>l</i>	Property measured during mechanical loading
<input type="checkbox"/> <i>u</i>	Property measured during mechanical unloading
<input type="checkbox"/> <i>cr</i>	Critical
<input type="checkbox"/> <i>x,y,z</i>	Property in the <i>x,y,z</i> direction
<input type="checkbox"/>	Average of a property

Abbreviations

AES	Auger electron spectroscopy
BSE	Backscattered electron imaging
DSC	Differential scanning calorimetry
DTA	Differential thermal analysis
EDX	Energy dispersive X-ray spectroscopy
LVDT	Linear variable displacement transducer
MMC	Metal-matrix composite
SEM	Scanning electron microscopy
TGA	Thermogravimetric analysis
XPS	X-ray photoelectron spectroscopy

All alloy compositions are in wt.% unless specified otherwise.

1 Introduction

1.1 Cellular materials

Cellular structures are widespread in natural materials - bone, wood and leaf structures are all examples. These structures combine a relatively high stiffness and strength with a low density, and are generally used in situations where weight needs to be minimised, often with the size and shape of the cells matched to requirements in different parts of the structure to improve efficiency. Cellular structures also provide enhanced resistance to damage or sudden fracture, as their relatively open structures can absorb large tensile and compressive strains[1].

It is perhaps not surprising that the properties of natural cellular structures have been emulated in manufactured engineering materials[2]. Polymeric foams are widely used as a protective casing in packaging, and as an impact resistant material in applications such as cycle helmets, principally due to their ability to undergo large compressive strains and absorb significant quantities of energy at a relatively low compressive stress[3]. They are also used as a light structural material, for example as a core material in sandwich panels, due to their high specific bending stiffness and strength[4].

Metals can absorb large amounts of energy in deformation due to dislocation motion. Metallic foams could thus provide an engineering material with the advantageous mechanical properties of polymeric foams, suitable for use in situations where higher yield stresses and energy absorption are required.

1.2 Development of metallic foams

Metallic foams can be broadly divided into two categories: closed-cell foams, which contain sealed pores, and open-cell foams, where the porosity is contiguous. Both types of foams have been in development for over 50 years. However, for most of this time they have been viewed as an academic curiosity rather than a serious engineering material. Two-dimensional metal honeycomb structures, which share many of the properties of metallic foams, have found widespread use in the aviation industry[5, 6]. This owes much to the reliability of the production processes: whereas honeycombs have uniform structures which can easily be checked for reliability, current metallic foams are either too costly and complicated to produce, or have stochastic cell structures which are too irregular to be considered as an engineering material.

The mid-1990s saw a surge in interest in the development of metallic foams, which corresponded with significant improvements in the manufacturing processes available[7]. In addition to a large number of individual research projects, two large research programmes were

launched: the four-year Multidisciplinary Research Initiative on Ultralight Metal Structures linked research in UK and US universities from 1996, and the DFG Priority Programme for Cellular Metals was launched by several German universities in 1999. Many of the findings are reviewed in Chapters 2-4. Several companies have recently begun the commercialisation of metallic foams.

1.3 Uses of metallic foams

Open-cell foams provide a tortuous structure with a large surface area, with high electrical and thermal conductivity. This has led to their use in a number of profitable niche applications such as catalyst supports, heat exchangers, high temperature filters, consumable battery electrodes and electromagnetic absorbers.

No single material property of closed-cell metallic foams is exceptional. The selling point of such foams in general, and aluminium foams in particular, lies in a combination of properties not shown by any other material - notably high compressive strength, low density, and the ability to undergo a high degree of permanent plastic deformation at an almost constant yield stress. Two main uses have been suggested: as an impact absorber, and as a light structural material[8].

Impact absorber

When compressed, foams undergo only limited elastic deformation before the onset of plastic collapse. This generally involves the propagation of a localised band of failed cells throughout the material at almost constant stress, accompanied by extensive plastic deformation. The isotropic structure of foams means uniform deformation is possible for any direction of loading. In principle, metal foams are thus attractive in terms of the amount of plastic deformation they can undergo per unit mass, since the cell walls are relatively unconstrained. Foams that exhibit sufficiently ductile local collapse can be used as a buffer against any type of impact, for example to protect the occupants of cars or as a blast protection material. In practice, premature structural failure often prevents this potential being realised, as discussed further in Chapter 4.

Light structural material

Foams intrinsically combine relatively high stiffness with lower density than their parent material. It is important to note that, if only the direct strength is considered, foams often have a similar or slightly worse performance than solid material of the same weight. The advantage of foams becomes apparent when bending stresses are considered as a function of weight. The mass distribution of cellular structures increases the overall moment of inertia of the material, giving a far higher specific bending stiffness and strength than for the corresponding weight of bulk metal. This makes foams useful as high-strength, low-density load-bearing components in

automotive and aerospace applications, with most workers envisaging some form of bonded structure, where foam is used as a central element encased in an outer metal sheet[9, 10]. Compared with sandwich constructions produced using conventional honeycomb materials these potentially offer simpler and lower-cost production, and increased resistance to shear due to the isotropic nature of foams. Foams can also be used to fill beams or pipe structures, where they offer increased structural rigidity. However, the low tensile strength of most metallic foams, combined with the difficulty of using a stochastic material in a structural role, mean that much of the initial development of metallic foams has been concerned with use as an impact absorbing material.

Although metallic foams show considerable potential, there remain formidable obstacles to their widespread use. One is the difficulty of mass-producing foams at a reasonable cost. Many processes developed to foam metals incorporate too many complex or rate-limiting steps, or are so sensitive to production parameters that it is impossible to use them on a large scale. Others involve the use of costly additives, or impose unduly narrow restrictions on the materials that can be foamed. The processes that produce foams at a sufficiently low cost and high rate for large-scale use are at present incapable of producing foams with sufficient reproducibility or structural reliability to be considered as an engineering material.

1.4 Structure of this thesis

The current state of the art with regards to the production of metallic foams is reviewed in Chapter 2. Chapter 3 reviews the production of closed cell foams with gas generating agents, and presents the issues that affect the stability of standing liquid foams. The mechanical properties of currently available foams, and their relation to features of the foam macro- and microstructure, are reviewed in Chapter 4.

The experimental procedures used in the present work for foam production, and the techniques used in the characterisation of the materials used and the cellular structures obtained, are specified in Chapter 5.

Structural and microstructural features of the foams produced are examined in Chapter 6. Chapter 7 discusses the mechanisms and characteristics of foam production using calcium carbonate, and Chapter 8 presents and discusses results concerning the bulk mechanical behaviour of these foams, and the influence of the cell structure and microstructure on these properties. Finally the principal results of this thesis, and their implications for the field of metallic foam research and production, are summarised in Chapter 9.

2 Types of Metallic Foam & Overview of their Production

A wide range of processes have been developed to produce metallic foams, ranging from general foaming techniques applicable to almost any metal to specialised and highly specific processes. These differ in the nature of the foams produced, as well as the ease of processing, the degree to which control can be obtained over the foam structure by adjusting process parameters, the scope for tailoring the metals and alloys used to requirements, and the potential for adapting the processes to rapid and cost-effective industrial production. In this chapter a critical overview is given of the processes developed to date.

2.1 Key features of metallic foam production

Although many metallic foams are indeed produced by forming a foam of a liquid metal and freezing it before the cell structure collapses, the term 'metal foam' is here applied more widely, to encompass any metal with a high degree of porosity. The process used to produce a metal foam defines many of the properties of the foam, including the level of porosity which can be obtained, the nature, scale, shape and uniformity of the porous regions, and the extent to which the porous regions are interconnected. Some processes offer scope for fine-tuning the structure for a given application by adjusting processing parameters. The microstructure of the parent metal is also important, with some processes imposing restrictions on the metals or alloys which can be used, or requiring the addition of other materials which can have a deleterious effect on mechanical properties. The degree of reproducibility of a process is also important: any process which is unduly sensitive to slight variations in processing parameters is likely to produce less uniform foams, susceptible to the presence of flaws and defects. Last, but not least, the complexity and speed of the process, whether it can be run continuously or as a batch process, and whether it is capable of producing net-shape foamed components (avoiding the need for subsequent machining) will directly affect the cost of the end product[11].

2.2 Production of open-cell foams

2.2.1 Processes based on sintering

Sintering of metal powders

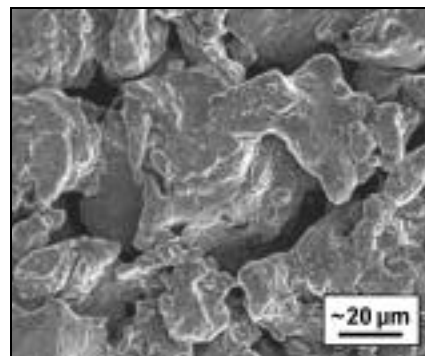
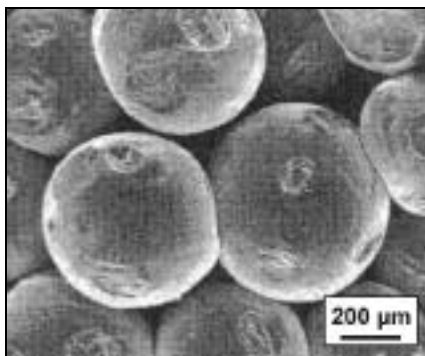
Arguably the simplest method of producing an open-celled foam consists of sintering powdered metals, usually produced by gas atomisation[12], at a temperature close to their melting point to fuse the particles together to produce a material with interconnected porosity. Sintering is often carried out in a vacuum or inert atmosphere to prevent surface oxidation, and typically takes 1-2 hours. The porosity of the end product, shown in Figure 2.1, depends on the packing efficiency of the powder. It is usually low, with relative density – defined as the ratio of the density of the foam, ρ^* , to that of the metal, ρ_s , between 0.5 and 0.8. Lower density can be obtained by mixing particles of a volatile fugitive material with the powder, which evaporates or decomposes at the sintering temperature to leave additional voids in the structure. Chemical

foaming agents which release a gas at high temperatures can also raise the porosity, if sintering temperatures are sufficiently high to allow limited plastic flow[13-15].

Figure 2.1:

(a) Porous titanium made by sintering of powders in a reducing atmosphere [16].

(b) Porous stainless steel produced by cold isostatic compression followed by liquid-phase sintering[17].



(a)

(b)

Metal fibres pack to give significantly higher porosity than powders (with $\rho^*/\rho_s \sim 0.05$), as shown in Figures 2.2 & 2.3[18].

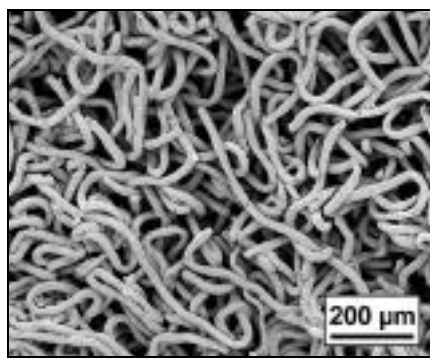


Figure 2.2: SEM micrograph of a porous material produced by sintering extruded stainless steel fibres.

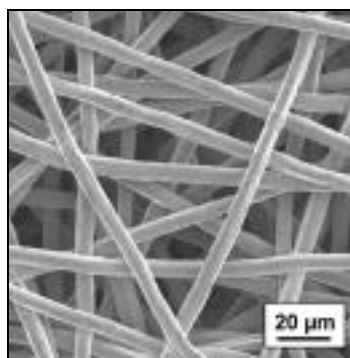
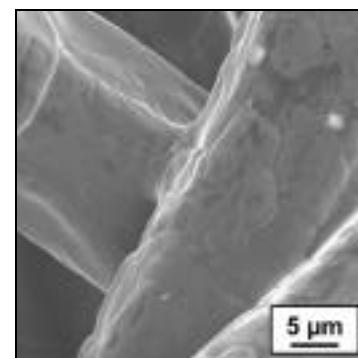


Figure 2.3: SEM micrograph of a porous material produced by sintering drawn stainless steel fibres, and an enlarged view of a sintered joint between two fibres.

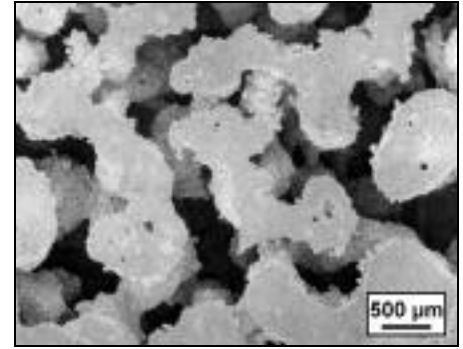


Reactive sintering

Sintered material foams have a relatively poor specific strength. Stress is concentrated at weak contact points in the narrow sintering necks, where failure occurs, while the bulk of the mass in the centre of particles has little effect[16]. This can be avoided by reactive sintering, where two powders which will react exothermically to form an intermetallic compound are mixed, pressed to form a porous compact, and ignited[19]. The exothermic reactions release sufficient heat to propagate the reaction through the sample[20, 21]. The porosity of the compact generally increases by 10-25% on reaction, and the particles coalesce to form a closely bonded open-cell foam. To date Fe-Al systems (producing FeAl_3 , FeAl_2 and Fe_2Al_5) and Ni-Ti (producing NiTi) have been foamed, as shown in Figure 2.4.

Figure 2.4:

A porous structure formed by reactive sintering of an equiatomic mixture of Ti and Ni[21].



This type of process is rapid and energy efficient, with $\rho^*/\rho_s \sim 0.45$ and cell sizes of under 1 mm obtained. The range of alloys that will react is, however, limited by the need for an appropriate reaction, and the intermetallic compounds can be brittle.

Sintering of hollow spheres

Lower densities can be obtained if hollow powders are used[22]. Gas atomisation of metals inevitably produces a proportion of hollow particles, with diameter under 1 mm, that can be separated from dense powders by a sedimentation process[23]. Larger hollow spheres can be produced by a process illustrated in Figure 2.5. Hollow 'green' spheres of diameter ~ 4 mm can be made with a slurry containing dispersed metallic particles, a binder, stabilising and dispersing agents, and a continuous volatile phase, and subsequently fired to fuse the metal particles and evaporate the other phases[24, 25]. They can also be produced directly from molten aluminium, as shown in Figure 2.6[26].

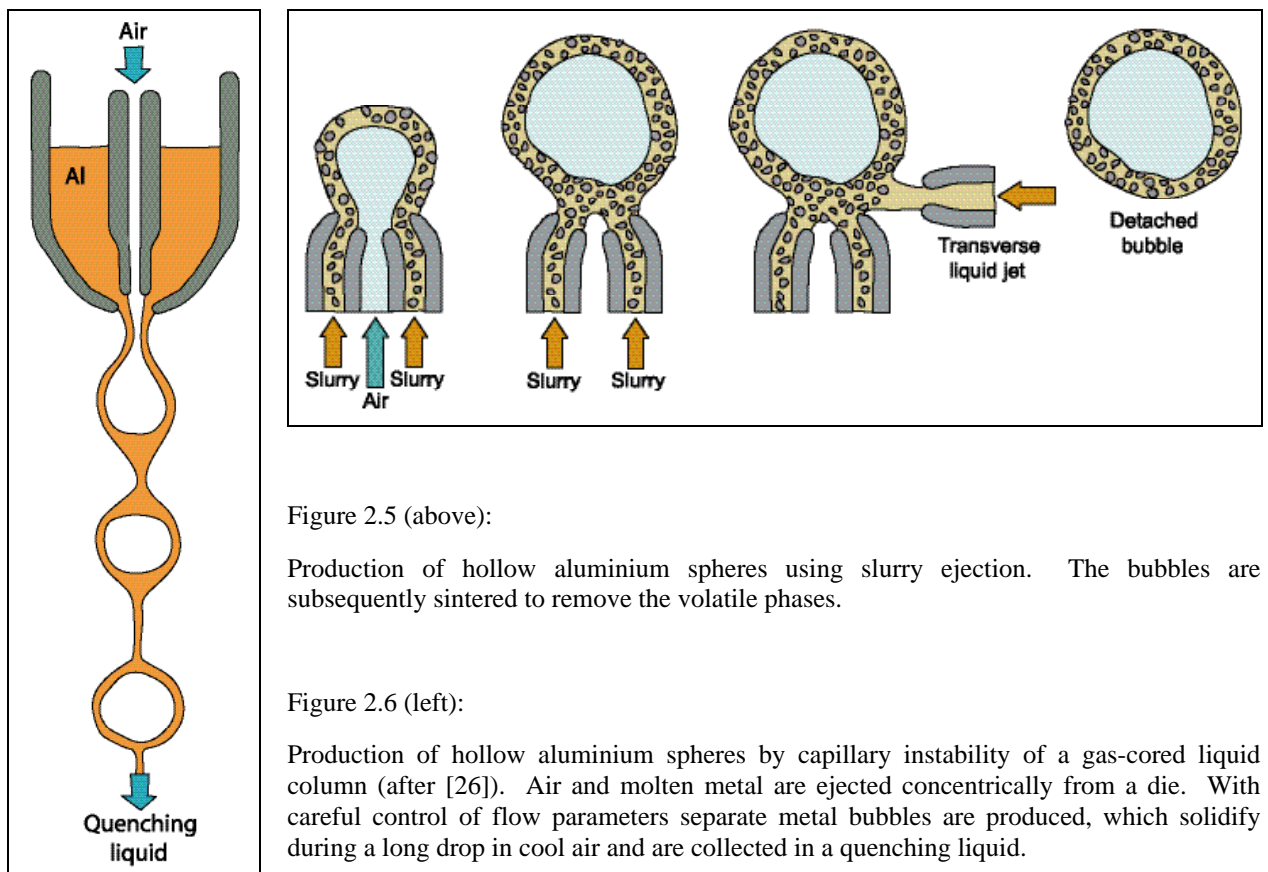


Figure 2.5 (above):

Production of hollow aluminium spheres using slurry ejection. The bubbles are subsequently sintered to remove the volatile phases.

Figure 2.6 (left):

Production of hollow aluminium spheres by capillary instability of a gas-cored liquid column (after [26]). Air and molten metal are ejected concentrically from a die. With careful control of flow parameters separate metal bubbles are produced, which solidify during a long drop in cool air and are collected in a quenching liquid.

Hollow spheres are bonded together by sintering for up to 24 hours, either in a reducing atmosphere or in air with the spheres coated with a bonding slurry[27]. As the spheres can easily be sorted by size, the foams produced can have highly uniform structures with $\rho^*/\rho_s \sim 0.1-0.2$.

Hollow sphere foams have recently been produced at lower cost by using spheres of expanded polystyrene as a template for the spheres, as shown in Figure 2.7. Sintering the compact burns out the polystyrene, evaporates the volatile component of the slurry and fuses the spheres together[28]. This process offers a slightly lower processing cost, as there is only one heating step, and no requirement for precise flow control. The spheres can be more effectively compacted, improving contact between the spheres[29].

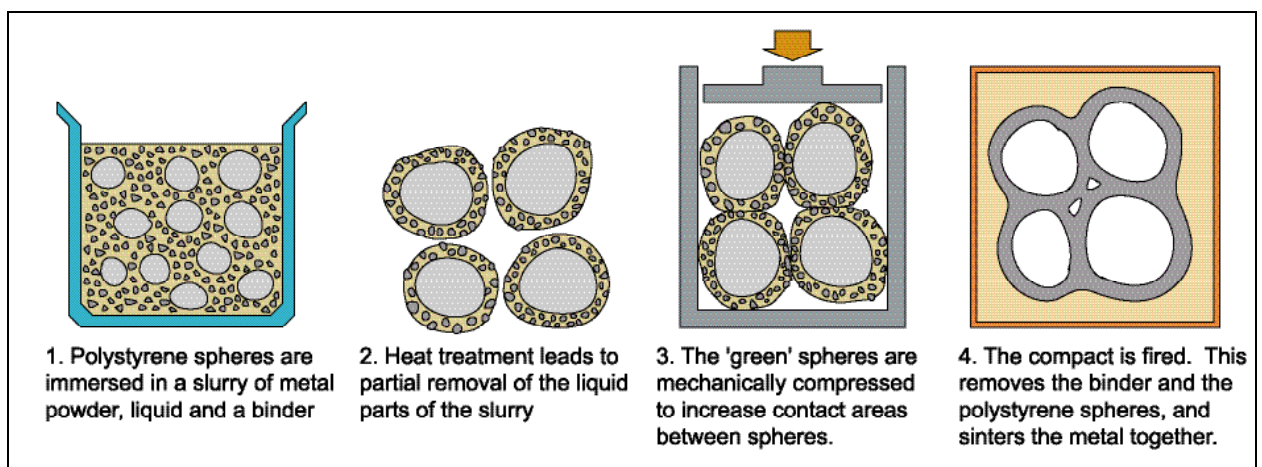


Figure 2.7: Production of a hollow sphere foam using slurry-coated polystyrene spheres as a template.

Hollow sphere foams, shown in Figures 2.8-2.10, have interesting properties, with a controlled mixture of open and closed porosity, and can be produced as a net-shape product with a high degree of uniformity. However the cost and complexity of production make them unlikely to find widespread application.

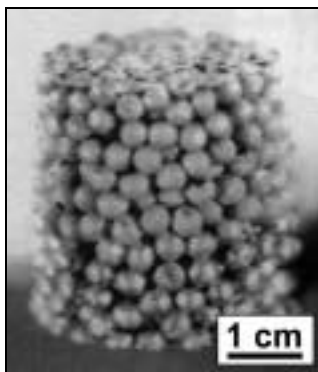


Figure 2.8: A foam produced by sintering expanded polystyrene spheres coated with a slurry containing stainless steel[28].

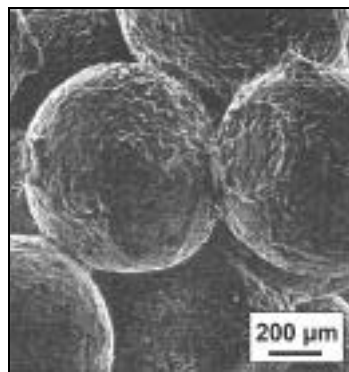


Figure 2.9: Necking between stainless steel spheres bonded using a magnetite slurry[30].

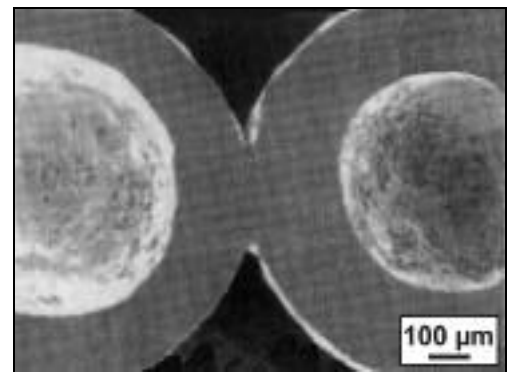


Figure 2.10: Cross section showing necking between hollow Ni spheres sintered at 1300°C for 24 hours[23].

2.2.2 Investment casting

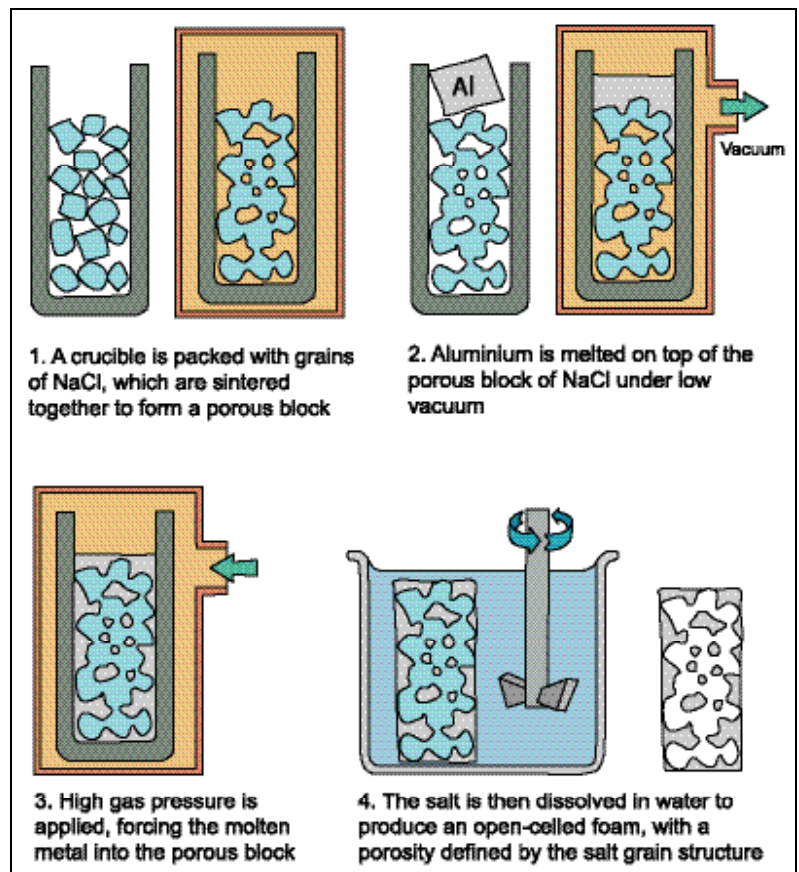
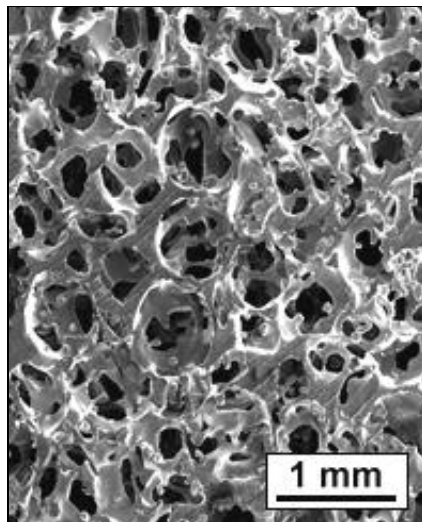
Use of disposable templates of the cell structure

A variety of casting processes, mainly used in the production of open-cell foams, are based on the use of disposable templates of the cell structure. In the earliest such process, coarse rock salt (NaCl) was sintered in air for a few hours to fuse the grains together, effectively forming a mould of an open cell foam[31, 32]. Molten metal was then poured in to infiltrate the pores, and the salt dissolved to produce an open-cell foam with cell size of ~ 3-4 mm.

The use of hot-wall infiltration, which reduces the tendency of the metal to solidify before full infiltration is achieved, and of combinations of partial vacuum and high pressure applied during the infiltration process, have recently made it possible to produce far finer-scale structures, as shown in Figure 2.11. The foams thus produced have cell sizes as small as 400 μm , with ρ^*/ρ_s of 0.2-0.3[33, 34].

Figure 2.11:

Production of open-cell foams with a disposable sintered salt template of the cell structure, and SEM micrograph of a typical foam produced.



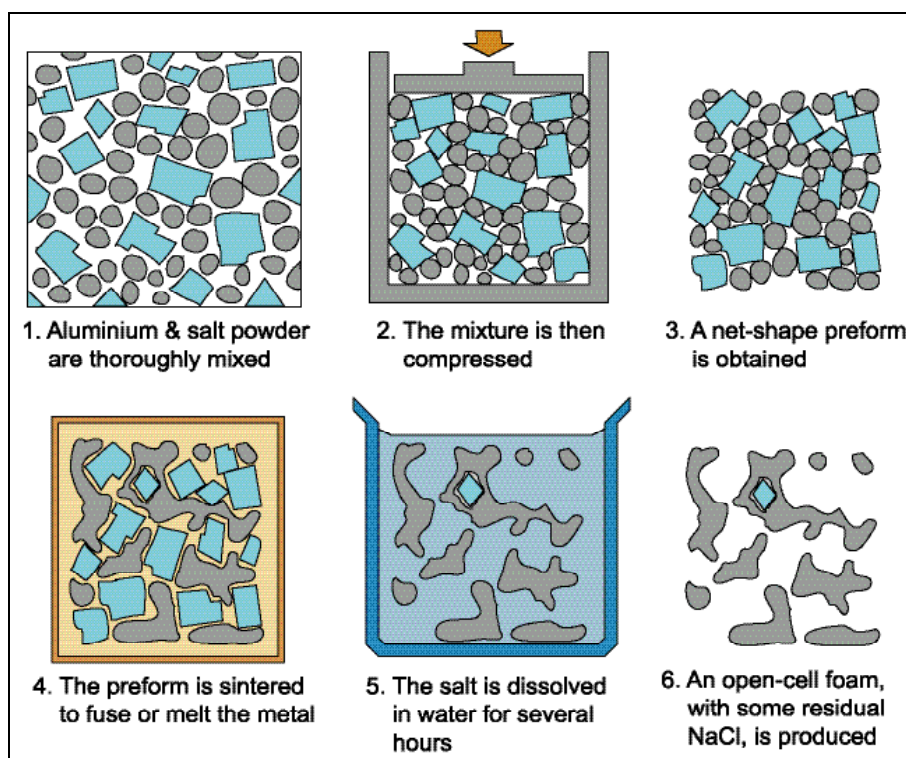
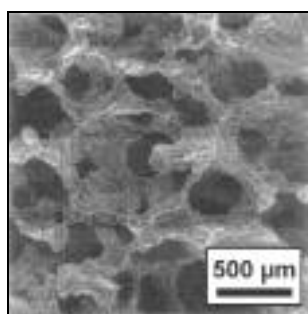
Infiltration processes do not require expensive metallic powders or fibres, and almost any alloy can be used provided it melts at a temperature below that where the template melts. As the elements forming the mould can be carefully controlled, the foams produced are characterised by a high degree of structural uniformity. The process is relatively complex, requiring extended sintering and dissolution. The lower limit of cell size and the upper limit of batch size obtainable

are determined by the need for full infiltration of often tortuous templates and dissolution of the salt in a reasonable time.

In a variant of the process, shown in Figure 2.12[35], powdered metal has been mixed with powdered salt and compacted to form a dense block. This is then sintered, above or below the melting temperature of the metal (but below that of the salt), followed by dissolution of the salt, producing foams with $\rho^*/\rho_s > 0.2$. The process is unlikely to find widespread use, as it combines the complexity of the pressure infiltration process with an additional requirement for relatively costly powdered metal. It appears to produce fewer connections between the salt grains, leading to a denser, less porous structure, containing residual NaCl.

Figure 2.12:

Production of a foam by mixing and sintering salt and aluminium powders, and removing the salt, and SEM micrograph of a foam thus produced[35].

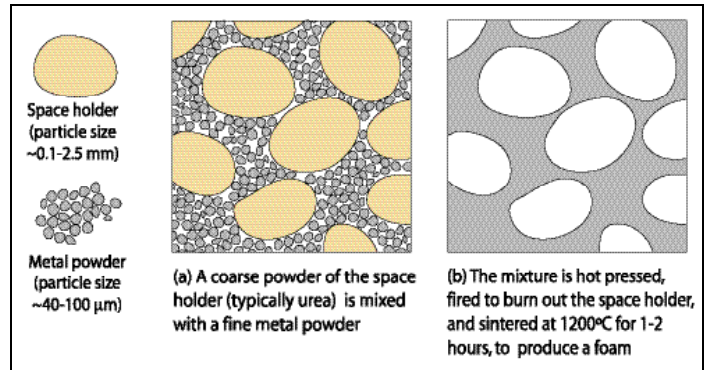


In another approach[36], polystyrene particles are mixed with an adhesive resin, and fired to produce an interconnected resin-coated mould. High pressure (460 MPa) is then used to infiltrate the mould with metal in under 0.2 s, before the polymer decomposes. The polystyrene is burnt out to produce an open-cell foam with ρ^*/ρ_s of 0.14-0.27 and cell size of 1-3 mm. This costly process is restricted to the production of small samples.

In a process shown in Figure 2.13, primarily used to produce closed-cell foams of metals and alloys with high melting temperatures, a mixture of powdered metal and a volatile space holder is compacted and sintered to form closed cell foams with ~ 1 mm cell size and $\rho^*/\rho_s > 0.25$ [37, 38].

Figure 2.13:

Production of closed cell foams by sintering of powders with a space holder



Infiltration of a hollow sphere compact

Hollow spheres can also be used as a template of the cell structure. Ceramic or metallic spheres with diameter as small as $\sim 60 \mu\text{m}$ are loosely packed, sometimes preheated, and infiltrated under relatively low pressure ($\sim 0.5 \text{ bar}$) with molten metal, as shown in Figure 2.14[39-42]. The spheres can be sorted by size and arranged in highly regular structures, or randomly dispersed[43]. The limited packing density which can be achieved with spheres of uniform diameter means ρ^*/ρ_s is usually over 0.4[44].

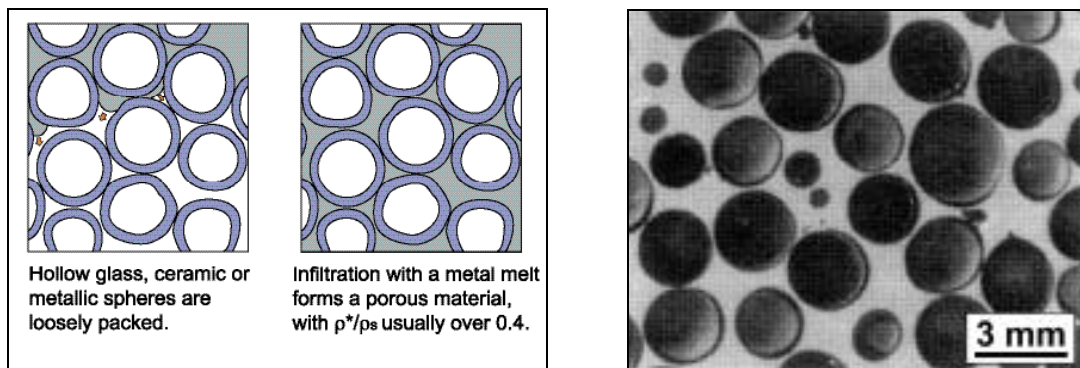


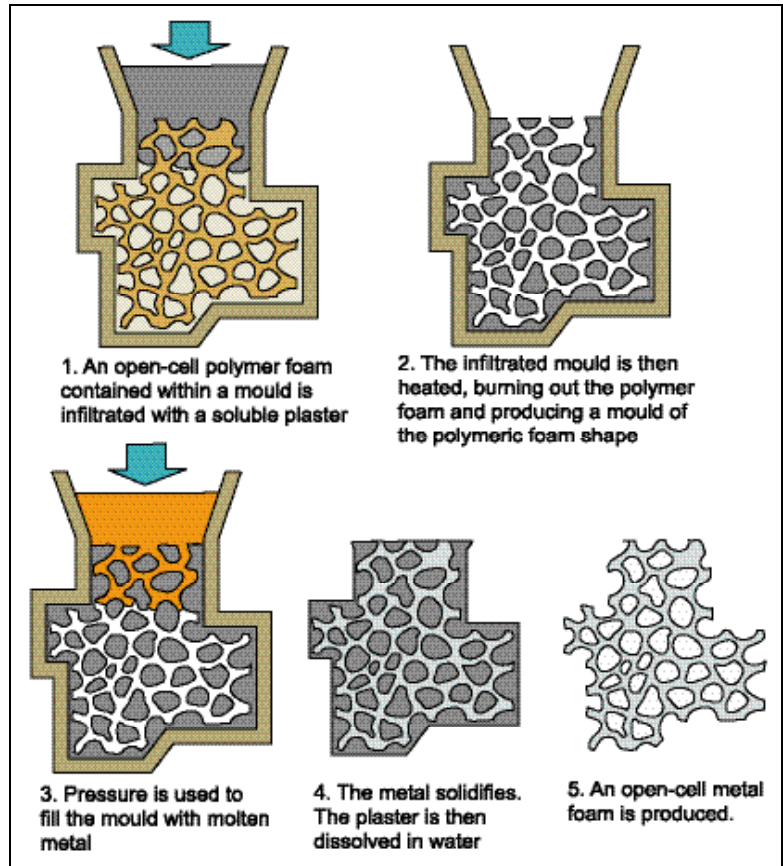
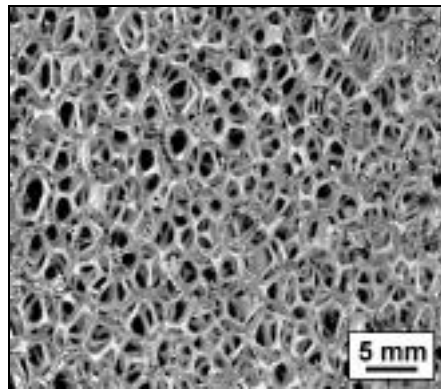
Figure 2.14: Infiltration of hollow spheres, and a closed-cell foam produced by infiltrating alumina spheres with magnesium[41].

Replication of a polymeric foam structure

The relative ease of producing high-porosity open-celled polymeric foams with uniform cell structures has prompted their use as templates in the production of metallic foams by two-stage investment casting processes[45-47]. As shown in Figure 2.15, the polymer – generally polyurethane – is infiltrated with plaster and fired to burn out the polymer. The mould is then filled with molten metal, often aided by combinations of vacuum and external pressure, and the plaster is dissolved.

Figure 2.15:

Production of an open-cell foam using a polymeric foam as a template, and image of a Duocel™ foam produced by ERG Inc[48].



Foams can be produced with a wide range of metals and alloys, with ρ^*/ρ_s as low as 0.03. This process shares many of the advantages and disadvantages of processes employing salt templates. The lower limit of cell size, and the upper limit of batch size, are similarly constrained by the need for full infiltration of a tortuous mould, and for full dissolution of the plaster. Areas of varying porosity, or even solid metal, can be incorporated as the polymer mould is assembled[46, 49]. Duocel™ foams produced by this method are used as heat exchangers, liquid and gas baffles, high-purity porous electrodes, and chemical filters[48].

Chemical decomposition on a disposable precursor

Open-cell polymer foams can also be used as a deposition template, as shown in Figure 2.16. A polymeric foam is coated with a substance which absorbs infrared radiation, generally carbon black[50] or appropriate pigments[51]. Radiation locally heats the coated surface, which is exposed to an atmosphere of $\text{Ni}(\text{CO})_4$ gas. This decomposes at high temperature to $\text{Ni}_{(s)}$ and $\text{CO}_{(g)}$ at the hot surface, coating the polymer with nickel. The polymer is subsequently burnt out to produce an open-cell foam with hollow struts.

With no direct restriction on cell size, extremely fine-scale foams can be produced. The range of metals is, however, limited by the need for a suitable deposition reaction. The foams produced, sold under the trade name Incofoam™, are used as filters and porous battery electrodes.

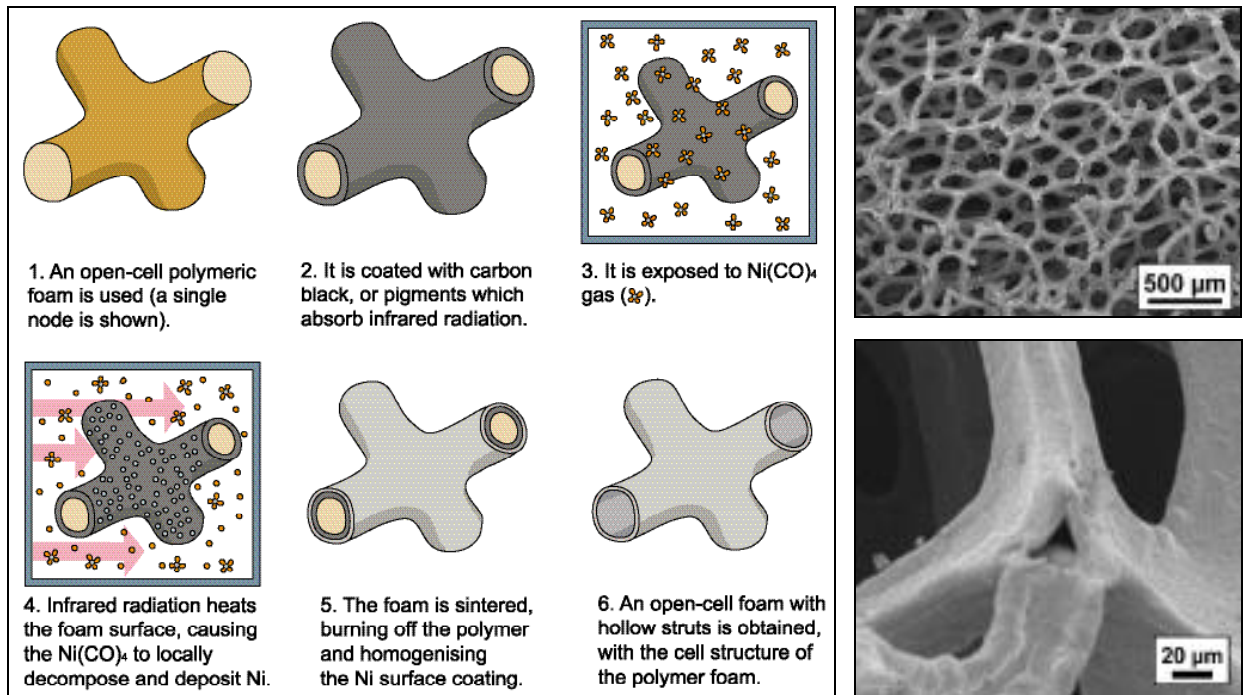


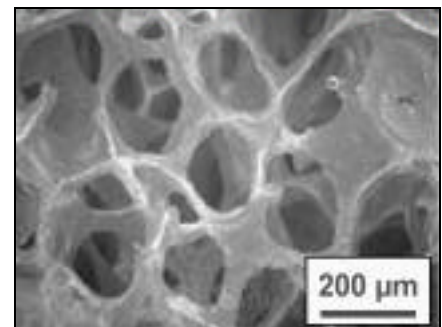
Figure 2.16: Production of an open-cell nickel foam by chemical decomposition on to a disposable polymeric precursor, and SEM micrographs of an open-cell Incofoam™ nickel foam at two levels of magnification, showing the hollow struts.

Electrodeposition on a disposable precursor

In a similar process, metal is electroplated on to the surface of an open-cell foam. The surface of the polymer is made to conduct, by coating with carbon black[51] or vaporising a thin metal layer on it[52]. It is then electroplated and sintered to remove the polymer. A Celmet™ porous electrode thus produced is shown in Figure 2.17.

Figure 2.17:

SEM micrograph of a Celmet™ aluminium foam produced by electroplating of a conducting polymer foam.



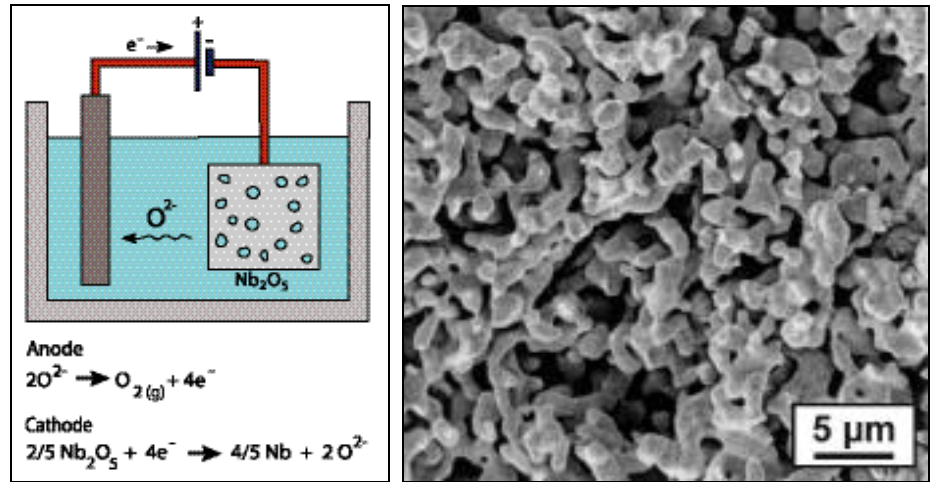
2.2.3 Exploiting chemical characteristics

Porous materials by direct deposition

A recent process[53, 54] to extract reactive metals such as Nd, V, Nb and Ti by electro-deoxidation of their oxides in a molten salt solution produces the metals in the form of an extremely fine open-cell foam, as shown in Figure 2.18.

Figure 2.18:

Electrolytic cell for the reduction of pellets of the oxides of reactive metals, and SEM micrograph of an Nb foam produced by electro-deoxidation of Nb_2O_5 .



To produce Ti foams, a voltage of $\sim 3 \text{ V}$ is applied to the oxide in a bath of molten CaCl_2 at 950°C for 12 hours. Although costly and relatively hazardous, this process can produce foams on an extremely fine scale.

Directional solidification

The large difference in solubility of hydrogen between liquid and solid metals can be exploited to produce porous metals by the controlled solidification of metal-gas eutectic systems[55, 56]. In the GASAR process, a high pressure of hydrogen is applied to a molten metal to dissolve gas in the melt. The melt is then transferred to a mould with a cooled base, as shown in Figure 2.19, prompting directional eutectic solidification at $\sim 5 \text{ mm s}^{-1}$. Gas released at the solidification front nucleates elongated pores, in much the same way as a lamellar structure can be formed in a metal-metal eutectic.

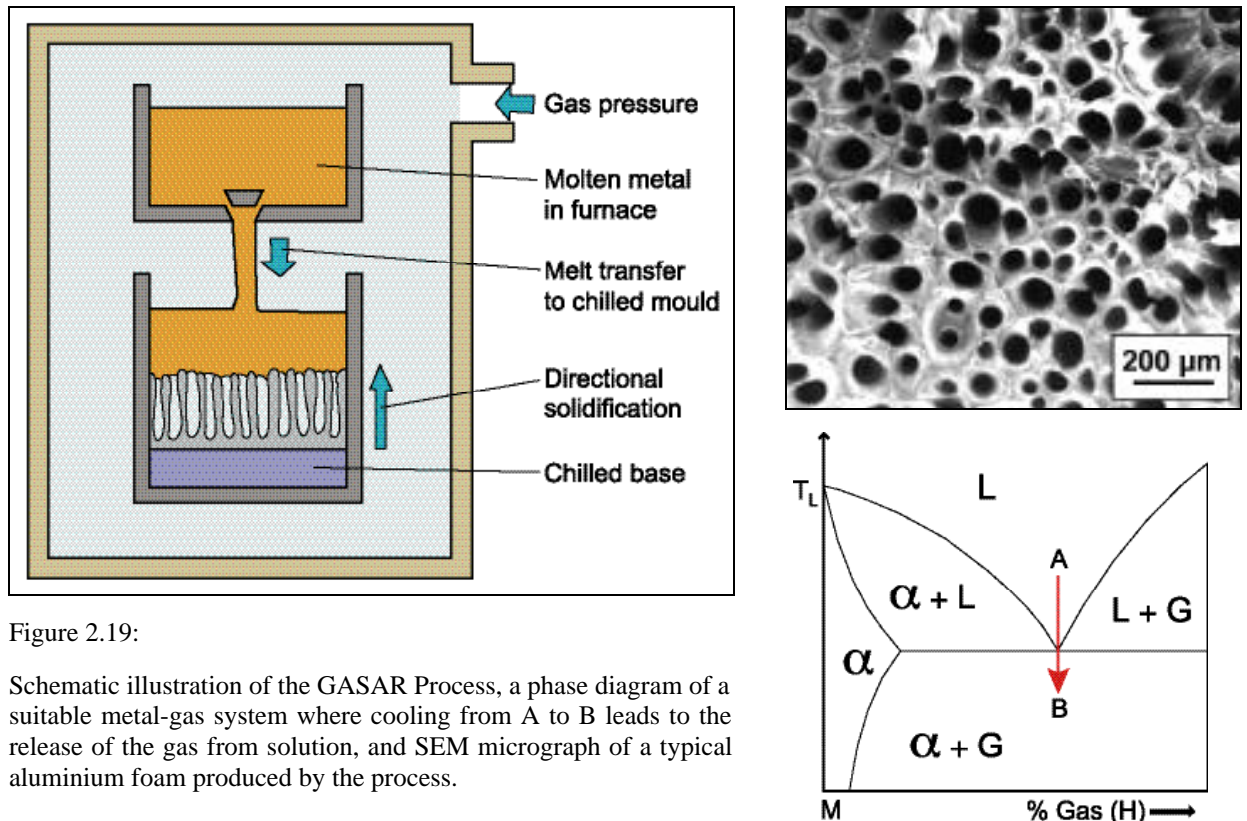


Figure 2.19:

Schematic illustration of the GASAR Process, a phase diagram of a suitable metal-gas system where cooling from A to B leads to the release of the gas from solution, and SEM micrograph of a typical aluminium foam produced by the process.

The foams obtained – sometimes called lotus structures – have been produced with Ni, Cu, Al, Fe and Mg, with pore diameter between 10 μm and 5 mm and minimum ρ^*/ρ_s of 0.35[57]. The cell structures are sensitive to fluctuations in pressure and cooling rate[58, 59]. The explosive nature of hydrogen means its use near metal melts is hazardous; however recent results suggest nitrogen is equally suitable for the foaming of iron[60]. The complexity of the production process probably precludes the widespread use of such foams.

2.3 Production of closed-cell Foams

2.3.1 Exploiting chemical characteristics

Alloy systems with a volatile phase

In an early process shown in Figure 2.20, a metal is melted inside a pressure vessel with another metal of significantly lower melting point, and heated to a temperature where the more volatile component will vaporise[61, 62]. The high pressure causes the molten metal to become supersaturated with vapour. The pressure is then suddenly released, prompting the rapid expansion of the volatile phase contained within the molten metal, producing a foam of mostly closed pores with a diameter of 1-3 mm.

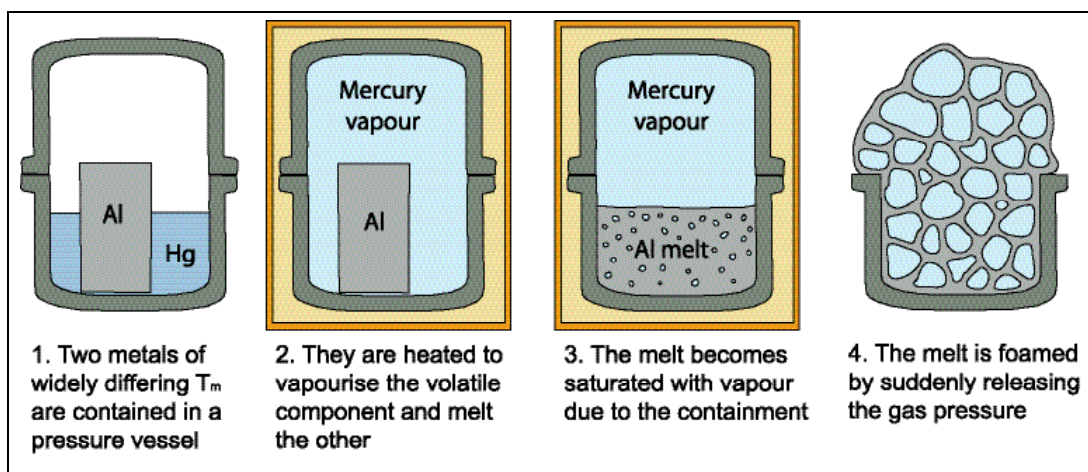


Figure 2.20: Production of a foam by expansion of a supersaturated volatile phase

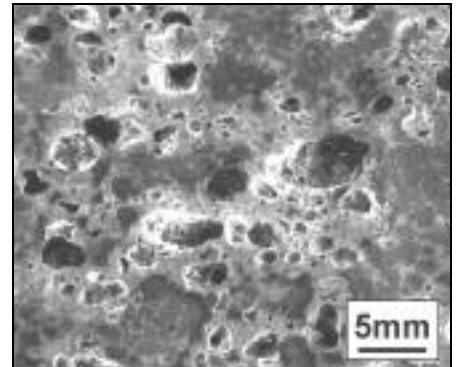
All the volatile metals suggested - mercury, magnesium, zinc and cadmium - are hazardous, and the process involves handling rapidly expanding metals at elevated temperatures. In variants on this process, applying external pressure of hydrogen, and mixing the melt with ammonia and maintaining sufficient external pressure to prevent its escape, sought to avoid the use of volatile metals[63]. With no clear way to stabilise the foam against immediate collapse, and little scope for control over the cell structure, such methods were never widely used. In a variant on the process, a solid mercury-copper amalgam was heated at temperature sufficient to drive off the mercury, to form porous copper[64].

Porosity caused by diffusion

The Kirkendall effect has been used to generate porous materials. Powders of two metals - one of which is chosen to have significantly higher diffusivity than, and solid solubility within, the other - are mixed, compacted, and annealed for 20-50 hours. The component with the higher diffusivity diffuses preferentially into the other component creating pores. A porous material thus produced is shown in Figure 2.21. ρ^*/ρ_s of ~ 0.6 has been achieved in Zn-Al[65] and Cu-Ni[66] systems. Severe restrictions on the metals that can be used, and extended processing times, mean that this process has few advantages over powder sintering.

Figure 2.21:

A porous structure formed by Kirkendall diffusion, containing 73% Zn, 27% Al, formed by annealing an Al-Zn mixed powder compact for 48 hours[65].



2.3.2 Direct addition of gas to metals

The simplest method of foaming a liquid melt, illustrated in Figure 2.22, involves direct injection of bubbles of gas. The key requirements are for a method of producing and efficiently dispersing fine bubbles, and of keeping them in place long enough for solidification to occur before they escape[67-69]. The foaming gas is dispersed with a rotating impeller. Bubbles rise to the melt surface, and are drawn out on a conveyor belt, gently rolled while still partly molten to produce a smooth surface, and cooled. Continuous sheet of solid foam is produced, as shown in Figure 2.23. This type of process has been commercialised by Norsk Hydro™, Alcan™ and Cymat™ Corporation.

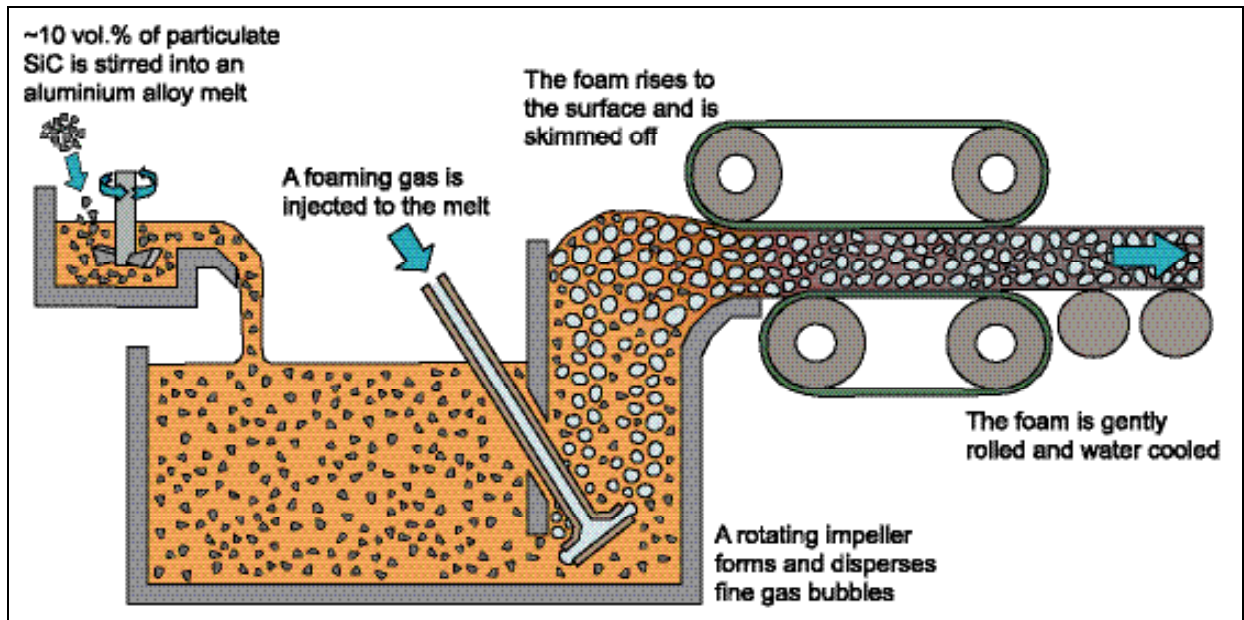
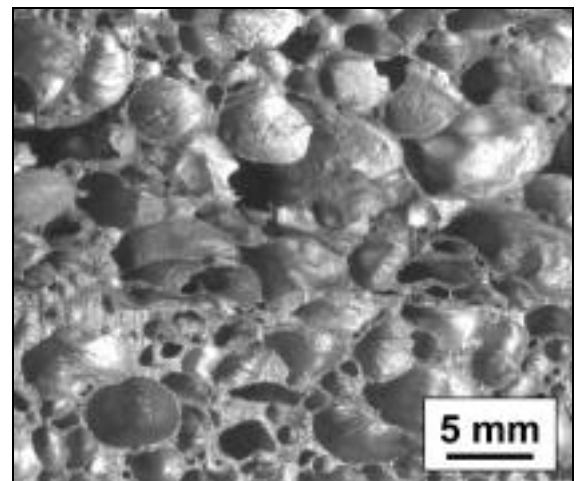


Figure 2.22:

Process for the continuous production of foams by direct gas injection, after [67].

Figure 2.23:

Optical cross section of an Alcan™ Al-9wt.% Si foam produced by direct injection of gas to a viscosity-enhanced melt.



The free standing liquid foams produced are inherently unstable. Drainage of molten metal towards the base of the foam produces density gradients in the foam sheets[70]. Bubbles coalesce under the action of surface tension, giving rise to larger cells in the centre of the sample, which is cooled more slowly, and at the top of the foam where the cell walls are thinner. In order to minimise these effects, fine refractory powders or fibres – typically 10 vol.% of 10 μm SiC – are mixed into the melt. This increases the melt viscosity, as well as segregating preferentially to the gas-liquid interface to act as a surfactant material[63, 71]. Combined with vertical extraction of the foam to eliminate the density gradients, this enables foam sheets to be continuously produced in large volumes at low cost, which are currently used in the large-scale production of blast- and impact-resistant doors. Work concerning the stability of liquid foams is reviewed in Chapter 3.

The foams have a fairly irregular structure, since the volume fraction of refractory particles that can be added is limited to levels that do not completely eliminate melt drainage and cell coalescence. The process relies on a relatively low viscosity for efficient dispersion of the gas bubbles from the impeller, limiting the extent to which the viscosity can be raised. Stirring of

the melt to aid gas dispersal is possible, but can destroy the foam structure by destroying the molten walls between adjacent bubbles.

2.3.3 Use of foaming agents

Rather than bubbling gas directly to molten metal, a powdered chemical foaming agent, which is stable at room temperature but releases a gas at the melt temperature, can be stirred into the melt[72-74]. Titanium hydride (TiH_2), the only foaming agent used commercially, decomposes to titanium and hydrogen gas at temperatures above $\sim 400^\circ C$ by the reaction:



Direct addition of foaming agent to a thickened melt

The foaming agent can be added directly to molten metal, as illustrated in Figure 2.24. Provided the powder can be dispersed evenly before the onset of decomposition, the hydrogen released forms pores throughout the metal. As with the direct addition of gas, it is necessary to stabilise the molten foam against collapse, which is usually achieved by adding a reactive alloying element such as calcium[75] or magnesium[76] to the melt, and stirring it vigorously while air is bubbled through it. This raises the viscosity by generating a dispersion of fine solid oxide particles *in situ*.

This process is used commercially to produce AlporasTM aluminium foams[77-79]. Air is stirred into a melt containing 1.5 wt.% Ca for 6 minutes at $680-720^\circ C$, forming fine solid particles of CaO and $CaAlO_4$. 1.6 wt.% of TiH_2 is then added to the melt, which is held at $680^\circ C$ for 4-15 minutes. The initial gas produced is mostly burnt off, but the foam then expands[75]. A ductile and relatively uniform cell structure is obtained in batches of up to 160 kg, with ρ^*/ρ_s of 0.05-0.3 and cell size of 2-10 mm[70].

One drawback is the high cost of the foaming agent and the calcium. Although effective at producing large blocks of foam in regular shapes, the requirement for stirring of the full volume to disperse the foaming agent throughout the volume also means the process cannot produce complex net-shape components. Attempts have been made to develop injection techniques using metallic foams, whereby a melt is injected into a die as it foams, but with only limited success: heating and cooling rates are difficult to control across the sample, and the injection pressure is necessarily low to avoid crushing the molten foam, favouring irregular cell structures with density markedly decreasing with distance from the injection point[80, 81].

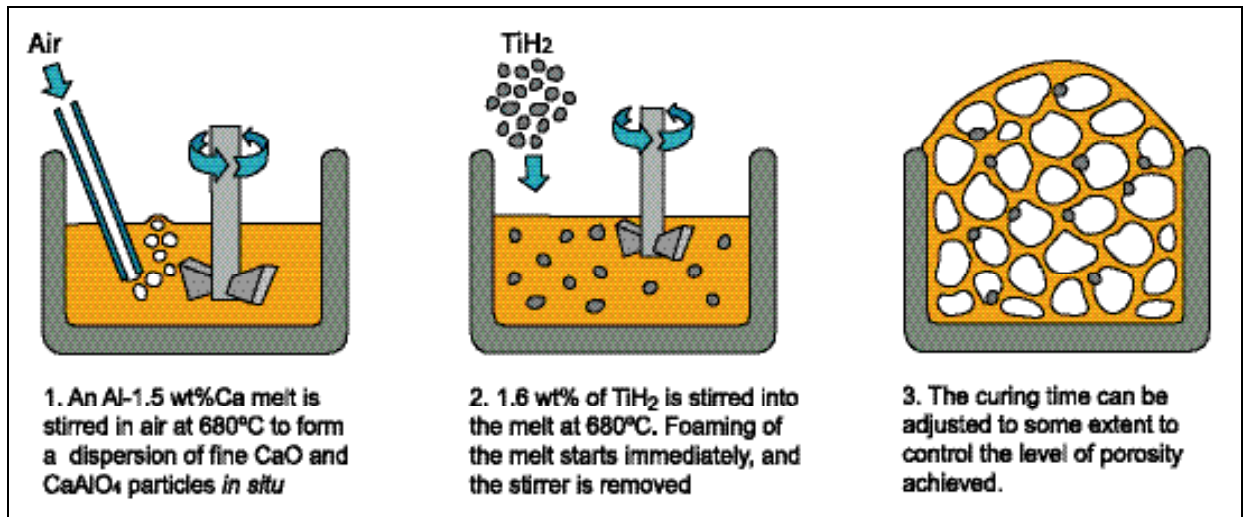
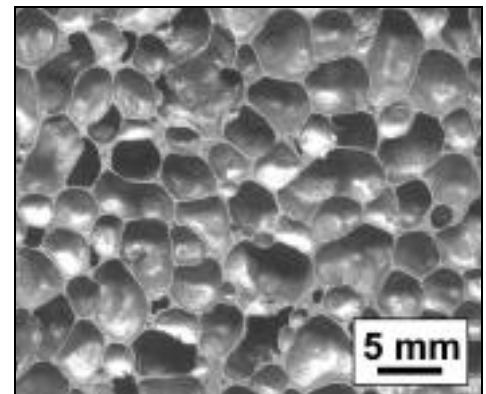


Figure 2.24:

Direct foaming of a viscosity-enhanced melt by a chemical foaming agent, and optical cross section of an Alporas™ Al-1.5wt.% Ca foam.



Production of a foamable precursor

The use of chemical foaming agents provides more control over the final cell structure than the direct injection of a gas. However, it remains relatively difficult to control the foaming process, given the requirement for full powder dispersion. Several processes have therefore been developed which separate the dispersion of the foaming agent within the melt from the decomposition of the agent to form a foam. Typically, powdered metals are mixed with a foaming agent at room temperature, and compacted to form a 'foamable precursor' material, which is subsequently 'baked' by heating it inside a shaped mould above the metal melting temperature to form a foam.

This provides a number of advantages over a single step process. Since foaming is not taking place during mixing, the powdered foaming agent can be thoroughly mixed in the metal, meaning that finer powders can be used, and the powder can be more uniformly dispersed. A foamable precursor is produced which can be stored indefinitely, and cut sections of it can be foamed in moulds with complicated shapes, without the need for access by a stirrer, to produce net-shape components with a solid outer skin. Whereas in the direct addition of a foaming agent to a melt, the temperature at which foaming takes place is restricted by the need to accommodate the stirring of the powder into the melt prior to full thermal decomposition, in a two stage

process the foaming temperature and time, and hence the porosity and cell structure, can be precisely tailored to requirements.

The foamable precursor must be impermeable to gases, or any gas produced can simply escape, meaning some form of consolidation is required to fuse the mixed powders. Various routes to consolidation are illustrated in Figure 2.25[82]. Extrusion, at 440°C and ~ 80 MPa, generates sufficient localised friction between the particles to break up their surface oxide film and bond them together. Preliminary compaction by cold isostatic pressing can facilitate extrusion[83]. As an alternative to extrusion, the powder mixtures can be consolidated by hot isostatic pressing at 400-450°C, sometimes with preliminary cold pressing to facilitate handling. The powder particles are joined together primarily by diffusion. This process apparently allows foaming agents which decompose at temperatures under 400°C to be used, as the high pressure prevents premature thermal decomposition[84-86].

Although surfactant or viscosity enhancing agents can easily be added to the initial powder mixture, they are not normally required, since the large surface area of the gas-atomised metal powders used is covered with a sufficient quantity of native oxide to stabilise the liquid foams against collapse.

Such processes have been used to foam aluminium, bronze, copper, steel, lead and magnesium[84, 87-89], and are used commercially to produce Foaminal™, Alulight™ and Fraunhofer™ foams of various Al-Mg-Si alloys with ρ^*/ρ_s of 0.11-0.37 and cell sizes of the order of millimetres[90]. The cell structure of the foams can be carefully controlled by adjusting the time and temperature at which the foamable precursor is foamed, in contrast to processes where TiH₂ is added directly to melts.

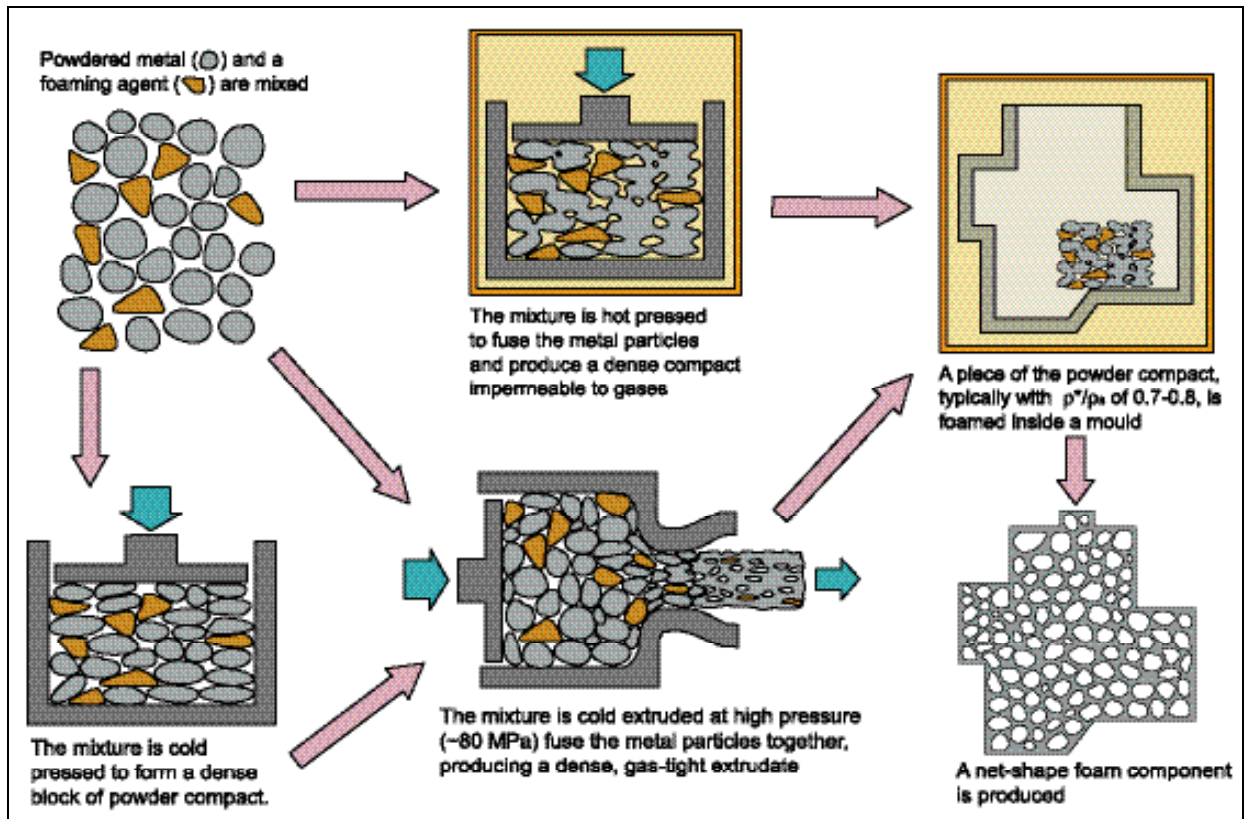
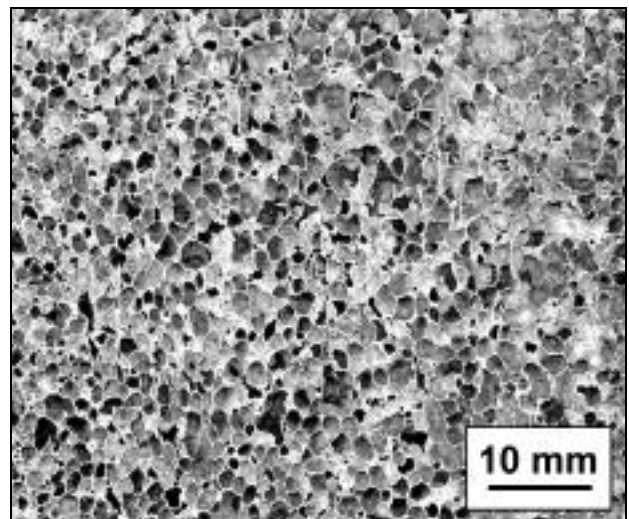
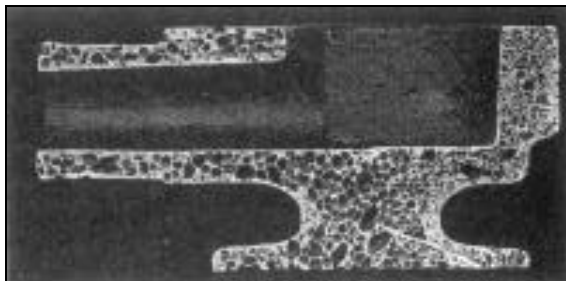


Figure 2.25:

Processing routes used in the production of foams based on powder metallurgy, an aluminium foam produced using a powder precursor, and a shaped component, with a rather irregular cell structure, produced by baking a foamable precursor in a shaped mould[80].



Although the use of foamable precursors offers notable advantages over direct foaming of melts, both in terms of ease of process control and the scope for forming shaped foam castings with controlled cell structures, the high cost of powdered metals has provided a strong incentive to develop cheaper melt-based processes[11].

Production of a foamable precursor by the melt route

In the FORMGRIP process (Foaming of reinforced metal by gas release in precursors), recently developed by Gergely and co-workers[91, 92], a foamable precursor is produced using molten metal, as shown in Figure 2.26. The foaming agent, TiH_2 , is subjected to a preliminary thermal heat treatment – typically for 24 hours at 400°C , followed by one hour at 500°C – to generate a TiO_2 diffusion barrier on the surface[93]. This delays the evolution of hydrogen

sufficiently for the TiH_2 to be dispersed thoroughly into an aluminium melt, and the melt solidified, before significant foaming takes place. The foaming agent is mixed with powdered aluminium in the weight ratio 1:4 prior to addition, to facilitate the mixing process. In order to stabilise the molten foam, ~ 10 vol.% of particulate SiC is added to the melt in a preliminary step. The resulting foamable precursor material has ρ^*/ρ_s of ~ 0.75 , due to gas incorporated during the mixing stage and limited decomposition of the hydride before the metal was solidified.

The precursor is then baked to form foams with ρ^*/ρ_s of 0.1-0.3 and cell size of 2-8 mm. A key advantage of the process is that - since the mixing and foaming stages are independent - the porosity and cell size can be closely controlled by choosing appropriate time and temperature of foaming[94].

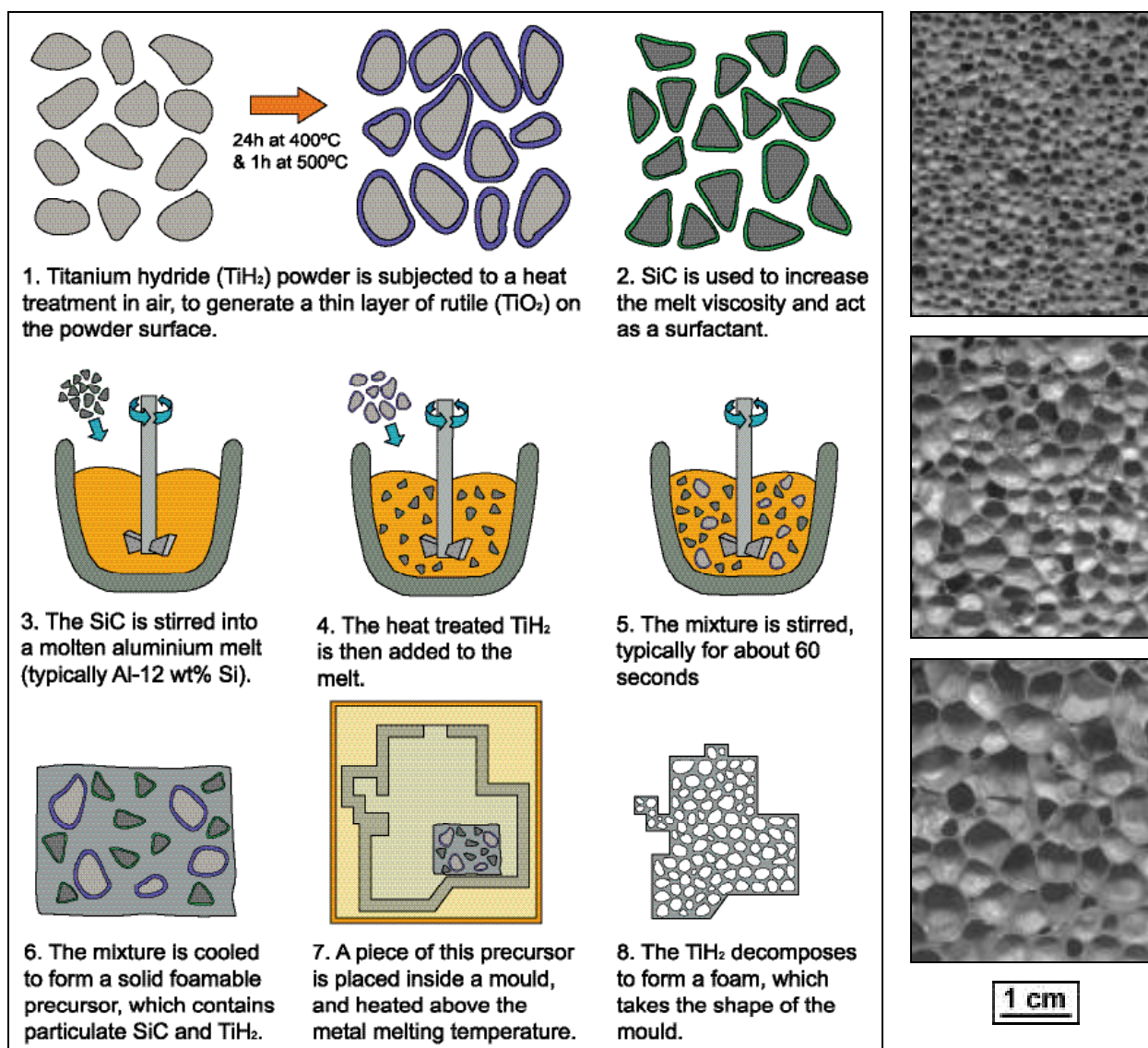
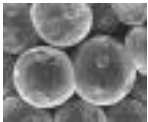
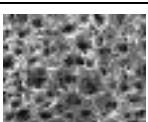
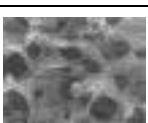
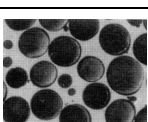
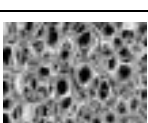


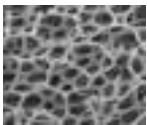
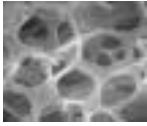
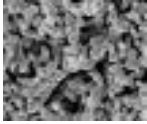
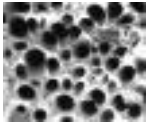
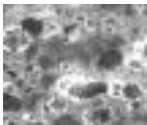
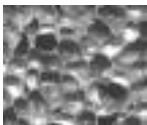
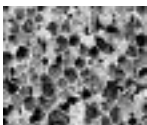
Figure 2.26: Schematic illustration of the FORMGRIP foaming process, and a range of foams produced by adjusting the foaming temperature and time.

This process combines the low cost of melt-based processing with the enhanced control over the foaming process associated with foamable precursors. Complex moulds can be filled with foam, and ceramic components have been incorporated into foam castings. Drawbacks with the process are the requirement for a lengthy heat treatment, and the relatively high cost and hazardous nature of TiH_2 (which is pyrophoric when in fine powdered form).

2.4 Summary of production methods

This chapter has provided an overview of the processing routes currently used to produce highly porous metals, ranging from highly specific techniques to broad processing routes. The following table summarises, for each process, the porosity levels obtained, the range of metals that can be used, the scale and nature of the porosity, and any notable advantages and limitations.

Process Type, trade name(s)	ρ^*/ρ_s	Typical metals which are used	Scale & nature of the porosity	Principal advantages	Principal limitations	Example (& image width)
2.2.1 Sintering of metal powders	0.4 - 0.8 (low ρ^* requires fugitive spacers)	Any (though the choice affects the sintering time).	Interconnected porosity.	Reasonably homogenous cell structure, net-shape product. Porosity can be graded to some extent.	Slow (sintering 6-24h), high cost of metal powders, limited to low porosity foams.	 1.5 mm
2.2.1 Sintering of metal fibres	> 0.05	Any (though choice affects sintering time).	Interconnected porosity.	As above, though generally lower ρ^*/ρ_s can be obtained than using powders.	Slow (sintering 6-24h), high cost of metal fibres.	 0.6 mm
2.2.1 Reactive sintering of metal powders	> 0.4	A mixture of metals which readily reacts (Fe-Al, Ti-Ni).	< 1 mm. Mixed open and closed.	Process is energy efficient and fast, good mechanical bonding of powders.	Products can be brittle, restricted range of metals, nature of porosity difficult to control.	 2.5 mm
2.2.1 Sintering of hollow metal spheres	0.13 - 0.3	Fe, Ti and Ni alloys.	0.1 - 8 mm. Closed cells separated by open pores.	Potential for highly uniform structures with high porosity, net-shape product.	Very high cost, complex process, long processing time.	 20 mm
2.2.2 Infiltration of a sintered salt preform	0.2 - 0.3	Any alloy (subject to appropriate preform material).	0.4 - 3 mm. Open-cell.	Wide range of alloys can be used, net-shape product, possibility for graded porosity.	Long sintering and dissolution times, hence high cost. Lower limit on cell size due to need for dissolution.	 40 mm
2.2.2 Mixing powdered salt and metal, sintering	0.2 - 0.4	Any alloy (subject to appropriate preform material).	0.5 - 5 mm.	Wide range of alloys can be used, net-shape product.	As above, also powdered metal is expensive, residual salt in foam.	 2 mm
2.2.2 Infiltrating a hollow sphere compact	> 0.45	Any alloy. Spheres usually made of range of glasses and ceramics.	2 - 10 mm. Spherical closed cells.	Potential for close control of cell size, net-shape structures, any alloy can be used.	Maximum porosity is limited by packing geometry. Spheres are expensive. Limited batch size.	 11 mm
2.2.2 Replication of a polymer foam structure (ERG Duocel™)	0.02 - 0.4	Any.	> 2 mm. Open cells.	Net-shape foams with a highly uniform structure. No restrictions on alloy type. High porosity.	Relatively costly process, limited batch size.	 25 mm

2.2.2 Chemical deposition on a polymer foam (Incofoam™, Recemat™)	0.01 - 0.3	Mainly Ni - dependent on available reactions.	> 50 µm. Open-cells with hollow struts.	Produces foams with high porosity and a very fine cell structure.	Costly process, limited batch size. Limited range of metals possible.	 2 mm
2.2.2 Electrodeposition on a polymer foam (Celmet™)	0.05 - 0.3	Any metal which can be deposited (Ni, Cu...).	> 50 µm. Open-cells with hollow struts.	Similar results to chemical deposition on a polymer foam.	Electrodeposition unsuitable for alloys.	 0.8 mm
2.2.3 Foams obtained by electro-deoxidation of the metal oxide	~ 0.5	Al, B, Cr, Fe, Nb, Nd, V to date.	< 20 µm. Open-cell.	Extremely fine foams can be obtained.	Costly, hazardous, process. Limited size that can be produced.	 0.035 mm
2.2.3 Directional solidification (Gasar™)	0.25 - 0.95	Al, Ni, Fe, Cu, Mg, Zn, Cr - usually reasonably pure.	0.01 - 10 mm. The cells are elongated parallel tubes.	Makes an unusual structure.	Costly and complex process, control difficult.	 1 mm
2.3.1 Alloys with a volatile phase	Not recorded	Relatively low melting points (Al, Zn), mixed with Hg.	Unknown: presumably irregular.		Hazardous process, complex apparatus, limited range of alloys, probably irregular structure.	No pictures available of these foams
2.3.1 Porosity caused by diffusion	> 0.7	Al-Zn; Cu-Ni.	< 600 µm. Scattered and irregularly shaped closed pores.		Extended sintering required. Very low porosity obtained.	 20 mm
2.3.2 Adding gas to stabilised metal melt (Cymat™, Alcan™, Hydro™)	0.05 - 0.16	Al alloys with about 10 vol.% of added refractory particles.	3 - 25 mm. Irregularly shaped closed cells.	A low-cost process. Continuous production possible.	Irregular foam structure, density gradients. Ceramic particles lead to brittleness. Not net-shape.	 25 mm
2.3.3 Add foaming agent (TiH ₂) to thickened melt (Alporas™)	0.05 - 0.2	Al alloyed with 2wt.% Ca. There must be a thickening agent.	5 - 10 mm. Closed cells. Reasonably uniform structure.	A large scale batch process with good reproducibility and process control. Low-cost, ductile foams.	Not net-shape. High cost of Ca and TiH ₂ .	 35 mm
2.3.3 Foamable precursor (Al + TiH ₂) by powder metallurgy (Alulight™)	> 0.1	Powdered metals with surface oxide.	2 - 8 mm. Closed cells. Uniform structure.	Good process control. Net-shape product.	Powdered metals are expensive to produce and handle. Prone to density gradients. TiH ₂ is expensive.	 15 mm
2.3.3 Foamable precursor (Al + TiH ₂) by melt route (Formgrip™)	> 0.05	Al alloys + 10 vol.% of refractory particles.	1 - 8 mm. Closed cells. Uniform structure.	Good process control. Net-shape product.	TiH ₂ is expensive. Need for heat treatment of TiH ₂ .	 50 mm

3 Production of Closed-Cell Foams using Gas Generating Agents

Aspects relating to the foaming of metal melts by foaming agents, and the structural evolution of liquid foams, are reviewed. The requirements for a foaming agent are discussed, and thermodynamic aspects of existing and potential foaming reactions are considered. Factors affecting the stability of foamed melts are discussed, including viscosity and surface tension, as well as the effect of dispersed solid phases and surfactants. Microstructural and thermodynamic aspects of the metal-ceramic systems commonly used in the production of foams are reviewed.

3.1 Gas generating agents

3.1.1 The use of gas generating agents

The key advantage of chemical foaming agents is that foaming powders can be efficiently dispersed throughout the melt by stirring prior to thermal decomposition. In processes where gases are bubbled directly into a viscous melt, the only method of dispersion of the gas bubbles is their natural tendency to rise towards the surface of the melt and the pushing effect of neighbouring bubbles, as stirring of the melt after addition of the bubbles causes cell coalescence and rapid deterioration of the foam.

In contrast to the direct addition of gases, which produces full size bubbles immediately, the use of foaming agents gives rise to a gradual chemical decomposition and progressive expansion of bubbles. This may allow the bubbles to rearrange to avoid local density variations, for surfactant particles to stabilise the pores as they grow by arranging themselves on the gas/melt interface, and/or for progressive stabilisation of the surfaces by chemical reaction between foaming gas and metal melt.

3.1.2 Requirements for a gas generating agent

The principal requirement of a foaming agent is for the temperature at which decomposition is thermodynamically favourable to match that at which the metal melts. If the decomposition temperature is too low, the reaction will proceed rapidly as the powder is added to the melt, leaving insufficient time to disperse the foaming agent evenly. If it is too high, the foam may collapse before solidification, and the processing temperature may be economically unfavourable. The kinetics of the decomposition reaction are important: foaming must be sufficiently rapid for the desired porosity to be obtained before the foam collapses or bubbles escape. The volume of gas given off for a given volume of foaming agent is also significant: chemicals with larger gas-evolving capability require less mixing. The foaming agent should have similar density to, and be wetted by, the melt, in order to promote uniform dispersion. The foaming chemical, and any gases given off, should ideally be neither toxic nor flammable, and the foaming chemical should not have undesirable side reactions with the melt.

3.1.3 Current gas generating agents

In principle, any material that is stable at room temperature but releases a gaseous component at an elevated temperature is a potential foaming agent. This includes hydrated inorganic chemicals such as calcium chloride, cupric sulphate and barium iodide, as well as hydrated layered minerals such as vermiculite [72-74]. When heated above the decomposition temperature – typically between 400 and 1300°C – these chemicals are dehydrated and the water vapour thus released can be used to foam a melt. Metal compounds including hydrides, oxides, nitrides, sulphates and carbonates, are also suitable: at a sufficiently elevated temperature, they all undergo a chemical decomposition of the form:



The vast majority of work on the foaming of melts is concerned with aluminium, due primarily to its low density, relatively low melting point, and resistance to corrosion. Pure aluminium melts at 660°C, and aluminium-silicon and aluminium-magnesium alloys, widely used in metallic foams, have melting temperatures as low as ~ 575°C.

Early patents suggest a wide range of potential foaming agents, including CdCO₃ and MgCO₃[14], long chain organic molecules [95], (NH₄)₂CO₃[15], Vermiculite and similar hydrated siliceous materials[74], and metal sulphates and carbonates in general[74]. However titanium hydride, TiH₂, and zirconium hydride, ZrH₂, and are the only foaming agents to be widely used in practice[72, 73, 96-98], with only TiH₂ used commercially[82]. It decomposes by the reaction:



$$G^0 \text{ (kJ mol}^{-1}\text{)} = 453 - 0.58 T(\text{K})$$

The free energy change of this reaction, G^0 , is plotted as a function of temperature in Figure 3.1. All elements are assumed to be in their standard state, with the gases produced at atmospheric pressure: a reasonable estimate of the situation inside cells in a liquid foam. The direct decomposition of TiH₂ in an atmosphere of hydrogen gas thus occurs at ~ 750°C. In practice foaming with TiH₂ takes place rapidly at lower temperature, and TiAl and TiAl₃ intermetallics have been observed at the interface between TiH₂ particles and the melt[99, 100], suggesting other reactions are taking place. ΔG for several possible alternative reactions

between the foaming agent particles and components of the melt is also plotted in Figure 3.1, again assuming unit activity of Al and Si.

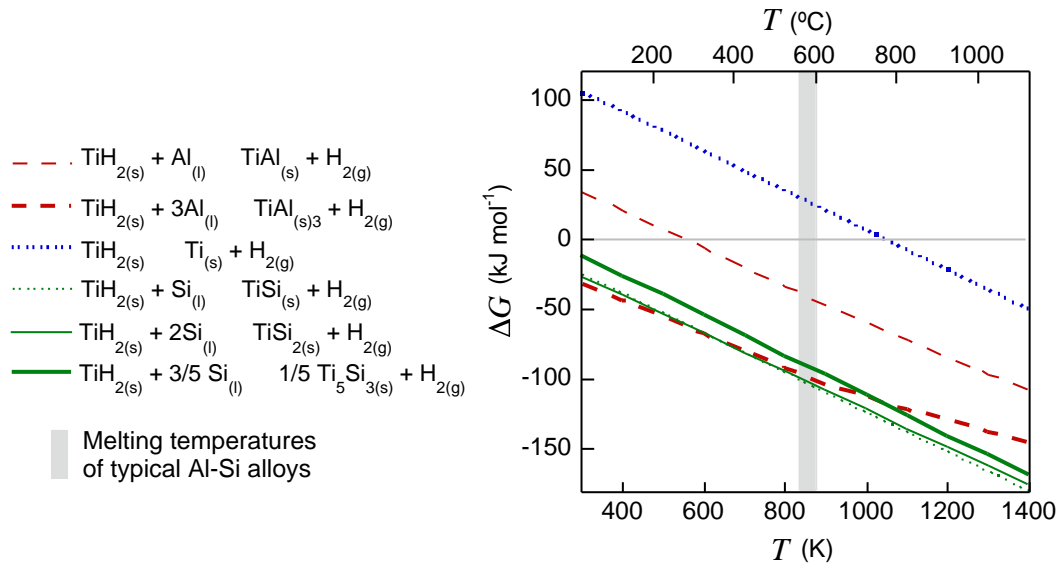


Figure 3.1: ΔG for the thermal decomposition of TiH_2 (reaction [3.2]), and for several possible gas-evolving reactions of TiH_2 in an Al-Si alloy melt (calculated with data from reference [101, 102]). All components have unit activity, and $p_{\text{H}_2} = 1 \text{ atm}$.

Controlled thermal decomposition

A process used to form barrier layers of oxide on powder particles was patented in 1976[103], in which ZrH_2 was heated in air at $\sim 470^\circ\text{C}$ for ~ 20 minutes, prompting the displacement reaction:



This treatment delayed the onset of the thermal decomposition, and moderated the rate at which decomposition took place. In the FORMGRIP process (§2.3.3) a similar treatment is applied to TiH_2 , to generate a TiO_2 diffusion barrier on the powder surface by the displacement reaction[93]:



Figure 3.2 shows thermogravimetric analysis (TGA) measurements of the decomposition of TiH_2 samples subjected to various pre-treatments.

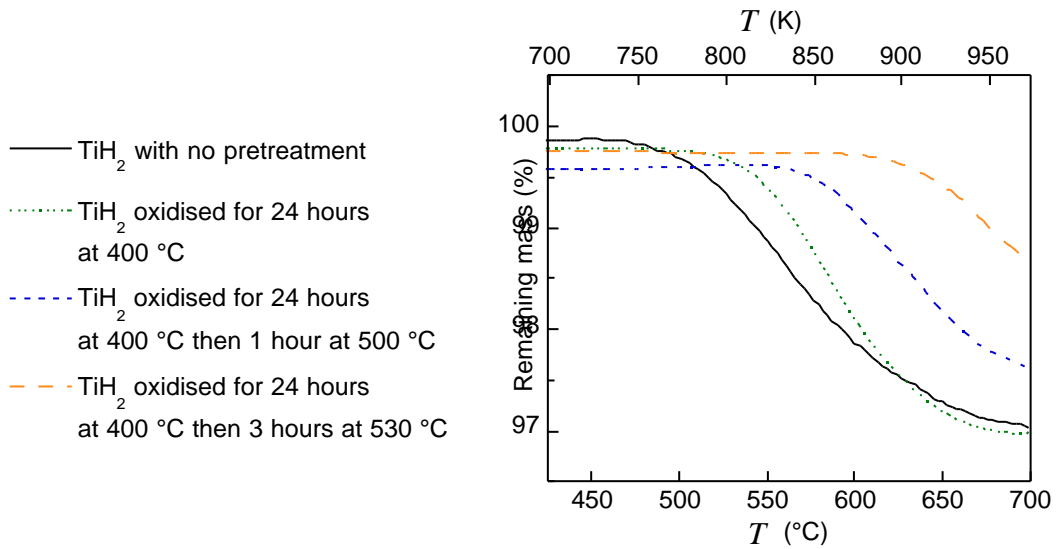


Figure 3.2: The effect of thermal pre-treatment on the thermal decomposition of titanium hydride [91]. Measurements were made for powdered samples at a constant heating rate of $20^{\circ}\text{C min}^{-1}$ in an inert atmosphere.

Although not directly comparable with decomposition inside a foam cell, where the hydrogen atmosphere can inhibit the reaction, the results demonstrate a significant kinetic delay in the onset of decomposition. This is sufficient to allow the production of an intermediate foamable precursor with low porosity, which can be foamed in moulds to produce shaped articles. Mechanically deforming the precursor accelerates foaming, with coarser cell structures obtained, apparently by breaking the TiH_2 particles and removing the constraint of the oxide layer[100].

With the mixing and foaming steps separated, the foaming temperature and time can be adjusted over a complete range, so that the foaming process and resulting cell structure can be closely controlled[91, 94]. There remain significant drawbacks to the use of TiH_2 , including the cost of the raw material and thermal pre-treatment, and the hazardous nature of fine powders. Careful process control is required to obtain reproducible cell structures, as even pre-treated TiH_2 has rapid decomposition kinetics, with a strong sensitivity to fluctuations in foaming temperature and a risk of overbaking.

3.1.4 Metal carbonates as gas generating agents

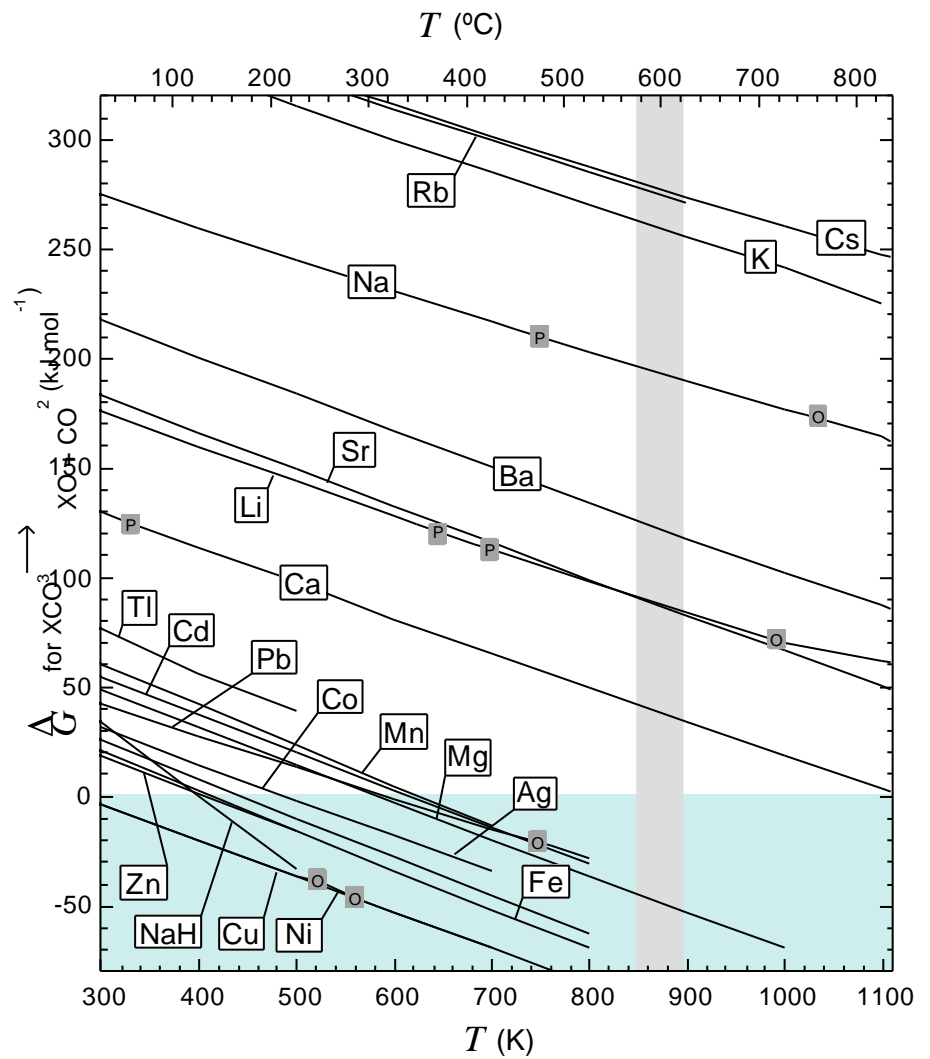
In this work, the potential of metal carbonates as gas-generating agents is examined. The free energy, ΔG , for the decomposition of most known carbonates is plotted in Figure 3.3 for reactions of the form:



Figure 3.3:

ΔG of reaction [3.5] for one mole of various metallic carbonates, for p_{CO_2} of 1 atm, based on tabulated data from several sources[101, 102, 104-108].

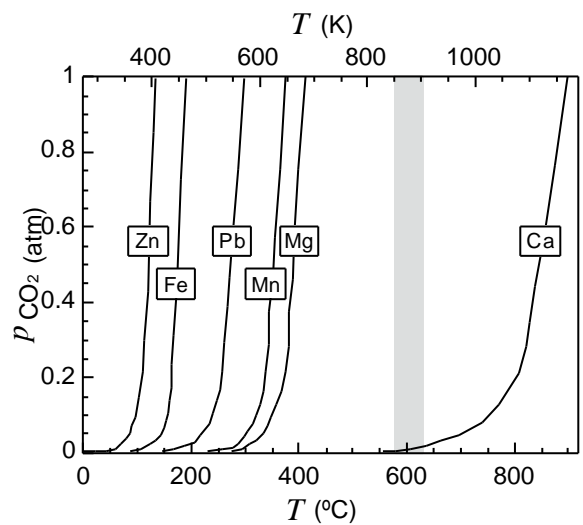
- Carbonate phase change
- Oxide phase change
- Melting temperatures of typical Al-Si alloys



This immediately indicates that most carbonates are either too unstable for use as a foaming agent for aluminium – as shown by the equilibrium partial pressures of CO_2 , p_{CO_2} , over selected carbonates in Figure 3.4 – or decompose at far too high a temperature, possibly justifying the lack of interest in carbonates to date.

Figure 3.4:

Equilibrium p_{CO_2} over metal carbonates[109]. The grey band marks the range of melting temperatures of typical Al-Si alloys.



Calcium carbonate

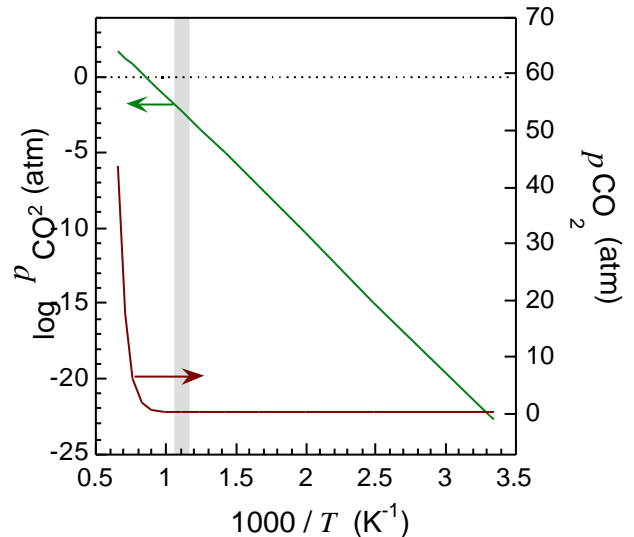
CaCO_3 , the closest match, has density comparable to that of Al at 2710 kg m^{-3} , and has been used to foam glass[110] by the reaction:



$p\text{CO}_2$ for this reaction is plotted as a function of temperature in Figure 3.5.

Figure 3.5:

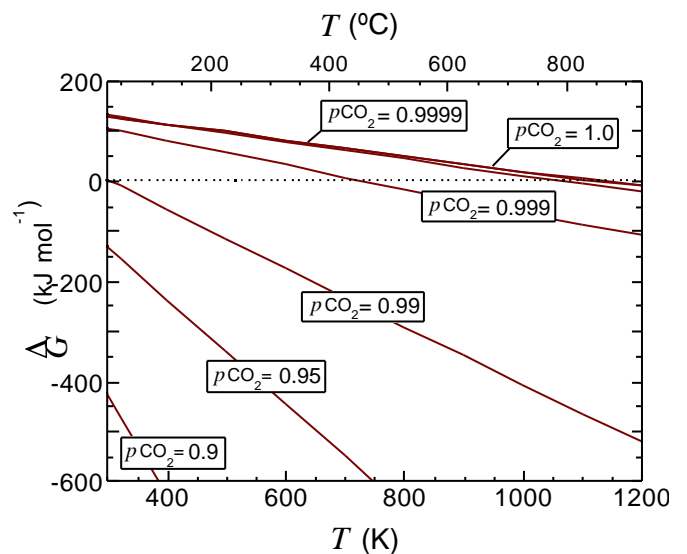
Equilibrium $p\text{CO}_2$ for reaction [3.6] (data from[108]). The grey band marks the range of melting temperatures of typical Al-Si alloys.



Although thermal decomposition in an atmosphere of pure CO_2 takes place well above the melting temperature of aluminium alloys, the single step reaction is thermodynamically favourable at the melting temperature with a small drop in $p\text{CO}_2$, as shown in Figure 3.6. CaCO_3 could therefore be used to foam aluminium if $p\text{CO}_2$ inside the cells can be reduced.

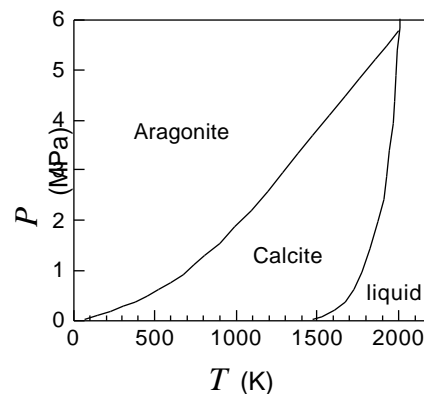
Figure 3.6:

Calculated ΔG for reaction [3.6], for several values of $p\text{CO}_2$.



CaCO_3 exists in two main polymorphs: calcite, with a trigonal crystal structure, and aragonite, with an orthorhombic symmetry. Their relative stability is plotted in Figure 3.7. The aragonite polymorph has a lower activation energy for decomposition than calcite[111].

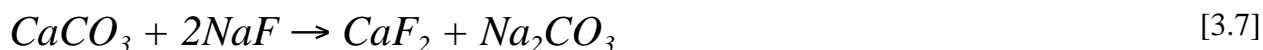
Figure 3.7:
Stability of calcite and aragonite polymorphs of
CaCO₃



The thermal decomposition of calcite has been studied by differential thermal analysis (DTA), thermogravimetric analysis (TGA), and dynamic X-ray diffraction[112-116]. There is significant scatter in the results, with decomposition in an inert atmosphere taking place slowly at $T > 500^{\circ}\text{C}$, and reasonably rapidly at $\sim 650\text{-}700^{\circ}\text{C}$. The observed decomposition temperature is influenced by $p\text{CO}_2$ [113, 117, 118], with the onset of decomposition typically raised to over 900°C in pure CO_2 . The effect of $p\text{CO}_2$ on decomposition kinetics remains unclear[119, 120]. Larger CaCO_3 particles, with a smaller surface area and larger gas diffusion distance within particles, decompose more slowly[118, 121]. There has been little systematic work concerning the effect of powder purity, owing mainly to the difficulty of separating purity differences from other factors such as particle shape, surface area and crystalline structure. However, high purity carbonates do appear to decompose slightly more slowly than impure natural limestones[118, 122]. Cleaning of powder samples has been observed to delay decomposition, suggesting dirt or adsorbed gas may provide surface sites for the nucleation of CaO [114].

Analysis by TGA and DTA presents several limitations. The decomposition of bulk powdered samples is strongly influenced by the rate of removal of CO_2 , which is in turn dependent on the particle size and packing efficiency of the powder, the gas removal rate, and the sample size[123-125]. A study of the thermal decomposition of monolayers of CaCO_3 particles found that their decomposition rate was significantly higher than that of conventional powder samples[114].

During the course of this project it was reported independently by Nakamura that CaCO_3 can be used to foam aluminium in a variant on the AlporasTM process, using Ca as a thickening agent[126]. Foaming was achieved by applying a 30 nm surface coating to the foaming particles:



Ion exchange takes place in a warm solution for 40 minutes, followed by drying in air at 120°C for 12 hours. The coating is reported to aid wettability. The coated foams had ρ^*/ρ_s of 0.37, showing extensive drainage and an irregular cell structure of mostly interconnected pores, while uncoated CaCO_3 was unable to foam the melt. The pore size of carbonate foams (quoted as 1.1 mm) was 60% of that of similar hydride-based foam (quoted as 1.8 mm), although the difference appears more marked in the specimens shown (shown in Figure 3.8). The authors attribute the difference in cell size entirely to enhanced wettability of the foaming agent, which is assumed to increase the number of bubble nucleation centres and assist in the evolution of gas.

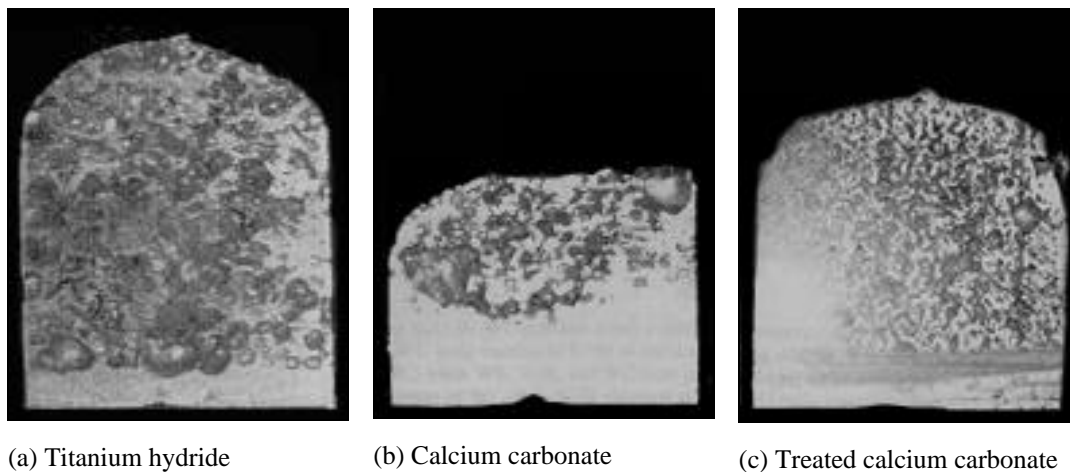


Figure 3.8: Foams produced with TiH_2 , as-received CaCO_3 , and CaCO_3 subjected to a surface treatment to aid wettability[126].

3.2 Stages in the evolution of a foam structure

3.2.1 Cell growth

The cell structure develops by the stages shown in Figure 3.9. The shape of cells is initially controlled only by surface tension, producing a dispersion of near-spherical pores. With continued expansion the pore shapes become increasingly angular, as motion of bubbles relative to each other becomes increasingly difficult, ultimately forming a three dimensional network of polyhedral cells[94, 127, 128]. A number of terms used to characterise such polyhedral cell structures are labelled in Figure 3.10.

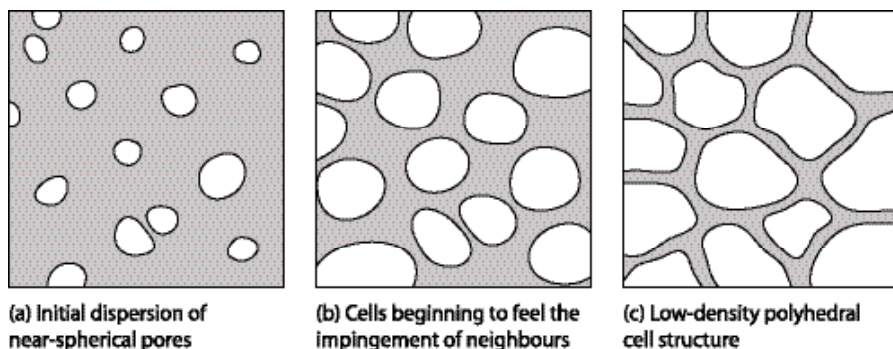


Figure 3.9: Schematic evolution of cell structure as ρ^*/ρ_s decreases during foaming of a melt by a dispersed foaming agent.

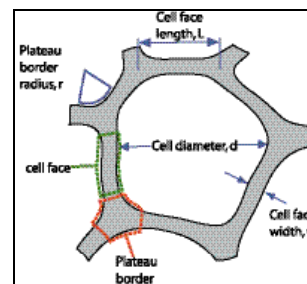


Figure 3.10: Cell structure terminology and notation

3.2.2 Drainage and collapse

Gravity drainage is a common reason for the collapse of foams, giving rise to density gradients, and in extreme cases the local features shown in Figure 3.11. A related issue is coalescence of neighbouring cells, illustrated in Figure 3.12. The thinning of cell faces at their midpoints is typically the result of surface tension making the cells more rounded, and of drainage removing material from the top of the foam.

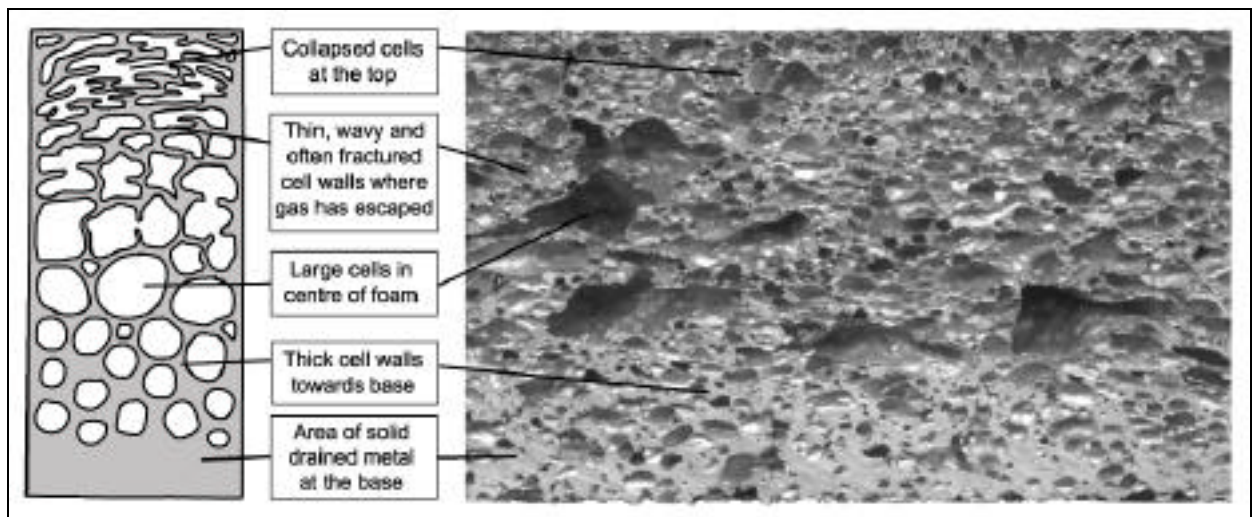
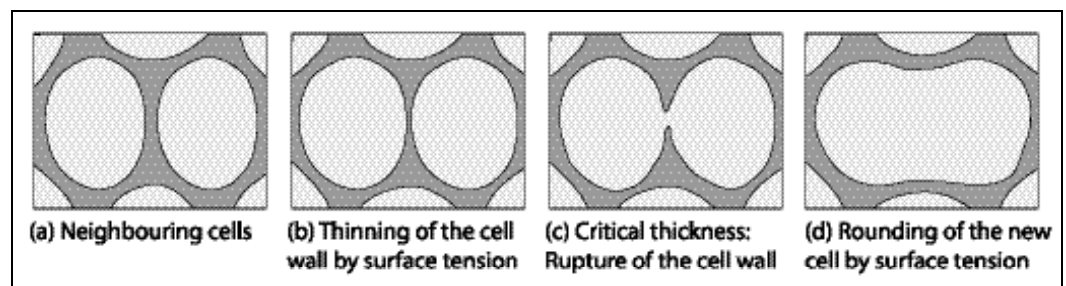


Figure 3.11: Sketch illustrating characteristic features resulting from foam drainage, and a cross section of an Alcan™ foam sample produced by direct injection of gas to a melt (§2.3.2) shown at approximately real size, which exhibits several of these features.

Figure 3.12:
Stages of cell coalescence



Current understanding of the evolution of the cell structures of melt-based foams is based mainly on the interpretation of the structure of solidified foams subjected to various thermal histories, with the cell structure of foams subjected to interrupted foaming assumed to be representative of that in the early stages of foam evolution[128]. A range of techniques under development offer the potential to further understanding of the effect of material and processing parameters on the evolution of the cell structure. Neutron radiography has been used to measure the evolution of density profiles due to drainage during the foaming process[129], while the use of high-intensity synchrotron X-ray radiography has allowed the evolution of cell structures, and processes such as drainage and cell coalescence, to be observed in real time[130, 131], enabling investigation of the effect of holes and defects in foamable precursor material on the cell structure obtained. Numerical modelling of the growth and interaction of cells in a molten

foamable precursor material also offers the potential to evaluate the effect of a range of material properties and process parameters[132, 133]. This approach has demonstrated the importance of cell face stability on the foam structure, and could ultimately enable foaming processes such as the filling of complex shaped moulds to be predicted. However, all these techniques remain under development.

3.3 Metallic and aqueous foams

A large body of literature exists concerning the formation and stability of aqueous foams, although it has only limited relevance to metallic foams. The cell faces in metallic foams are typically at least an order of magnitude thicker than in aqueous foams[131, 134], so capillary effects are reduced and gravity drainage is less influenced by surface properties. Metallic foams often include solid stabilising phases distributed within the melt, in contrast to the cell faces in aqueous foams, which usually have uniform composition apart from the presence of a film of surfactant molecules. Heterogeneous phases can also be present in metal alloys, and the reactivity of the metal may allow reactions during foaming. There has been relatively little work to date concerning the stability of metallic foams, and the mechanisms advanced to explain their stability, while often plausible, are correspondingly speculative[128].

3.4 Factors affecting the stability of foam structure

3.4.1 Gas diffusion

In aqueous foams, pressure differences between cells of different sizes causes coarsening by Ostwald Ripening[135]. The gas pressure within a cell due to surface tension is inversely related to its radius of curvature. The difference in pressure between adjacent cells with principal radii of curvature r_1 and r_2 takes the form[2]:

$$P = T \left(\frac{1}{r_1} - \frac{1}{r_2} \right) \quad [3.8]$$

Extending this principle to any bubble within the structure, it can be shown that a bubble of radius r will grow at a rate[136]:

$$\frac{dr}{dt} = C \left(\frac{1}{\bar{r}} - \frac{1}{r} \right) \quad [3.9]$$

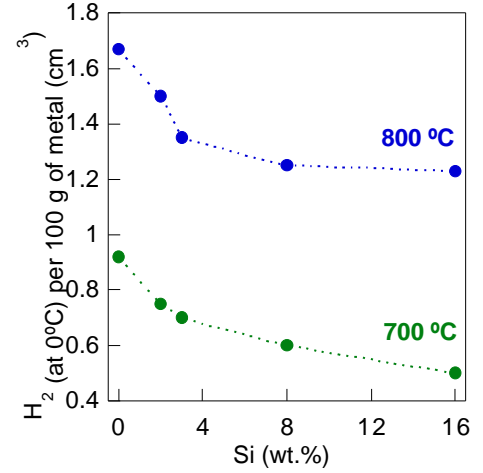
where \bar{r} is the mean bubble radius in the foam. Bubbles with $r > \bar{r}$ will therefore grow at the expense of those smaller bubbles with a higher surface area-to-volume ratio. In principle, there will always be potential for gas diffusion: even if all bubbles are initially of the same size, bubbles at the outer edge have a curved outer surface and lose gas to the atmosphere.

The extent to which diffusion takes place is, however, limited by the diffusivity and solubility of the gas in the molten metal, and the solubility of most gases is negligible: only H₂

has significant solubility in molten aluminium, and as shown in Figure 3.13 the solubility is significantly reduced by alloying with Si[137, 138]. The thicker cell faces in metallic foams, and the tendency for cell surfaces to be lined with solid surfactant particles, further limit gas diffusion. As metallic foams are only maintained in the liquid state for a short time, it seems reasonable to assume that the effect of gas diffusion on the cell structure is negligible.

Figure 3.13:

The solubility of H₂ in Al-Si alloys as a function of the concentration of Si, expressed as the volume of gas at 0°C and atmospheric pressure which will dissolve in 100 g of metal [138].



3.4.2 Cell rearrangement

If decomposition takes place to a differing extent in adjacent cells giving rise to pressure differences that cannot be accommodated by diffusion, cells may rearrange to exchange neighbours to redistribute pressure. Alternatively, cell faces with a low surface tension may be curved.

3.4.3 Viscosity

Viscosity requirements

To create a uniform distribution of cells, bubbles should be retained within a melt until the foam can be solidified, which generally means reducing the velocity at which the bubbles rise. An estimate of the influence of bubble size and melt viscosity on the terminal velocity $v_{terminal}$ of a gas bubble in a melt can be obtained by balancing the buoyancy of the bubble with the viscous drag of the melt. For a bubble of diameter d , the buoyancy force is equal to the mass of the melt displaced by the bubble:

$$F_{buoyancy} = \frac{1}{6} \pi d^3 \rho_{liquid} g \quad [3.10]$$

Stokes' Law gives the drag in a melt with viscosity η :

$$F_{drag} = 3 \pi \eta d v_{terminal} \quad [3.11]$$

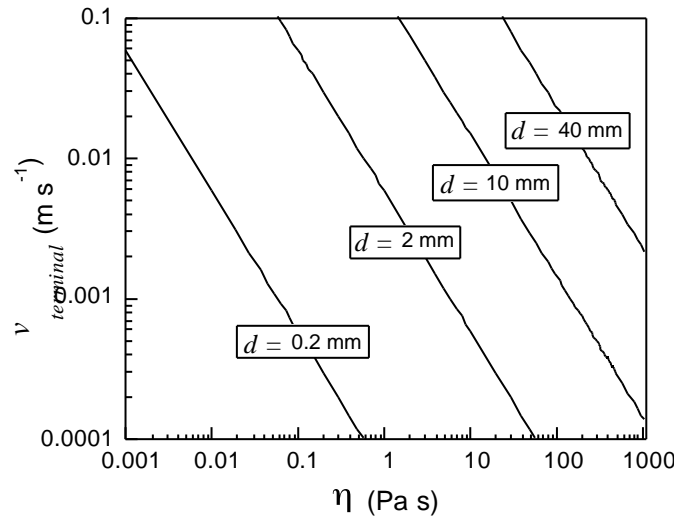
Equating [3.10] and [3.11]:

$$v_{terminal} = \frac{1}{18} \rho_{liquid} g \frac{d^2}{\eta} \quad [3.12]$$

Figure 3.14 shows the values of $v_{terminal}$ thus obtained.

Figure 3.14:

$v_{terminal}$ as a function of η for several values of d .



In order to estimate the melt viscosity required to produce a stable cellular structure, a rough estimate of the criteria required for a stable foam is useful. It is hence assumed that a foam structure will be stable if η is sufficiently high to reduce $v_{terminal}$ of bubbles within it to an acceptable level. For a total foaming time of 10 minutes, it is assumed that the foam will be unstable and liable to drainage or collapse if the bubbles move by a distance larger than their own radius during this time. A bubble of $r = 2$ mm would thus require a melt viscosity of ~ 7000 Pa s to be stable.

Viscosity of molten alloys

The temperature dependence of the viscosity pure aluminium takes the following form, where $\eta_o = 0.149$ mPa s, and $Q = 16.5$ kJ mol⁻¹[138]:

$$\eta = \eta_o \exp\left(\frac{Q}{RT}\right) \quad [3.13]$$

This is plotted in Figure 3.15, showing a weak temperature dependence with $\eta = 0.0014$ Pa s at its melting point, comparable to that of water. Figure 3.16 shows the effect of alloying elements on η . The most common alloying elements, Mg and Si, cause a small reduction in viscosity[139]. It is clear that the viscosity of metals is insufficient to stabilise a foam structure.

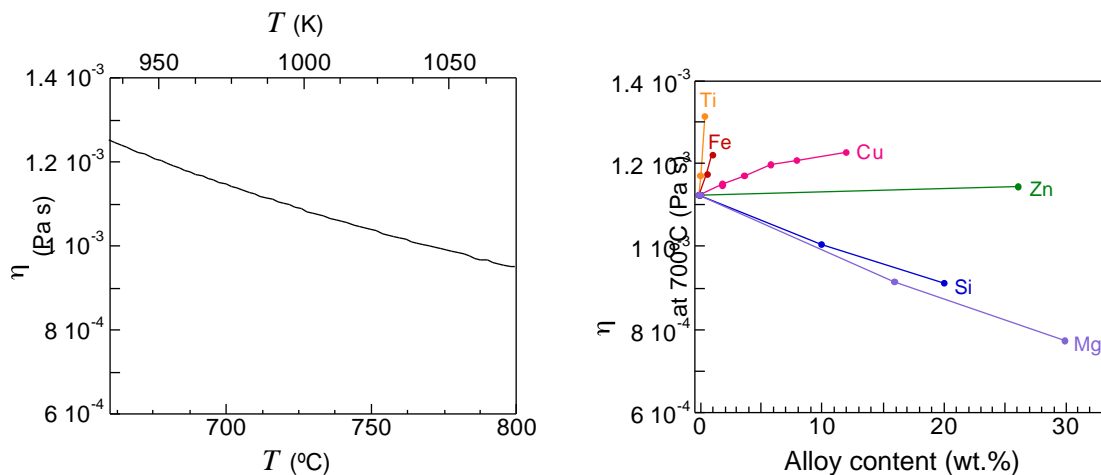


Figure 3.15: The effect of temperature on the viscosity of liquid aluminium according to equation [3.13].

Figure 3.16: The effect of alloying content on the viscosity of liquid aluminium (compiled from [139]).

Viscosity of two-phase systems

Incorporating or generating a dispersed solid phase in the melt can increase the viscosity. An empirical relation for the viscosity, η , of a liquid of intrinsic viscosity $\eta_{(f=0)}$ containing a fraction f of a dispersed solid phase was developed by Thomas [140]. For $f < 0.25$, 97.5% of a range of experimental data was fitted by:

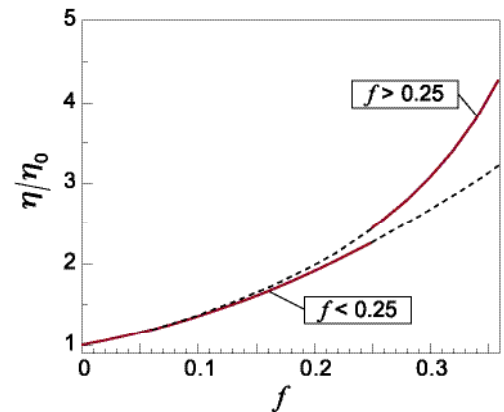
$$\frac{\eta}{\eta_{(f=0)}} = 1 + 2.5f + 10.05f^2 \quad [3.14]$$

A more effective match at higher f is provided by the extended expression:

$$\frac{\eta}{\eta_{(f=0)}} = 1 + 2.5f + 10.05f^2 + 0.00273\exp(16.6 f) \quad [3.15]$$

It was noted that the particle size was significant. Colloidal interactions between small ($< 10 \mu\text{m}$) particles significantly increased the viscosity, and it was suggested that larger particles also increase the viscosity due to loss of angular momentum when they collide. There is some evidence that larger particles are more likely to migrate towards the centre of capillary tubes, reducing the viscosity[140]. Expressions [3.14] and [3.15], plotted in Figure 3.17, are based on extrapolations of measured data for several particle sizes over the range where size effects are negligible.

Figure 3.17:
The effect of f on η/η_0 , according to equations [3.14] and [3.15].



In practice, the apparent viscosity at low f can be markedly higher than predicted, with 10 vol.% of solid increasing η by between a factor of two and several orders of magnitude[141-144]. The particle shape is significant, with the higher surface-to-volume ratios of angular particles and fibres apparently having an enhanced effect on the viscosity. Observations in Al-Si alloys with Al_2O_3 particles have demonstrated a linear relationship between fluidity and the surface area of the solid phase, although there has been little systematic work in this area[141, 145-147].

The viscosity of many two-phase systems is markedly non-Newtonian, with slurries exhibiting marked pseudoplastic[145] or Bingham plastic[148] behaviour, as illustrated in

Figure 3.18. They sometimes show thixotropic behaviour, with a reduction in apparent viscosity with time[142, 149, 150], although this is not observed in all cases[151]. These effects are attributed to the formation of loose agglomerated networks of solid particles: there appear to be hydrodynamic interactions between the particles and the liquid, as well as non-hydrodynamic interactions between the particles, although the nature of these particle interactions is not fully understood[143, 148].

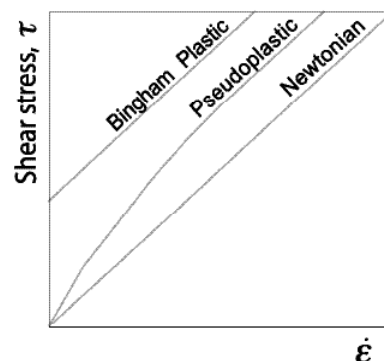


Figure 3.18:

Schematic variation of shear stress with strain rate for common types of fluid [152]. The viscosity is given by the gradient of such plots.

3.4.4 Methods of generating a solid-liquid system

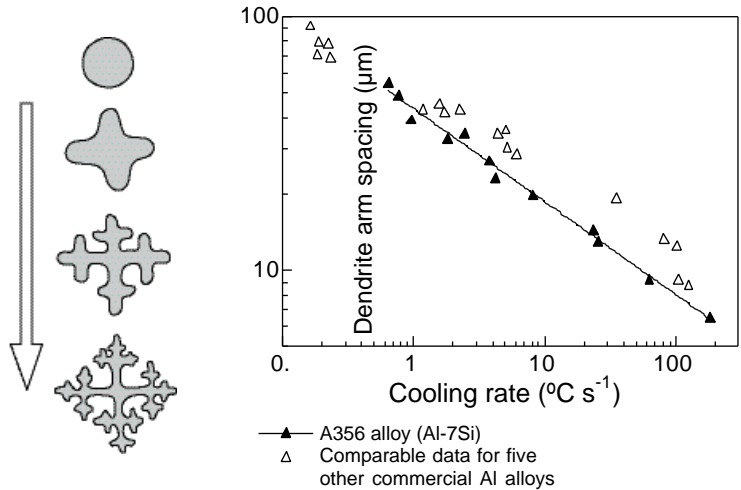
Foaming of a semisolid melt

Semisolid melts, containing a dispersion of solidified metal particles, are formed by interrupted cooling of an alloy with a large difference between liquidus and solidus temperatures[153, 154]. The solid phase, usually in the form of dendrites, needs to be sufficiently fine to generate a slurry on the scale of the cell face thickness.

If it is assumed that five or more dendrite arm spacings across the cell face thickness are required, a dendrite spacing of no more than 4-40 μm is required to stabilise typical cell faces. Figure 3.19 shows experimental measurements of primary dendrite arm spacing as a function of cooling rate [155, 156]. Cooling rates up to 100°C s^{-1} would be required to stabilise the finest cell faces, which is not easily achieved. Careful thermal control is required to prevent remelting of fine dendritic structures. Although there is some potential for refinement of dendrites by rapid shearing, the dendrites also become more rounded, which reduces their viscosity-enhancing effect[145, 147, 155]. Experimental results appear to confirm that semisolid melts do not provide sufficient enhancement of viscosity for effective stabilisation of foams[157].

Figure 3.19:

Schematic change in the structure of precipitates in a semisolid melt with increasing cooling rate, and experimental measurements of primary dendrite arm spacings in a range of aluminium alloys as a function of cooling rate[155].



Solid phase due to precipitation

As mentioned in section 2.3.3, solid phases can be generated *in situ* by localised reaction of the melt to generate a fine dispersion of a solid phase. Typically 0.2-8 wt.% of magnesium or calcium is added to the melt, followed by bubbling of air through the melt accompanied by vigorous stirring[75, 76, 158]. The affinity of the alloying elements for oxygen prompts the generation of fine oxide precipitates throughout the melt, raising its viscosity sufficiently to stabilise bulk foams. In a variant on this principle, MnO₂ has been admixed as an oxidising agent, with similar results[159].

Native solid phase

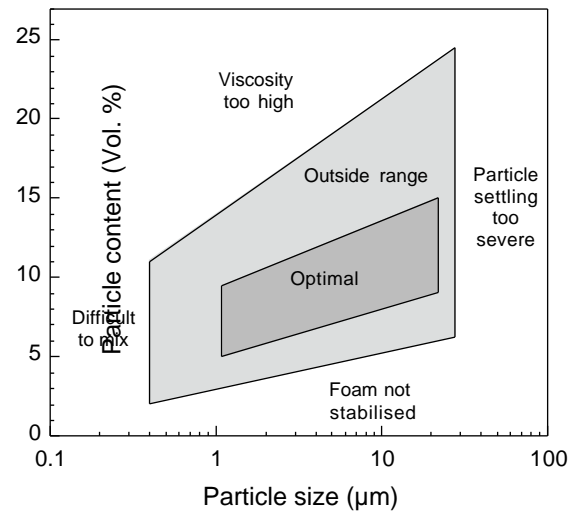
Although the effect is rarely mentioned explicitly, the metal powder-based production processes described in section 2.3.3 rely on the native oxide present on the surface of the powder particles to stabilise the molten foams. The oxide is dispersed during extrusion or compaction to form a three-dimensional network of particles in the foamable precursor, which is apparently maintained in the foams, at least in the early stages of the foaming process[132]. The effect of the oxidation state of the precursor powders was recently studied, demonstrating that foams produced with powders with a lower oxygen content were notably less stable[160].

Solid phase by addition of refractory particles

Solid refractory particles can be added to metal melts to increase their viscosity[74]. Suggested stabilising agents in aluminium include Talc, Micas and Vermiculites, although only Al₂O₃[161] and SiC[68] have been widely used. To enable efficient dispersion within the melt, the particles must be efficiently wetted by aluminium. Empirically determined limits on the size and volume fraction of particles that can be incorporated in the Al-SiC_p system are presented in Figure 3.20.

Figure 3.20:

Proposed limits on the size and volume fraction of SiC particles which can be added to molten aluminium to enhance its viscosity [68, 162].



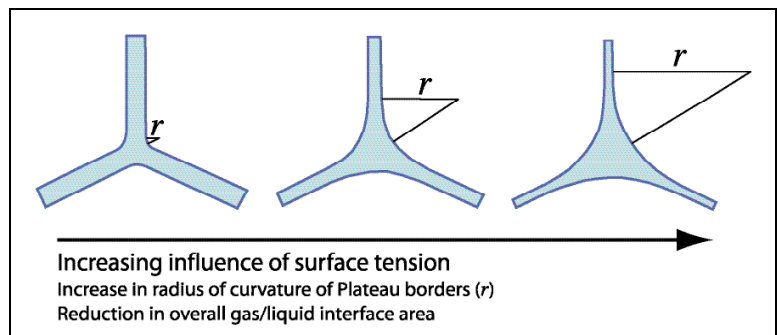
The use of fibres has also been suggested, both in terms of a strengthening material and as a more effective means of raising viscosity, but dispersion of fibres is difficult[71, 163-165].

3.4.5 Surface tension

Aqueous liquids do not foam without the presence of some form of surfactant which lowers the surface tension, and the same would be expected of molten metals[166]. The action of surface tension on polyhedral cells leads to progressively rounder cells with wider Plateau borders and thinner cell faces, as shown in Figure 3.21. This is accompanied by drainage of melt from the cell faces to the Plateau borders.

Figure 3.21:

The effect of surface tension on Plateau Borders

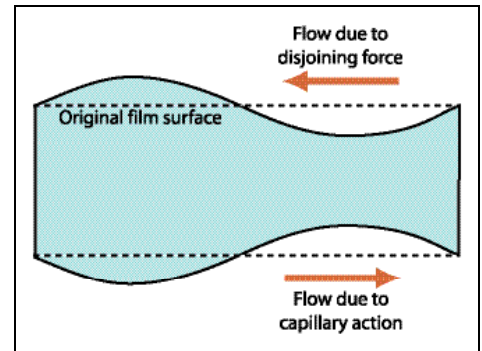


Any species that preferentially migrates to the gas-liquid interface, to resist change in the surface area, will lower the interfacial energy in a foam. By limiting the effect of surface tension on bubbles, this reduces the driving force for flow of material from cell faces to Plateau borders, and hence the rate of thinning and collapse of cell faces. The quantity of surfactant is significant: if it is too low, there is an insufficient quantity for uniform coverage, and if it is too high, there will be sufficient surfactant to cover the surface regardless of the movement of the cell faces.

Intermolecular attractive forces can be significant in thin films. Molecules in a thinner part of a film have fewer neighbours, and hence experience a weaker attractive field - and hence higher chemical potential - in the film than in adjacent thicker regions. In a momentary

perturbation of the film, illustrated in Figure 3.22, the molecules may agglomerate in the thicker region of the film, accentuating the perturbation. This is counteracted by the action of surface tension, which seeks to re-establish the initial surface area, although if the amplitude of a perturbation equals that of the film, surface tension causes its rapid retraction to the nearest plateau border. Although important in aqueous foams, this effect is unlikely in the thicker, particle-stabilised cell faces found in metallic foam, where electrostatic forces are not significant.

Figure 3.22:
Disjoining force in a thin aqueous film

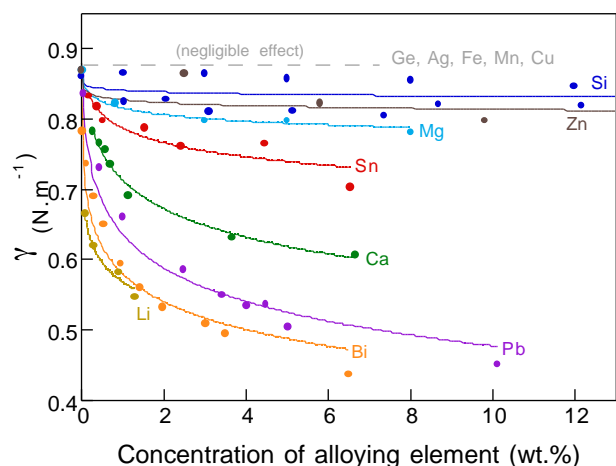


3.4.6 Surfactants

Solute phase surfactants

Surface-segregating alloys affect the surface tension of molten metals, as shown in Figure 3.23. Changes due to Si and Mg appear to be additive[167]. The most common alloying elements - silicon, zinc and magnesium - have only a small effect. The addition of bismuth has been investigated in the context of foaming aluminium by Miyoshi *et al*[79], showing an apparently increased tendency towards collapse. However, the effect of the alloy on the surface tension could not be isolated from changes in the melting point, making interpretation of such experiments difficult.

Figure 3.23:
Measured γ of binary aluminium alloys at their melting point (collated from[139, 167]).

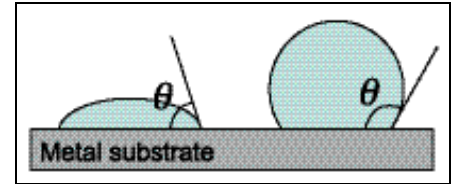


Solid phase surfactants

Surface-segregating solid phases are more effective surfactants. The efficiency of surfactant particles is closely related to the wettability of the particles by the melt, characterised by the equilibrium contact angle of the melt with the solid, θ , illustrated in Figure 3.24.

Figure 3.24:

Contact angles for wetting ($\theta < 90^\circ$) and non-wetting ($\theta > 90^\circ$) liquid-metal contact.



Solids will tend to lie preferentially at the gas/metal interface provided the surface energy of the solid-gas interface is less than the sum of the surface energy of the solid-liquid and liquid-gas interfaces[168]:

$$\gamma_{solid-gas} < \gamma_{solid-liquid} + \gamma_{liquid-gas} \quad [3.16]$$

The three surface energies are related by the Young-Dupré equation, obtained by resolving the mechanical equilibrium of surface tension parallel to the solid surface:

$$\gamma_{solid-gas} = \gamma_{solid-liquid} + \gamma_{liquid-gas} \cdot \cos\theta \quad [3.17]$$

Substituting $\gamma_{solid-liquid}$ from [3.16] in [3.17] gives the following condition for surface segregation:

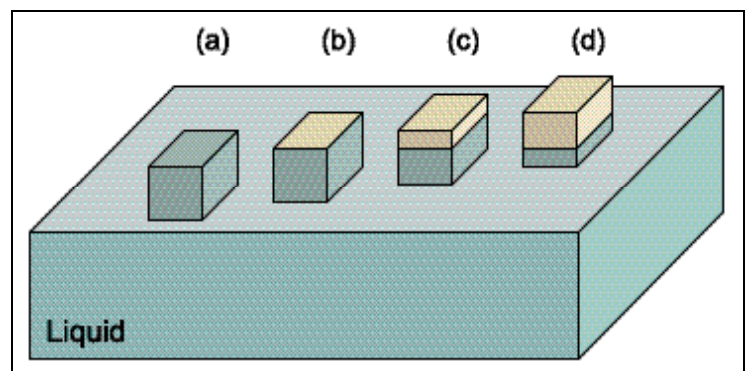
$$\gamma_{liquid-gas} \cdot \cos\theta < \gamma_{liquid-gas} \quad [3.18]$$

The relation is satisfied for all θ over 0° . It follows that unless a solid particle is fully chemically bonded to the melt, with $\theta = 0^\circ$, it will preferentially segregate to the surface of a melt-gas interface. Considering the schematic solid particle shown in Figure 3.25, provided $\theta > 0^\circ$ the transition from (a) to (b) is spontaneous, whereas the transition from (b) to (d) will only occur if θ is over 90° [143].

Figure 3.25:

Schematic surface positions for a solid particle at a liquid-gas interface (after [143]):

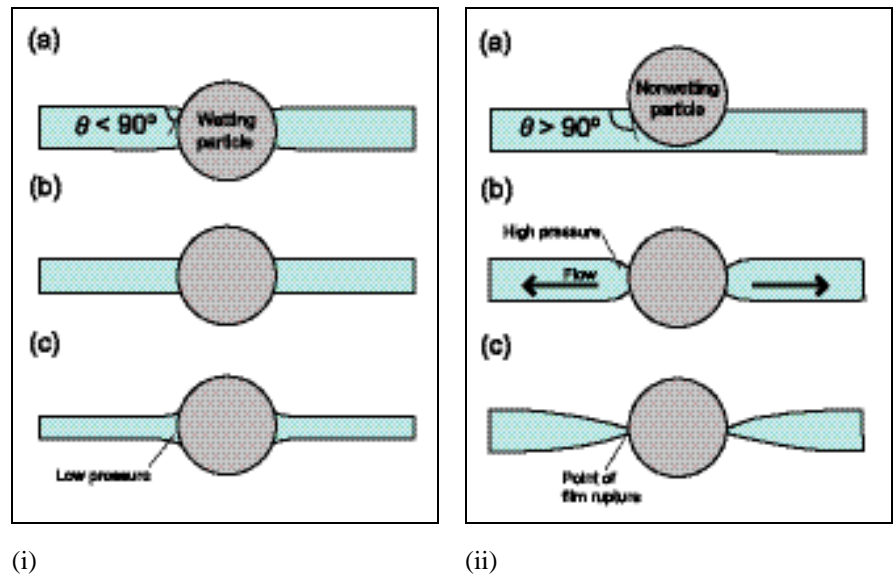
- (a) Particle completely immersed in the liquid
- (b) Particle flush with the liquid surface
- (c),(d) Particle protruding from the surface



The effect of θ has been studied experimentally in aqueous foams. Aveyard *et al* found that spherical particles with θ of $75 - 95^\circ$ stabilise aqueous foams, with optimum stability at $\theta = 90^\circ$ [169]. The stability range is generally reduced for angular particles[170, 171]. Not all surface-segregating particles will stabilise thin films: many commercial foam suppressants are based on fine, weakly hydrophilic particles. If the particle size is comparable to the film thickness, hydrophobic particles (with $\theta > 90^\circ$) can bridge thinning films as they attempt to maintain the optimum contact angle at the particle-liquid-gas interface, as shown in Figure 3.26[170-173]. This enables the surfaces of the film to come into contact as equilibrium θ is restored, promoting rapid rupture. This effect has been observed by high-speed photography in aqueous films[174].

Figure 3.26:

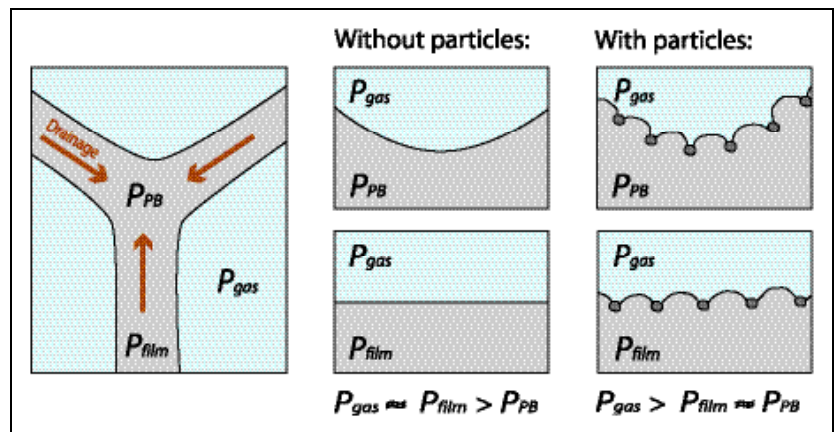
The effect of (i) wetting and (ii) non-wetting particles on the stability of foams, after [170].



Partially hydrophobic particles have been noted to enhance the stability of aqueous foams[175, 176]. Various mechanisms have been advanced for this stabilisation, which could be the result of clusters of particles contained within the foams which resist drainage in Plateau borders counteracting a reduced surfactant effect. It has also been proposed that they alter local cell curvature and hence cell pressure, as illustrated in Figure 3.27[175], although there is no evidence for such an effect.

Figure 3.27:

Proposed reduction of the capillary pressure difference between cell edges (with pressure P_{film}) and Plateau borders (with pressure P_{PB}) by particles pinning the exposed metal surface, providing uniform local film curvature (after [175])

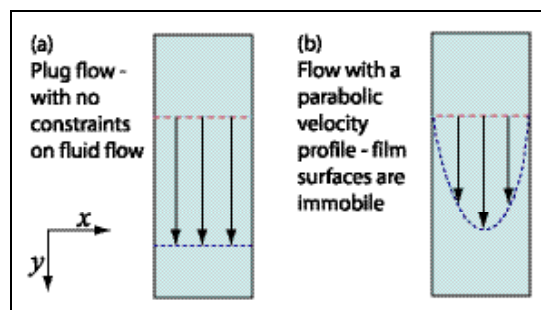


Conversely, hydrophilic particles with low θ may segregate only weakly to surfaces, where they are readily detached by flow effects and have relatively little stabilising effect[176].

As illustrated in Figure 3.25, the stability of particles lining the surface means that there is an energy barrier to the removal of particles from the interface. A surface fully lined with surfactant particles can thus acquire a degree of rigidity, and resist change in area. As shown schematically in Figure 3.28 for the case of a vertical liquid film in a foam, with no surfactant present every element in the film will experience the same acceleration due to gravity, and the entire film will collapse into the liquid at a uniform rate[172]. If a surface layer of particles is present which resists a reduction in the surface area, a tangential force acts in the plane of the surface. A viscous shear then acts between parallel draining molecules, producing a parabolic velocity profile, and limiting the rate of drainage.

Figure 3.28:

The effect of an unconstrained surface and an immobile surface on flow profiles in draining liquid films (after [172]).



Solid-phase surfactants in metal systems

There has been relatively little work to date concerning the effect of solid-phase surfactants in metal systems. The value of θ in a metal-solid system depends on intermolecular forces (Van der Waals interactions and polarisation), as well as chemical interaction at the interface[177, 178]. If a surface chemical reaction takes place between the particle and the melt, the particles may be irreversibly attached to the metal with $\theta = 0^\circ$, with reversible physical bonds giving higher θ .

SiC particles in aluminium foams are known to segregate to the liquid-gas interface[70, 162, 179], and aluminium foams are more effectively stabilised by larger volume fractions of SiC, with a critical concentration of $\sim 8 - 10$ vol.% apparently required for effective foaming[179]. However, it is difficult to isolate the influence of particle surfactants on the stability of metallic foams from the effect of associated changes in viscosity on melt drainage. Gergely *et al* found that increasing the size of the SiC particles added in the FORMGRIP process (§2.3.3) from $13 \mu\text{m}$ to $63 \mu\text{m}$ markedly reduced the stability of the foams produced, apparently by increasing the critical thickness below which particles make contact with both sides of the cell faces and prompt face rupture and cell coalescence[134].

Wübben *et al* recently foamed powder-route foamable precursors under conditions of microgravity[180, 181]. The precursors consisted of compacted lead powder with varying oxide content, with PbCO_3 as a foaming agent. The results demonstrated that the absence of gravity was insufficient to stabilise the foams with low oxide content, as shown in Figure 3.29. Although the distribution of the solid stabilising phase was not directly observed, solid particles were assumed to act as surfactants, and it was suggested that the role of the particles is primarily in preventing cell coalescence, with their effect on melt viscosity having only secondary importance.

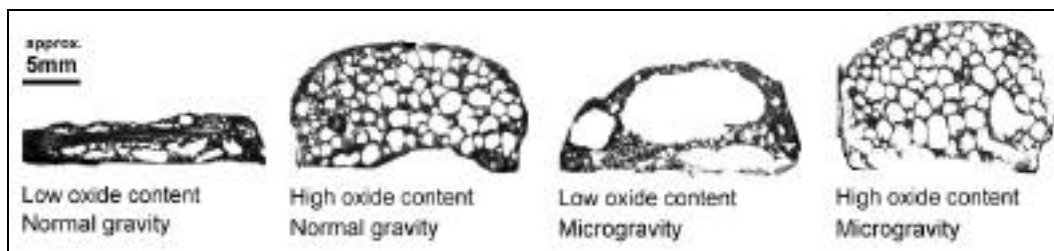


Figure 3.29: Lead foams produced by foaming powder metallurgy-based foamable precursor with 0.06 and 0.16 wt.% oxide content, for ~ 30 seconds under 1 g and microgravity[181].

3.4.7 Oxidation of aluminium

Adsorbed oxygen

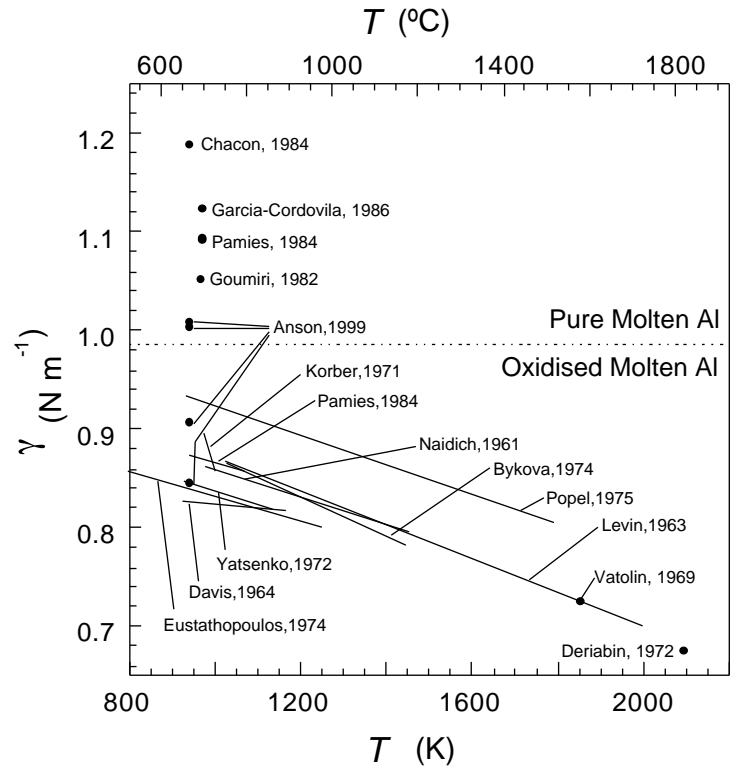
The high reactivity of aluminium leads to the formation of thin oxide films by reaction [3.19], even under high vacuum conditions[177, 182-187].



These films are flexible and do not appear to significantly impair the fluidity of the aluminium. However, they do affect its surface tension, as shown in Figure 3.30. The scatter reflects the difficulty of accurate measurement[188]. The lower values, with σ under 1 N m^{-1} , reflect the general temperature dependence of the 'oxidised surface' surface tension[189]. The higher values were obtained in experiments where particular care was taken to exclude oxygen, implying the surface tension of a 'pure' surface is $\sim 1.05\text{-}1.11 \text{ N m}^{-1}$. Elevated temperature (over $\sim 1100 \text{ K}$) and external agitation make the thin films unstable[190].

Figure 3.30:

Compilation of values for the surface tension of pure aluminium measured under vacuum ($P < 10^{-4}$ Pa), based on reference[191] with additional data from references [184, 185, 192].



The surface tension measurements parallel those of Al_2O_3 at higher temperatures, implying that the chemisorbed oxygen is irreversibly transformed to a bulk-like aluminium oxide[191]. It is thought that a single monolayer of adsorbed oxide is sufficient to reduce the surface tension to the 'oxidised' value, and that at lower coverage islands of solid oxide are present[182].

Surface oxidation has even been observed on aluminium surfaces held in pure hydrogen: it appears that even trace amounts of oxygen react with the aluminium preferentially to the hydrogen[184, 193], which is consistent with the favourable thermodynamics of the reaction:



$$\Delta G \text{ (kJ mol}^{-1}\text{)} = 0.2068.T(\text{K}) - 999$$

This can only be avoided by the presence of highly reactive elements such as Mg or Zr[183], which oxidise preferentially to get the oxygen.

Formation of thicker oxide films

Significantly thicker oxide layers would be expected in an oxidising environment. At 650°C, for example, the ratio of $pCO:pCO_2$ required to prevent oxidation of aluminium is $\sim 10^{15}:1$ [194]. Even relatively thin films have been noted to limit the fluidity of molten aluminium, preventing equilibrium droplet shapes being reached in wetting measurements [192].

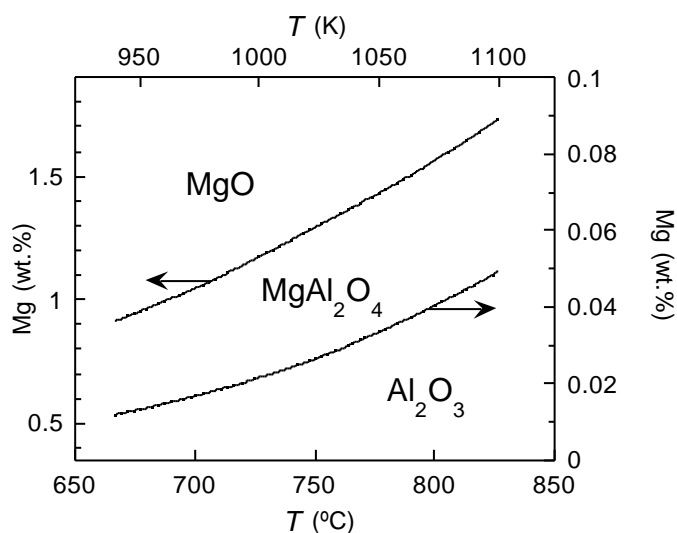
Rault studied the oxidation of liquid Al-Mg melts at 850°C in air. An oxide film formed immediately, which became wrinkled with oxide ruptures as the film was stretched[195]. The colour of the films, attributed to interference phenomena, suggested a film thickness under 0.5 µm. The strength of oxide films on molten melts in air is apparently sufficient to hinder the entry of solid particles to the melt[196].

Surface segregation of magnesium

Alloying elements with lower surface tension than the parent alloy tend to segregate to the surface, potentially affecting both the surface tension of the melt and its tendency to oxidation[178, 197]. Oxide films in Al-Mg alloys – particularly those formed in strongly oxidising environments – are usually enriched in magnesium[198-200], with a surface enrichment factor of 27 reported in rapidly solidified Al-0.7Mg melts[201]. If the surfaces are oxidised, Kaptay showed theoretically that elements with increased chemical affinity to oxygen have a more enhanced tendency to segregate to the surface, further reinforcing the degree of segregation of Mg[191].

The relative stability of Al₂O₃, MgAl₂O₄ and MgO is shown in Figure 3.31. A surface concentration of 0.02 wt.% of Mg is sufficient for reduction of Al₂O₃ to form MgAl₂O₄ at 650°C, with MgO and MgAl₂O₄ the dominant surface phase even in low-Mg alloys[202-204].

Figure 3.31:
Thermodynamic stability of Al-Mg oxides in Al-Mg alloys[205, 206].



Oxidation of solid aluminium

Solid aluminium surfaces also oxidise very rapidly, although the rate falls to a negligible value once a limiting thickness of the surface oxide is reached[201, 207]. This limit – known as the Mott thickness – is ~2 nm at room temperature, and is relatively insensitive to the oxygen partial pressure. Above ~ 200°C the film grows very gradually on a scale of several days to a significantly larger thickness[208].

3.4.8 The influence of the cell structure on stability

Cell face thickness

There appears to be a minimum cell face thickness, below which films will rupture, typically 50-80 μm in Al-Si alloys and as high as 100 μm in pure aluminium foams[127, 130, 131, 209]. It is sometimes suggested that this may be a critical thickness, below which faces are inherently unstable, although the cause of any such instability remains uncertain[86]. The thickness is generally limited by the foaming process used, and influenced by various interdependent parameters, including the size, shape and volume fraction of the solid phase present, the geometry of the foam structure, the metal alloy, and the processing temperature and time. There is evidence of a loose correlation between the size of solid stabilising particles and the thickness of cell faces[179, 210].

Tortuosity

The tortuosity and scale of the network of cell faces and Plateau borders in liquid cellular structures will further influence the rate of drainage in metallic foams, with increased viscous drag in thinner cell faces and narrower channels. The non-Newtonian flow and thixotropy noted in Al-SiC melts discussed in section 3.4.3 were concerned with bulk melts, and a range of other effects may occur for flow in narrow constrained channels - for example, it could be argued that movement of SiC is more difficult in thin cell faces, or that changes in ϕ will have more effect on drainage in foams with a high particulate content. However, little is known of the distribution of the often fine solid phases in most metallic foams.

3.4.9 Modelling of drainage

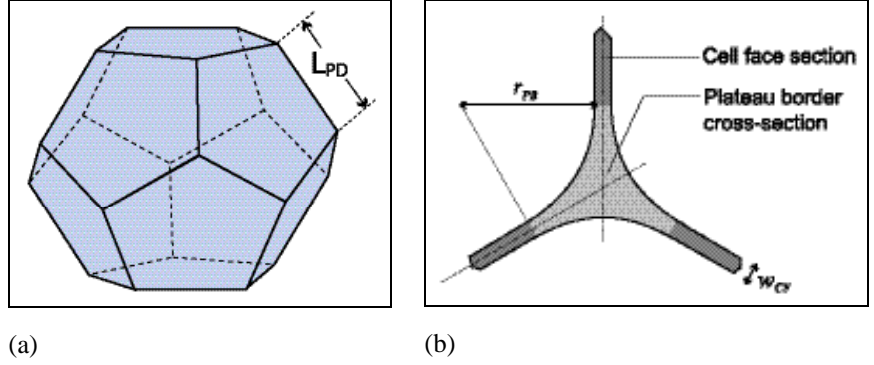
Gergely and Clyne recently developed a numerical model to simulate the drainage of liquid within standing liquid foams[134, 210-212]. The model allows the effect of various parameters on the extent of drainage to be explored. The principal advantage of this model, relative to other treatments of drainage in foams in the literature, is that it is designed to model drainage within the relatively thick cell faces and Plateau borders of metallic foams (§3.3).

It is based on the representation of a foam in terms of a sequence of pentagonal dodecahedral cells. The pentagonal dodecahedron, illustrated in Figure 3.32, is commonly used as a realistic representation of cells in melt-based foams due to its regularity, which makes derivation of the relationship between structural parameters relatively straightforward, and the reasonable correspondence between its shape and that of real cells in liquid foams. The cell faces are assumed to be planar, and joined by curved Plateau borders (§3.2.1) with a radius of curvature r_{PB} .

Figure 3.32:

(a) A pentagonal dodecahedron of side length L_{PD} .

(b) A cross-section of a Plateau border with its radius of curvature, r_{PB} , and the width of the adjoining cell face, w_{CF} , labelled.



Two factors affecting the flow of liquid within the structure are considered: drainage of liquid from the cell faces to the Plateau borders due to the influence of surface tension, and flow of liquid within the Plateau borders. The latter includes both gravity-driven flow, and a capillarity-related pressure gradient, due to differences in the radius of curvature along the height of the foam which develop with continued drainage, which acts against the gravity-driven flow.

Drainage of liquid from the cell faces to the Plateau borders is caused by the difference in pressure between the planar cell faces and the Plateau borders. The pressure in the cell faces is equal to that in the adjoining cells, whereas the Plateau borders have curved surfaces, and a correspondingly lower pressure due to the effect of surface tension. The difference in pressure in the Plateau borders and the cell faces, ΔP , is determined to be:

$$P = \frac{\gamma}{r_{PB}} \quad [3.21]$$

where γ is the surface tension, and r_{PB} is the radius of curvature of the Plateau border (Figure 3.32 (b)). Cells are not allowed to coalesce, although drainage from individual cell faces ceases when a minimum cell face thickness, $w_{CF,min}$, is reached.

The cell surfaces are assumed to be rigid. In order to model the flow of melt from cell faces to Plateau borders due to the difference in pressure caused by surface tension (equation [3.21]), the faces of the pentagonal dodecahedron (Figure 3.32 (a)) are approximated as circular disks of radius d_{CF} , with an area equal to that of the pentagons. A Reynolds-type equation is used to determine the rate of reduction of the width of the cell face due to P , with the result:

$$-\frac{dw}{dt} = \frac{2v^3}{3\eta} \frac{P}{(d_{CF}/2)^2} \quad [3.22]$$

where w is the width of the cell face, η is the melt viscosity, and ΔP is the pressure difference between the cell face and the Plateau borders given by equation [3.21]. It is assumed that any melt lost from the cell face is redistributed to adjacent Plateau borders, and that drainage from

the cell face to the Plateau borders ceases once a minimum value of the cell face thickness is reached.

The average velocity of liquid flow within a Plateau border due to a pressure gradient dP/ds along its axis s , assuming that the surfaces are immobile, is given by:

$$v_{PB} = \frac{1}{C} \frac{A_{PB}}{\eta} \frac{dP}{ds} \quad [3.23]$$

where C is a constant related to the shape of the Plateau border cross section, A_{PB} is the cross-sectional area of the Plateau border, and dP/ds is the gradient in pressure parallel to the axis of the Plateau border.

Consideration of the orientation of the variation in P due to capillarity effects (caused by variation in r_{PB}), gravity, and the orientation of Plateau borders, the following result is obtained for the average velocity of liquid flow in a Plateau border of radius of curvature r_{PB} and orientation θ to the vertical axis z :

$$v_{PB} = \frac{1}{C} \frac{A_{PB}}{\eta} \left[\rho g \cos\theta + \gamma \frac{d}{d(z/\cos\theta)} \frac{1}{r_{PB}} \right] \quad [3.24]$$

The first term in the brackets accounts for gravity drainage of the melt, and the second for pressure differences caused by capillary effects.

The above equations are used to derive an expression for the conservation of material within a section of a Plateau border dz tilted at an angle θ to the vertical, during a time increment dt , as a function of both height z and time t :

$$\begin{aligned} dz \frac{A_{PB}(z+dz, t) - A_{PB}(z, t)}{\cos\theta} &= A_{PB}(z, t) v_{PB, \theta}(z, t) dt - A_{PB}(z+dz, t) v_{PB, \theta}(z+dz, t) dt \\ &+ \frac{dz}{\cos\theta} \frac{n_{CF}}{L_{PD}} \frac{2\pi w^3(z, t)}{3\eta r_{PB}(z, t)} dt \end{aligned} \quad [3.25]$$

where A_{PB} is the cross-sectional area of the plateau border, L_{PD} is the length of the Plateau border, and n_{CF} and n_{PB} are the number of cell faces and Plateau borders respectively in a pentagonal dodecahedron unit cell. The third term on the right-hand side of the equation represents the amount of liquid a Plateau border section receives from adjacent cell faces. This term is set to zero if the cell face thickness, w_{CF} becomes equal to the minimum value $w_{CF, MIN}$.

After substitution of [3.24] into [3.25], and taking into consideration that the Plateau borders are randomly oriented in foams, the conservation equation is expressed in partial differential form:

$$\frac{\partial}{\partial t} A_{PB}(z,t) + \frac{\partial}{\partial z} [A_{PB}^2(z,t) C(z,t)] = \frac{n_{CF}}{n_{PB}} \frac{2\pi w(z,t)}{3\eta r_{PB}(z,t)} \frac{1}{L_{PD}} \quad [3.26]$$

where:

$$C(z,t) = \frac{1}{3} \frac{1}{49\eta} \rho g + \gamma \frac{1}{\partial z} \frac{1}{r_{PB}(z,t)} \quad [3.27]$$

Equation [3.27] includes a factor $1/3$, which is the average of $\cos^2\theta$ over all possible three-dimensional orientations of the Plateau borders.

The input structure for the model is shown schematically in Figure 3.33, and consists of a homogenous column of foam of height H divided into U volume elements, denoted $u = 1, u = 2 \dots u = U$, each of which contains one pentagonal dodecahedron unit cell (i.e. 10 Plateau borders, and six cell faces). The input parameters include the cell size d , the initial gas fraction in the foam f_G , the liquid surface tension, γ , viscosity, η , and density, ρ , and total drainage time t_D . The initial radius of curvature and volume of the Plateau borders are obtained by calculating the maximum w_{CF} (with $r_{PB} = 0$), reducing w_{CF} by 10%, and calculating the corresponding r_{PB} and V_{PB} . A boundary condition at the base of the column allows melt to flow into a reservoir once the liquid fraction exceeds 0.26 (which corresponds to a value of r_{PB} where the pentagonal dodecahedron is effectively spherical). The effect of a dispersed solid phase – such as the SiC particles used in FORMGRIP foams (§2.3.3) – on the rate of liquid flow is approximated by the use of an effective melt viscosity.

The algorithm flowchart of the model is shown in Figure 3.34. The initial distribution of liquid is uniform. Structural parameters, such as r_{PB} and w_{CF} , are initially the same for all the cells, and are calculated based on the input parameters. The change in volume of the Plateau borders in the top cell in the column ($u = 1$) due to flow of melt from the cell faces to the Plateau borders, and due to gravity and capillarity-driven melt flow, is calculated. Surplus melt from the top cell is then allowed to drain into the cell below ($u = 2$). A new volume of the Plateau border and cell face of the top cell are then calculated, and corresponding structural parameters (f_G, r_{PB}) are determined. The extent of drainage of melt from the second cell ($u = 2$) to the third cell ($u = 3$) is then similarly calculated. A new volume of the Plateau border and cell face of the second cell are then calculated, and corresponding structural parameters (f_G, r_{PB}) are determined, based on the volume after the flow of mass down to the third cell ($u = 3$) as well as any flow of melt from the first cell ($u = 1$). This process is repeated until the base of the column is reached. The calculation is then repeated for the next time step dt , again starting at $u = 1$ but with the new structural parameters for each cell, and progresses for N steps until the total drainage time $N \cdot dt$ is reached, when an output of – for example – f_G as a function of height is obtained.

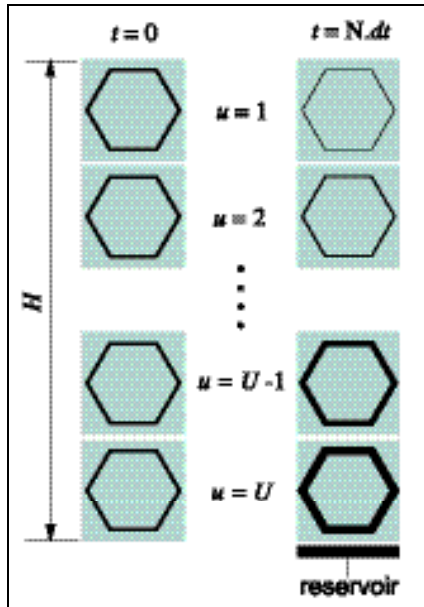


Figure 3.33: Schematic diagram of the model for melt drainage, showing the melt distribution at $t = 0$ and $t = N.dt$ [212].

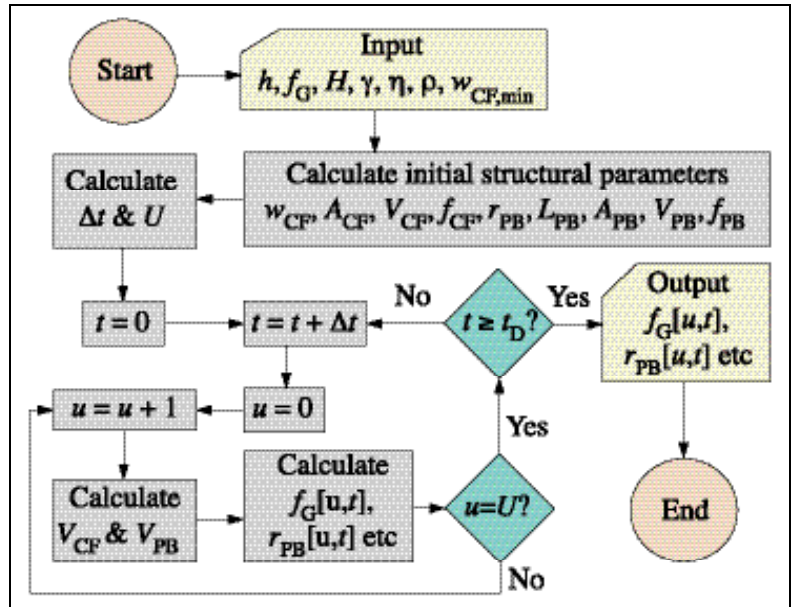


Figure 3.34: The overall algorithm flowchart of the model [212].

3.5 Components of the Duralcan™ metal-matrix composite

3.5.1 Silicon

The main alloy used hitherto for foaming is a metal matrix composite material with a dispersion of fine SiC particles in a hypoeutectic Al-9% Si matrix. Al-Si alloys are widely used as casting alloys, due primarily to their high fluidity and low solidification shrinkage. The system has an irregular eutectic with a faceted Si phase, at 577°C and 12.7 at.% Si, as shown in Figure 3.35. A skewed coupled zone, prompted by the more rapid growth of the aluminium phase, means primary dendrites of aluminium are usually present even in eutectic microstructures[156].

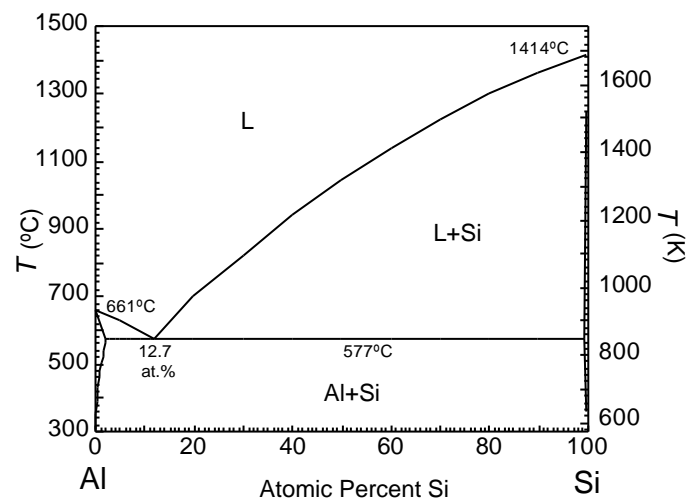
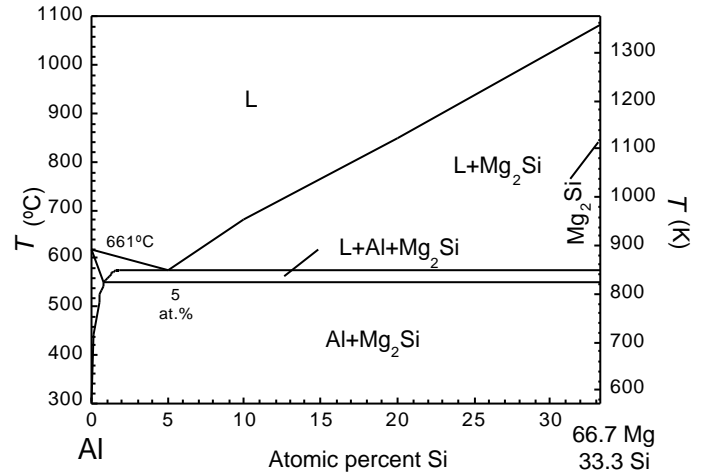


Figure 3.35:
The aluminium-silicon phase diagram.

3.5.2 Magnesium

The composite contains ~ 0.5% wt.% Mg, to allow precipitation hardening by the growth of Mg_2Si , as represented by the pseudo-binary Al- Mg_2Si phase diagram in Figure 3.36[206]. The Mg also acts as a surfactant, reducing any Al_2O_3 and SiO_2 that may be present at the Al-SiC interface in order to aid wetting of the SiC[188, 213].

Figure 3.36:
Al- Mg_2Si pseudo-binary phase diagram[214].

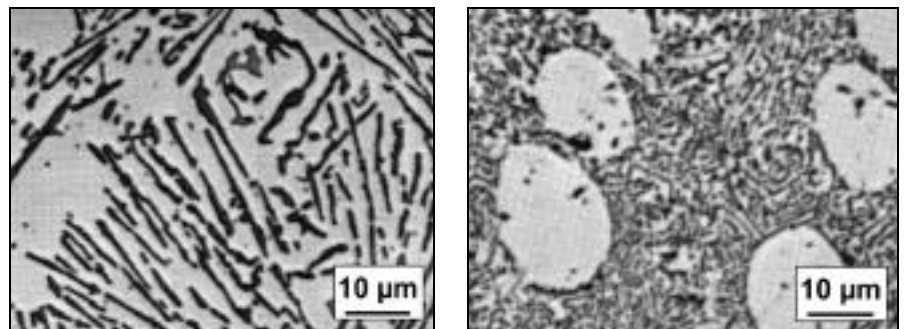


3.5.3 Strontium

Trace amounts of strontium are added to refine the microstructure, by prompting the growth of Si in an irregular fibrous structure rather than as large flakes, as shown in Figure 3.37. The precise mechanism by which this modification takes place remains unclear[215]. Sodium has a similar effect, but is more easily lost to evaporation or oxidation during remelting or foaming processes.

Figure 3.37:

An unmodified eutectic Al-Si alloy in the unmodified (left), and the same alloy composition modified with sodium (right)[215].



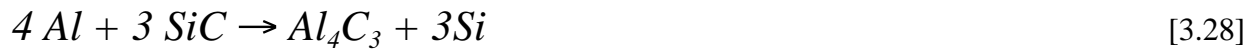
3.5.4 Silicon carbide

Particulate silicon carbide is added to the metal-matrix composite, mainly to enhance wear resistance. The small difference in stability between α - and β -phases of SiC mean both are often present[216]. Although the equilibrium contact angle of Al with SiC is 34°[177], measured Al-SiC contact angles are usually over 90° at processing temperatures, due to the presence of adsorbed surface contaminants[217]. The SiC is sometimes subjected to heat treatments and coatings prior to addition to aid wettability.

3.6 Processing phenomena

3.6.1 Formation of aluminium carbide

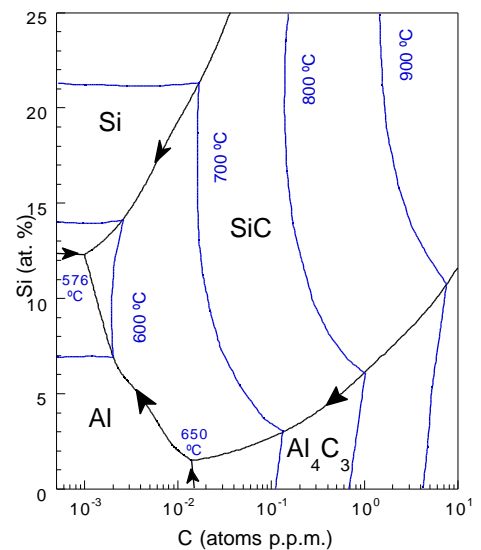
The reaction of SiC with liquid aluminium to form Al_4C_3 is thermodynamically favourable at temperatures above $\sim 650 - 700^\circ C$ by the reaction:



The reaction takes place rapidly at high temperatures in pure metals, as observed by X-ray diffraction and transmission electron microscopy[218]. At lower temperatures, there is a wide scatter of experimental results, though the reaction proceeds very slowly if at all at temperatures under $\sim 700^\circ C$ [192, 216]. The reaction is inhibited by a high Si activity[219]. An experimentally determined projection of the metastable Al-Si-C liquidus is shown in Figure 3.38, showing that SiC is formed in preference to Al_4C_3 in Al-Si-C melts with melting temperature under $650^\circ C$ [220].

Figure 3.38:

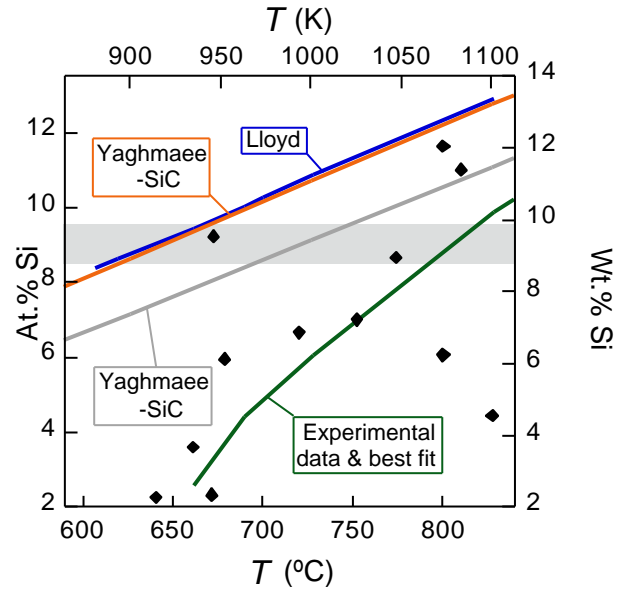
Liquidus projection of the Al-rich corner of the metastable Al-C-Si phase diagram[220].



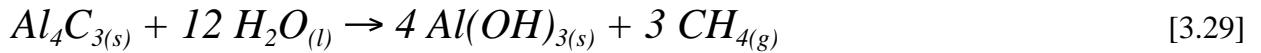
Thermodynamic predictions of the content of Si in the melt required to inhibit reaction of the SiC to form Al_4C_3 are shown in Figure 3.39[221-223]. The less stable β -SiC is expected to require a Si content $\sim 20\%$ higher than α -SiC to prevent reaction[216]. Experimental measurements are also shown: there is significant experimental scatter, with the thermodynamic limits as an upper bound, presumably reflecting slow reaction kinetics and the difficulty of detecting Al_4C_3 .

Figure 3.39:

Thermodynamic calculation for SiC[221, 222], separate calculation for -SiC and -SiC[216], and collected experimental observations of the proportion of Si required in the melt to completely inhibit reaction of SiC with aluminium to form Al_4C_3 [206]. The grey band represents the Si content of Duralcan™ MMCs.



Determination of the presence of finely dispersed Al_4C_3 precipitates is notoriously difficult, and is achieved by measuring the volume of methane evolved, typically during a month, by the hydrolysis reaction[224]:



This is particularly difficult in foams: infiltration of water into closed cell foams can take a comparable time, the surface area is unknown, and gas evolved within cells will not necessarily escape.

The effect of Mg on the stability of the reaction was recently modelled by Yaghmaee and Kaptay[216], based on activity data for elements in alloys, showing that raising the Mg content raised the required Si content, where $C_{(T)}$ is a temperature related constant:

$$X^{cr} Si_{(Al-Si-Mg)} = X^{cr} Si_{(Al-Si)} + C_{(T)} \cdot X_{Mg}$$

$$C_{(T)} = 0.229 + 0.644 \times 10^{-3} \cdot T(K) - 0.445 \times 10^{-6} \cdot T(K)^2 \quad (\text{for } -SiC) \quad [3.30]$$

$$C_{(T)} = 0.125 + 0.758 \times 10^{-3} \cdot T(K) - 0.465 \times 10^{-6} \cdot T(K)^2 \quad (\text{for } -SiC)$$

3.6.2 Gravity settling of particles

SiC, with density 3.7 g cm^{-3} , will settle in an aluminium melt of density 2.7 g cm^{-3} , giving rise to gradients in concentration[222, 225]. The eddy currents generated by induction heating are sufficient to maintain fine SiC particles in suspension. The terminal settling velocity of spherical particles of diameter d_p can be estimated (§3.4.3):

$$v_{terminal} = \frac{1}{18} (\rho_{solid} - \rho_{liquid}) g \frac{d_p^2}{\eta} \quad [3.28]$$

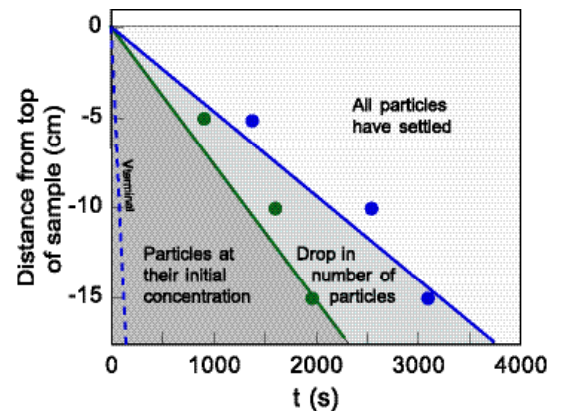
This predicts $v_{terminal}$ of $\sim 4 \text{ mm s}^{-1}$ for $10 \mu\text{m}$ SiC particles of $d_p \sim 10 \mu\text{m}$ in liquid aluminium. Semi-empirical analysis showed that for high particle concentrations of $90 \mu\text{m}$ particles, the settling is hindered by interactions with other particles, giving rise to the reduced settling velocity[226]:

$$v/v_{terminal} = (f)^C \quad [3.29]$$

C is a constant, varying between 2.39 and ~ 5 for turbulent and laminar flow respectively, predicting settling at under 1% of $v_{terminal}$. Studies of the settling of $\sim 10 \mu\text{m}$ SiC particles in Al demonstrated that the reduction in v is less marked, apparently due to agglomeration of particles[226, 227]. Figure 3.40 shows experimentally measured settling times for $14 \mu\text{m}$ SiC particles in an Al-7Si-0.33Mg alloy, which show that settling takes place at a rate significantly lower than $v_{terminal}$.

Figure 3.40:

Settling profile as a function of distance from the melt surface for an aluminium melt containing 5 vol.% SiC particles with $d = 14 \mu\text{m}$, determined by measurement of electrical resistance at several heights[226]. The rate of settling predicted by equation [3.28] for the terminal velocity of a single SiC particle is shown as a dotted line.

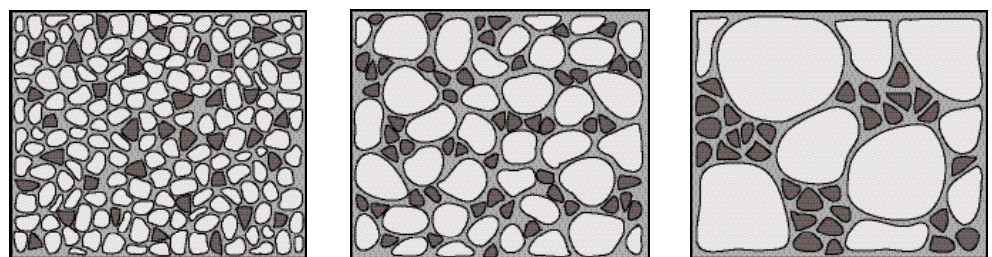


3.6.3 Particle pushing during solidification

In the Al-SiC_p system, provided the solidification front advances below a critical velocity, SiC particles are invariably pushed ahead of growing Al dendrites, becoming segregated to the last interdendritic pools of liquid[143, 146, 228, 229]. The extent to which pushing takes place depends mainly on the scale of the dendrites, which is determined by the cooling rate and alloy content (§3.4.4)[221]. As shown in Figure 3.41, dendrites on a scale comparable to that of the SiC particles have little effect on their distribution, while larger dendrites give rise to clusters of ceramic particles.

Figure 3.41:

The effect of cooling rate, and dendrite scale, on SiC clustering.

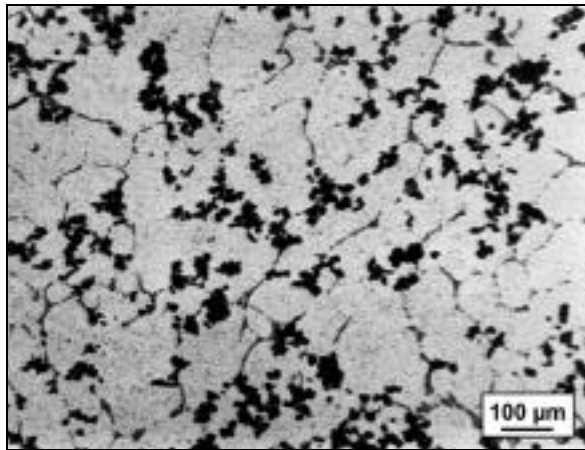


(a) Rapid cooling

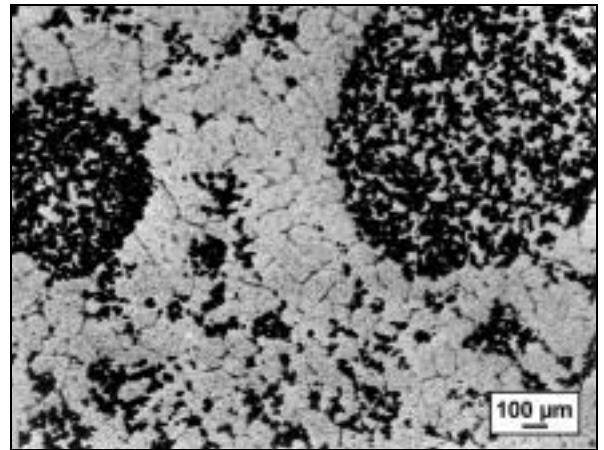
(b) Intermediate cooling rate

(c) Slow cooling

Figure 3.42 shows the effect of different cooling conditions on the extent of SiC clustering in an Al-Si alloy containing particulate SiC[230].



(a)



(b)

Figure 3.42: Optical micrographs of solidification-processed MMCs, showing (a) ceramic particles located in intercellular regions, and (b) large clusters of particles separated by particle-denuded regions[230].

4 Mechanical Properties of Closed-cell Aluminium Foams

The hierarchy of structure present in foams is discussed, and characteristic features of the mechanical properties of closed-cell foams are described. The differences between brittle and ductile failure in compression are discussed, and the structural and microstructural factors which cause such differences in compression mode are discussed. Various approaches to modelling the mechanical behaviour of such foams are reviewed, with the aim of linking features of the cellular structure to the bulk mechanical properties. The effect of various forms of structural irregularity on the mechanical properties is reviewed in light of this comparison.

4.1 Levels of scale

Metal foams can be characterised on three levels of scale. On one level, they can be considered as a bulk engineering material, ignoring the nature of the porosity altogether: material properties of interest are stiffness, strength, toughness and density, as well as the manner in which the foams undergo plastic yielding and work hardening. It is essential that these parameters are reproducible for a given type of foam, and preferable that there be scope within a production process for tailoring the values of these parameters to requirements.

On a second level, they can be viewed as an assembly of cells. Properties of interest include the range and distribution of cell size within a typical specimen, the cell shape, the manner in which the cells are arranged relative to each other, and the thickness, length, straightness and cross sectional profile of the cell faces. With a view to optimising the mechanical properties of foams, there has been much recent work exploring the relation between these aspects of the cell structure and the bulk material properties.

On a third level, the microstructure of the metal making up the foam is also significant. Since the width of cell faces is often comparable to the scale of features of the metallographic structure, the distribution of phases can be significant. The production of metal foams can entail the addition or generation of finely divided solid phases to act as stabilisers or surfactants, which may also affect mechanical performance. Relatively little is known about the relation between microstructure and bulk properties.

4.2 Tensile, compressive and shear deformation

The elastic properties of commercially available metallic foams have been widely studied, and are generally similar in tension and compression, at least for small strains[225, 231, 232].

Arguably the most important property of metallic foams is their ability to absorb large amounts of energy in compressive plastic deformation, while transmitting a low and approximately constant load. A consequence of this is that the compressive deformation of metallic foams has been studied more extensively than tensile deformation. The absence of a

comprehensive evaluation of the tensile properties of metallic foams to date is also a reflection of the difficulty of obtaining conclusive measurements of these properties. Plastic deformation in tension is closely related to the failure mode of the foam, with failure by the propagation of cracks or regions of plastic yielding along weak paths in the structure. The measured failure stress is strongly influenced by the presence of defects in the structure[233], with studies of tensile failure invariably noticing a considerable scatter in measurements[234]. Large numbers of tests, and a probabilistic approach to failure, are thus required to analyse the distribution of measured values[235]. Measurements of plastic failure in compressive deformation, although also influenced by the presence of local inhomogeneities in the cell structure (as discussed in later sections), are more indicative of average bulk properties.

The tensile yield strength of a closed-cell metallic foam is usually similar to, or lower than, the compressive yield strength. Several studies have found the tensile and compressive yield strength of Alporas™ foams (§2.3.3), which fail in tension by local plastic yielding, to be similar[159, 225, 233, 236]. In contrast, Andrews *et al*[225] noted that Alcan™ foams fail by rapid crack propagation, and have a markedly lower yield stress in tension than in compression. This is in apparent contradiction to the result of Von Hagen and Bleck on the same foams[234], where the strengths of Alcan™ foams were found to be similar in compression and tension. This may, however, be a consequence of the wide range of experimental scatter in the latter work, which was attributed to irregularity in the specimens.

The use of metallic foams in sandwich structures has given rise to investigations of its shear strength, and the effect of multiaxial and cyclic loads have been touched upon, although there has been little systematic experimental work in these areas[8, 237, 238].

4.3 Deformation of metallic foams in compression

4.3.1 Low-strain behaviour

Figure 4.1 shows a schematic stress-strain curve for the initial compression of a typical closed-cell metallic foam with a stochastic cell structure. A characteristic feature is the absence of a region of fully recoverable deformation: the tangent modulus in the initial loading curve is appreciably lower than that recorded when the foam is subsequently unloaded. Hysteresis is also commonly observed during unloading-reloading cycles.

Figure 4.1:

Schematic stress-strain curve for the early stages of deformation of a stochastic closed-cell metallic foam with two unloading-reloading curves, showing the yield stress $\sigma_{yield,upper}$ and the elastic modulus on initial loading, E_l , and unloading, E_u .

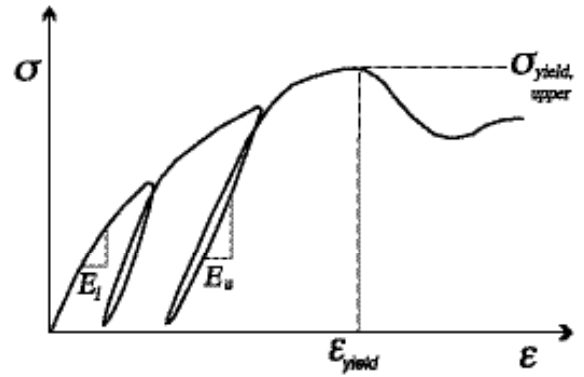


Image-matching software has recently been applied to series of images of foams being incrementally deformed, in order to better understand the irreversible deformation of foams at small loads[239-241], revealing that almost all of the elastic deformation is concentrated in discrete bands, typically separated by at least 3 - 4 cell diameters. Both the number of bands, and the extent of deformation within individual bands, increase with continued deformation. Localised plastic deformation of cell faces is noted in some cells within these bands, accounting for the non-linear initial loading curve.

It is worth noting that the localised nature of elastic deformation appears to be a direct result of the irregularity of melt-based foams. In open-cell metallic foams with a relatively uniform cell structure, made by replication of polymeric foams (§2.2.2), there is no difference observed between loading and unloading modulus, and similar image-matching during the early stages of deformation has shown that elastic deformation is more homogenous[225, 239].

Although the elastic modulus is of prime importance for the structural use of aluminium foams, it is thus sensitive to local variations in cell structure and the measurement technique used. The unloading modulus is most commonly quoted as the 'elastic modulus'. It has been claimed that techniques such as ultrasonic measurement of stiffness can measure the modulus of the structure prior to any local deformation[242], although this technique has yet to be widely applied to cellular metals, and the 'unstressed' modulus is arguably of limited relevance to potential applications.

The elastic Poisson's ratio for most foams is around 0.33[243], although in view of the localised nature of the deformation, at least in stochastic foams, a wide scatter in measured results is to be expected.

4.3.2 Yielding & Plastic collapse

Deformation bands

Large-scale plastic yielding of closed-cell, melt-based metallic foams is generally initiated by the co-operative plastic collapse of a single band of cells over the full cross section of the specimen. This failure occurs in one of the bands of concentrated local deformation that develop during the first, nominally elastic, stage of deformation, often in a region of low local density[239, 240, 244]. Extensive deformation of cell faces occurs within this band, leading to local densification, at which point plastic failure occurs in another band of uncollapsed cells. The formation of this band of collapsed cells is normally accompanied by a drop in the load supported by the foam, as shown schematically in Figure 4.1.

Regions of foam that have undergone complete plastic collapse thus coexist with regions that have undergone only elastic deformation. Even at relatively high macroscopic plastic strains, the continued yielding occurs by crushing of undeformed material, giving rise to an approximately constant plateau stress: stage 2 of the schematic stress-strain curve in Figure 4.2. The localised nature of large-strain in foams means that engineering stress and strain are always quoted.

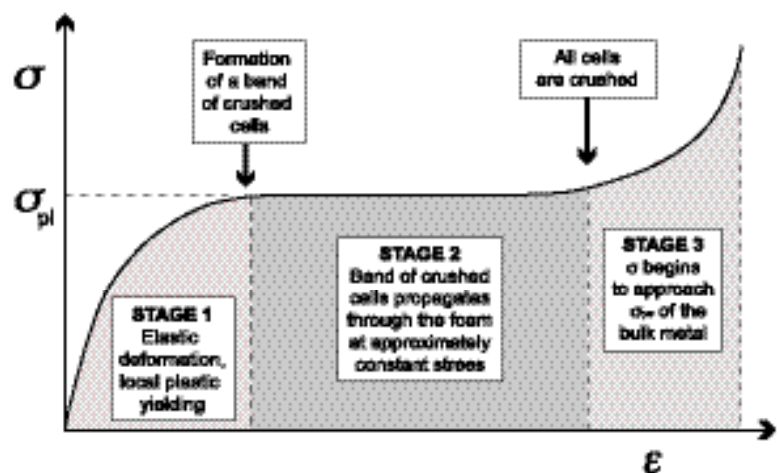


Figure 4.2:

Three stages in the stress-strain curve for a metallic foam subjected to large compressive strain.

Plastic collapse sometimes proceeds by the propagation of the initial band of collapsed cells normal to its plane throughout the specimen[70, 159], although the successive failure of several discrete collapse bands, separated by regions of uncollapsed foam, has also been reported in several studies[231, 235, 245, 246]. It appears that the latter studies generally concern foams with particularly irregular cell structures, suggesting that the presence of multiple failure bands is a consequence of regions of locally high density in the cell structure preventing continued propagation of the initial failure band[244], prompting plastic collapse elsewhere in the foam [235]. Bastawros *et al*[241] state that failure of a band of cells stiffens its environs, and that the

failure band will thus not propagate normal to its plane, although no reason is provided for why this should be the case.

Densification

As the collapse of bands of cells continues, a point is reached where no open space remains for deformation by bowing or buckling, characterised by a sharp rise in the stress-strain curve as the strength of the foam approaches that of the parent metal (Stage 3 in Figure 4.2). The engineering strain at which densification occurs, ε_d , is given by the following empirical relation, based on data for foams with ρ^*/ρ_s between 0.02 and 0.4[247-249]:

$$\varepsilon_d = 1 - 1.4 \frac{\rho^*}{\rho_s} \quad [4.1]$$

The factor of 1.4 accounts for small voids trapped within the material even when no further cell deformation is possible.

Poisson's Ratio

The plastic Poisson's ratio has usually been found to be approximately zero, since virtually no lateral movement is normally observed during plastic collapse[231, 250]. The large amount of free space means the initial collapse bands can follow the path of least resistance in non-uniform foams, and are often locally observed at angles of 45° or more to the compression direction[162, 240]. The hydrostatic yield strength is of similar magnitude to the uniaxial yield strength[237].

4.4 Brittle and ductile collapse modes

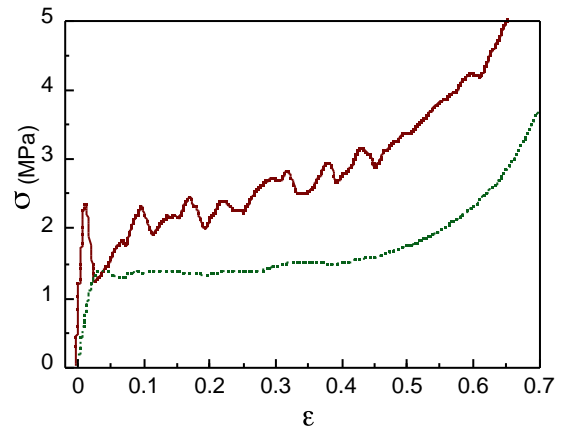
The plastic collapse behaviour of closed-cell metallic foams can be divided into two broad categories, generally referred to ductile and brittle collapse. Ductile collapse is characterised by a relatively smooth plateau in the stress-strain curve, sometimes with a gradual rise due to strain hardening or progressive densification. In brittle collapse yielding is accompanied by a marked drop in the measured load, followed by marked serrations in the stress-strain curves as the foam is crushed. Stress-strain curves characteristic of the two types of failure are shown in Figure 4.3. Work hardening can give rise to a gentle rise in the stress-strain curve. It is only observed in foams which undergo ductile collapse and have a low alloy content, and presumably reflects work hardening of the metal alloy[231, 235, 251].

Figure 4.3:

Compressive stress-strain curves for cubic specimens of a ductile (Alulight™) and brittle (Alcan™) foam [225]. The specimens had at least seven cell widths in each direction.

— Brittle Alcan™ foam
Al-15 vol.% 10-20 μm SiC
Foamed by injection of air

⋯ Ductile Alporas™ foam
Al-2 vol.% Ca, stirred in air
Foamed with 1-3 wt.% TiH₂



Importance of the mode of collapse

When considering foams for use as energy absorbing materials, two key parameters are the energy absorbed per unit mass during compression and the stress at which this energy is absorbed. The former is given by the area under the stress-strain curve multiplied by the initial density of the foam. Depending on the application, the shape of the curve before the stress exceeds a critical value, σ_c , may be important. As illustrated in Figure 4.4, a marked load drop after yielding, or rapid work hardening, may occur. In general, these are undesirable [70, 231]. The plateau stress $\sigma_{plateau}$ can sometimes be tailored to match σ_c for a given application, albeit at the expense of a reduced densification strain ϵ_d .

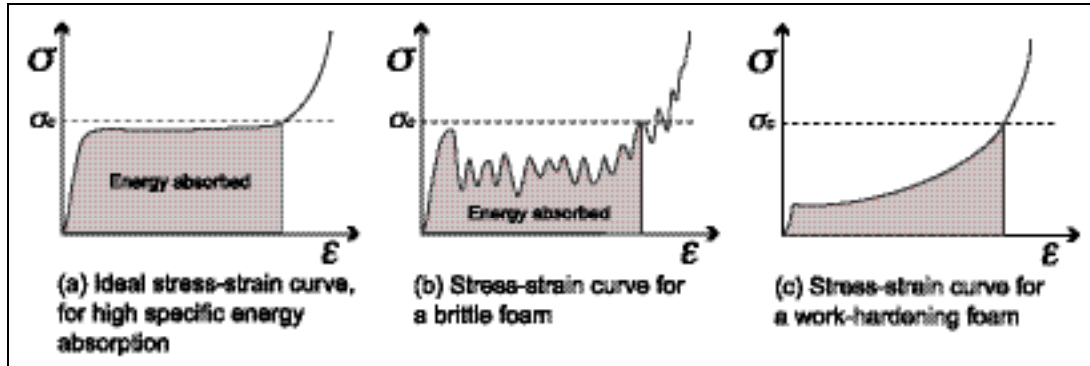


Figure 4.4: Schematic stress-strain curves for: (a) an 'ideal' foam, (b) a foam undergoing brittle collapse and (c) a foam with extensive work hardening. The region of useful energy absorption until a critical compressive load σ_c is reached is shaded.

Brittle and ductile collapse in commercially available foams

The reasons why foams fail in brittle or ductile manner remain unclear. Much of the experimental work concerning the failure of metallic foams has been concerned with the commercially available foams reviewed in Chapter 2 [70, 225, 232, 234]. No clear correlation between the mode of collapse and the geometry or homogeneity of the cell structure has been found. These studies have consistently noted that Alcan™ foams are markedly more brittle than Alporas™ or Alulight™ foams, an observation which is jointly attributed to the high silicon (~ 7 wt.%) and particulate SiC (~ 15 vol.%) content of the Alcan™ foams. The metal matrix of commercially available foams containing particulate SiC invariably has a high Si alloying

content to prevent reaction of the SiC with the aluminium (§3.6.1), and the particles are found in the interdendritic region of the metallic microstructures, and are thus associated with other coarse intermetallic phases. It is thus difficult to isolate the effect of the dispersed SiC from that of the potentially brittle Al-Si metallographic microstructure by comparison of the properties of commercially available foams.

The effect of the metallographic microstructure

Three studies have examined the effect of varying the metallographic microstructure independently of that of the presence of solid refractory particles. Thornton and Magee[231] first studied the effect of alloy content on the mode of yielding, by comparing the compressive failure of Al, Al-7Mg, and solution-treated Al-7Mg foams. However, the high degree of irregularity of the foams studied limits the conclusions that can be drawn.

This recently prompted Fusheng and Zhengang[159] to replicate the experiments using more homogenous foam structures, produced with pure aluminium and Al-10Mg melts using a process similar to that used to produce Alporas™ foams (§2.3.3). The stress-strain curves obtained are shown in Figure 4.5 (a) and (b). Deformation of the pure aluminium foams occurred by plastic yielding of the cell faces, and is characterised by a smooth plateau stress, with gradual work hardening. In contrast deformation of the Al-10Mg foams occurred by brittle fracture of the cell faces, with stress-strain curves characterised by a load drop after the onset of plastic yielding followed by pronounced serrations. As the foams were otherwise similar, apart from a smaller cell size in the Al-10Mg foams, this implies that the metallic alloy has a significant influence on yield behaviour. Specimens of the Al-10Mg foam were subjected to a heat treatment of 450°C for 20 hours, which was assumed to take any precipitates into solution. The resulting stress-strain curves are shown in Figure 4.5 (c), suggesting that the removal of precipitates prompts a reduction in the magnitude of the serrations.

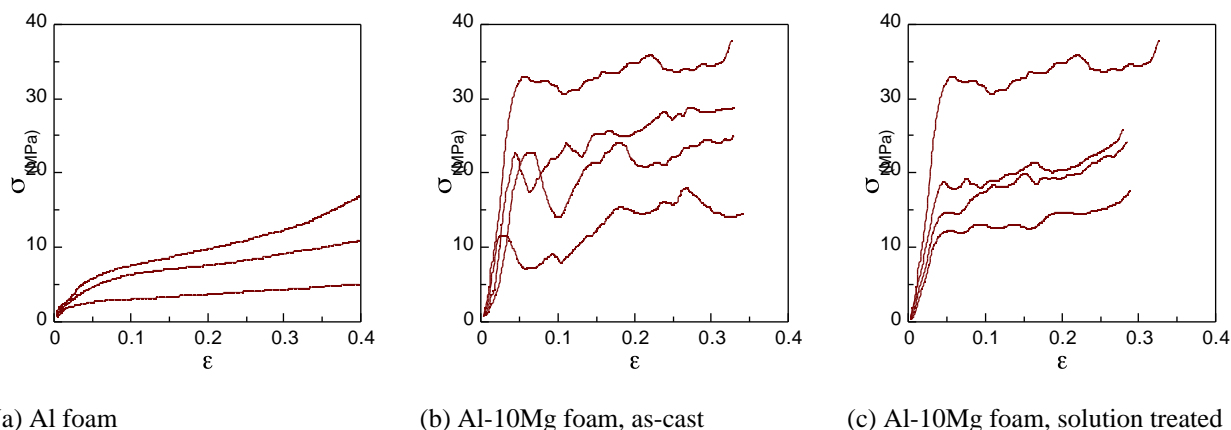


Figure 4.5: Stress-strain curves for specimens of foams with ρ^*/ρ_s between 0.15 and 0.30, demonstrating the effect of the metal alloy on the extent of serrations in the stress strain curve. The foams in plot (c) were formed by solution treatment of the foams in plot (b) at 450°C for 20 hours.

Markaki and Clyne[99] recently examined the correlation between the mechanical properties and the observed metallographic microstructure of powder-based Al-1Mg-0.6Si and Al-12Si-0.6Mg Alulight™ foams. The Al-1Mg-0.6Si foams had a dendritic microstructure, and underwent progressive ductile collapse by buckling of cell faces, with a smooth loading curve.

The Al-12Si-0.6Mg foams, with similar cell structures, had a less ductile microstructure of Al dendrites separated by a coarse Al-Si eutectic microstructure. These failed by highly localised brittle collapse, accompanied by ejection of cell face fragments from boundary cells, with some serrations visible in the stress-strain curve. Scanning electron microscopy of tensile failure surfaces of the foams was consistent with a difference in ductility, with the Al-12Si-0.6Mg foam showing significantly less ductile dimpling than the other foams.

The effect of a dispersed solid phase

The inclusion of angular SiC particles is known to reduce the ductility and fracture toughness of bulk metal-matrix composites, with increasing SiC content reducing the extent of ductile dimpling on fracture surfaces[221, 252], although it remains unclear whether fracture is a result of the opening of voids inside clusters of particles, or failure of the particle-matrix interface. The same might be expected in metallic foams containing SiC inclusions, with debonding at the particle/matrix interface sometimes observed in the preliminary stages of fracture of Al-SiC_p foams[162]. Kenny found that varying the volume fraction of particles from 10 to 20%, and the material from SiC to Al₂O₃, had little effect on compressive failure characteristics[161], although the cell structures of the foams considered were so irregular that interpretation of the results is difficult.

4.5 Relating bulk mechanical properties to cell structure

Early studies of the mechanical properties of foams were largely empirical[231]. However, the large number of structural parameters in cellular structures, and the difficulty of varying them independently, make it difficult to evaluate their influence on the mechanical performance of a foam. Modelling the properties of idealised cellular structures can provide an insight into the relative importance of particular structural features, as well as providing an upper bound estimate of the mechanical performance that can be achieved in a cellular structure. Modelling the deformation of simplified non-ideal structures can also provide some indication of the effects of various types of structural inhomogeneity on the bulk mechanical properties.

At the simplest level, a particular type of deformation is assumed in order to link properties by dimensional analysis, with any constants of proportionality being determined empirically. In

a more analytical approach, a periodic cell geometry is assumed, and a geometrical model for its deformation derived using structural mechanics, allowing forces and distortions at the strut level to be directly related to bulk properties. These models produce general expressions for the mechanical behaviour of periodic foams, although they necessarily rely on idealised models of the foam structure. Predicting the deformation of more realistic cellular structures, and structures which incorporate a degree of non-periodicity, requires numerical finite element modelling (FEM) of specific cell arrangements. The basis of various models, and the predictions obtained, are reviewed in section 4.6.

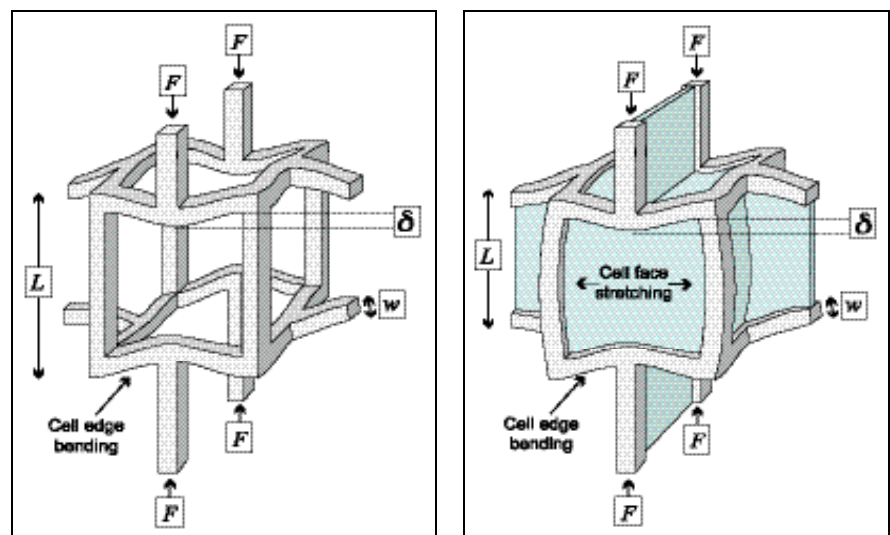
4.6 Modelling elastic deformation

4.6.1 Dimensional Analysis of elastic deformation

In order to derive a relation between the bulk stiffness of the foam and the relative density, Gibson and Ashby, Gibson and Ashby[2, 238, 253] assume that linear elastic deformation of open-cell foams is primarily the result of bending of cell struts, and apply dimensional analysis to the simplified unit cells shown in Figure 4.6.

Figure 4.6:

Elastic deformation of a simplified unit cell in an open-cell foam by bending of cell struts, and of a simplified unit cell in a closed-cell foam in which both bending of cell struts and stretching of cell faces contribute to the elastic stiffness[253].



The relative density of a low-density open-cell foam, ρ^*/ρ_s , is assumed to with the thickness, w , and length, L , of the cell edges as:

$$\frac{\rho^*}{\rho_s} = C_1 \frac{w}{L}^2 \quad [4.2]$$

where C_1 is a numerical constant dependent on the cell geometry. Compression or tension of the foam causes the struts to be loaded at their midpoint. The deflection of a single strut, according to standard beam theory, is:

$$\delta = \frac{F L^3}{E_s I} \quad [4.3]$$

For small deflections, the deflection of the bulk structure is directly proportional to the deflection of the individual beams. The force, F , is related to the bulk stress on the foam, σ , by

$F \propto \sigma L^2$, and the strain, ϵ , is related to the displacement, δ , by $\epsilon = \delta/L$. The Young's modulus for the foam, σ/ϵ , is thus given by:

$$E^* = C_2 \frac{E_s I}{L^4} \quad [4.4]$$

Using these relations between t , L , and ρ^*/ρ_s , and the fact that the second moment of area of one of the cell struts is related to the dimensions by $I \propto w^4$, the following power law relation is obtained:

$$\frac{E^*}{E_s} = C_3 \left(\frac{\rho^*}{\rho_s} \right)^2 \quad [4.5]$$

When extending this analysis to closed cell foams, the stretching of the membranes in the cell faces also has to be considered, with the following relation obtained:

$$\frac{E^*}{E_s} = C_4 \phi^2 \left(\frac{\rho^*}{\rho_s} \right)^2 + C_5 (1 - \phi) \frac{\rho^*}{\rho_s} \quad [4.6]$$

The second term accounts for the stretching of the cell faces. Surface tension generally draws material from the centre of the cell faces to the edges (§3.2), giving rise to thin cell faces which have relatively little effect on the mechanical performance of the foam[235]. This is accounted for by the parameter ϕ , which denotes the fraction of the total material in the Plateau borders. The mechanical properties of many nominally closed-cell foams lie somewhere between those of an 'ideal' closed cell foam with uniform cell face and edge thickness ($\phi = \rho^*/\rho_s$), and those of an open cell foam ($\phi = 1$), as illustrated in Figure 4.7. The model relies on the assumption of a thin membrane, and although the range of ϕ over which the model remains valid is not specified, Gibson and Ashby apply a lower limit of $\phi = 0.6$ in practice[2].

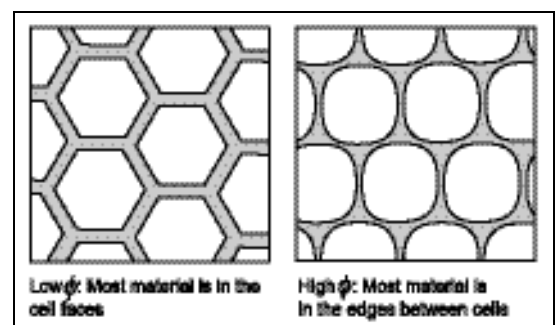


Figure 4.7:
Two-dimensional representation of foam structures of different ϕ .

In the original derivation of equation [4.6], an additional term is incorporated to account for compression of gases within the cell. Although significant in polymeric foams, the higher stiffness of metallic foams means the effect of gas pressure is negligible[2]. The numerical constants C_3 , C_4 and C_5 were derived by fitting of the power law to a wide range of experimentally determined stiffness data, most of which was for polymeric foams, with the general result that all three constants are close to unity.

Figure 4.8 shows measured E^*/E_s as a function of ρ^*/ρ_s for a range of closed-cell metallic foams (with ϕ between ~ 0.6 and ~ 0.8), and the predictions of equations [4.5] and [4.6] for foams with various ϕ . Assuming that the foams have similar cellular structure, and performing a least-squares best fit of equation [4.6] to the data with $C_3 = C_4 = C_5 = 1$, suggests $\phi = 0.88$, a relatively high value when compared to the experimentally observed ϕ in these relatively thick-faced closed-cell foams, suggesting that the metallic foams have lower relative stiffness than the polymeric foams for which the constants were derived. There is a wide range of scatter in the experimental data, with some closed-cell metallic foams having E^*/E_s under that predicted for an open-cell polymeric foam. Possible sources of the scatter, and the apparent underperformance of some closed-cell metallic foams, are discussed in section 4.9.

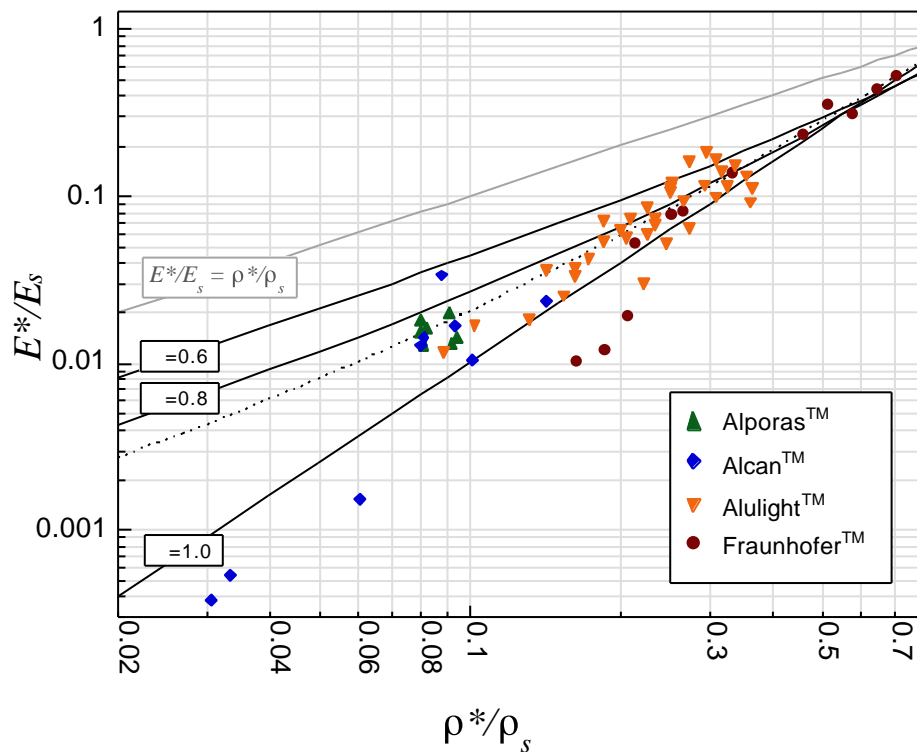


Figure 4.8: E^*/E_s according to equation [4.5], and equation [4.6] with $\phi = 0.6, 0.8$ and 1.0 , and $C_3 = C_4 = C_5 = 1$.

Experimentally determined values of E^*/E_s for AlporasTM, AlcanTM, AlulightTM and FraunhoferTM closed-cell aluminium foams of various densities (§2.3.2-2.3.3) are also plotted (after [238]).

A least-squares best fit line is also plotted for the collected melt-based metallic foams, shown as a dotted line, where the values of C_4 and C_5 were fixed at 1 and ϕ was fitted to the data. This corresponds to $\phi = 0.88$.

4.6.2 Analytical modelling of elastic deformation

Analytical calculation of the deformation of segments of a cell structure under an applied load can be used to provide a direct link between the shape and geometry of the struts and bulk deformation, avoiding the need for an empirical determination of the constants of proportionality in equations [4.5] and [4.6]. Two approaches are reviewed here: one in which a cellular material

is assumed to consist of an array of randomly oriented struts, and one in which the deformation of a small segment of an idealised unit cell under a load is considered.

Deformation of a fibre array

In a recent approach by Markaki and Clyne[254, 255], the elastic deformation of a three dimensional isotropic array of joined fibres is modelled. An applied load is assumed to be distributed across a number of fibres oriented at various angles to the vertical, joined by rigid connections. Standard beam theory is applied to determine the deflection of a single fibre oriented at a given angle to the compression axis, with orientation constrained at both ends. The fibres are assumed to exhibit a spherically symmetric distribution of alignment, and the stiffness is obtained by summation of the resolved deflection of individual fibres parallel to the compression axis. The following relation is obtained, with j representing the average aspect ratio (length/width) of the length of fibre between successive fibre joints:

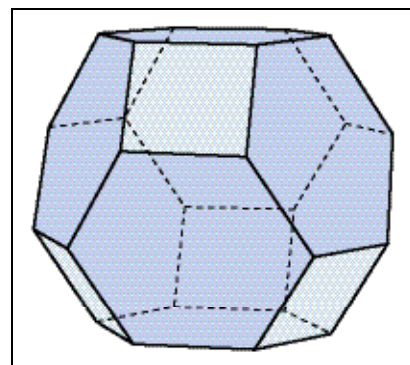
$$\frac{E^*}{E_s} = \frac{9}{32} \frac{1}{j^2} \frac{\rho^*}{\rho_s} \quad [4.7]$$

Deformation of an idealised unit cell

The elastic properties of a structure consisting of a periodically repeated cell unit can be modelled analytically. Although tetrahedral units with four struts joining have been used as a representative element of a foam structure in this context[256], most work concerns the deformation of tetrakaidecahedral cells. The tetrakaidecahedron, illustrated in Figure 4.9, is thought to be the most efficient single space-filling unit cell, and is generally considered to represent an ideal foam structure[257, 258].

Figure 4.9:

The tetrakaidecahedron, with 14 faces (8 regular hexagons, and 6 squares). The sides are sometimes slightly curved to obtain more realistic (120°) contact angles between adjacent cell faces.



Modelling work in this area has been primarily concerned with polymeric foams, and hence applies to cellular structures with ρ^*/ρ_s somewhat lower than that usually encountered in metallic foams. Zhu *et al*[259] and Warren and Kraynik[258, 260] independently derived the elastic modulus open-cell, low-density tetrakaidecahedral cell structures by consideration of the force-displacement relations for individual struts in the unit cell, obtaining similar results. For Plateau borders of triangular cross-section[259]:

$$\frac{E^*}{E_s} = \frac{0.726 \left(\frac{\rho^*}{\rho_s}\right)^2}{1 + 1.09 \frac{\rho^*}{\rho_s}} \quad [4.8]$$

The value of E^* obtained is nearly isotropic. The shape of the cross section is significant: Zhu *et al* predict that replacing the triangular cross section with a curved one more representative of a Plateau border in a closed cell foam gives rise to an increase in modulus[259]:

$$\frac{E^*}{E_s} = \frac{1.009 \left(\frac{\rho^*}{\rho_s}\right)^2}{1 + 1.514 \frac{\rho^*}{\rho_s}} \quad [4.9]$$

Warren and Kraynik predict a 36% increase in E^*/E_s for the same shape change.

4.6.3 Finite element modelling of elastic deformation

The deformation of cellular materials can also be predicted by FEM. Kraynik *et al*[258] modelled the deformation of an idealised low-density ($\rho^*/\rho_s \ll 1$) tetrakaidecahedral cell structure with closed cells and cell faces of uniform thickness. The Plateau borders were ignored, with $\phi \sim \rho^*/\rho_s$. The following relation was obtained (again with nearly isotropic E^*):

$$\frac{E^*}{E_s} = 0.34 \frac{\rho^*}{\rho_s} \quad [4.10]$$

Simone and Gibson[261] subsequently extended this approach to closed-cell foams with more clearly determined Plateau borders and ρ^*/ρ_s of up to 0.2, finding that:

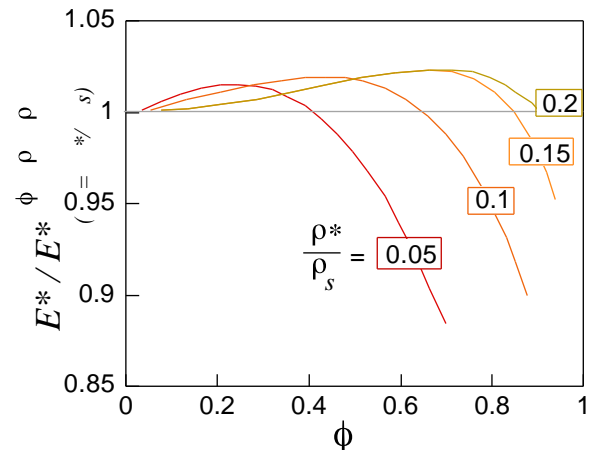
$$\frac{E^*}{E_s} = 0.316 \frac{\rho^*}{\rho_s} + 0.319 \left(\frac{\rho^*}{\rho_s}\right)^2 \quad [4.11]$$

This is equivalent to equation [4.6] with $\phi = 0.68$, $C_4 = 0.69$, and $C_5 = 1$.

In the same study, the effect on the stiffness of varying the solid distribution (in terms of ϕ) was modelled for an idealised node. Results are shown in Figure 4.10, where the upper bound of ϕ represents a situation where the entire cell face is part of a gently curving Plateau border.

Figure 4.10:

The effect of ϕ on $E^*/E^*_{(\phi=\rho^*/\rho_s)}$ as predicted by finite element modelling [261]. The values are normalised by the value of E^* for a tetrakaidecahedral foam with uniformly thick cell faces, and hence no Plateau borders with $\phi = \rho^*/\rho_s$. The predicted stiffness was nearly isotropic.



It was predicted that changes in ϕ only have a small effect on the bulk stiffness in foams with $\rho^*/\rho_s = 0.15$. Increasing ϕ initially increases the stiffness, as the increase in bending moment of the Plateau border outweighs the reduction in the moment of inertia of the cell faces. At higher ϕ , stiffness is reduced due to the high compliance of the cell faces.

4.6.4 Upper bound models

The ultimate upper bound of uniaxial stiffness which can be obtained in a cellular material is where $E = \rho^*/\rho_s$, although this cannot be realised in an isotropic material. Various models for the upper-bound elastic properties of idealised cellular solids are reviewed by Grenestedt[262]. Perhaps of most interest is the Hashin-Shtrikman model for the stiffness of isotropic closed-cell cellular solids, which is derived for a solid composed of hollow spheres which all have the same ratio of face thickness to diameter, with various sizes to fill the entire space[263]. The following relation is obtained:

$$\frac{E^*}{E_s} = 0.59 \frac{\rho^*}{\rho_s} \quad [4.12]$$

This is commonly considered to constitute the upper bound of E^*/E_s which can be obtained in an isotropic cellular solid.

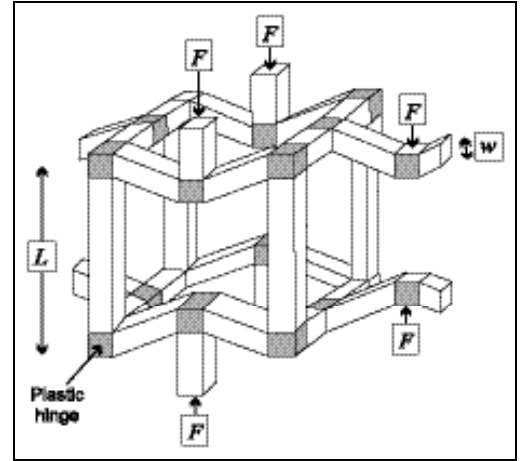
4.7 Comparing the predictions

The predicted stiffness of cellular solids according to the approaches used to model elastic deformation reviewed in section 4.6 are compared in Figure 4.11. Models referring primarily to closed-cell foams are presented as solid lines, with dotted lines for models referring to open-cell foams. It should be noted that some of the models apply only to foams with low ρ^*/ρ_s . Predictions of the analytical fibre-based model of Markaki and Clyne[254, 255] are plotted for a fibre aspect ratio of 3, 4 and 5 between nodes.

Despite the range of techniques employed, the models are in reasonable agreement with the semi-empirical dimensional analysis predictions of Gibson & Ashby[2], which are most widely used as a benchmark against which the stiffness of newly developed foams is measured.

Figure 4.12:

Plastic hinges (shaded) in a schematic open-cell foam [264].



The following relationship is obtained, linking the plastic collapse stress when the foam begins to fail by crushing, σ_{pl}^* , the yield stress of the solid metal, σ_{ys} , and the relative density of the foam, for $\rho^*/\rho_s < 0.3$:

$$\frac{\sigma_{pl}^*}{\sigma_{ys}} = C_6 \left(\frac{\rho^*}{\rho_s} \right)^{3/2} \quad [4.13]$$

For a closed-cell foam, for $\rho^*/\rho_s < 0.2$:

$$\frac{\sigma_{pl}^*}{\sigma_{ys}} = C_7 \phi \left(\frac{\rho^*}{\rho_s} \right)^{3/2} + C_8 (1 - \phi) \frac{\rho^*}{\rho_s} \quad [4.14]$$

Comparison of the predictions with experimental data for a wide range of polymeric foam structures with $\phi = 1$ suggests that $C_6 = C_7 = 0.3$. Due to a lack of suitable experimental data, the value of C_8 was estimated by finite element modelling to be 0.4.

Figure 4.13 shows experimentally determined yield stress data for a range of commercially available aluminium foams, and the predictions of equations [4.13] and [4.14] with the constants determined empirically for polymer foams. Applying a least-squares fit to the experimental data according to equation [4.14] provides an best-match ϕ of 0.70, although the scatter in the experimental data is significant, with many closed-cell metallic foams having lower σ^*/σ_s than that predicted for open-cell polymeric foams for which the constants C_6 and C_7 were derived. In contrast to the stiffness data of Figure 4.8, there is some apparent variation between types of foam - with the relatively irregular Alcan™ foams having consistently lower normalised yield stress than the other foams. The observed scatter in σ^*/σ_s , and the relatively low normalised yield stress of some metallic foams in comparison with polymeric foams, is thought to be the result of local defects in the cell structure. Various types of defect, and their predicted effect on the bulk yield stress, are reviewed in section 4.9.

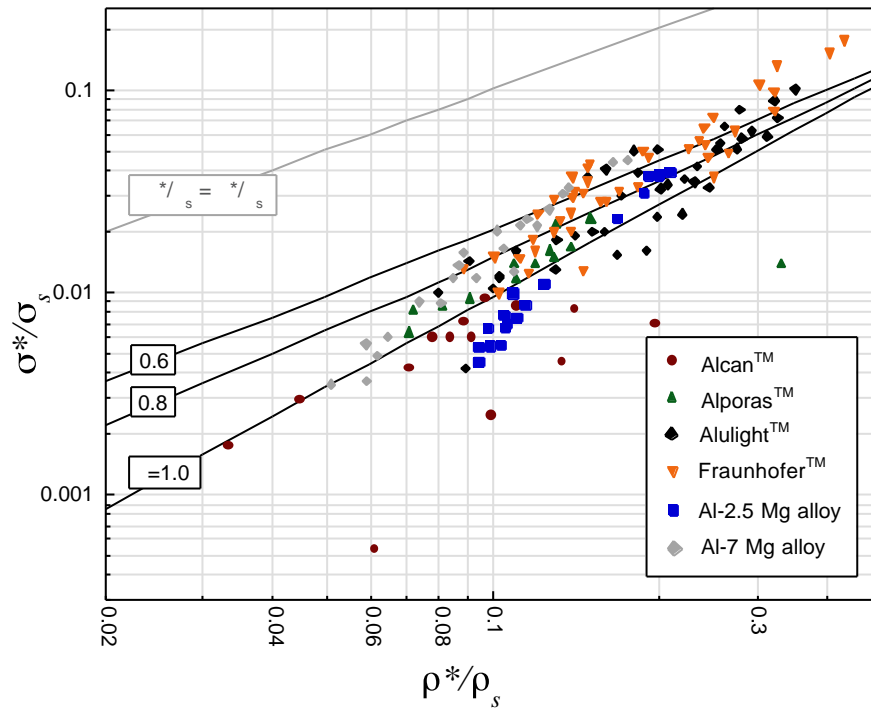


Figure 4.13: σ^*/σ_s according to equation [4.13], and equation [4.14] for $\phi = 0.6, 0.8$ and 1.0 , with $C_6 = C_7 = 0.3$ and $C_8 = 0.4$.

Experimentally determined values of σ^*/σ_s for Alporas™, Alcan™, Alulight™, and Fraunhofer™ closed-cell aluminium foams of various densities (§2.3.2-2.3.3), as well as the Al-Mg foams studied by Thornton and Magee[231], are also plotted (after [238]).

4.8.2 Other approaches

The localised, defect-sensitive nature of plastic yielding in metallic foams (§4.3.2) makes prediction of yield stress in real foams by analytical methods difficult. Analysis of the plastic yielding of a single tetrakaidecahedral unit cell by finite element modelling was used by Simone and Gibson[261] to predict the yield stress of uniform closed-cell foams with ρ^*/ρ_s under 0.2 , with the result:

$$\frac{\sigma^*}{\sigma_s} = 0.445 \frac{\rho^*}{\rho_s} + 0.335 \left(\frac{\rho^*}{\rho_s}\right)^2 \quad [4.15]$$

This is compared with the results of dimensional analysis in Figure 4.14.

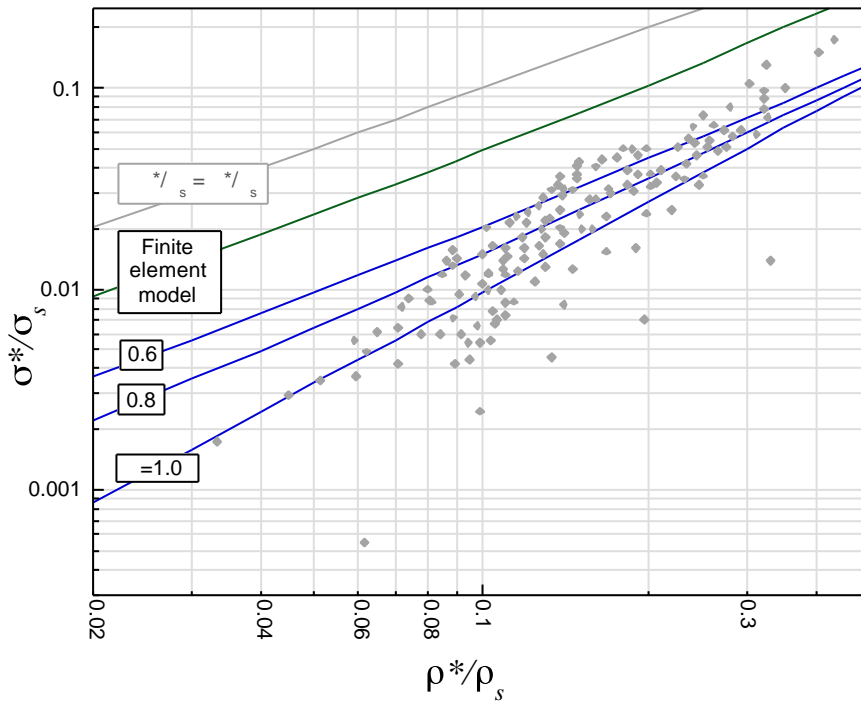


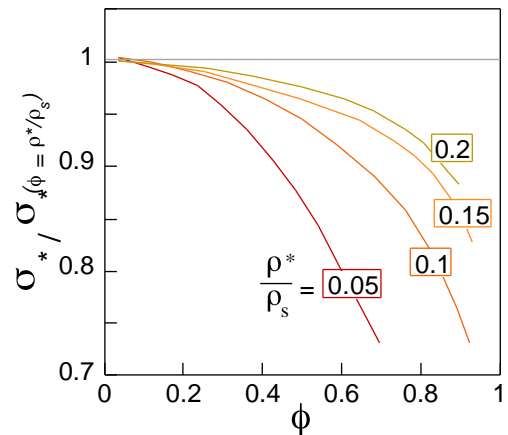
Figure 4.14: Predicted σ^*/σ_s as a function of ρ^*/ρ_s according to equation [4.15][261]. The dimensional analysis results of equations [4.13] and [4.14] are also plotted with various values of ϕ (labelled on the curves), with $C_6 = C_7 = 0.3$, and $C_8 = 0.4$. The experimentally determined values of σ^*/σ_s for various stochastic commercial foams in Figure 4.13 are also plotted.

The prediction is significantly higher than that obtained by the dimensional analysis (which, for closed-cell foams, incorporates a degree of empirical observation and finite element modelling), and the experimental data for real metallic foams, suggesting that there is considerable scope for increasing the relative yield stress of metallic foams by modifying the cellular structure.

The effect of variable ϕ on the collapse strength σ^*/σ_s of an idealised tetrakaidecahedral unit cell was also investigated. The results demonstrated a significant influence in the case of lower-density foams, as shown in Figure 4.15 for foams of various densities[261].

Figure 4.15:

The effect of ϕ on σ^*/σ_s , predicted by finite element modelling of the deformation of an idealised tetrakaidecahedral cell [261].



The peak stress decreases with the formation of a Plateau border, as the net area of the cross sectional area of the edges is reduced, reducing its resistance to deformation. The effect of ϕ on yield stress is more pronounced than that on elastic modulus, but remains relatively small for the range of ϕ found in typical closed-cell foams.

4.9 Accounting for non ideality

As shown by the comparison of the elastic and plastic deformation of ideal structures with that of real metallic foams in sections 4.6-4.8, the measured elastic stiffness and yield strength of real foams are generally subject to considerable scatter, and generally fall short of that which might be expected based on modelling of the mechanical properties of regular cellular structures. The key to enhancing the specific stiffness and strength of stochastic cell structures lies in understanding the extent to which general and local structural features affect the bulk mechanical properties, and how their effect can be controlled. This might be achieved by a combination of modelling and direct observation of deformed foams. The following sections explore the effect of various features of a stochastic cellular structure in more detail, and examine the degree to which the presence of such features is thought to affect bulk mechanical properties.

4.9.1 The effect of generalised irregularity in cellular structure

The most visible difference between melt-based foams and the idealised foam structures modelled in sections 4.6 and 4.8 is that the cell distribution is stochastic, with a range of cell size and local geometry. The effect of irregular cell configurations is relatively difficult to predict, requiring large-scale finite element modelling of perturbed cell structures. To date, such analysis has only been performed for low-density foams, for which the details of deformation on the cell level were simplified.

Grenstedt and Tanaka[265] used a Voronoi foam as a representation of an irregular cell structure. Voronoi foams are formed by generating a three dimensional array of points, separated by a minimum distance, and dividing the space into cells which represent all the space closer to a given point than any other point: adjusting the minimum separation of the points allows varying degrees of irregularity to be generated throughout the structure. Analysis of the elastic deformation suggested that the effect of non-uniformity on the stiffness is small. However this approach has only, to date, been applied to the modelling of polymer-based cellular structures, with $\rho^*/\rho_s \sim 0.03$ and planar cell faces of uniform thickness.

The results cannot be directly related to metallic foams, where cell faces are generally thick and often exhibit local curvature. A reasonably uniform distribution of elastic strain was

also assumed, which is demonstrably not the case in melt-based closed-cell foams, in which elastic deformation is far more localised (§4.3.1).

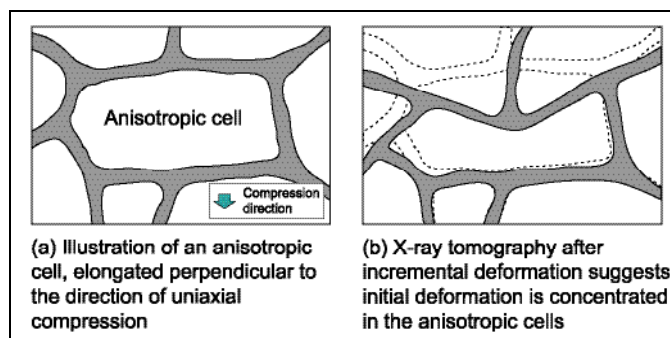
4.9.2 The effect of missing cell faces

More extreme localised anisotropy - where a single cell face is missing, for example - may significantly reduce the stiffness and strength of foams. Silva and Gibson[266] used FEM modelling to explore the effect of removing cell faces in a two-dimensional Voronoi honeycomb. For a honeycomb of $\rho^*/\rho_s = 0.15$, a 10% reduction in density due to face removal was predicted to lower the yield stress by 60%, with the same reduction in density applied by uniformly thinning the cell faces predicting only a 20% reduction.

X-ray tomography of partially deformed Alporas™ foams by Bart Smith *et al*[239] suggested that morphologically defective cells - in particular those in which T-shaped junctions are found between cell faces, equivalent to a missing cell face - are particularly common in the initial band of collapsed cells. This suggests that they provide initiation points for plastic collapse, although the low spatial resolution of the tomography in this study limits the conclusions that can be drawn. A schematic illustration of the initial deformation of a cell with an apparent cell face missing is reproduced in Figure 4.16. Krizst *et al*[244] studied thin specimens where all the cells could be seen in cross section, and also noted that large elongated pores perpendicular to the load direction collapse first.

Figure 4.16:

Illustration of the configuration of an elongated cell with an apparently missing cell face in cross section, (a), and the same cell immediately after the onset of plastic yielding in compression, (b), as detected by X-ray tomography (after [239]).



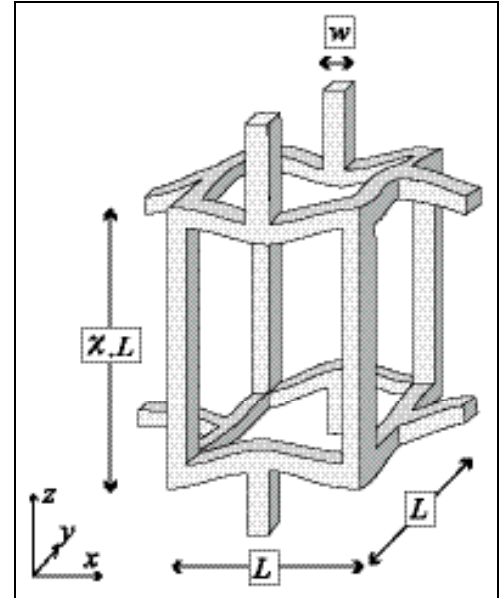
Recent improvements in the resolution of X-ray tomography have made it possible to generate three-dimensional structures based on real foam specimens, and thus establish direct relations between structural parameters and FEM predictions of plastic deformation. However, this technique remains in an early stage of development[267].

4.9.3 The effect of uniform cell size anisotropy

Cells may be uniformly elongated in a particular direction, as shown schematically in Figure 4.17, with correspondingly anisotropic bulk mechanical properties. The dimensional analysis approach of Gibson and Ashby has been extended to account for the deformation of a uniform array of elongated cells [268].

Figure 4.17:

A schematic elongated open cell, subject to compression parallel to the z dimension (after [268]).



For cells elongated by a factor χ in the z direction, the ratio of elastic modulus and plastic collapse stress in transverse directions is given by:

$$\frac{E_z^*}{E_x^*} = \frac{2\chi^2}{1 + (1/\chi^3)} \quad [4.11]$$

$$\frac{(\sigma_{pl}^*)_z}{(\sigma_{pl}^*)_x} = \frac{2\chi}{1 + (1/\chi)} \quad [4.12]$$

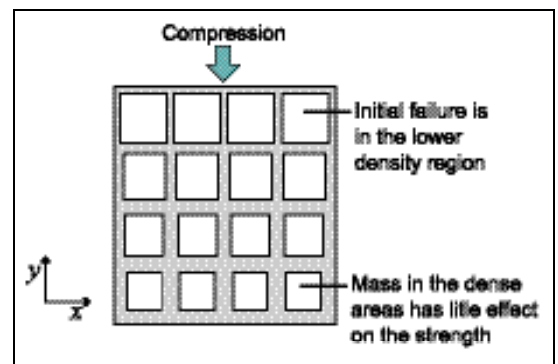
These relations, and the prediction that the Young's modulus is more sensitive to anisotropy than the collapse stress, are consistent with experimental measurements on rigid polyurethane foams[268]. Although the relations [4.11] and [4.12] have yet to be applied to closed-cell foams, observations of the properties of anisotropic open-cell Duocel™ aluminium foams (§2.2.2) by Andrews *et al*[225] and Nieh *et al*[269] are broadly consistent with these predictions.

4.9.4 The effect of density gradients

Density gradients, illustrated schematically in Figure 4.18, are undesirable: in compression, initial failure will take place in the lower density regions[235, 244, 270, 271]. With the material distribution not being optimised, the foam is weaker in practice than would be expected based its on average density.

Figure 4.18:

Schematic illustration of the most common form of anisotropy, due to density gradients.



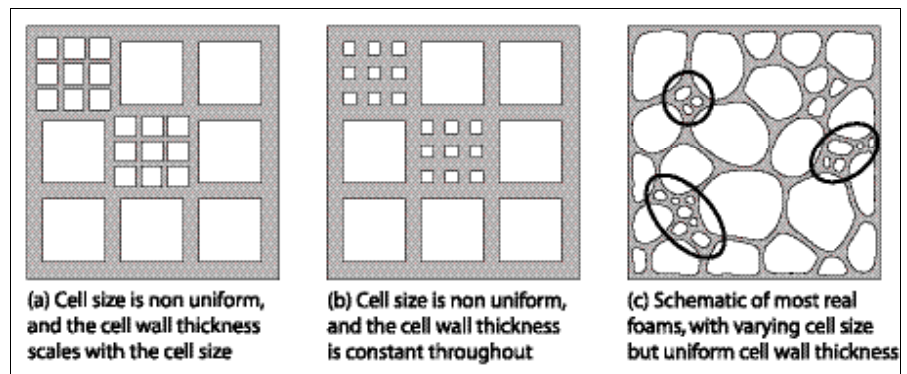
4.9.5 The effect of local variations in density

The properties of a foam should be independent of the cell size, provided the foam has a structure with a uniform ratio of cell face thickness, w , to cell face length, L , as shown schematically in Figure 4.19. In (a), w scales with L , with a correspondingly uniform density. In practice this is virtually never the case in melt-derived closed-cell foams as the cell face thickness is relatively uniform, meaning that regions of smaller cells have higher local density and contain a high fraction of the total mass[272]. Such a foam is represented schematically and illustrated in (b) and (c). Initial failure occurs in weaker areas away from these nodes, which do not contribute to the efficient use of material in the structure.

Figure 4.19:

Two schematic consequences of cell size variation, and the situation in most real closed-cell melt-derived foams, with high-density nodes circled.

([c] after [273])



Surface protrusions, which carry little or no load, also represent material that is structurally 'wasted'. By analogy, abnormally large cells - effectively low-density regions - can initiate failure, and unusually weak or thin areas in cell faces will act as a focus for initial plastic deformation.

4.9.6 The effect of waviness and curvature of cell faces

The presence of non-planarities, such as curves and wiggles in the cell faces, is thought to significantly impair the mechanical performance of metallic foams. Analytical models [274] and FEM simulations[275] of simplified cell structures have indicated that much of the difference between the performance that foam structures are theoretically capable of and the measured properties of foams is attributable to the presence of curved and corrugated cell edges or faces.

In reference [275], modelling of the deformation of a periodic cellular structure, in which all cell faces have identical curvature, showed that curvature of cell faces causes a marked reduction the yield stress and elastic modulus, as shown in Figure 4.20.

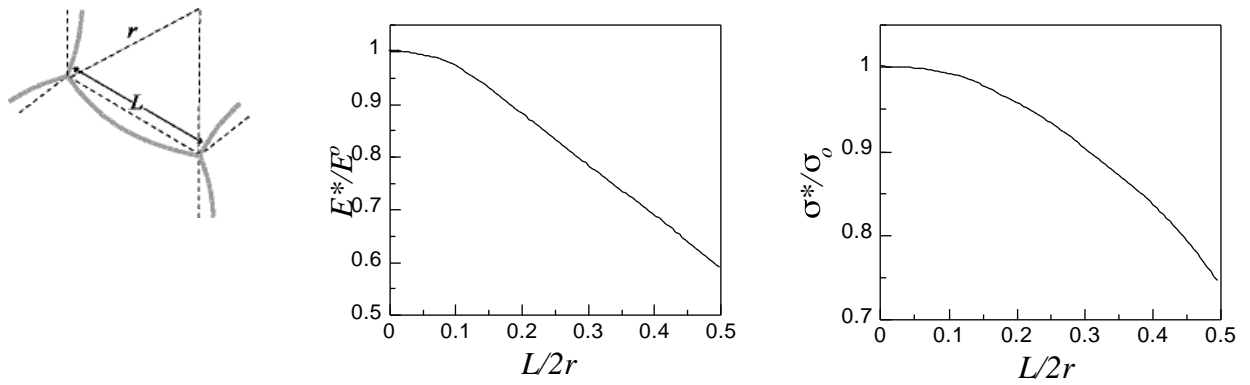
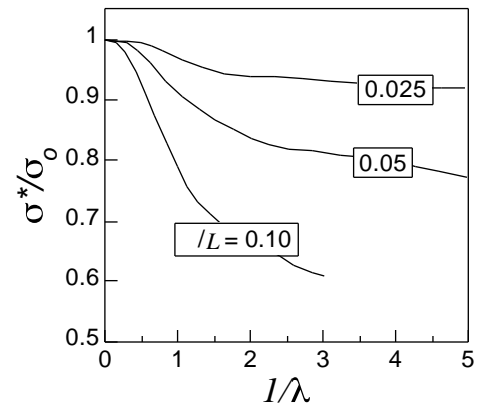
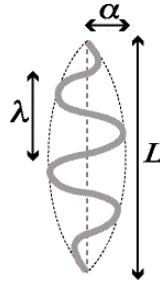


Figure 4.20: The effect of the radius of cell face curvature, r , on the normalised modulus and peak (yield) stress of a tetrakaidecahedral cell structure with cell faces of length L and curvature r , as illustrated, and $\rho^*/\rho_s=0.15$ (from [275]).

Corrugations have an even more marked effect, as shown in Figure 4.21 for the peak stress (the effect is similar for modulus).

Figure 4.21:

The effect of cell face corrugation on the normalised peak (yield) stress of a tetrakaidecahedral cell structure with $\rho^*/\rho_s=0.1$, where L is the cell edge length, α is the amplitude of the corrugations, and λ is the wavelength of the corrugations (from [275]).



Grenestedt determined an upper bound solution for a single cell face subject to wavy imperfections by FEM, predicting a similar reduction in modulus [274]. The effect of such defects in non-periodic structures, in particular those in which deformation gives rise to local stress concentrations, remains to be determined.

There has been relatively little experimental work on this aspect to date, principally due to the difficulty of isolating the effect of cell face morphology from that of other structural features, and the difficulty of characterising the degree of cell face curvature within a sample. Comparisons between otherwise similar foams exhibiting different degrees of cell face curvature, and observations of lower yield stresses in compression than in tension, suggest that foams with curved and wavy cell faces do indeed have inferior properties[225, 232, 276]. X-ray tomography of foams in the early stages of deformation has recently established that cell faces showing appreciable curvature facilitate plastic yielding[240].

4.10 Strain rate effects

Strain rate dependency in polymeric foams is usually attributed to increased resistance to gas flow[250] or viscoelasticity of the cell face material[264]. Studies of Alulight™[277] foams

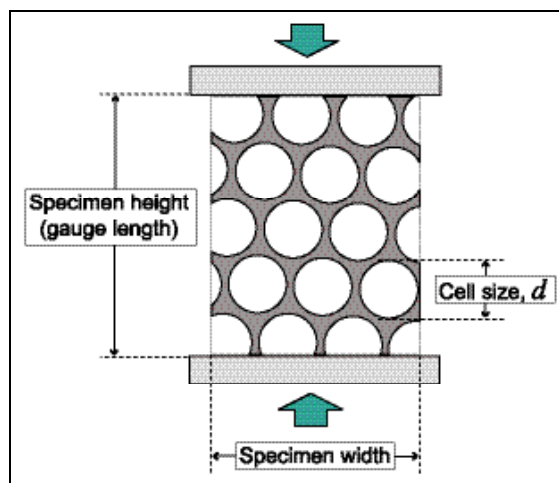
over a wide range of strain rates revealed no significant strain-rate dependency. One study of Alporas™ foams observed no strain rate dependency[246], although most note an increase in yield stress of $\sim 33\%$ on increasing $\dot{\epsilon}$ from 10^{-5} s^{-1} to 10^{-1} s^{-1} , with a more pronounced dependency at strain $\dot{\epsilon} > 3 \times 10^{-3} \text{ s}^{-1}$ [88, 276, 278-280]. As the strain rate dependency of bulk aluminium is weak, and unlikely to be significant, it has been suggested for the rise in yield stress at high loading rates is due to resistance to movement of gas between cells after rupture, and micro-inertial effects resulting from the highly localised nature of some of the deformation. Although the phenomenon is not yet fully understood, it is clear that strain rate effects are not significant within the range of strain rates used in quasi-static mechanical testing.

4.11 Cell size, specimen size & boundary conditions

The mechanical properties of finite specimens of foams are not necessarily comparable with those of the bulk foam. Studies have been undertaken with a view to establishing the limiting specimen dimensions below which the mechanical properties diverge from those of the bulk foam. The following section reviews measurements made on small specimens of commercial foams in terms of the ratio of specimen size to cell size, D/d , along the specimen width or height, as illustrated schematically in Figure 4.22.

Figure 4.22:

Specimen height, and specimen width, of a foam specimen subjected to uniaxial compression.

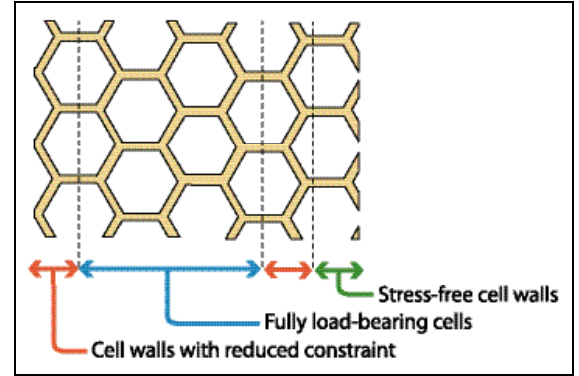


Effect of specimen width

The negligible lateral expansion of foams, coupled with the highly localised nature of deformation, mean the effect of plastic constraint due to loading plates is relatively unimportant in all but the thinnest specimens. However, the cells at the edge of a specimen may not be fully load-bearing, as modelled analytically and numerically by Onck et al[281]. An idealised two-dimensional foam with a free edge, where cells were either not load-bearing or had reduced constraint, as shown in Figure 4.23, was analysed, with the model subsequently extended to three-dimensional structures.

Figure 4.23:

Reduced load carrying ability in a foam due to edge effects



It was suggested that the yield stress of a foam specimen of finite size, $\sigma^*_{(specimen)}$, is related to the yield stress of the bulk foam, $\sigma^*_{(bulk)}$, by the following relation, where D/d represents the ratio of specimen width to cell size:

$$\frac{\sigma^*_{(specimen)}}{\sigma^*_{(bulk)}} = \frac{\left(\left(\frac{D}{d}\right) - \frac{1}{2}\right)^2}{\left(\frac{D}{d}\right)^2} \quad [4.13]$$

Experimental results obtained by Andrews *et al*[282] for cuboid closed-cell Alporas™ foam specimens with dimensions $D \times D \times 2D$, and for cylindrical open-cell Duocel™ foams with the same aspect ratio, are also plotted together with the predictions of equation [4.13] in Figure 4.24. The result of measurements by Bastawros *et al*[240] for cuboid Alporas™ foam specimens with $D/d \sim 13$ in the compression direction, ~ 8 in one transverse direction, and between 1.5 and 8 in the other transverse direction, are also plotted in terms of the smallest D/d .

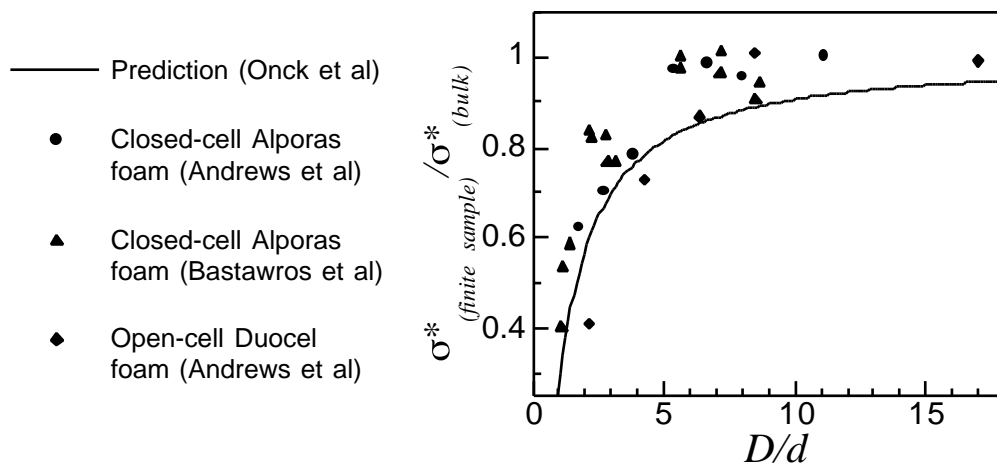


Figure 4.24: The effect of specimen dimensions on the yield stress of a specimen, $\sigma^*_{(finite\ specimen)}$, normalised by σ^* of the bulk foam, $\sigma^*_{(bulk)}$, as predicted by equation [4.13]. Experimental data are plotted for open-cell (Duocel™, §2.2.2) and closed-cell (Alporas™, §2.3.3) foam specimens.

Although experimental scatter is significant, a marked reduction in σ^* is seen for $D/d < 5$, with specimens with $D/d > 5$ having properties representative of the bulk material. There has been little work to date concerning other types of foam, although McCullough *et al*[235] reported identical yield properties for specimens of Alulight™ foams with D/d of 5 and 15 in the smallest dimension, which is consistent with the experimental observations for Alporas™ foams.

It is worth noting that the mechanism of failure is dependent on the specimen aspect ratio: Bastawros *et al*, who studied specimens with variable aspect ratio, report that specimens with $D/d \approx 2$ failed by lateral buckling rather than crushing, while Andrews *et al* attribute the reduction entirely to the effect of unconstrained cell faces.

Effect of specimen height

It would appear that the number of oscillations in a stress-strain curve showing serrations (§4.4) should be related to the number of cells along the gauge length (specimen height), although this is seldom commented upon in the literature. Bart-Smith *et al*[239] studied the onset of plastic failure in closed-cell Alporas™ foams subjected to uniaxial compression, and - unusually for Alporas™ foams - noted stress oscillations after compressive yielding. The number of stress oscillations in the Alporas™ foams was apparently related to the number of deformation bands that can form. A similar observation was made by Krizst *et al*[244] in a study of the yielding of Alulight™ foams, while Bastawros *et al*[240, 241], in a study of Alporas™ foams, state that each serration corresponds to the collapse of a discrete band of cells within the gauge length.

Mukai *et al*[279] studied the compression of specimens of Alporas™ foam with small numbers of cells along the compression axis. The smallest specimens had $D/d \sim 1$ along the gauge length, and $D/d \sim 4$ in the other two axes. Despite some experimental scatter, these specimens had a yield and Plateau stress consistently $\sim 30\%$ higher than that of specimens with $D/d \sim 3$ in the compression axis, which in turn had comparable properties to large specimens with $D/d \sim 10$ in each dimension. Whether specimens with $D/d \sim 1$ are foams or merely irregular honeycombs is debatable, although the observation does confirm that there is a lower limit to D/d along the gauge length beyond which measurements become unrepresentative of the bulk properties. The reasons for this are not discussed, although plastic constraint due to the loading platens, and the absence of a suitable band of weak cells suitable for initiation of plastic collapse within the sample length, could both be significant. Von Hagen and Bleck[234] performed a similar study on specimens of an Alporas™ foam with specimen height varying between approximately 2 and 8 cells (the precise cell size was not specified). Considerable experimental scatter in measured σ_y^* made interpretation of the results difficult, although varying the sample height had no apparent effect on the yield stress or the degree of scatter in measurements.

Incremental strain mapping (§4.3.1) provides some insight into the size of the deformation zone. Studies of the compressive failure of Alporas™ foams by Bart-Smith *et al*[239] and

Bastawros *et al*[240], suggest that the stress concentrations associated with formation of compressive failure bands are localised to within 2-3 cell diameters, with several bands present at various points along the compression axis spaced at intervals of ~ 3 -4 cells. The distribution of these presumably reflects the distribution of regions of the cell structure containing local defects. This suggests that measurements made on small specimens could be misleading, both because the specimen size is smaller than the dimensions of the fracture zone, and because there may not be a suitable band of low-density cells for the initiation of a fracture zone within the gauge length.

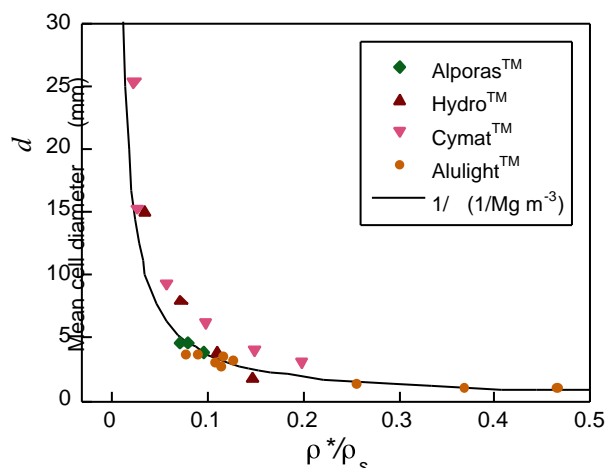
Some correlation would be expected between the number of serrations in the stress strain curve of a brittle foam, and the number of bands of cells liable to undergo plastic collapse. Few workers mention this explicitly, although Deshpande and Fleck[246] comment on a correlation between the number of serrations and the number of cells (and hence collapse bands) in the vertical direction, although these are only visible in dynamic compression at high strain rates.

Effect of cell size

There has been little work to date concerning the effect of cell size on the mechanical properties of larger specimens. This is partly a result of obtaining melt-based foams which have significant differences in cell size without associated differences changes in other parameters such as cell shape, chemical composition and density. It is not generally possible to significantly reduce the cell size in a melt-based foam, for example, without experiencing a corresponding increase in density, as suggested by the data various melt-based foams in Figure 4.25[10].

Figure 4.25:

Mean cell size as a function of relative density for four types of melt-based closed cell aluminium foam, the production of which is reviewed in Chapter 2 (from reference [10]).



In an attempt to examine the effect of cell size on the bulk properties of a foam, Miyoshi *et al*[272] used an unspecified method to reduce the both the cell size and the cell face thickness of Alporas™ foams. An increase in yield stress and plateau stress was noted in the modified foam, although the small range of cell size studied makes it difficult to draw clear conclusions from the study. A smaller cell size might be expected to minimise the influence of localised

defects in the cell structure, as well as - in a brittle foam - reducing the absolute magnitude of the serrations in the stress-strain curve by reducing the width of individual bands of collapsed cells.

5 Experimental Procedures

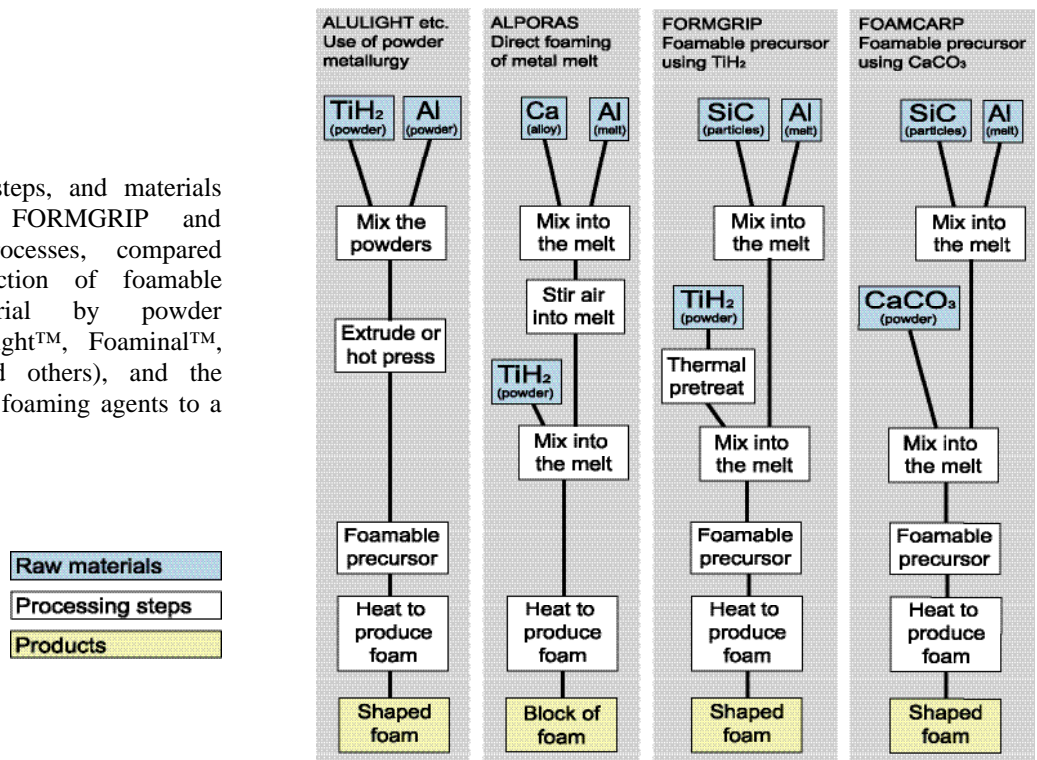
The FOAMCARP process, in which CaCO_3 is used to foam aluminium, is described, and the processing parameters that can be optimised and adjusted to tailor a foam to a particular application are discussed. The equipment and materials used in the foaming processes, and the means of measuring the extent of foaming during the process, are noted. Foaming chemicals are analysed by techniques including X-ray diffraction, scanning electron microscopy, particle size analysis, thermogravimetric analysis and differential scanning calorimetry. The foams produced are characterised by microscopy and image analysis, and scanning electron microscopy is used to explore surface and microstructural aspects of the foams, with chemical etching used to selectively remove phases. Auger and X-ray photoelectron spectroscopy are used to investigate the structure and composition of the cell surfaces. With a view to use as an impact absorbing material, samples of the foams produced are subjected to mechanical testing, and various optical and microscopy techniques are used to examine the effect of the cell structure and metal microstructure on bulk mechanical properties.

5.1 Production of foams

The FORMGRIP process, described in other works[91] and reviewed in Chapters 2 and 3, was used to produce TiH_2 -based foams. In the current work the FOAMCARP process – Foaming of aluminium MMC by chalk-aluminium reaction in precursors – is developed to produce CaCO_3 -based foams. Figure 5.1 illustrates the key steps of these processes, alongside those of several current commercial processes employing foaming agents reviewed in section 2.3.3.

Figure 5.1:

Key processing steps, and materials used, in the FORMGRIP and FOAMCARP processes, compared with the production of foamable precursor material by powder metallurgy (Alulight™, Foaminal™, Fraunhofer™ and others), and the direct addition of foaming agents to a melt (Alporas™).



Both FORMGRIP and FOAMCARP are two-stage processes. In the first stage, a powdered foaming agent is dispersed thoroughly in a melt consisting of an aluminium alloy and a fine dispersion of refractory ceramic particles, which is solidified before the initiation of foaming. In the second step, the foamable precursor material obtained is heated inside a shaped mould above the melting temperature of the metal, when the dispersed foaming agent undergoes

thermal decomposition to produce a dispersion of bubbles within the melt. This is cooled to solidify the foam, before it collapses under the influence of gravity or coarsens due to capillarity effects.

The main processing difference is that the FORMGRIP process requires a 25-hour thermal pre-treatment of the TiH₂ foaming agent, whereas CaCO₃ in the FOAMCARP process is added to the melt in the as-received state.

Alloys used

Duralcan™ Al-SiC metal matrix composites (MMCs), designated F3S 10S and F3S 20S, with different levels of ceramic particle content, were used as a base material for the production of metallic foams:

Alloy	Designation	SiC content (wt.%)	Particle size range	Average particle size
F3S 10S	Al-Si9-Mg	10	3-19 μm	9.3 μm
F3S 20S	Al-Si9-Mg	20	5-24 μm	12.8 μm

The following table lists the alloying constituents, in wt.%, of the matrix of the Duralcan™ MMCs, as well as various other alloys used in the foaming experiments, with the principal alloying elements shaded.

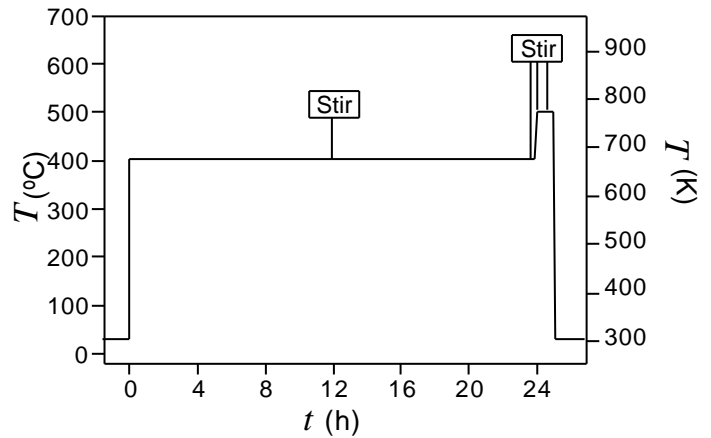
Alloy	Designation	Si	Fe	Cu	Mn	Mg	Ni	Zn	Sn	Ti	Pb	Others
1050	Commercially pure	0.25 max	0.4 max	0.05 max	0.05 max	0.05 max	-	-	-	0.05 max	-	0.03 max Al 99.5 min
LM6	Al-Si12	10.0 - 13.0	0.6 max	0.1 max	0.5 max	0.1 max	0.1 max	0.1 max	0.05 max	0.2 max	0.1 max	-
LM10	Al-Mg10	0.25 max.	0.35 max	0.1 max	0.1 max	9.5-11.0	0.1 max	0.1 max	0.05 max	0.2 max	0.05 max	-
LM25	Al-Si7-Mg	6.5-7.5	0.5 max	0.1 max	0.3 max	0.2-0.45	0.1 max	0.1 max	0.05 max	0.2 max	0.1 max	-
6061	A-Mg1-Si-Cu	0.4-0.8	0.7 max	0.15-0.4	0.15 max	0.8-1.2	-	0.25 max	-	0.15 max	-	0.05 max 0.15 total
F3S10S	Al-Si9-Mg	8.5-9.5	0.2 max	0.2 max	0.03 max	0.45-0.65	0.03 max	0.03 max	0.03 max	0.2 max	0.03 max	0.03 max 0.15 total
F3S20S	Al-Si9-Mg	8.5-9.5	0.2 max	0.2 max	0.03 max	0.45-0.65	0.03 max	0.03 max	0.03 max	0.2 max	0.03 max	0.03 max 0.15 total

Foaming chemicals

Titanium hydride powder of 325 mesh powder size (< 44 μm) was supplied by Goodfellow Cambridge Limited. Prior to use, the powder was separated into 5 g batches in open crucibles, and subjected to the heat treatment in air shown in Figure 5.2.

Figure 5.2:

Heat treatment applied to the TiH₂ powder prior to use in the FORMGRIP process, consisting of 24 hours at 400°C followed by one hour at 500°C, in an air furnace. The powder is removed from the furnace and stirred at the points labelled.



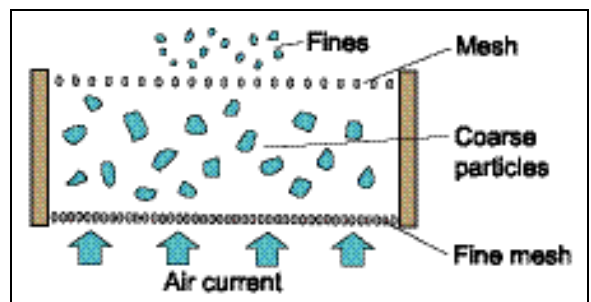
Three grades of high-purity CaCO₃ were supplied by Alfa Aesar Johnson Matthey GmbH: a ground powder of 98% assay purity, a precipitated powder of 99.5% purity, and a high-purity precipitated powder of 99.95-100.05% assay purity. Carboniferous limestone granules designated Minfil LG12 and Minfil LG24 were supplied by Omya UK Ltd, with $\rho_s = 2.7 \text{ g cm}^{-3}$ and the following reported composition:

Designation	Granule size	CaCO ₃	SiO ₂	Fe ₂ O ₃	Cr	Organic matter	HCl-insoluble residue
Minfil LG12	~ 1 mm	98.4 %	0.55 %	350 ppm	5 ppm	0.1 %	0.1 %
Minfil LG24	~ 2 mm	99.3 %	0.3 %	0.02 %	2 ppm	0.01 %	0.4 %

In order to generate powder sizes of the natural limestone comparable to those of the high purity CaCO₃ samples, these were ground using an automated mortar and pestle, and sieved into various powder size grades. Air separation, shown schematically in Figure 5.3, was subsequently used to obtain a narrow powder size distribution.

Figure 5.3:

Apparatus used for the air separation of ground limestone powders.



In parts of the process, a refractory brushable boron nitride paint containing 31% of boron nitride, supplied by Alfa Aesar Johnson Matthey GmbH, was used as an anti-wetting agent to coat mould surfaces that would be in contact with molten aluminium.

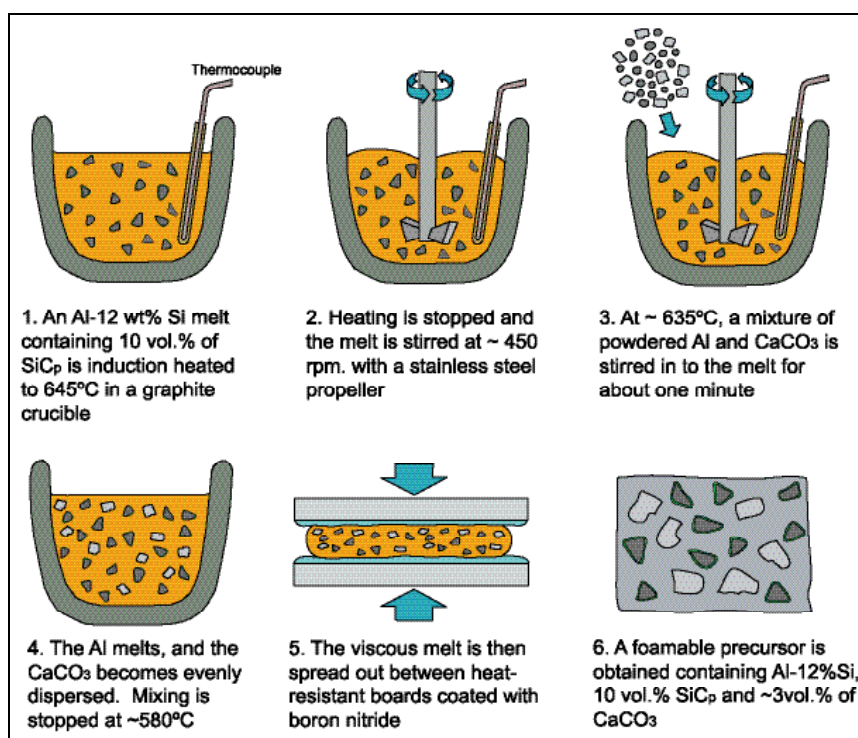
The FOAMCARP process: Production of the foamable precursor

The process is illustrated schematically in Figure 5.4. 1 kg of the metal melt is placed in a graphite crucible surrounded by induction heating coils, and heated to 645°C (about 60°C higher than the melting point of most of the alloys used). Temperature measurement is carried out using a K-type thermocouple in a protective alumina sheath located in the crucible the side of the melt. The induction heating permits efficient heating, maintains the SiC in suspension, and

levitates the metal slightly. When the temperature reaches 645°C, heating is stopped and the mixture is allowed to cool. At 640°C a steel propeller is introduced to the melt, and the stirring speed is increased to 450 rpm.

A range of quantities of CaCO₃ were added, with the optimum level was found to be 3 wt.% of the total foam mass (33 g in the 1.1 kg melts used). Neither CaCO₃ nor TiH₂ is particularly well wetted by molten aluminium, so, in order to assist the incorporation of the foaming agents in the metal melt, they are mixed with powdered aluminium (Al-12Si) prior to addition. A CaCO₃:Al mass ratio of 1:2 was found to be most effective. The mixture of powders is introduced to the melt at 635°C, and dispersed by the stirring for ~ 60 s while the mixture cools.

At 580°C stirring is stopped, and the increasingly viscous melt is poured onto a heat resistant board coated with boron nitride, compressed to form a flat sheet ~ 20 mm wide, and left to solidify in air.



Points to note are that at the mixing temperature the stainless steel stirrer, which was uncoated, is prone to some dissolution during the process. This can give rise to a small iron content in the melt. The melt is also in contact with graphite during the mixing process. As the mixing takes place in air, a small amount of surface oxide may be incorporated into the melt.

The precursor thus produced typically has ρ^*/ρ_s of 0.8-0.85, this porosity being partly a result of gas entrapment during mixing, and partly due to premature release of a small quantity of foaming gas.

The FOAMCARP process: Foaming of the foamable precursor

In the second stage of the process, sections of the foamable precursor of various dimensions (up to $60 \times 60 \times 25$ mm) were placed in a mould assembly, as shown in Figure 5.5, and subjected to heat treatments to melt and foam the metal. Graphite moulds were initially used, due to the non-wettability of graphite by molten aluminium. However these proved fragile and short-lived, and were replaced with shaped moulds of stainless steel coated with a boron nitride suspension, with no significant difference in thermal performance noted between the mould types. The temperature during foaming was monitored using a thermocouple inserted in a hole drilled in the precursor material.

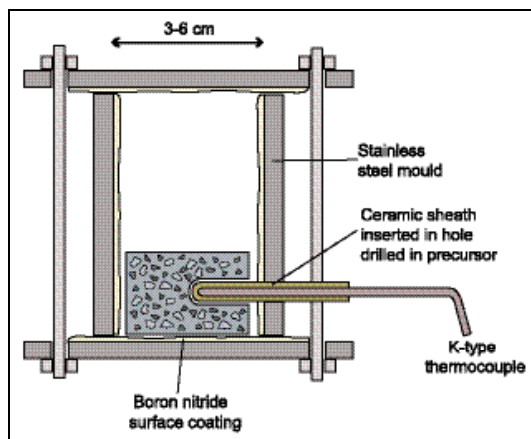
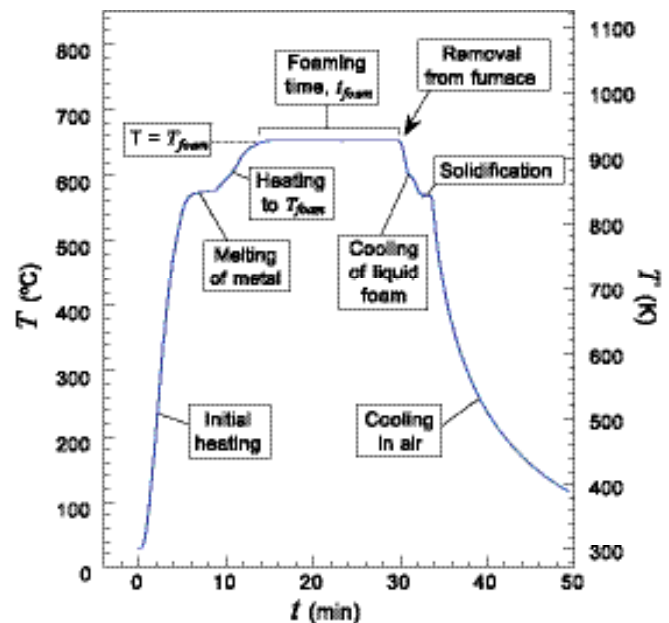


Figure 5.5: The stainless steel mould assembly

Figure 5.6: Typical measured temperature profile of a foam formed with $T_{foam} = 650^\circ\text{C}$ and $t_{foam} = 900$ s.



The foamable precursor is 'baked' to form a foam by placing the mould assembly containing the precursor in a furnace preheated to the desired temperature. A typical thermal profile is shown in Figure 5.6. The main variables are the foaming temperature T_{foam} , which is equal to the temperature of the furnace, and the foaming time t_{foam} , defined as the time between the foam reaching T_{foam} and being removed from the furnace. In experiments where baking was interrupted, it was noted that limited foaming takes place before T_{foam} is reached. In order to establish optimum processing parameters, and produce foams with a range of density and cell size, a wide range of foaming times and temperatures were employed.

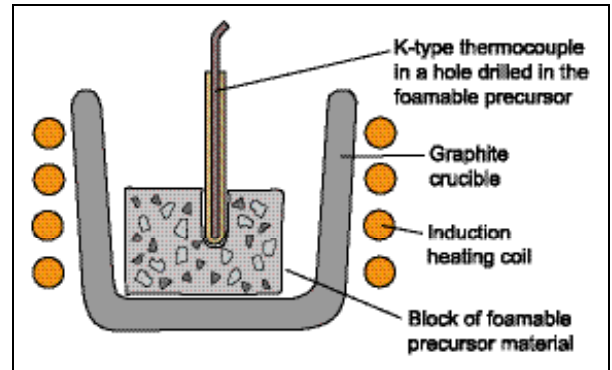
In the FORMGRIP process, TiH_2 based foams are usually produced by baking precursors at 630°C for 1-2 minutes depending on the desired ρ^*/ρ_s . The CaCO_3 foams require longer baking times (5-15 minutes) and slightly higher temperatures (typically 650°C) for optimum foam production. Once t_{foam} has elapsed, the thermocouple is removed and the mould assembly is left to cool in air.

Foaming by induction heating

Foams were also produced by induction heating of foamable precursor materials, as illustrated in Figure 5.7. The temperature was measured by a thermocouple inserted in the precursor, and was approximately controlled during foaming by adjusting the level of heating. The foams were cooled in air.

Figure 5.7:

Experimental apparatus for temperature monitoring during the foaming of a block of a foamable precursor material by induction heating.

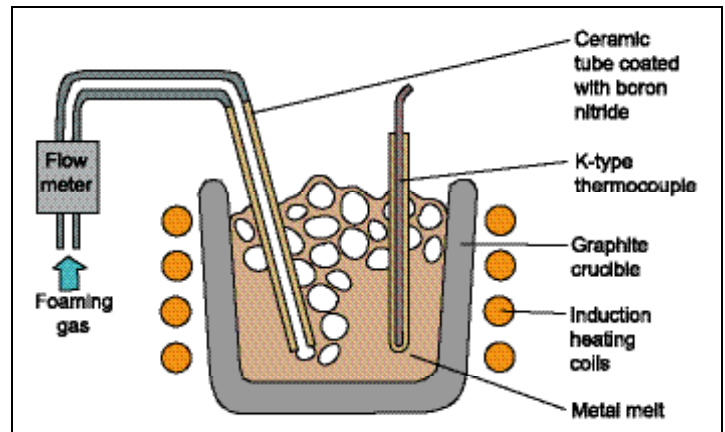


Direct foaming of metal melts

Small samples of various alloys were foamed by the direct injection of various gases, as illustrated in Figure 5.8. The alloys were melted and heated to the foaming temperature using an induction heating system. The rate of heating was then reduced to maintain an approximately constant temperature ($\pm 20^\circ\text{C}$), while gases were injected to the liquid metal at a controlled rate. The foams were cooled in air.

Figure 5.8:

Experimental apparatus used in the direct foaming of metallic melts by the injection of gases.



5.2 Analysis of the materials used

5.2.1 Particle size measurement

The size of the foaming powders was measured by low angle laser light scattering, using a Malvern™ Mastersizer E machine. The powders, all of which are virtually insoluble, were dispersed in water that was placed in the path of a collimated laser beam. The particles were kept in suspension by continuous recirculating flow, and prevented from agglomeration by the use of ultrasound. The measurement of particle size is based on the inverse relationship between

particle size and the ability of the particles to scatter light[283], with the degree of scattering measured by a series of concentric photosensitive silicon detectors.

5.2.2 Scanning electron microscopy

The powdered foaming agents were scattered onto sample holders coated with a double-sided conducting tape, gently sprayed with air to dislodge partially attached particles, and coated with a thin gold film by sputter deposition, for examination by scanning electron microscopy (SEM).

5.2.3 Thermal analysis

Thermogravimetric analysis (TGA) and differential scanning calorimetry (DSC) were used to monitor the decomposition of the powders in an inert atmosphere. Loosely packed powder samples of ~ 15 mg were placed in open platinum or alumina crucibles and subjected to various heat treatments, with changes in mass measured by a microbalance. A flow rate of 20 ml per minute of commercial purity N₂ or CO₂ was maintained throughout the experiments.

5.3 Microscopy

5.3.1 Specimen preparation

Cross sections of the foams produced were cut into various sections for optical microscopy. The use of cutting blades was found to cause extensive smearing of the finer cell walls, causing the disappearance of many of the smaller cells on the surface. Samples were therefore cut by electro-discharge machining, to minimise damage to fine cell wall structures and ensure that the entire cell structure remained visible.

The samples were then infiltrated with a low-viscosity two-component epoxy resin. The samples were held in place as shown in Figure 5.9, with repeated cycles of vacuum and atmospheric pressure subsequently used to force the resin into the smallest pores. The resin-mounted samples were then ground flat using successively finer grades of silicon carbide grit paper, with between 20 and 390 grains per square centimetre and water lubrication. In some cases, when looking for phases that might be hygroscopic, isopropanol was used as a lubricant.

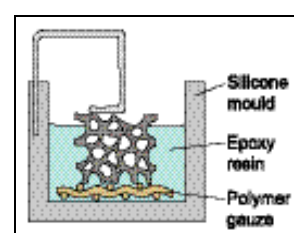


Figure 5.9: Vacuum mounting equipment for the preparation of planar metallographic specimens of porous materials

5.3.2 Image analysis

Mounted foams were scanned after the grinding stage with an optical scanner for analysis using Zeiss™ KS400 image analysis software. In order to obtain accurate measurements of the cell sizes, some retouching of the scanned images was done manually. The scanning software

was not capable of distinguishing the features of the finest cell sizes in some samples, but nonetheless appeared to provide a good estimate of the distribution of cell size.

Measurement of the 'cell size' in a cross section of a foam gives a measure of the diameter of a randomly intercepted cross section of a cell, $d_{intercept}$. Provided the foam structure is isotropic, $\bar{d}_{intercept}$ is directly proportional to the true average diameter of the cells within the material, \bar{d} [284, 285]:

$$\bar{d} = \frac{3}{2} \bar{d}_{intercept} \quad [5.1]$$

5.3.3 Optical microscopy

The samples were then polished for five minutes, using 6 μm polycrystalline diamond paste and a PA-W hard polishing cloth (both supplied by MetPrep Ltd). This was followed by polishing with a colloidal suspension of 0.06 μm SiO_2 particles (supplied by Struers Ltd) until an optically smooth surface was obtained.

Samples thus produced were directly observed by light microscopy, using a Zeiss™ Axiotech 25HD microscope. The distribution of Al, Si, SiC and various intermetallic phases and foaming agents can be observed without chemical etching.

5.3.4 Scanning microscopy: Planar samples

Samples were then prepared for SEM analysis using a Jeol™ JSM 5800 LV scanning microscope by coating them with a thin layer of gold, in order to prevent charging of non-conducting phases and the polymer resin. The back-scattered electron image was used for observation of the distribution of the various phases. Localised energy dispersive X-ray spectroscopy (EDX) was used to provide compositional analysis. Differences in hardness between the foams and the polymer mounting resin gave rise to some relief, detectable by optical profilometry, which could affect the examination of phases close to the sample surfaces. Foams were therefore electroplated with a layer of copper before mounting, in order to ensure edge preservation.

5.3.5 Scanning microscopy: Three dimensional samples

Samples of the foamable precursors and foams produced were directly observed in the SEM. The presence of non-conducting phases meant that gold coating of all samples was necessary. This enabled close inspection of surface features, and the distribution of foaming agents and surfactant particles. EDX was again used to provide compositional analysis.

In order to reveal the presence of oxide phases and refractory ceramics, some samples were etched with concentrated sodium hydroxide solution for approximately 5 minutes, before being washed thoroughly in water and gold coated. The alkaline solution was found to dissolve the aluminium, while leaving its metallic oxide and the refractory phases intact.

5.4 Spectroscopy

5.4.1 X ray diffraction

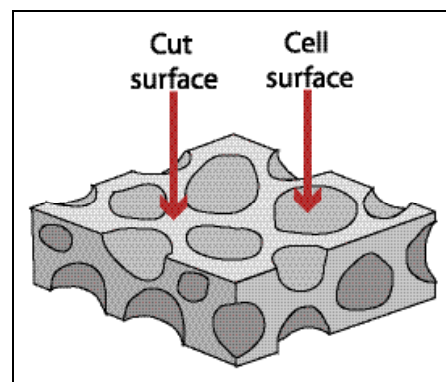
Samples of the foaming agents used were analysed before and after thermal treatment by X-ray powder diffraction, in order to identify any crystalline phases present. Powdered specimens of foams were prepared for analysis by X-ray powder diffraction by submerging them in liquid nitrogen and crushing them into a fine powder. The powders were maintained in a water-free environment throughout the process, in order to preserve any hygroscopic phases. In some cases a high-molecular-weight grease was used to hold the powders in place at high diffraction angles during measurements, giving rise to an identifiable broad peak at low angles in the X-ray spectra which was ignored in subsequent analysis.

5.4.2 X-ray photoelectron spectroscopy

X-ray photoelectron spectroscopy (XPS) was used to analyse the inside cell surface of foams produced using either TiH_2 or CaCO_3 foaming agents. Measurements were also made on polished cross sections of cell walls in the same specimens, as shown in Figure 5.10, in order to compare the properties of exposed surfaces with those of the bulk material. The samples were cut with diamond coated copper blades, and cleaned in isopropyl alcohol in an ultrasonic cleaner. The samples were exposed to the atmosphere at room temperature prior to measurements.

Figure 5.10:

Points of analysis on a schematic foam specimen by X-ray photoelectron spectroscopy.



XPS spectra were acquired using a Thermo VG Scientific™ Sigma Probe spectrometer equipped with a micro-focus monochromatic AlK source. An X-ray spot size of 150 μm was used. The spectrometer was controlled by a Thermo VG Scientific™ Advantage data system. For each specimen position, a survey spectrum was recorded, together with high-resolution spectra of the XPS core levels of interest.

The presence of an element produces a characteristic peak, the magnitude of which can be loosely correlated with the concentration of the element. In general it is not sensitive to the chemical environment or oxidation state of the element, with the exception of Al where slightly different peak positions are recorded for atoms in the metallic, covalent and ionic states.

5.4.3 Auger electron spectroscopy

Auger electron spectroscopy (AES) was used to characterise the cell surfaces of samples in a similar manner to that shown in Figure 5.10. The higher spatial resolution and small analysis depth of AES make it possible to characterise the variation in concentration of elements as a function of depth. AES spectra were acquired using a VG Scientific™ Microlab MkII scanning Auger electron spectrometer equipped with a field emission source operating at 15 kV and a hemispherical sector analyser (operated at the setting CRR = 4). Dayta Pisces™ software was used to control the system and acquire spectra digitally. Differentiated spectra were obtained numerically.

Sputtering by Ar⁺ ions, with a VG scientific™ EX05 ion gun operated at 5 kV, was initially used to remove inevitable surface contamination, and subsequently to provide depth profile analysis in the samples. Although etching allows the depth profiles in different specimens to be compared, it is difficult to directly quantify the depth of etching; an approximate calibration is generally achieved by comparison with samples of similar geometry, which have known composition and depth profile.

5.5 Mechanical testing

5.5.1 Sample preparation

Samples of the foams were sectioned using a low-speed rotary saw with a diamond-coated blade, to provide cuboid specimens with parallel faces for mechanical testing. The density of the specimens was determined using a simple volumetric technique, weighing the sample and measuring their external dimensions. The effect of the cell size on the mechanical properties was explored using samples with a wide range of dimensions.

For reasons discussed later, it was not possible to produce foams with the same cell size and density with the FORMGRIP and FOAMCARP processes. Thus, in order to explore the effect of the metallic microstructure of hydride and carbonate based foams independently of the influence of varying scales of cell structure, similar samples of the two foams were also produced containing controlled ratios of specimen size to cell size (D/d).

5.5.2 Equipment parameters

Samples were uniaxially compressed with a servo-hydraulic compression-testing rig fitted with parallel compression plates, which were lubricated before the tests. A constant rate of compression was used, and the load was measured using a 19 kN load cell. The samples were initially compressed to the yield point at a constant strain rate of 0.05 mm min^{-1} . Thereafter, compression continued at 0.5 mm min^{-1} . A separate linear variable displacement transducer (LVDT) was used to measure the strain of the foam for most samples, although for the largest samples the integral LVDT of the compression tester was used. Since the samples typically failed at loads well under those the compression tester was designed for, any error due to compression of the plates and machine are likely to be negligible.

Some tests were paused to allow repeated cycles of loading and unloading at 0.05 mm min^{-1} , in order to measure the elastic response of the foams. Others were interrupted at various stages of failure and the specimens sectioned and prepared for analysis by optical microscopy. Higher aspect ratio samples were fractured in tension, with the failure surfaces inspected by SEM.

5.6 Drainage

In order to assess the extent of drainage in liquid foams, specimens were sectioned horizontally into 5 mm segments, and the density of these sections measured, in order to measure the density of the foam as a function of height. Optical microscopy on mounted samples was used to manually determine the variation in cell wall thickness, and cell face curvature, as a function of height.

5.7 Cell coalescence

A specimen of hydride-based precursor material was submitted for in-situ foaming to be recorded by X-ray radioscopy at the European Synchrotron Radiation Facility. A furnace with two water-cooled aluminium windows was preheated to $\sim 800^\circ\text{C}$, and a small specimen of the foamable precursor material was lowered into the furnace on a platform. An X-ray beam, monochromated to $\sim 33 \text{ keV}$ and with a cross section of $40 \times 15 \text{ mm}$, was used to generate an absorption radiograph on a $\text{GdO}_2\text{S:Tb}$ polycrystalline powder screen, which converted the X-rays to light. An image of the evolution of the foam in cross section on the screen was captured with a charge coupled device (CCD) camera, with a frequency of 2 Hz.

6 Structural & Microstructural Features of the Foams Produced

Calcium carbonate is demonstrated to be an effective foaming agent for aluminium, with several notable advantages relative to the currently-used titanium hydride. Characteristic cell structures and microstructural features of foams produced with a CaCO_3 foaming agent are examined, and the properties of carbonate-based foams produced in the two-step FOAMCARP process are compared with those produced using the FORMGRIP TiH_2 -based process. Relative to the previously developed FORMGRIP process, a number of notable differences are noted, in terms of both the structure of foams produced and the influence of various parameters on the process. The most notable structural feature of carbonate-based foams is a smaller cell size and thinner cell faces. Foaming with CaCO_3 also gives rise to a marked increase in the stability of molten foams, with a large range of foaming temperatures possible, and an almost complete absence of melt drainage, even with extended foaming times. Many of these properties are attributed to the cell surfaces being covered by a thin oxide film formed early in the foaming process, the composition and morphology of which is characterised in detail. The implications in terms of the role of SiC are discussed, and the effect of various parameters on drainage and the stability of molten foams is explored. The applicability of the observed stabilising effects to other foaming processes is examined.

6.1 Performance of CaCO_3 as a foaming agent

Calcium carbonate was found to be a highly effective foaming agent for aluminium. It is capable of producing foams with similar porosity levels to those produced with titanium hydride, with several notable advantages. The chemical decomposition of calcium carbonate is more gradual than that of titanium hydride at the temperature of aluminium melts. This means that a two-stage foaming process, incorporating a foamable precursor, can be undertaken with the foaming agent in the as-received state, avoiding the requirement for prior thermal pre-treatment (§5.1). In contrast to the parallel work of Nakamura *et al* (§3.1.4), no chemical treatment was found to be necessary. The reduced rate of foaming also improves control over the foaming process, while the extremely low material cost and non-hazardous nature of the foaming agent and the decomposition products are also favourable.

Foaming was found to be most effective with addition of 3.3 wt.% of finely divided ($\sim 20 \mu\text{m}$) CaCO_3 powder. The pyrophoric nature of finely divided TiH_2 imposes a lower limit on the particle size that can be used. There is no such limitation on the use of CaCO_3 , although the difficulty of effectively dispersing fine powders imposed a lower limit of $\sim 10 \mu\text{m}$.

The optimal baking time to produce a foam was $\sim 600\text{-}900$ s at 650°C (as compared to $\sim 60\text{-}180$ s at 630°C for foaming of comparable melts with TiH_2). This produced foams with a highly uniform cell structure, with a relative density, ρ^*/ρ_s , of $\sim 0.15\text{-}0.2$. Foams formed of the F3S10S Al-9Si-0.5Mg alloy, containing 10 vol.% of SiC particles (denoted SiC_p) form the basis of the following discussion.

Examples of the effect of different foaming temperatures, T_{foam} , and times, t_{foam} , on the cell structure are shown in Figure 6.1, with higher foaming temperature producing a more irregular structure with $\rho^*/\rho_s \sim 0.1$. In view of the importance of closely controlling processing parameters when foaming with TiH_2 (§2.3.2-2.3.3), carbonate-based foams (produced by the FOAMCARP process, §5.1) were remarkably insensitive to the time and temperature of baking, with changes such as a 100°C increase in T_{foam} or an order of magnitude increase in t_{foam} giving rise to only relatively small changes in porosity.

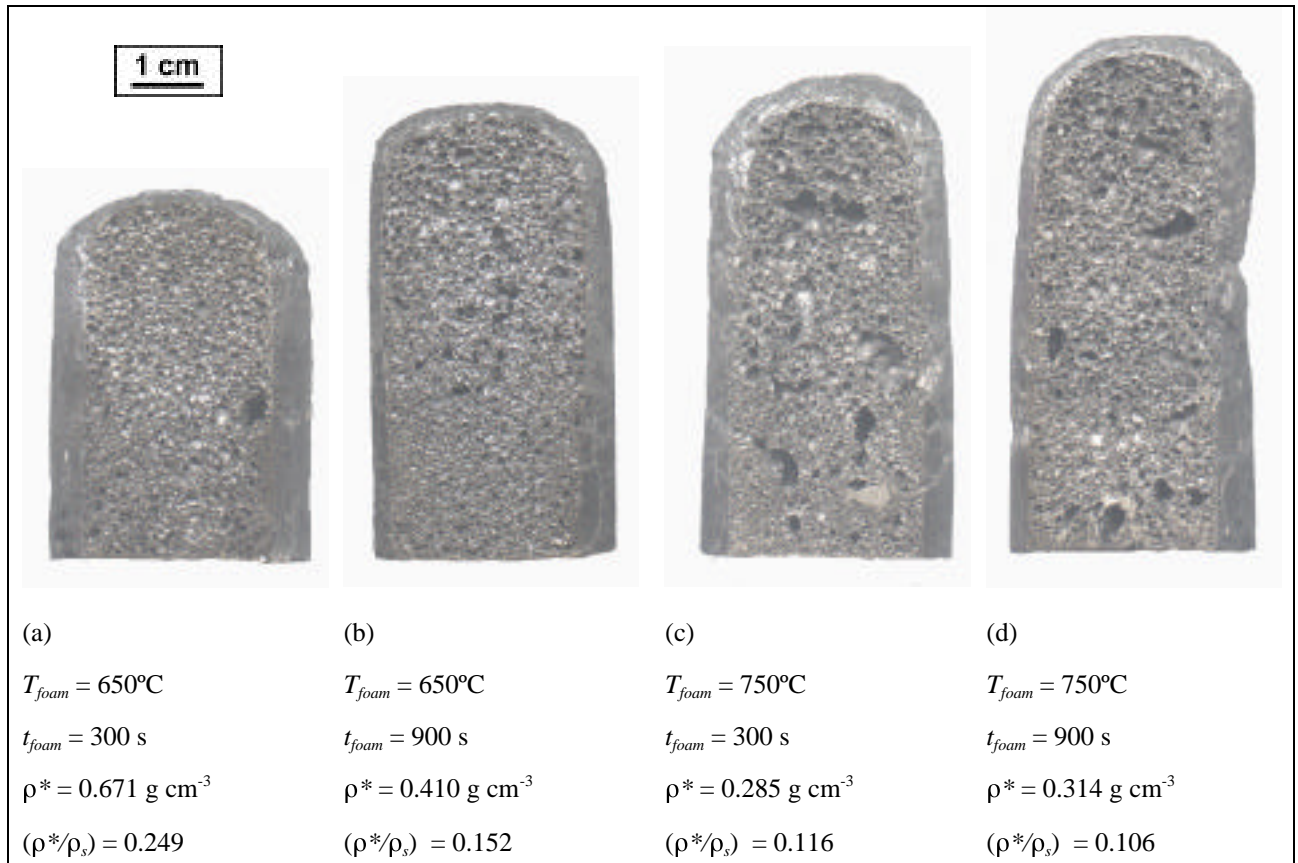


Figure 6.1: Cross sections of carbonate-based foams, showing the effect of foaming time (t_{foam}) and temperature (T_{foam}) on the cell structure and relative density (ρ^*/ρ_s) of a foamable precursor containing 10 vol.% of angular 9 μm SiC particles and 3.3 wt.% of CaCO_3 dispersed within an Al-9Si-0.5Mg matrix.

6.2 Features of carbonate-based foams

6.2.1 Cell structure

A cross-sectional cell structure of a typical carbonate-based foam is shown in Figure 6.2, compared with that of a typical hydride-based foam (produced by the FORMGRIP process, §2.3.3). The overriding difference between the foams is the consistently smaller cell size obtained in the carbonate-based process, with an average cell intercept diameter, $\bar{d}_{intercept}$, of $\sim 0.5\text{ mm}$, corresponding to \bar{d} of $\sim 0.75\text{ mm}$ (by relation [5.1]). This compared with a minimum $\bar{d}_{intercept}$ of 2-3 mm in hydride-based foams of comparable ρ^*/ρ_s . Apart from the difference in scale, the hydride- and carbonate-based foams have similar polyhedral cell structures, with straight or gently curved cell faces and apparently smooth cell surfaces. Corresponding

statistical measures of $\bar{d}_{intercept}$ in typical samples in a typical carbonate-based foam are shown in Figure 6.3.

Figure 6.2:

Typical cross sectional cell structures of carbonate- and hydride-based foams:

(a) Foam produced by foaming a foamable precursor with 1.5 wt.% of thermally pre-treated $\sim 70 \mu\text{m}$ TiH_2 particles dispersed within an MMC melt consisting of an Al-9Si-0.5Mg matrix containing 10 vol.% of angular $9 \mu\text{m}$ SiC particles, with $T_{foam} = 630^\circ\text{C}$ and $t_{foam} = 60$ s.

(b) Foam produced by foaming a foamable precursor with 3.3 wt.% of as-received $\sim 20 \mu\text{m}$ CaCO_3 particles dispersed within the same MMC melt, with $T_{foam} = 650^\circ\text{C}$ and $t_{foam} = 900$ s.

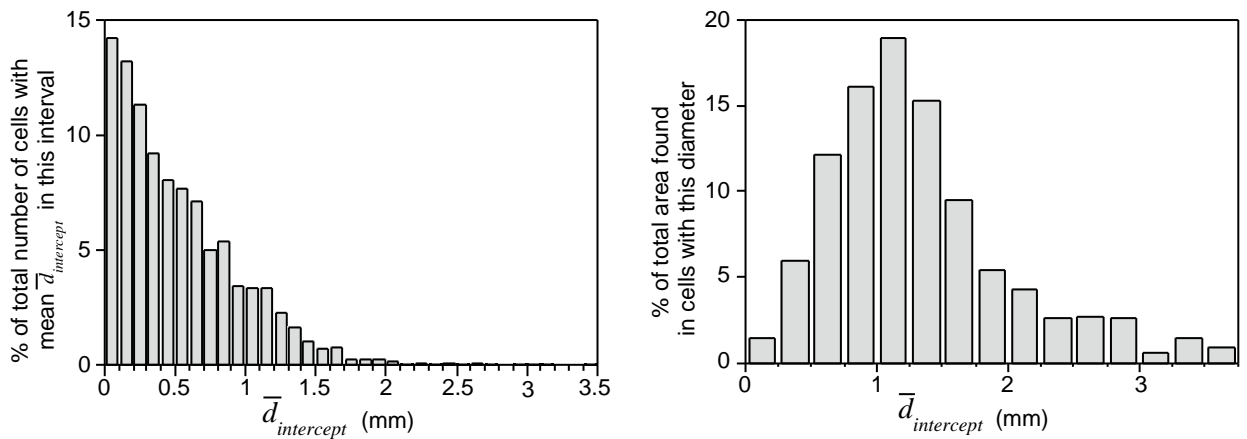
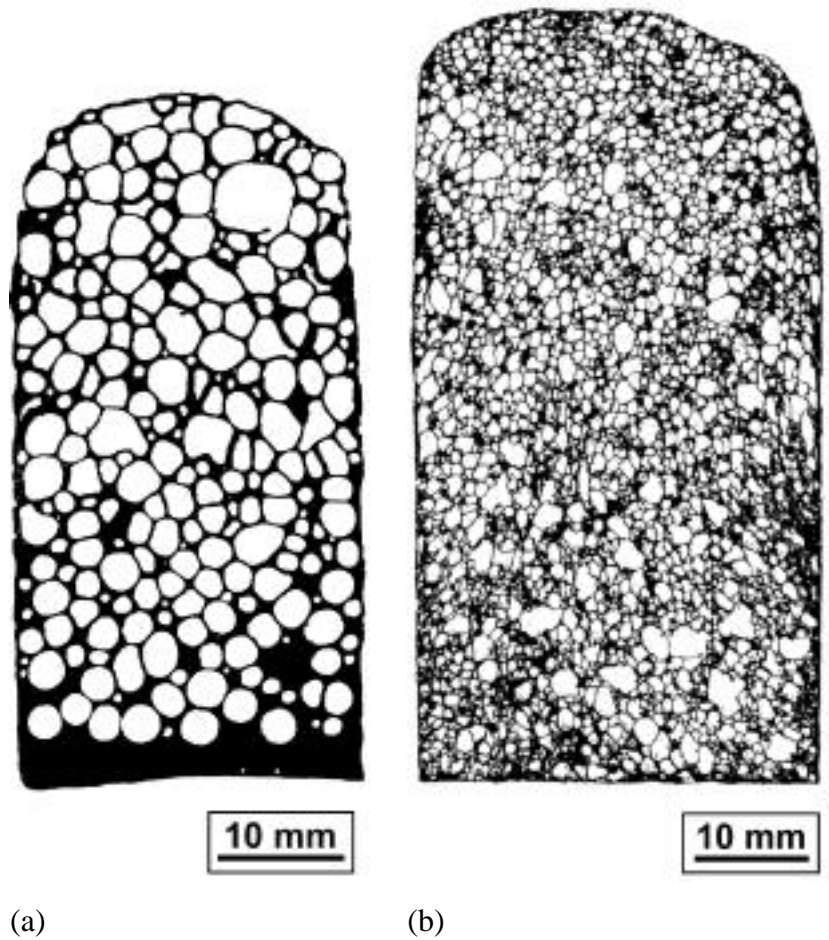


Figure 6.3: Distribution of $\bar{d}_{intercept}$ and cell size in a carbonate-based foam containing 3.3 wt.% of CaCO_3 , produced with $T_{foam} = 650^\circ\text{C}$ and $t_{foam} = 900$ s. Corresponding statistical measures are shown in the table below.

	Maximum	Mean	Median	Standard deviation
Intercept area (mm^2)	9.26	0.38	0.39	0.65
$\bar{d}_{intercept}$ (mm)	3.44	0.53	0.42	0.45

No significant difference in cell size was observed between the centre and the edges of the foams, suggesting that the slightly slower rate of cooling and solidification at the centre of the

foams does not affect the cell structure. There is a slight reduction in stability at higher foaming temperature, with a less homogenous cell structure and point defects such as abnormally large cells visible in foams produced at $T_{foam} = 750^{\circ}\text{C}$ (see Figure 6.1(d)).

Voids up to an order of magnitude larger than the surrounding cells are occasionally visible. These are usually associated with the presence of fold lines in the precursor material created during powder mixing, which are presumably coated with a large number of foaming agent particles. Foaming for short times, as shown in Figure 6.4, suggested that these develop into large pores in an early stage of foaming.

Figure 6.4:

A foamable precursor in an early stage of foaming of a typical carbonate-based foam ($T_{foam} = 650^{\circ}\text{C}$, $t_{foam} \sim 20$ s), showing the initial development of the abnormally large pores.

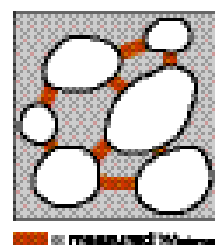


6.2.2 Cell faces

Cell faces in the carbonate-based foams are significantly thinner than any reported to date in foams produced by the melt route (§2.3.2-2.3.3). Measurements of the intercept cell face thickness between neighbouring cells – $w_{intercept}$ – in a typical specimen, are shown in Figure 6.5. The average $w_{intercept}$ is $46 \mu\text{m}$. There was little variation between the top and the base of the sample, with the large standard deviation partly reflecting the varying orientation of the cross section with respect to the cell face. The lowest $w_{intercept}$, representing the minimum thickness of perpendicularly aligned cell faces, is $\sim 10\text{-}15 \mu\text{m}$. In a typical hydride-based foam of similar density the cell faces are thicker at all points, and $\bar{w}_{intercept}$ increases towards the base of the sample. The minimum $w_{intercept}$, of $\sim 50 \mu\text{m}$, is approximately constant at all points in the specimen.

Figure 6.5:

The measure of $w_{intercept}$ the minimum perpendicular distance between neighbouring cells in cross section used as a measure of cell face thickness, and values of $w_{intercept}$ as a function of height in typical specimens of hydride- and carbonate-based foams.



	Hydride foam (μm)	Carbonate foam (μm)
$\bar{w}_{intercept}$ at top	98 ± 49	50 ± 43
$\bar{w}_{intercept}$ at middle	110 ± 58	42 ± 31
$\bar{w}_{intercept}$ at base	165 ± 125	47 ± 43
$\bar{w}_{intercept}$ averaged over foam	131 ± 97	46 ± 40

In view of the difference in cell size, the cell face aspect ratio w/L in the carbonate foams is similar to that of hydride-based foams of comparable ρ^*/ρ_s . In the hydride-based foams, there is a significant reduction in aspect ratio towards the base of the specimens.

It has been suggested that there may be a critical thickness of 50-100 μm , below which a cell face will rupture and retract, related principally to the alloy used (§3.4.8). Although this is consistent with observations in the hydride-based foam, it was not uncommon for the cell face thickness in carbonate-based foams to become very small, as shown in Figure 6.6, so this cannot be generalised to all metallic foams. The observations in the carbonate-based foams are consistent with the correlation between minimum cell face thickness and particle size mentioned in section 3.4.6. However it can be seen that, once particles make contact with both sides, cell face rupture is not inevitable in these foams.

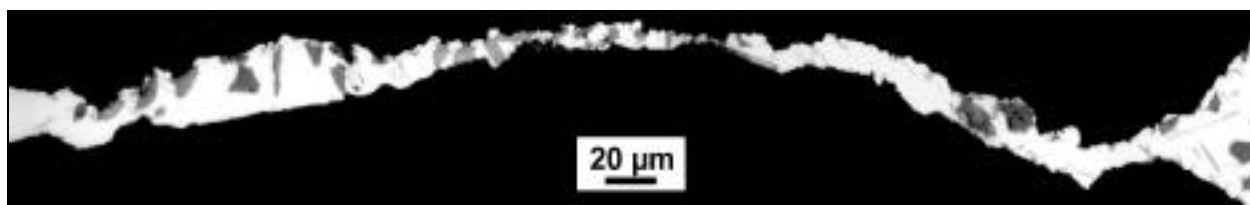
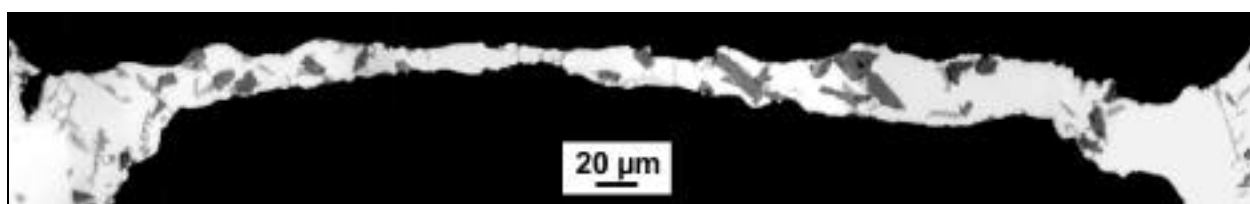
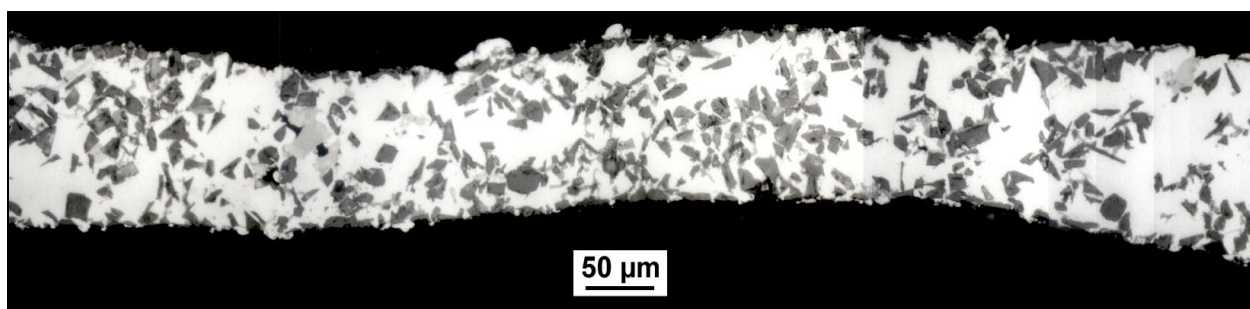


Figure 6.6: Optical micrograph of a polished cell face cross section in a carbonate-based foam, with $w_{intercept}$ approaching zero near its midpoint.

Figure 6.7 shows the microstructure of typical cell faces in carbonate- and hydride-based foams. The faces are mostly straight or very gently curved, with occasional wavy faces visible (particularly in the case of the thinnest faces - see Figure 6.6). Manually measured values of w/L for cell faces at several heights in typical specimens are shown in Figure 6.8. Neither hydride- nor carbonate-based foams exhibited pronounced cell face waviness.



(a)

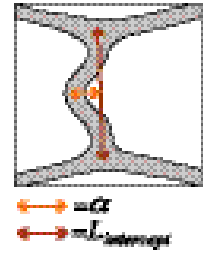


(b)

Figure 6.7: Optical micrographs of polished cross sections of typical cell faces in (a) carbonate- and (b) hydride-based foams. The dark grey particles are SiC, and the pale grey regions are Si.

Figure 6.8:

Cell face curvature in terms of $\alpha/L_{intercept}$ measured at several points in typical specimens of hydride- and carbonate-based foams



	Hydride-based foam	Carbonate foam
Average $\alpha/L_{intercept}$ at top	0.077 ± 0.078	0.066 ± 0.060
Average $\alpha/L_{intercept}$ at middle	0.045 ± 0.052	0.071 ± 0.064
Average $\alpha/L_{intercept}$ at base	0.009 ± 0.015	0.074 ± 0.070

At the top of both types of foam, where ρ^*/ρ_s is comparable, $\alpha/L_{intercept}$ is similar. The structure of the denser base regions of hydride foams is characteristic of an earlier stage in foam development, where cells do not impinge on their neighbours to the same extent (§3.2.1). The higher volume fraction of melt between cells in the dense base regions reduces $\alpha/L_{intercept}$.

6.2.3 Bulk porosity

Expansion of the carbonate-based foams reached a maximum after $t_{foam} \sim 600$ s, beyond which there was no further change in porosity. Molten foams appeared to be indefinitely stable at this temperature, with the structure gradually becoming more irregular over several hours. The limiting value of ρ^*/ρ_s was ~ 0.15 at $T_{foam} = 650^\circ\text{C}$, and 0.1 at $T_{foam} = 750^\circ\text{C}$.

This is in marked contrast to observations in hydride-based foams. Various stages of foaming are shown in Figure 6.9: a continuous increase in porosity with baking time is observed, to a point where the gas escapes and the foam collapses. The most uniform cell structures had ρ^*/ρ_s under ~ 0.15 . One consequence of this is a tendency to overbaking and collapse (§3.2.2) upon very slight increases in t_{foam} or T_{foam} . Extensive melt drainage is commonly observed even in the short T_{foam} required for foaming with TiH_2 , giving rise to density gradients, which become increasingly marked with foaming time.

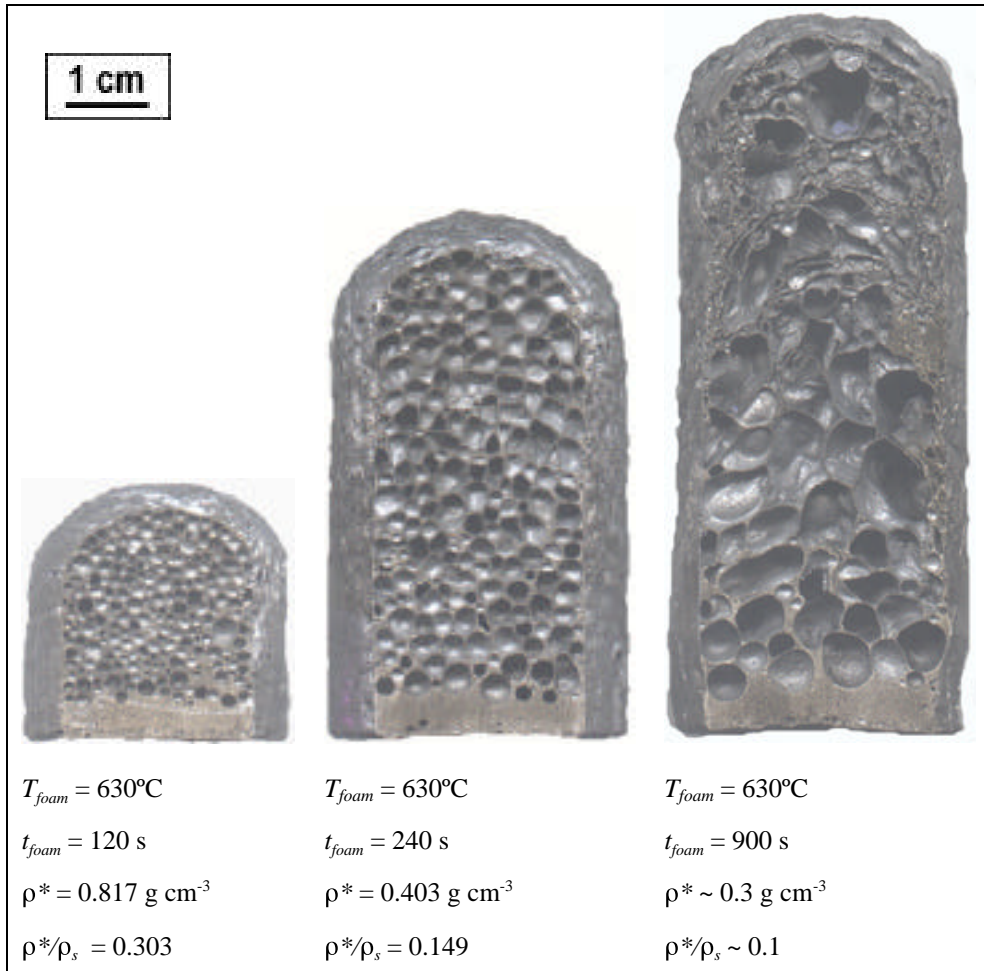


Figure 6.9: The effect of baking time on the cell structure of hydride-based foams. All the foams have the same mass ($35 \pm 1\text{ g}$), and were produced by foaming of a precursor material containing 0.15 wt.% of heat treated TiH_2 dispersed in an Al-9Si-0.5Mg melt containing 10 vol.% SiC_p .

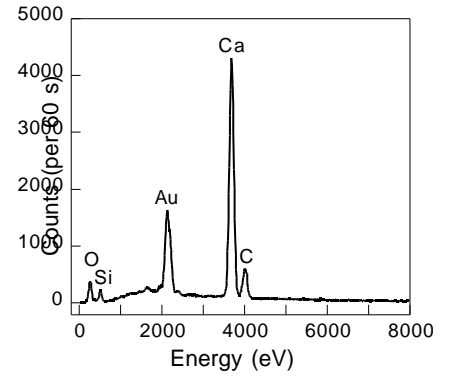
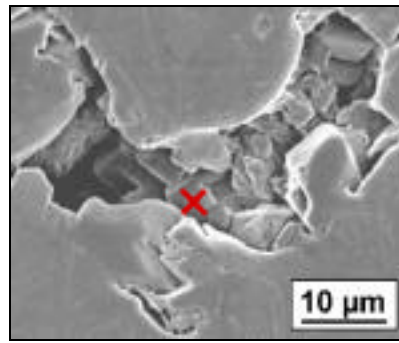
6.3 Calcium carbonate as a foaming agent

6.3.1 Distribution of foaming agents in the foamable precursor

Both the carbonate- and hydride-based foamable precursors have $\rho^*/\rho_s = 0.8$. The shape of the foaming agent particles does not change significantly during decomposition. Particles in the precursor material and foams were thus clearly identifiable by their appearance, with confirmation by energy dispersive X-ray spectroscopy (EDX). In the case of the carbonate-based foamable precursor material, the pores are non-spherical, and often lined with calcium carbonate particles, as shown in Figure 6.10. This suggests that the porosity is the result of air incorporated during the stirring process along with small areas of the surface of the melt, rather than decomposition of the foaming agent during the mixing stage. The particles of the aluminium powder mixed with the foaming agent to aid dispersion (§5.1) presumably merge with the melt, and are not visible in either type of precursor.

Figure 6.10:

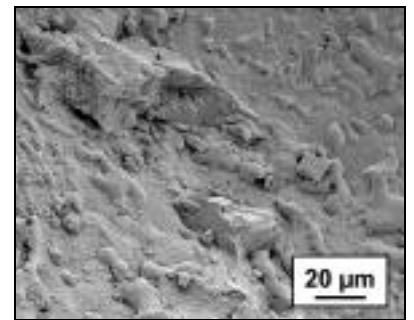
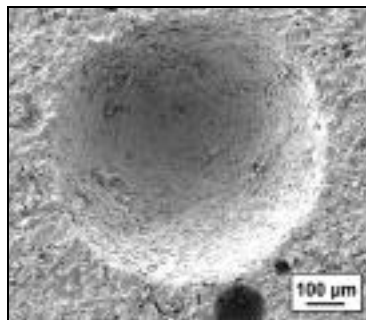
SEM micrograph of the internal surface of a pore in a foamable precursor containing 3 wt.% of CaCO_3 , and EDX spectrum of the (gold-coated) marked particle, confirming the presence of Ca.



A pore in a precursor of a hydride-based foam is shown in Figure 6.11. There is less evidence of clustering of the foaming agent powder, presumably reflecting the increased ease of dispersion of the larger particles used and the higher ratio of foaming agent to aluminium powder during incorporation. The pores are invariably spherical, with a relatively low concentration of TiH_2 particles scattered round a surface otherwise lined with SiC_p , suggesting that some decomposition has already taken place. This is consistent with observations of partial foaming in precursor cooled too slowly during production.

Figure 6.11:

SEM micrograph of a pore in a foamable precursor containing a dispersion of 1.5 wt.% of $\sim 70 \mu\text{m}$ TiH_2 particles, and enlarged view of two angular TiH_2 particles visible on the left of the pore.



6.3.2 Distribution of foaming agents in the foams produced

TiH_2 particles were found both on the surface (Figure 6.12) and embedded within cell faces (Figure 6.13). In the latter case the particles were often surrounded by a visible layer of a Ti-Al compound, identified by EDX as TiAl_3 . CaCO_3 particles were never embedded in the matrix, and were generally fairly loosely attached to the surface of cells (Figure 6.14), with no discernible reaction with the adjacent metal melt.

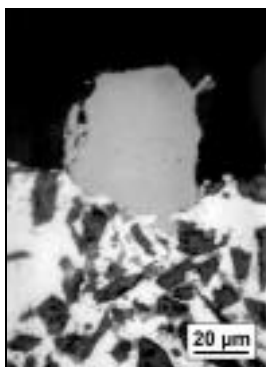


Figure 6.12: TiH_2 particle on a cell surface



Figure 6.13: TiH_2 particles embedded in a cell face (grey), surrounded by a Ti-Al compound (lighter grey)

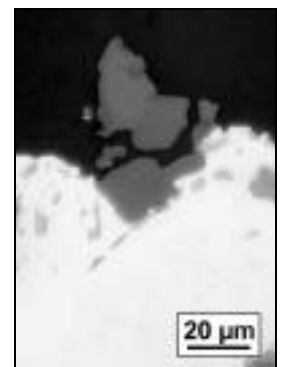


Figure 6.14: CaCO_3 particle on a cell surface

Assuming that the TiH_2 and CaCO_3 particles are spherical with a diameter of 20 μm and 70 μm respectively, a simple estimate shows that if every particle formed a separate cell in a foam with $\rho^*/\rho_s = 0.2$, the cell size in carbonate- and hydride-based foams would be approximately 0.05 mm and 0.25 mm, an order of magnitude smaller than the observed cell sizes. This is consistent with the observation of cell surfaces, in Figure 6.15, where several foaming agent particles can be seen in each cell. Nearly 100 particles were observed in some cells in carbonate-based foams.

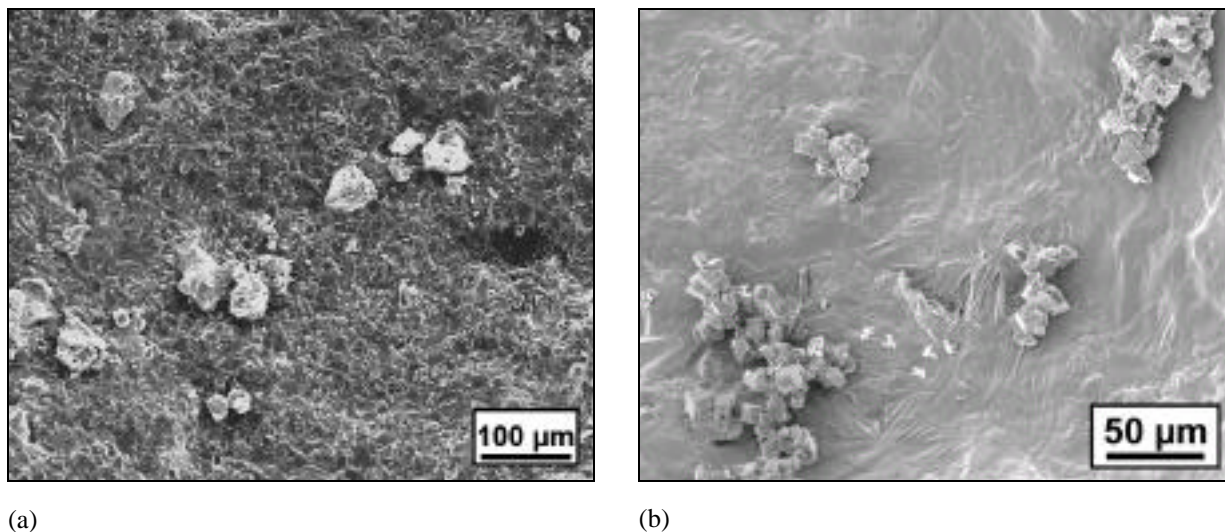


Figure 6.15: SEM micrograph of the cell surface in specimens of (a) hydride- and (b) carbonate-based foam, showing several surface-attached particles of the foaming agent.

The presence of several particles per cell is presumably due to incomplete dispersion of the foaming agent, evidenced by the presence of several particles present in pores in the foamable precursors. It may also be the result of coalescence of initially separate cells during the foaming process. With no direct relation between particle size and cell size, it is clear that using a more finely powdered foaming agent will not necessarily be effective in generating a finer cell structure, and that the smaller cell size in the carbonate based foams cannot simply be attributed to the finer foaming agent powders which can be used.

6.4 Silicon carbide particles

6.4.1 Surface distribution

Both hydride- and carbonate-based foams are stabilised by refractory SiC_p particles. However, the distribution of the SiC_p in the foams was found to be significantly different. The SiC_p is an active surfactant in the hydride-based foams, with $\sim 85\%$ of the pore surface covered by particles forming a close-packed network, as shown by the SEM micrograph of a typical cell surface in Figure 6.16.

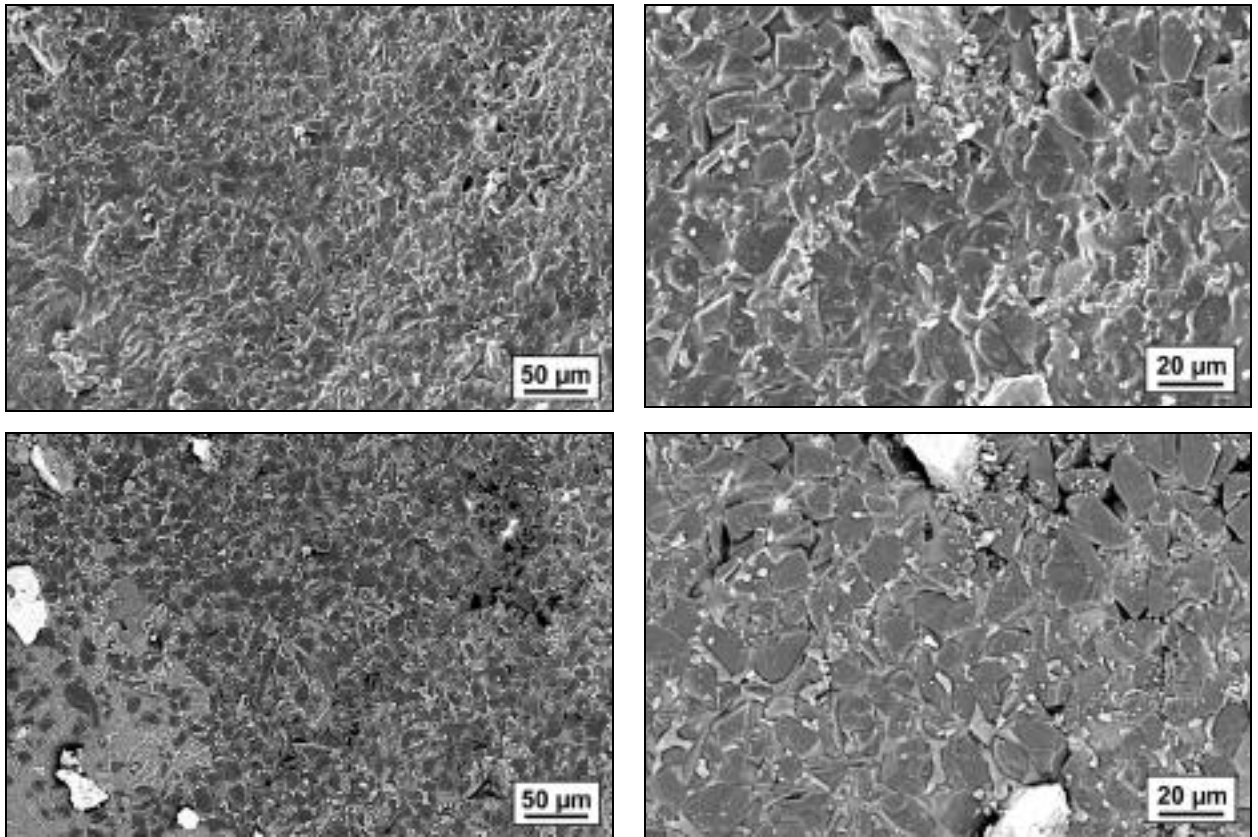


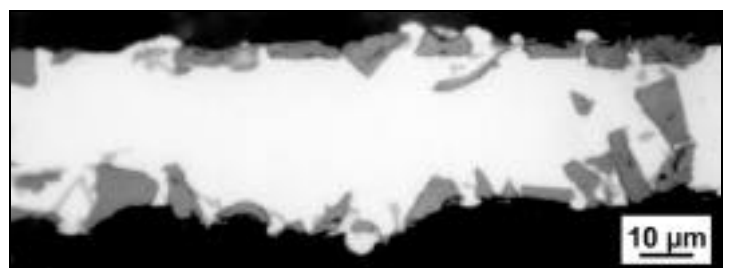
Figure 6.16: SEM micrograph of a typical cell surface in a hydride-based foam. The surface is shown at two magnifications in secondary electron (top) and backscattered electron (bottom) imaging mode. In the backscattered imaging mode the TiH_2 is white, Al is grey, and SiC is dark grey.

Examination of polished cross sections demonstrates that the surface concentration of SiC is significantly higher than that in the bulk, with the largest face of the particles generally aligned parallel to the surface, as shown in Figure 6.17. The particles line the surface fully, with angular faces exposed to give an apparently smooth surface. This does not offer any support for the stabilising mechanism proposed by Kumagai *et al* reviewed in section 3.4.6, whereby particles affect the surface tension by altering local curvature.



Figure 6.17:

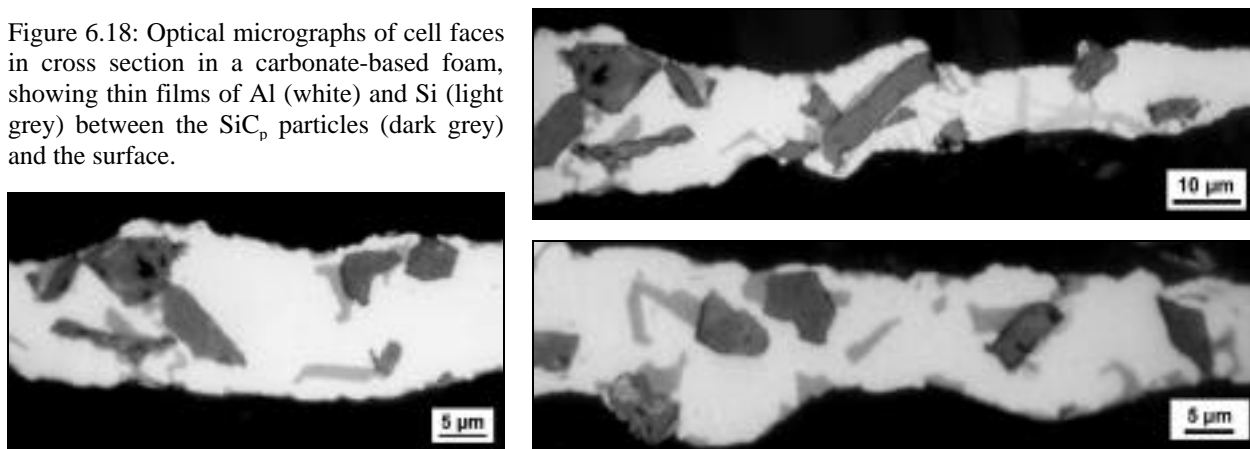
Optical micrographs showing cross sections of thin cell faces in a hydride-based foam, showing surface segregation of SiC particles (dark grey) and the degree of alignment of non-equiaxed particles.



In the carbonate-based foams, the SiC_p apparently actively avoids the surface. As shown in Figure 6.18, although SiC_p is often close to the surface, a continuous film of Al or Si is

invariably present at the interface. There is no reason to suspect that the wettability of the particles has changed during foaming: although SiC_p becomes gradually more wettable in pure aluminium due to the formation of interfacial Al_4C_3 , the high Si content present is sufficient to prevent this effect (§3.5.1).

Figure 6.18: Optical micrographs of cell faces in cross section in a carbonate-based foam, showing thin films of Al (white) and Si (light grey) between the SiC_p particles (dark grey) and the surface.



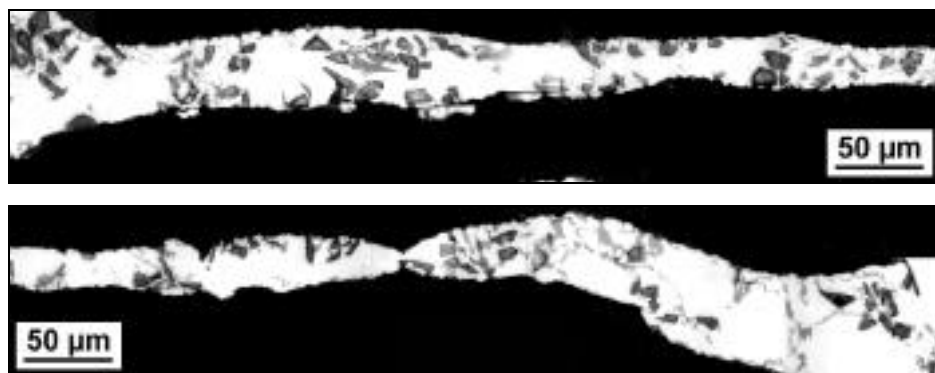
The macroscopic similarity of the cell structure of hydride and carbonate foams (§6.2) is remarkable in view of the marked difference in the distribution of nominally surfactant particles. This non-surfactant behaviour of SiC_p in the carbonate-based foams is attributed to the presence of a thin continuous surface film of solid oxide, which forms early in the foaming process and prevents the particles from reaching the surface, an effect that is discussed further in section 6.5.

6.4.2 Bulk distribution

In carbonate-based foams, particles were uniformly distributed throughout the foam, with a volume fraction similar to that in the bulk alloy. In the thinnest faces, the bridging particles apparently hold the two surfaces apart, giving rise to bumps on the surface of thinner cell faces (an example is visible in Figure 6.6). The limiting face thickness is thus related to the dimensions of the refractory particles. A thicker cell face in a carbonate-based foam is shown in Figure 6.19. Aside from its non-surfactant tendency, the bulk distribution of SiC_p is apparently random, with SiC_p generally associated with the interdendritic regions of eutectic Si as expected in this MMC (§3.6.3).

Figure 6.19:

Optical micrograph of a cross section of two ends of a relatively thick cell face in a carbonate-based foam.



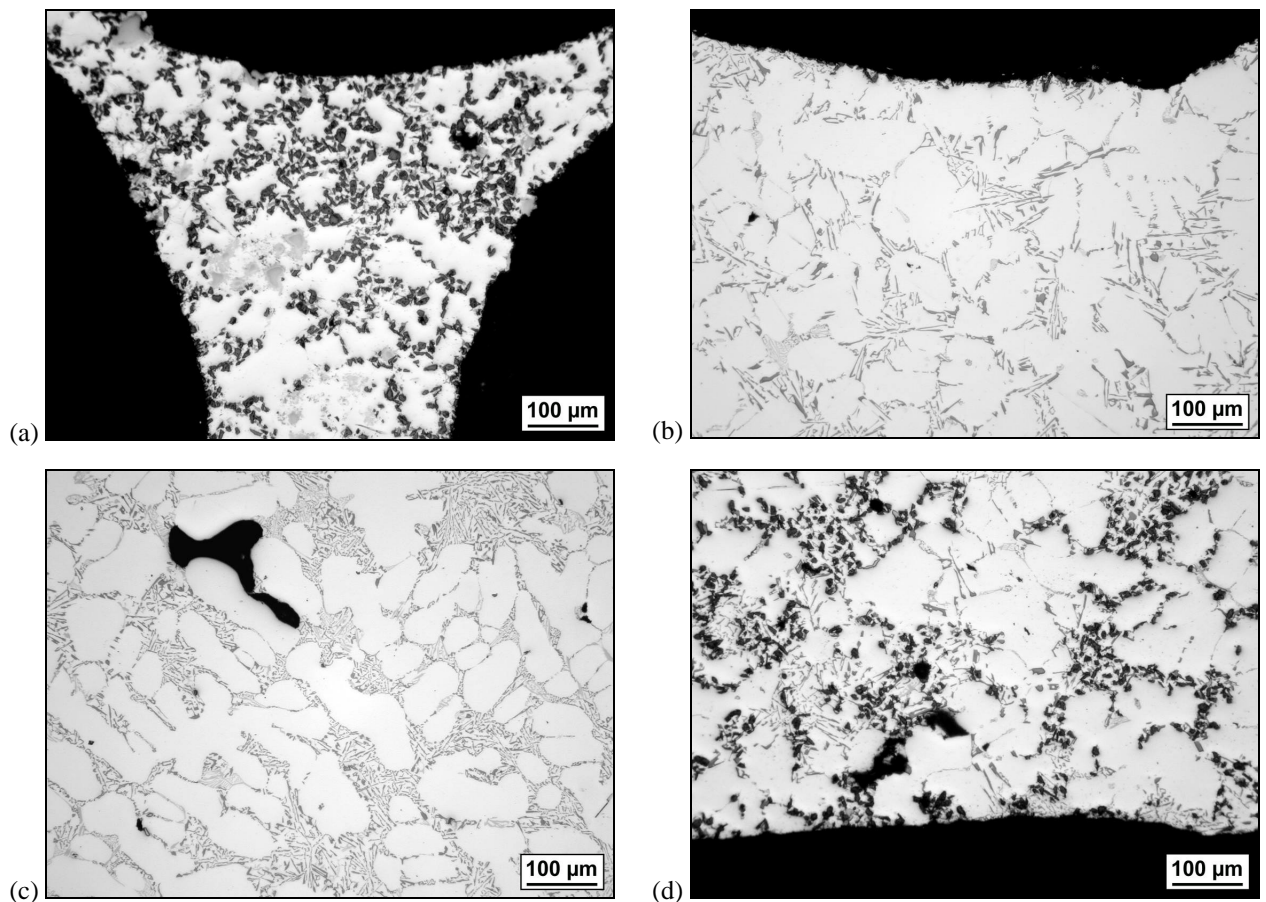
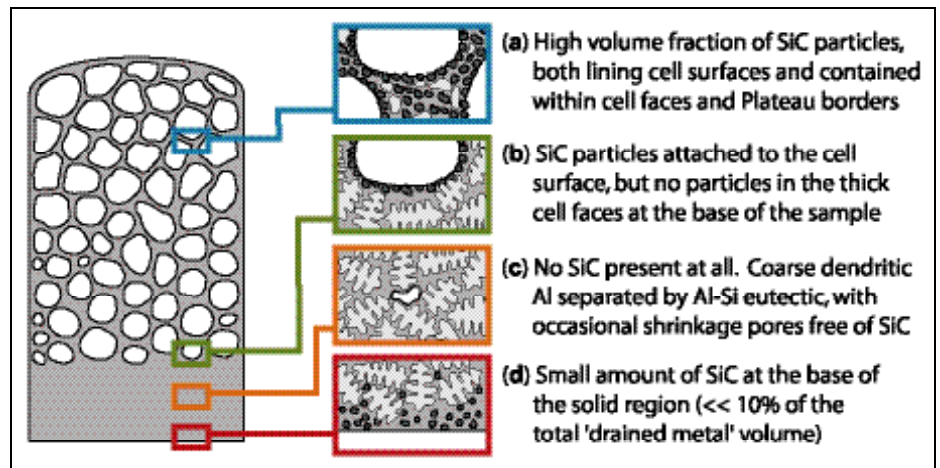
In hydride-based foams, the surfactant tendency means that the SiC_p volume fraction is markedly higher in cell faces than in the Plateau borders - but even within the Plateau borders

the local particle concentration, measured by linear intercept and image analysis, is significantly over the 10 vol.% of the bulk melt, with local concentrations invariably over 20 vol.% and sometimes approaching 30 vol.%.

This anomalously high concentration is attributed to relatively free drainage of the Al-Si melt through the relatively wide Plateau borders and cell faces, while the SiC_p remains attached to the surfaces of the cells or constrained by loose networks of solid particles in the narrow channels. This is consistent with measurement of the SiC_p content at various positions within a typical foam produced with a melt containing 10 vol.% SiC_p . A marked variation was observed, as depicted schematically in Figure 6.20. The top of the foam, (a), contains a high volume of SiC_p , with continuously lined surfaces and ~ 25 vol.% within the melt away from the surfaces. A far smaller fraction of SiC_p is found in the wider cell faces at the base, (b), almost all of which is attached to cell surfaces. The solid base, (c) & (d), which is characteristic of hydride-based foams, contains virtually no SiC_p – well under 10 vol.% of the volume of metal in the fully dense region.

Figure 6.20:

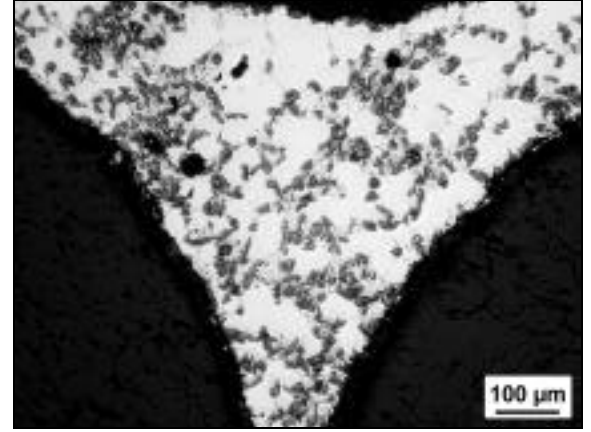
Illustration and corresponding optical micrographs showing the observed variation in the distribution and volume fraction of SiC_p with height in hydride-based foams. The specimen shown in the micrographs was produced with $T_f = 630^\circ\text{C}$ and $t_f = 120$ s, with an Al-9Si-0.5Mg MMC melt containing 10 vol.% of particulate SiC_p .



The volume fraction of particles in foams produced with MMC melts containing 20 vol.% SiC_p was also found to be 20-30 vol.%, with a typical Plateau border is shown in Figure 6.21. The similarity in concentration to that in foams produced with melts containing 10 vol.% SiC_p (Figure 6.20 (b)) suggests that this level of solid particles is required to stabilise the molten foam structure, and that relatively rapid drainage will occur until this level is reached.

Figure 6.21:

Optical micrograph of a Plateau border in the centre a hydride-based foam produced with an Al-9Si-0.5Mg MMC melt containing 20 vol.% SiC_p.



If it is assumed that the hydride-based foams consist of a fully dense base containing no SiC_p, with all the SiC contained within the initial melt being uniformly distributed within the foamed region, the SiC_p content in the foamed region can be estimated if the height of the solid base relative to that of the foam is known.

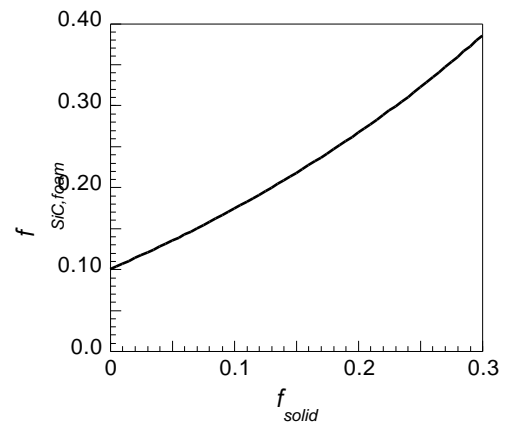
For a foam which has undergone melt drainage in which the foamed region has a density ρ^* , and the fully dense region at the base has a density ρ_s and occupies a fraction f_{solid} of the foam height, the SiC_p content in the foamed region is given by:

$$f_{SiC, foam} = \frac{f_{SiC} \cdot f_{solid} + [1 - f_{solid}] \cdot \rho^* / \rho_s}{[1 - f_{solid}] \cdot \rho^* / \rho_s} \quad [6.1]$$

This is plotted in Figure 6.22 for a foam with typical $\rho^*/\rho_s = 0.15$. The concentration of SiC_p is thus ~ 15-25% in foams with $f_{solid} = 0.1-0.15$.

Figure 6.22:

Relation between the area fraction of the fully dense, SiC_p-free region at the base of a foam which has undergone melt drainage, f_{solid} , and the local SiC_p content in the foamed region, $f_{SiC, foam}$, for a foam in which ρ^*/ρ_s of the foamed region is 0.15 (according to eqn. [6.1]).



6.5 The oxide film

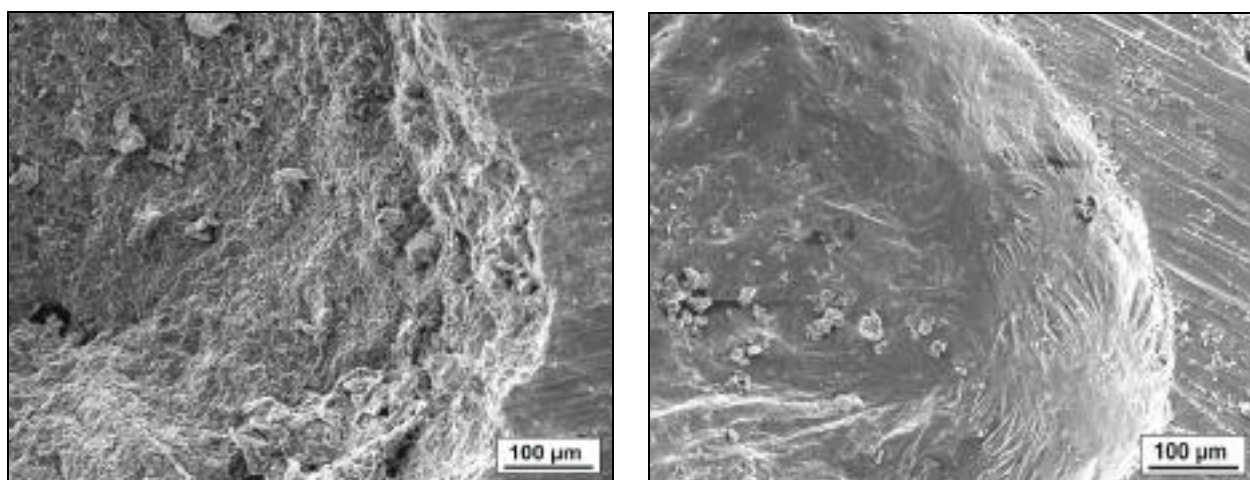
6.5.1 Surface features

As mentioned in section 6.4.1, the surface of cells in carbonate-based foams is thought to be covered in a thin continuous film of solid oxidised metal from the first stages of foaming. Whereas foaming with TiH₂ leads to a reducing hydrogen atmosphere inside the pores, the use of

CaCO_3 as a foaming agent gives rise to an oxidising atmosphere of CO_2 inside the pores, making the formation of such an oxide film likely.

Stretch marks

Cell surfaces of typical hydride- and carbonate-based foams are shown in Figure 6.24. In contrast to the rough, SiC_p -lined surface in the hydride-based foams, the carbonate-based foam has a smooth surface punctuated only by a scattering of CaCO_3 particles, with no SiC_p visible. Although sufficiently rigid to prevent SiC reaching the surface, the film does not appear to be sufficiently thick to restrict the growth of the cells, or local changes in cell shape, as evidenced by the presence of occasional 'stretch marks' on the surface. These are the source of the apparent surface roughness visible in the cross section in Figure 6.6.



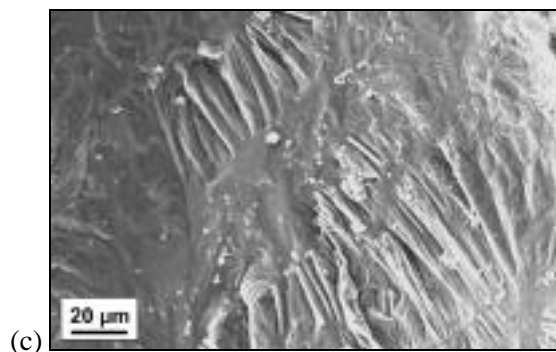
(a)

(b)

Figure 6.24:

SEM micrographs showing cut cross sections of a cell in (a) hydride- and (b) carbonate-based foams. The area at the right, with striations, is the cut cell face. Both the foams were produced with an F3S10S Al-9Si-0.5Mg MMC melt containing 10 vol.% SiC_p .

The stretch marks visible on the cell surface in (b) are enlarged in (c).



(c)

Tear bands

Another notable feature of carbonate-based foams is the presence of extended strips of apparently stretched film, shown in Figure 6.25 (a). In view of the close match between the shape of the two sides of the bands, the formation of these features is attributed to an increasingly thick oxide film becoming progressively more resistant to stretching, and instead undergoing brittle fracture, to form discrete solid islands (as illustrated in Figure 6.25 (b)). A new, thinner oxide film will immediately develop on the newly-exposed liquid metal. Since this new film initially constitutes the weak point of the surface structure, further growth of the cell preferentially stretches this part of the film, while relative movement of the rigid islands of thick

film to further accommodate cell expansion shears it to give rise to the distinctive parallel stretch marks.

Figure 6.25 (a):

SEM micrograph showing characteristic tear bands of stretched film in a foam produced using a CaCO_3 foaming agent.

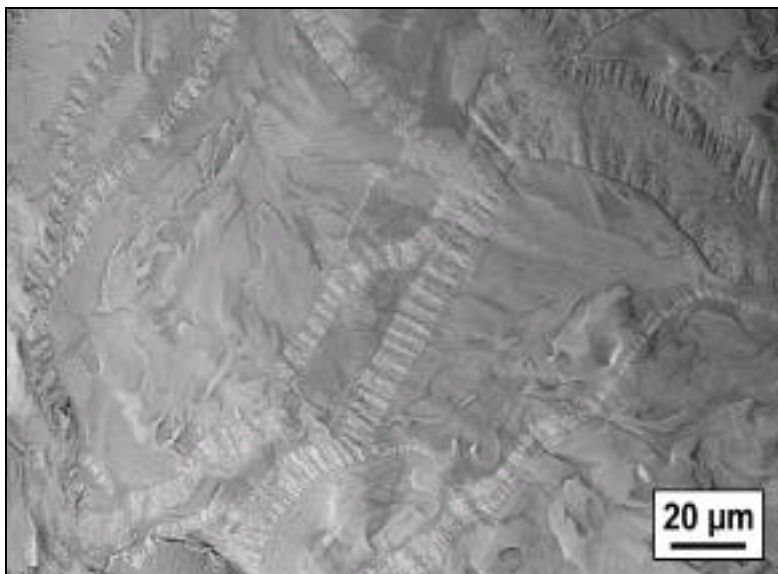
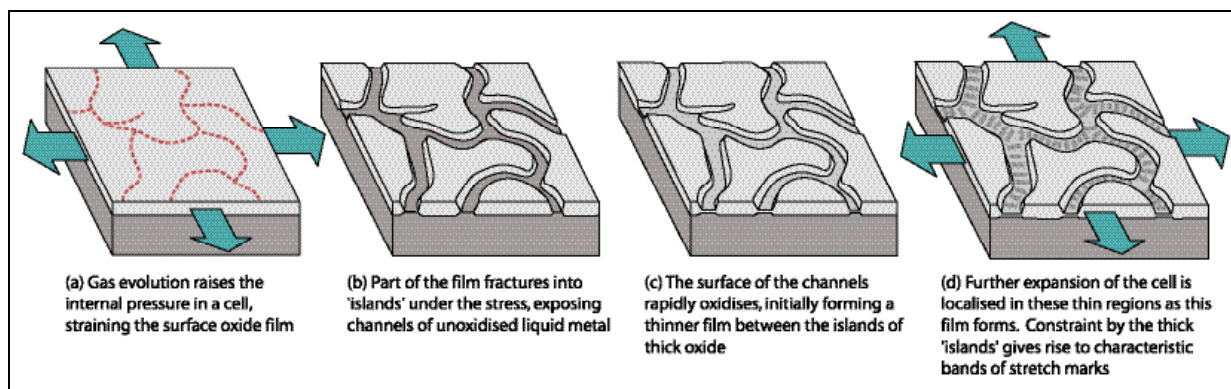


Figure 6.25 (b):

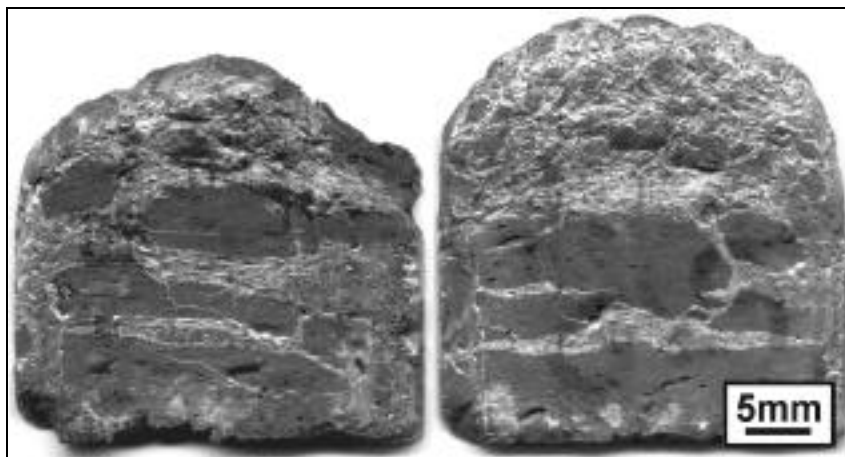
A postulated mechanism for the formation of the tear bands observed on the surface of carbonate-based foams.



The mechanical behaviour of the film is analogous to the effect of solid islands of thicker oxide scale on the outer surfaces of the foams, shown in Figure 6.26. It was noted that in the absence of a foaming agent, these external films have sufficient rigidity to contain cubes of molten melt in their original shape. The observation of internal tear bands demonstrates that the film at the cell surfaces also has finite mechanical strength. Its presence will therefore account for a far more marked effect on surface tension than the effects of thin adsorbed films reviewed in section 3.4.7.

Figure 6.26:

External view of foams produced with CaCO_3 . Islands of remnant oxide scale from the outer surface of the foamable precursor are visible as darker regions (with fine parallel striations from the cutting process), separated by regions of lighter metal exposed during the foaming process.

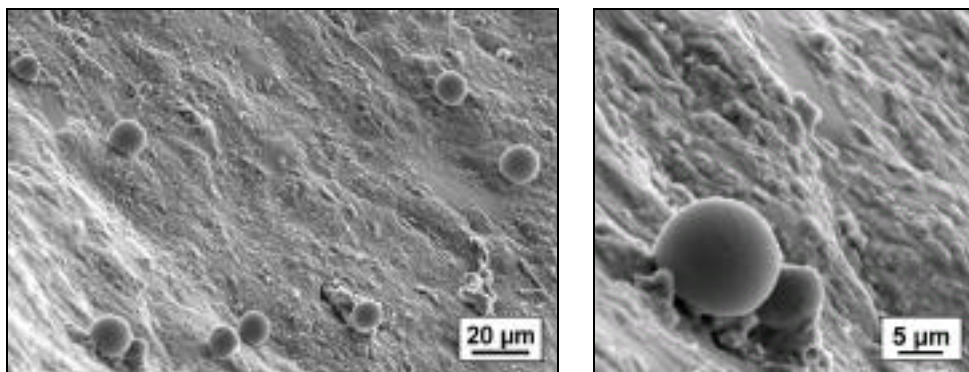


Surface droplets

Small surface spheres, shown in Figure 6.27, are sometimes attached to the surface. These are composed of aluminium, and are not similar in appearance to the aluminium powder used to aid incorporation of the foaming agent. It is thought that they are formed by melt seeping out of small holes in the oxide film, with flow subsequently constrained as the surface of the droplets oxidises.

Figure 6.27:

SEM micrograph of Al spheres on a cell surface in a CaCO_3 -based foam.



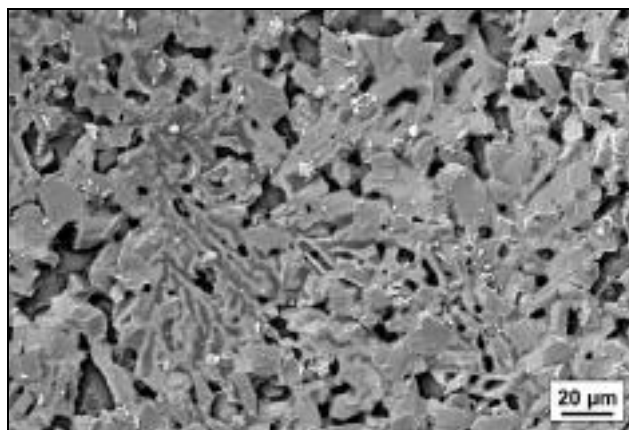
6.5.2 Characterisation of the oxide film

Chemical etching

Foam specimens were etched in concentrated sodium hydroxide in order to dissolve the metallic aluminium. In the hydride-based foams the metal regions were uniformly etched, as shown in Figure 6.28, to reveal a dense network of SiC_p particles loosely connected by residual metallic areas.

Figure 6.28:

SEM micrograph of a surface of a hydride-based foam etched in concentrated aqueous NaOH. Most of the material visible consists of SiC particles, separated by small amounts of residual Al. The darker grey area is Si-rich.



The result of etching a cross section of Plateau borders in a carbonate-based foam is shown in Figure 6.29, together with sketches of the cell geometry shown and the principal phases detected by EDX. The cut surface in the cross section was dissolved to reveal a network of SiC particles, in a similar manner to the cell surfaces in the hydride-based foams. On the surface of the cells, a thin film remained even after extended etching, while the metal under the layers was dissolved, resulting in occasional cracks in the layer. The particles visible in the holes in the films were confirmed to be SiC by EDX. This is consistent with the presence of a thin oxide film, with a thickness under $1\ \mu\text{m}$ on the surface of the carbonate foams.

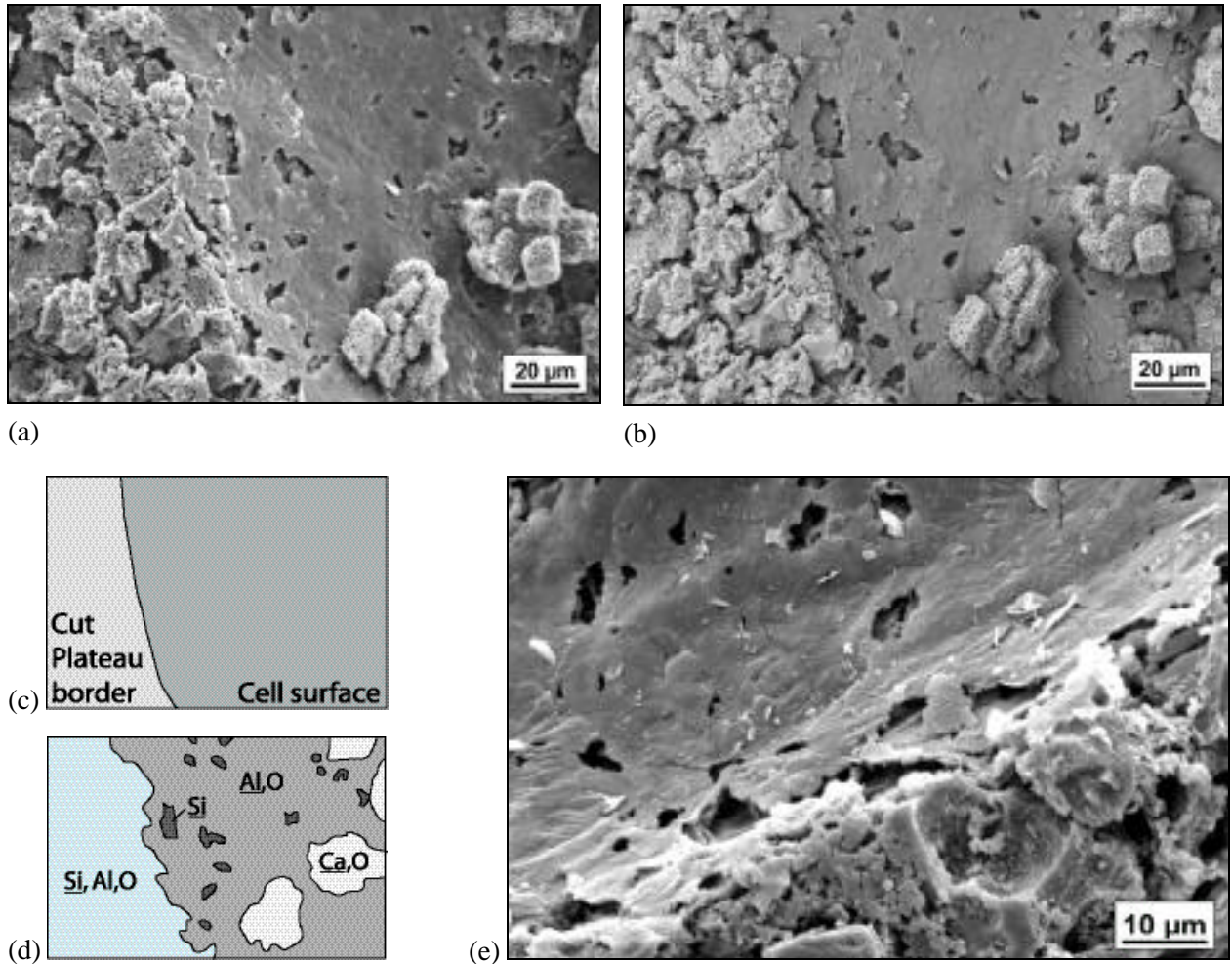


Figure 6.29: SEM micrograph of the edge of an etched cell surface and Plateau border in cross section in (a) secondary and (b) topographical backscattered imaging. The field of view is sketched in (c), and the composition of the main visible regions measured by EDX is illustrated in (d), with the principal element underlined. An SEM micrograph showing an enlarged secondary electron view of the edge of the continuous film is shown in (e).

Bulk chemical analysis

The solid film could be formed of Al_2O_3 , MgO , MgAl_2O_4 or even Al_4C_3 . X-ray diffraction of powdered specimens of hydride- and carbonate-based foams was used in order to identify the phases present. Diffraction patterns obtained, with the main diffraction peaks identified, are shown in Figure 6.30.

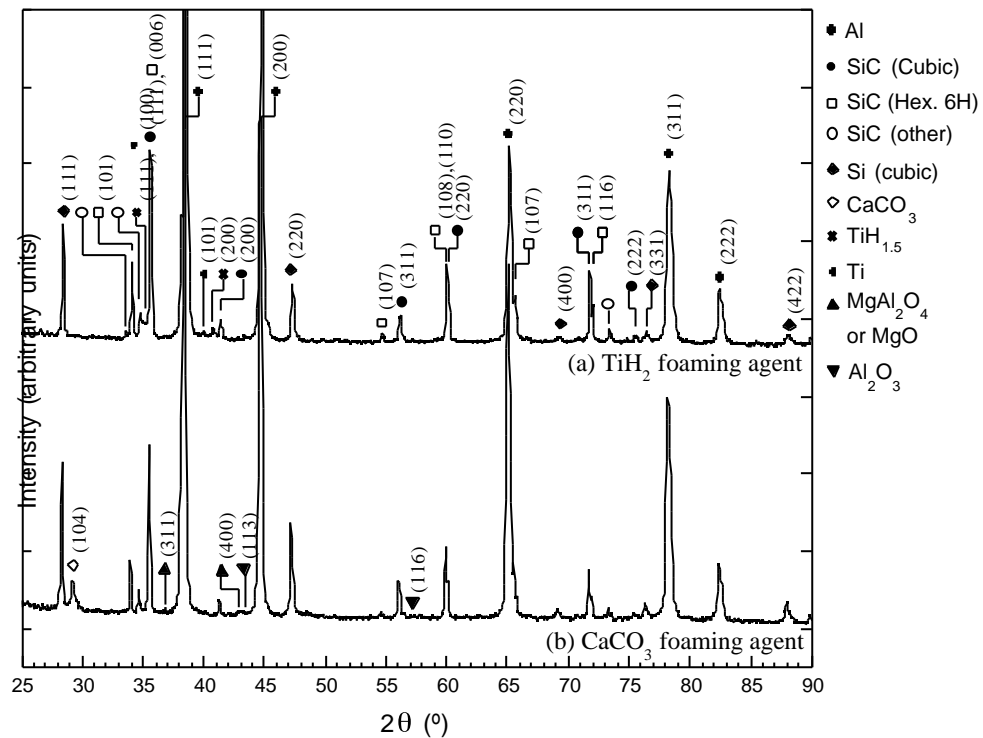


Figure 6.30: X-ray diffraction traces using CuK_α radiation obtained for:

(a) A FORMGRIP foam produced from a foamable precursor containing 10 vol.% of angular $9\ \mu\text{m}$ SiC particles and 1.5 wt.% of thermally pre-treated TiH_2 dispersed within an Al-9Si-0.5Mg matrix, with $T_{\text{foam}} = 630^\circ\text{C}$ and $t_{\text{foam}} = 60\ \text{s}$.

(b) A FOAMCARP foam produced from a foamable precursor containing 3.3 wt.% of as-received CaCO_3 dispersed within the same melt, with $T_{\text{foam}} = 650^\circ\text{C}$ and $t_{\text{foam}} = 600\ \text{s}$.

The diffraction patterns are, unsurprisingly, dominated by Al and SiC peaks. Several allotropes of SiC are present (\square , \bullet), presumably a result of the mechanism of production of SiC. The hydride-based foams contain traces of Ti (+) and $\text{TiH}_{1.5}$ (\times), while the carbonate-based foams have a peak due to CaCO_3 (\diamond). There are few other differences between the foams. The concentration of both MgAl_2O_4 (\blacktriangle) and Al_2O_3 (\blacktriangledown) was very low in the carbonate-based foam, and similar to that in the hydride-based foam, as visible in a more detailed scan of significant un-obscured peaks in Figure 6.31.

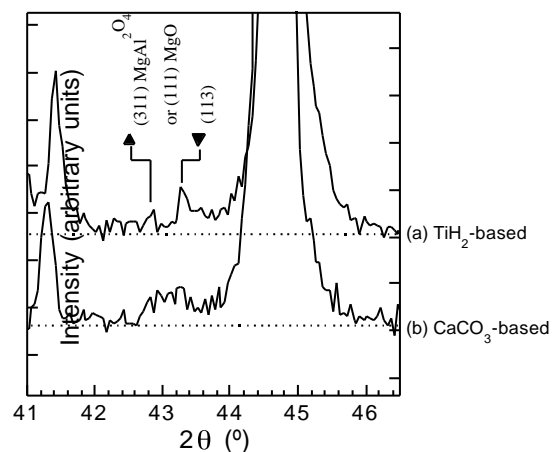


Figure 6.31:

High-resolution scan of a region of the diffraction patterns for the two foams in Figure 6.30 containing un-obscured Al_2O_3 , MgO and MgAl_2O_4 diffraction peaks.

Specimens of carbonate-based foams were produced with an extended t_{foam} of 6000 s, in order to allow any surface film to increase in thickness. The diffraction patterns thus obtained had a lower CaCO_3 peak and a small but distinct Al_2O_3 peak, as shown in Figure 6.32. The principal diffraction peak of Al_4C_3 , at $31.7^\circ 2\theta$, was still not detected. The total internal $\text{Al}_2\text{O}_3/\text{MgAl}_2\text{O}_4$ concentration, including any oxides incorporated during the production of the precursor, is ~ 1 vol.%.

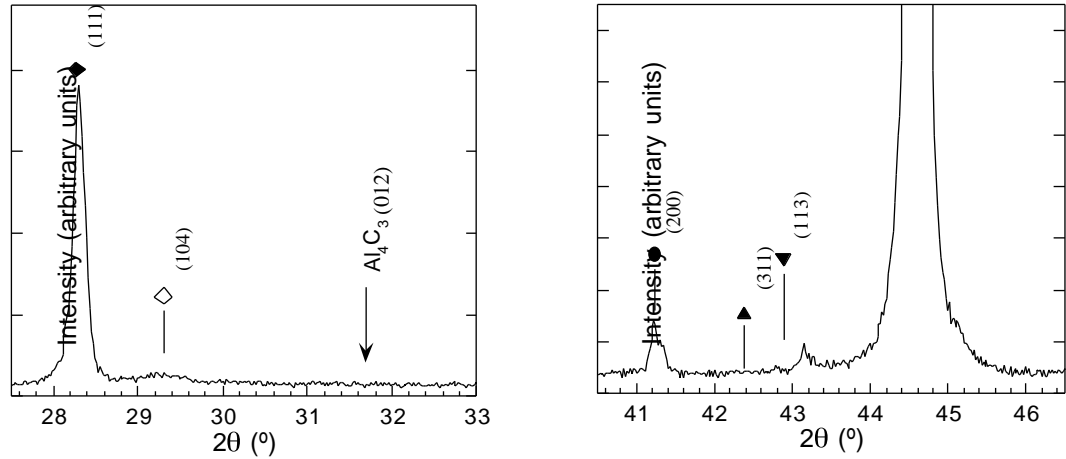


Figure 6.32: Sections of the CuK_1 diffraction pattern obtained for a foam of composition similar to specimen (b) in Figure 6.30, produced with $T_{foam} = 650^\circ\text{C}$ and an extended t_{foam} of 6000 s.

For a thin oxide film covering the surface of spherical cells of uniform diameter, the fraction of the film phase in the solid, f_{oxide} , can be related to the thickness of a surface film, w_{film} , and the cell diameter, d , by:

$$f_{oxide} = \frac{6 \left(1 - \frac{\rho^*}{\rho_s}\right) w_{film}}{\frac{\rho^*}{\rho_s} d} \quad [6.2]$$

As shown in Figure 6.33, the measured f_{oxide} of under 1 vol.% in a foam with $\rho^*/\rho_s \sim 0.15$ and $d \sim 2$ mm is consistent with a film thickness of under $0.7 \mu\text{m}$.

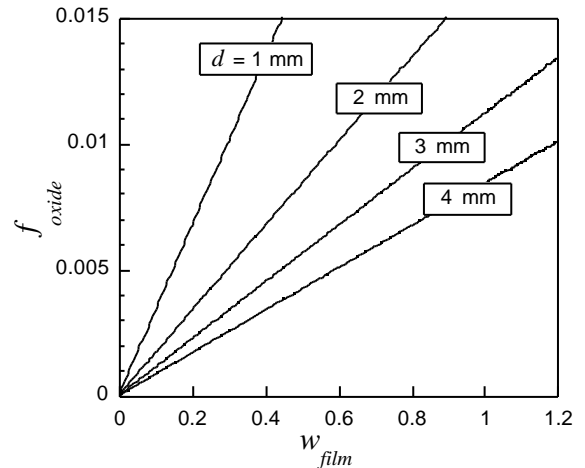


Figure 6.33:

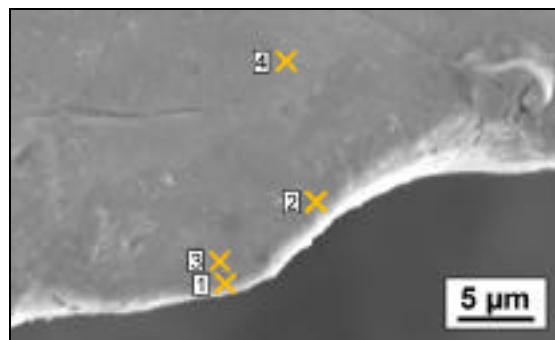
f_{oxide} as a function of w_{film} according to [6.2] for various values of d in a cell with $\rho^*/\rho_s = 0.15$.

Local chemical analysis

Figure 6.34 shows the edge of a cell face in a carbonate-based foam in cross section. EDX (§5.3.4) was used to measure the chemical composition at four points, at varying distances from the surface listed. The white layer is the result of surface relief, rather than changes in chemical composition; surface copper coating of the foam to remove this effect was not found to significantly alter the results of EDX analysis.

Figure 6.34:

SEM image (in backscattered imaging mode) of a mounted surface of a carbonate-based foam selected to be free of SiC, Si regions and visible non-Al phases, with the results of elemental analysis of the elements present by EDX at the labelled points 1 to 4. The composition ratios are normalised to remove carbon, as its concentration could not be measured reliably, and gold, which was deposited as a thin surface film to aid conductivity.



Point	Distance from surface	Al wt. %	Mg wt. %	Si wt. %	O wt. %
1	0.5 μm	42.6	13.7	0.0	43.7
2	1.5 μm	43.7	9.9	3.7	42.7
3	2 μm	64.8	5.7	0.0	29.6
4	9 μm	94.0	0.0	1.5	4.5

The enrichment of Mg in the 1-2 μm surface region is consistent with the tendency of Mg to migrate to the aluminium-gas interface reviewed in section 3.4.7. The oxygen content was markedly higher near the surface, and the significant presence of Mg is consistent with the presence of MgO or MgAl₂O₄, although the film is too thin for this technique to be used further or for surface phases to be visible by electron microscopy.

Surface chemical analysis

Elemental analysis of cut cross sections and cell surfaces of hydride- and carbonate-based foams (§5.4.2) by X-ray photoelectron spectroscopy (XPS), with an analysis depth of ~ 8 nm, provides a measure of the surface concentration of elements. The section of the spectrum covering the Al_{2p} and Mg_{1s} peaks is shown in Figure 6.35.

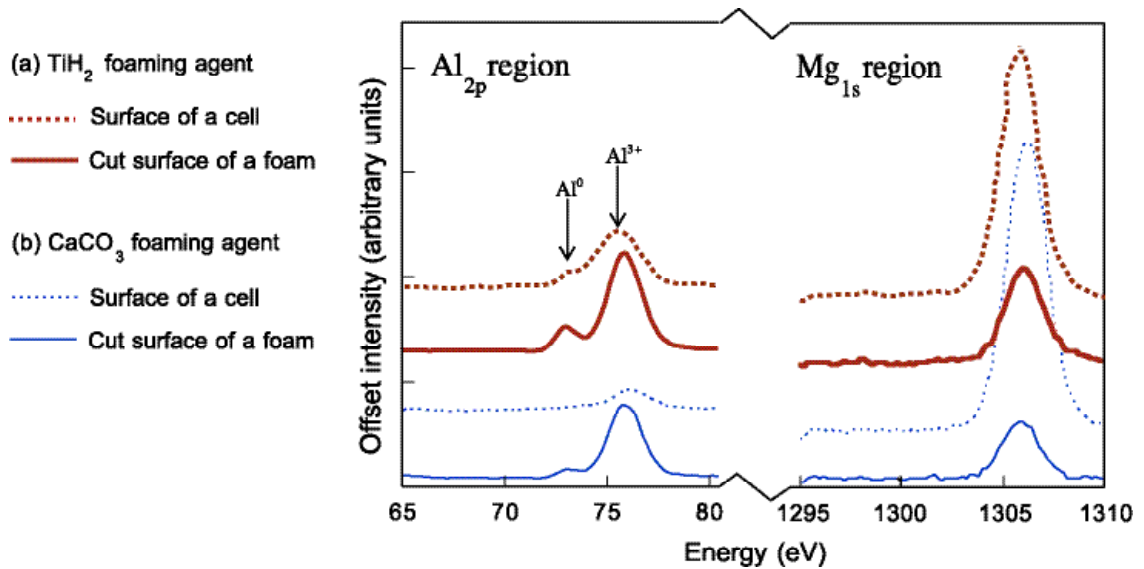


Figure 6.35: Sections of XPS spectra (normalised by the total intensity), showing the measured peaks for Mg_{1s} and Al_{2p} measured on both pore surfaces and cut surfaces exposed to air, for the following foams:

(a) A hydride-based foam, produced from a foamable precursor using 1.5 wt.% of thermally pre-treated TiH_2 dispersed within an Al-9Si-0.5Mg matrix containing 10 vol.% of surfactant particulate SiC, with $T_{foam} = 630^\circ C$ and $t_{foam} = 60$ s.

(b) A carbonate-based foam, produced from a foamable precursor containing 3.3 wt.% of as-received $CaCO_3$ dispersed within the same melt, with $T_{foam} = 650^\circ C$ and $t_{foam} = 600$ s.

A significant Mg_{1s} peak was recorded on the cell surface in both hydride- and carbonate-based foams, suggesting that the surface concentration of Mg inside the cells outweighs that of Al in both foams, despite a Mg concentration of only 0.5 wt.% in the bulk alloy. There was a particularly high surface concentration of Mg in the carbonate-based foam, where Al was barely detected in the analysis depth, which is consistent with the findings of work in the literature concerning the oxidation of Al-Mg melts (§3.4.7). Limited surface segregation of Mg was also detected on the cut surfaces.

The Al peak in XPS is split into separate peaks for metallic (Al^0) and oxidised (Al^{3+}) aluminium, at ~ 73 and 76 eV respectively. Since all the samples are oxidised to some extent due to atmospheric exposure, the presence of an Al^0_{2p} peak indicates that metallic aluminium is being detected beneath any oxide layer within the analysis depth, and that the layer is under ~ 8 nm thick. Small Al^0_{2p} peaks were detected on the cut surfaces of both foams, as well as on the cell surface of the hydride-based foams. No Al^0_{2p} peak was detected on the cell surface of the carbonate-based foams, although, given that the Al^{3+}_{2p} peak was also extremely weak relative to the Mg_{1s} peak, the presence of unoxidised Mg below an oxidised surface cannot be excluded. The Al^0_{2p} peaks are weak, implying that the film is thicker than the Mott thickness of 2 nm (§3.4.7), which is presumably the result of some heating during sample preparation.

Auger electron spectroscopy (AES), together with etching by Ar^+ ions, was used to further probe the concentration of elements at various depths in the specimen. The rate of etching by the Ar^+ ions varies with the geometry of the cells, as well as with the composition of the material. Since care was taken to obtain a comparable geometry, and the material is similar, it is possible to say that the etch rate is the same in the two samples. This allows relative concentration profiles, and hence the depth of the oxidised material in the two foams, to be compared. However, the rate of etching cannot be immediately correlated with the depth of etching.

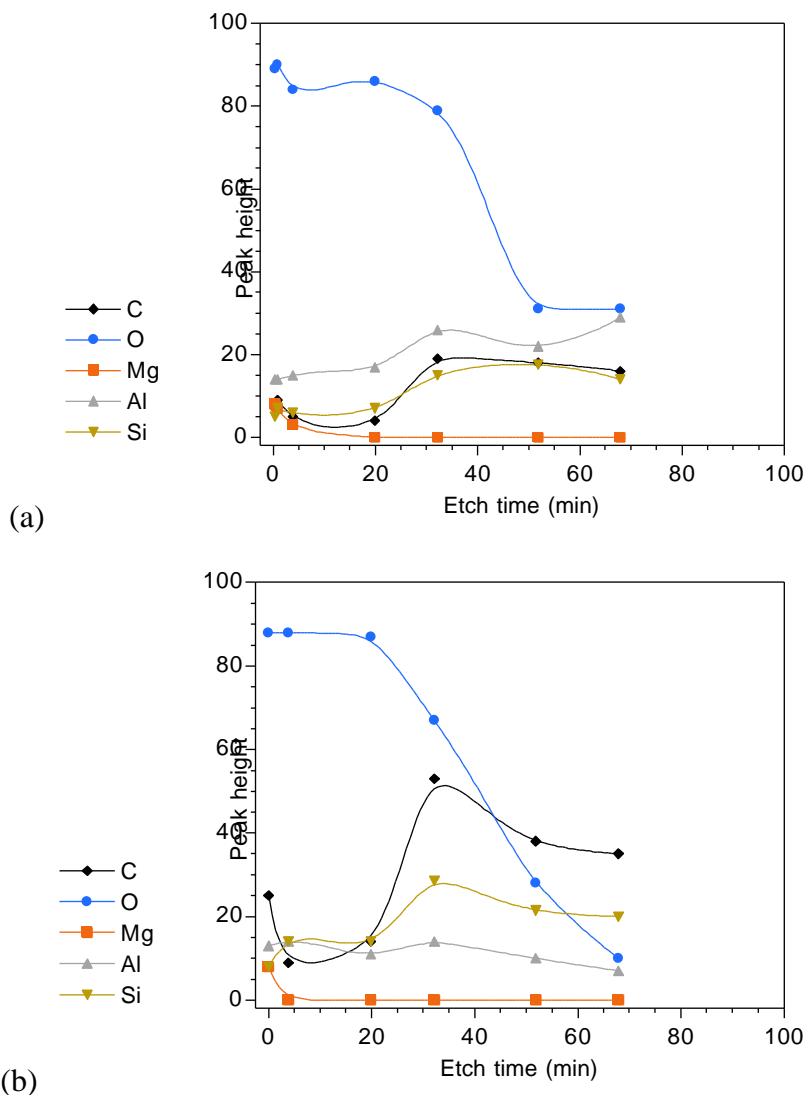
In hydride-based foams, the high spatial resolution of AES allowed separate examination of SiC particles and regions of exposed Al (§6.4.1) to be examined separately. The concentration profiles of C, O, Mg, Al and Si obtained are shown as a function of etching time in Figure 6.36.

Figure 6.36:

AES depth profiles of selected points on the surface of a foam produced with 1.5 wt.% of thermally pre-treated TiH_2 dispersed within an Al-9Si-0.5Mg matrix containing 10 vol.% of surfactant SiC_p , with $T_{\text{foam}} = 630^\circ\text{C}$ and $t_{\text{foam}} = 60$ s.

(a) Al region in a hydride-based foam

(b) SiC particle in a hydride-based foam



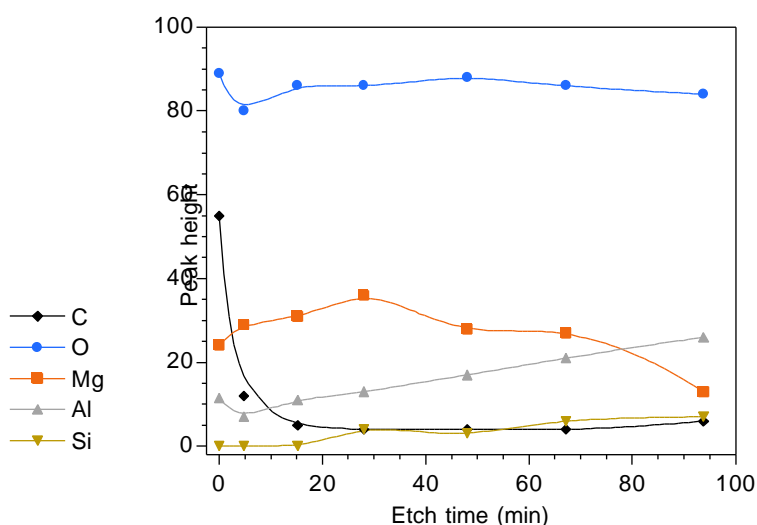
In the aluminium region, the concentration of O drops sharply after 40 minutes of etching. The Mg concentration is initially half that of the O, but drops rapidly with etching. In the SiC particle, a high initial concentration of O drops to reveal a composition of mainly Si and C, suggesting that the proprietary particle pre-treatment to aid wettability involves a degree of

heating or surface oxidation. The residual Al detected may be the result of contamination by re-sputtering during the ion etching.

The depth profile for a carbonate-based foam is shown in Figure 6.37. Etching for 100 minutes was unable to penetrate the oxide layer, indicating that the oxide thickness is significantly larger than that in the hydride-based foam. Mg is at a higher concentration than Al at the surface, with a progressive increase in the ratio of Mg to Al with etching depth. The increased foaming time may have helped the Mg diffuse towards the surface, and the increased oxidation may also contribute to the enhanced presence of Mg at the surface. The high activity of Mg at the surface of the oxidised Al-Mg melt is consistent with the XPS measurements and observations in the literature (§3.4.7).

Figure 6.37:

AES depth profile in a foam produced with 3.3 wt.% of as-received CaCO_3 dispersed within an Al-9Si-0.5Mg matrix containing 10 vol.% of SiC_p , with $T_{\text{foam}} = 650^\circ\text{C}$ and $t_{\text{foam}} = 600$ s. A general area on the cell surface, with no visible CaCO_3 particles, was examined.



6.6 Internal microstructure

A rough estimate of the cooling rate can be obtained by measuring the spacing of dendrite arms (§3.4.4). In wide Plateau borders, the spacing was typically $\sim 40 \mu\text{m}$ in both hydride- and carbonate-based foams, implying a cooling rate of $\sim 1\text{-}2^\circ\text{C s}^{-1}$. Aside from local variations in the concentration of refractory particles, the metallographic microstructures in the foams were similar to that of the metal matrix composite (§3.6.3).

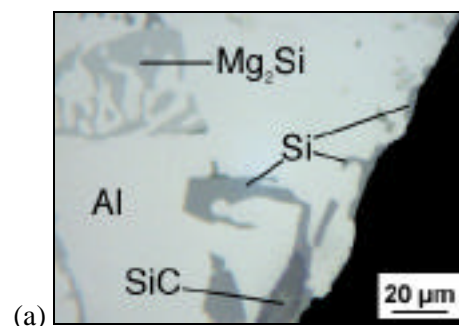
A cell face in a carbonate-based foam is shown in Figure 6.38, showing apparent segregation of Si to the surface, which was common in carbonate-based foams. The relatively low concentration of Si measured in the outer surface by XPS and AES (§6.5) suggests that this is the result of Si rejected from the aluminium dendrites during growth, rather than a tendency of the Si to migrate to the melt-gas interface. The low thermal conductivity of the gas in the cells means that the aluminium dendrites presumably grow outwards from the centre of the cell faces and Plateau borders, with the remaining Si accumulating between the dendrites and the thin oxide film to form these Si regions. Small quantities of the Mg_2Si intermetallic are visible

(§3.5.2). Reaction products containing Ti were only found in the immediate vicinity of embedded particles (§6.3), and no Ca reaction products were observed.

Figure 6.38:

(a) Optical micrograph of a cell edge in a carbonate-based foam with the principal phases (as detected by subsequent EDX of the same specimen) labelled.

(b) Optical micrograph of the same cell edge showing the distribution of areas of Si (light grey) in the vicinity of the surface.



6.7 Factors affecting structure and stability of standing foams

6.7.1 The effect of foaming agent & foaming gas

Limiting porosity

The effect of foaming agent on stability has already been mentioned: hydride-based foams expand continuously until gas escapes (as shown in Figure 6.9), while the porosity of carbonate-based foams reaches at a limiting value related to T_{foam} . This is thought to be a result of the strength of the gradually thickening oxide film, which resists expansion of the cells. The foaming reaction is also self-inhibiting, with the CO_2 produced preventing further decomposition. This effect is discussed further in Chapter 7.

Effect of foaming gas on surface tension

The generation of an oxide film significantly affects the stability of the cell structure. In foams produced with non-oxidising foaming gases, the SiC_p particles are the only surfactant material. The non-continuous surface coverage (§6.4.1) means the surface retains a degree of flexibility. The cells are thus able to contract and minimise their surface area, with associated drainage from cell faces to Plateau borders as the surface tension makes the cells more spherical.

In foams produced with oxidising gases, the surface can expand by oxide film rupture, and the formation of an oxide layer on the newly exposed melt (§6.5.1), although, since the surface cannot contract, there is no action of surface tension. The near-spherical shape of the pores is

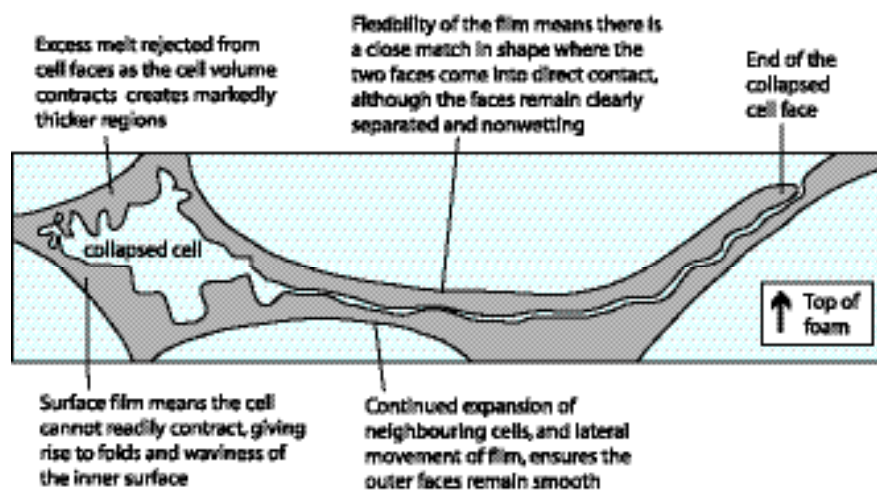
thus purely a result of the mechanical resistance of the oxide film to the increasing gas pressure: were the gas pressure in a cell to be reduced, the cell might not remain spherical.

Figure 6.39 shows a micrograph of a cell face in a carbonate based foam which has collapsed on to the one immediately below it during the foaming process, illustrating several of the consequences of a stable surface film. The surfaces have clearly come into contact and assumed a common shape, although the two regions of liquid aluminium have not merged and the entire interface remains clearly visible. The cell faces at the left are unusually wide, with a folded inner surface. The smooth surface of the surrounding cells offers evidence of limited rearrangement of cells to redistribute the excess film on the outer interface (§3.4.2), presumably constrained by restrictions on the relative slippage of films separated by a thin liquid layer. The presence of an oxide film causes the surface of the collapsed cell to fold, rather than retract, as the cell volume is reduced. The surfaces on the outside of the collapsed region remain smooth, as the continued evolution of gas keeps the film stretched. The excess melt as the surface of the cell retracted has not drained away or been redistributed, instead locally forming thicker regions.



Figure 6.39:

Optical micrograph of a collapsed cell face in a carbonate based foam, and sketch labelling several features present that illustrate the effect of continuous flexible surface films on foam stability.

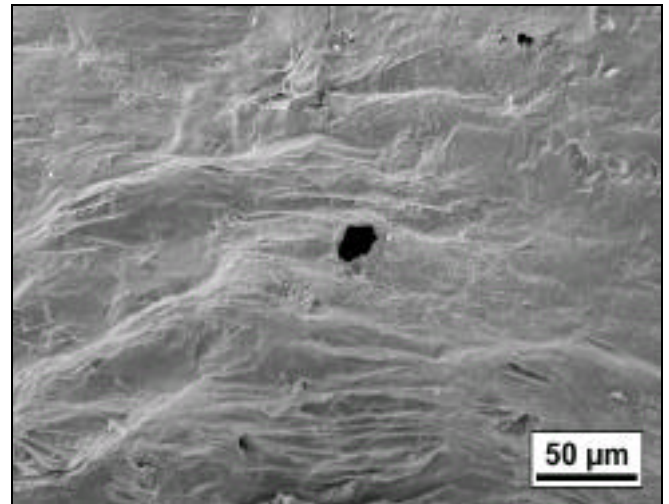


Effect of foaming gas on cell face rupture

A direct consequence of the enhanced surface stability of solidified carbonate-based foams is that the cell faces contain stable holes, as shown in Figure 6.40. In the absence of the stabilising oxide film, surface tension would favour retraction of the remaining face to form a new cell.

Figure 6.40:

SEM micrograph showing an apparently stable ruptured cell face in a carbonate-based foam with $T_{foam} = 650^{\circ}\text{C}$ and $t_{foam} = 600$ s.



In hydride-based foams, ruptured cell faces are only seen in isolation in specimens that have undergone complete collapse, where gas has escaped from the foam to produce a partly open cell structure.

Neutron radiography, providing a uniaxial density map of the entire foam (§5.7), was used to observe *in situ* fracture of cell faces in the hydride-based foams. Figure 6.41 shows sequential stages of cell face fracture over 2 seconds. A dark face between two cells is visible at 0.0 and 0.5 s. The image at 1.0 s the face is significantly thinner, and by 1.5 s the face has completely retracted, with a larger, spherical cell clearly visible.

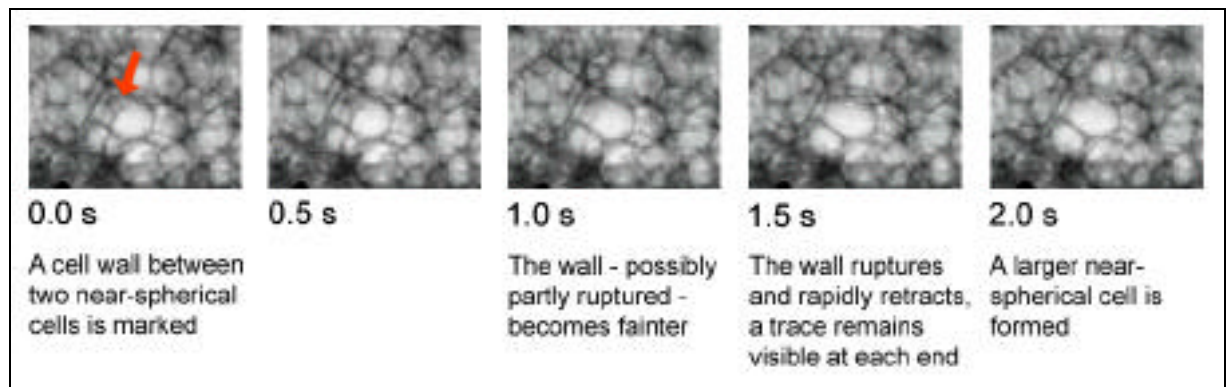


Figure 6.41: Rupture of a cell in a foam produced with 1.5 wt.% of TiH_2 in an Al/SiC_p melt, as observed by neutron radiography (© IFAM).

Together these effects account for the difference in cell size between the carbonate- and hydride-based foams discussed in section 6.2.1. Although cell faces in carbonate-based foams may rupture as a result of differing gas pressure, or continued cell face thinning due to expansion of the cell structure, there is no driving force for retraction of the face, and hence no significant coarsening of the cell structure. Cell faces may move locally (as visible in Figure 6.39), but the instability of the hydride-based cell structures is eliminated by the use of an oxidising gas.

The potential for this rupture and retraction of cell faces also explains the highly efficient tessellation of SiC_p on the surface of cells in hydride-based foams. Steric hindrance due to protrusion of particles already present on the surface into the melt (Figure 6.17) means that the degree of coverage observed (Figure 6.16) is unlikely to arise due to particles spontaneously approaching the free surface of an expanding cell.

If two spherical cells merge to form a new spherical cell with the same total volume, the total surface area will decrease by just over 20%, with the SiC_p remaining on the surface of the new cell as the ruptured cell face retracts. Repeated coalescence of cells will thus gradually increase the surface coverage, while the agitation during the rupture process may provide the angular SiC_p particles with the opportunity to align themselves most efficiently with the surface.

Effect of foaming gas on cell structure

In the absence of an oxidising gas, the cell structure of the hydride-based foams is controlled primarily by surface tension. Cell faces become thinner as surface tension draws liquid into the Plateau borders. Rupture is likely as the thickness of the cell face approaches that of the particles, leading almost immediately to complete retraction of the cell faces, with the remaining melt ejected into the already wide Plateau borders to drain towards the base of the foam. The cell structure of the carbonate-based foams is controlled by the efficiency of dispersion of the foaming agent, with clusters of particles of the foaming agent developing into cells (§6.3).

6.7.2 The effect of melt drainage in carbonate-based foams

Experimental observations

The marked drainage in the hydride-based foams compares with an almost negligible rate of drainage in the carbonate foams. The low rate of drainage is partly a result of the smaller cell size, and correspondingly higher effect of surface viscosity, in the carbonate-based foams. Cell coalescence in the hydride-based foams (Figure 6.41) is associated with rapid rejection of melt from cell faces to adjacent Plateau borders, which will widen them and force melt flow and redistribution. The stability of ruptured cell faces in carbonate-based foams means that the faces remain narrow, with a strong influence of surface viscosity and a complete absence of forced melt flow and redistribution.

As shown in Figure 6.42, a typical foam baked at 650°C for $t_{\text{foam}} = 900$ s exhibits no significant gradient in cell size or density. Figure 6.43 shows a comparable plot for a foam produced with $T_{\text{foam}} = 650^\circ\text{C}$ with an extended t_{foam} of 45 minutes. Although a more pronounced density gradient caused by drainage within the melt is visible, the change remains small and

there is still no solid base region. The average ρ^*/ρ_s is similar to that of the foam with $t_{foam} = 900$ s.

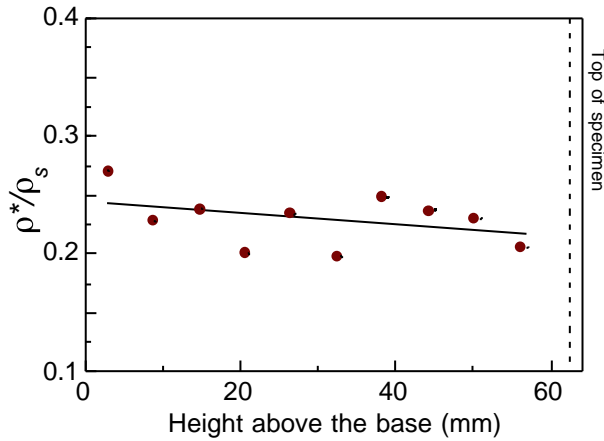


Figure 6.42:

Measured ρ^*/ρ_s as a function of height above the base of the sample, for a CaCO_3 -based foam baked formed of an Al-9Si-0.5Mg melt containing 10vol.% SiC_p with $T_{foam} = 650^\circ\text{C}$ and $t_{foam} = 900$ s (9 minutes).

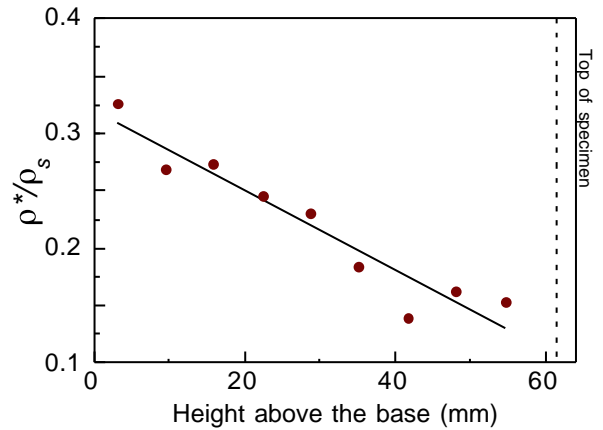


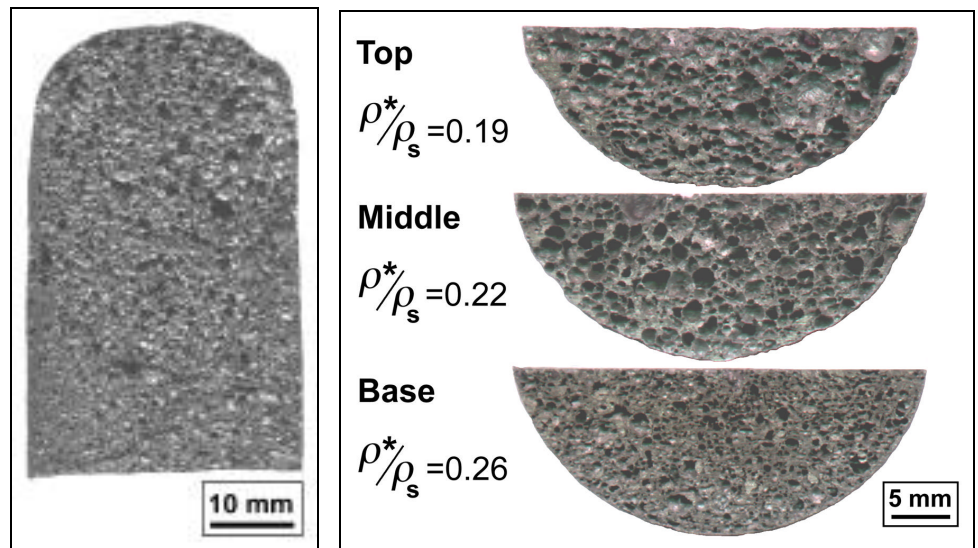
Figure 6.43:

Measured ρ^*/ρ_s of sections of a foam sample produced by foaming a precursor identical to that in Figure 6.42 with $T_{foam} = 650^\circ\text{C}$ and an extended $t_{foam} = 2700$ s (45 minutes).

Cross sections showing the cell structure of the foam in Figure 6.43 at various heights are shown in Figure 6.44. Although drainage of metal has occurred during the extended foaming time, the effect on the cell structure is relatively small. The cell size has increased by a factor of approximately 2, with a more marked increase in cell size at the top of the foam.

Figure 6.44:

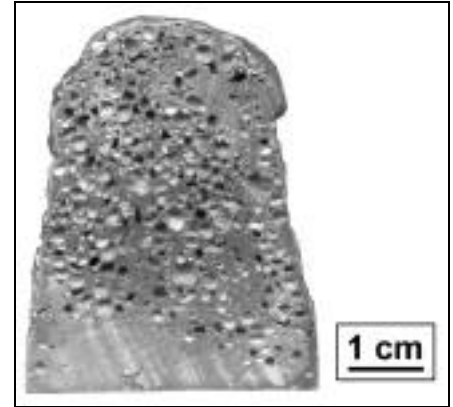
Vertical cross section of the foam sample in Figure 6.43, and horizontal cross-sections taken at various heights above the base of the foam.



The extreme case of a foam held at $T_{foam} = 650^\circ\text{C}$ for $t_{foam} = 9$ hours is shown in Figure 6.45. There is a region of solid material at the base of the foam, and a clear density gradient. This indicates that melt drainage is still occurring in the carbonate-based foams, but at a far slower rate. Inspection of the wide faces of the larger cells showed that they were formed by the superposition of several layers of collapsed cell faces. It is worth noting that, unlike in the case of the hydride-based foams shown in section 6.2, there is no evidence of overbaking or extensive escape of gas from the foam.

Figure 6.45:

Foam produced by foaming precursor identical to that in Figure 6.42 at $T_{foam} = 650^{\circ}\text{C}$ for $t_{foam} = 9$ hours.



Modelling of drainage

The drainage model of Gergely and Clyne, reviewed in section 3.4.9, was applied to investigate the effect of varying cell diameter on the rate of melt drainage. The input structures were designed to be representative of those of the carbonate- and hydride-based foams, with cell diameter of 1 mm and 2.5 mm respectively. All the other parameters were equal, and chosen to match those of the Al-Si foams. The initial gas fraction f_G was set to 0.79, corresponding to $\rho^*/\rho_s \sim 0.21$ in the solidified foam, a typical value for foaming of carbonate- and hydride-based foams at 650°C .

Profiles of f_G as a function of height above the base of the foam obtained with the two cell sizes are shown in Figure 6.46. As expected, both foams reach a point where the driving force for gravity drainage is balanced by that for upwards capillary flow of melt. This is reached at $t = 4400$ s in the fine-celled 'carbonate' foam, and $t = 7000$ s in the larger-cell 'hydride' foam, with no subsequent change in the density gradient (as shown by the line for $t = 14000$ s, which is represented by | symbols for each foam). In the 'carbonate' foam, this equilibrium corresponds to a point where the density gradient is slight, whereas the 'hydride' foam exhibits a pronounced density gradient at this point, with a solid region at the base.

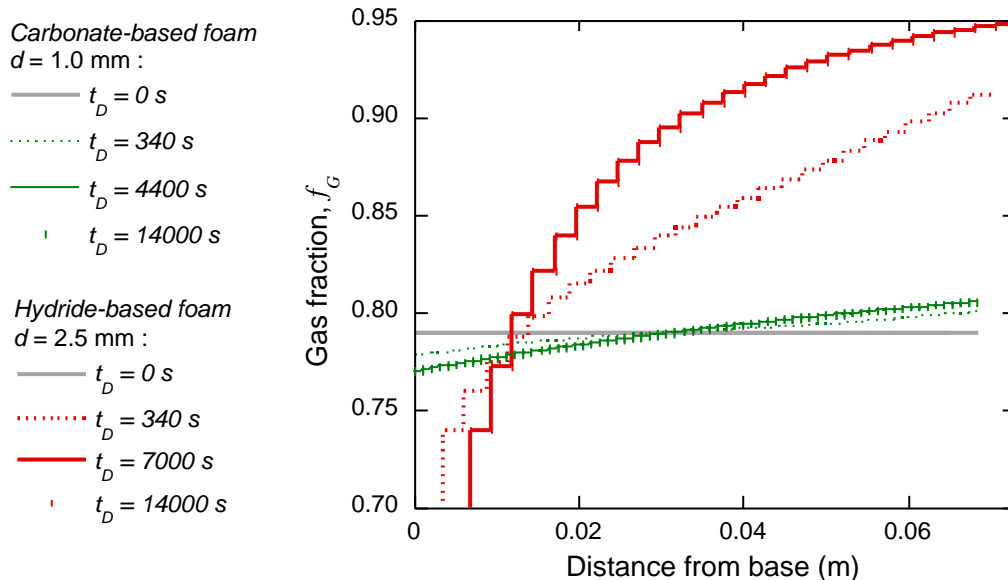


Figure 6.46: Predicted density gradient at various drainage times according to the model developed by Gergely and Clyne (§3.4.9), for cell diameters typical of those observed in typical carbonate-based foam ($d = 1$ mm) and hydride-based foam ($d = 2.5$ mm), with the following parameters in each case: $\gamma = 0.5$ N m⁻¹, $\rho = 2.74$ Mg m⁻³, $\mu = 0.4$ Pa s, $w_{CF,min} = 60$ μ m, and with an initial value of f_G of 0.79 at $t = 0$ s.

The agreement of these models with observations implies that the finer nature of the cell structure is sufficient in itself to significantly reduce the extent of drainage. There are several other factors, not incorporated into the model, which can have an effect. One of the most important is the dimensions of the stabilising solid phase relative to that of the channel, which could facilitate the formation of localised barriers to melt drainage. This is discussed further in the following section. Another is the possibly significant effect of the surface oxide film on the surface tension in carbonate-based foams (§6.7.1). The effect of sudden flows of melt into the Plateau borders as cell faces rupture (in the present model cell faces effectively stabilise at a minimum value of w) may also be significant. However it is clear that the retention of a fine-scale cell structure should in itself be sufficient to provide a degree of stability against melt drainage.

6.7.3 The effect of silicon carbide content

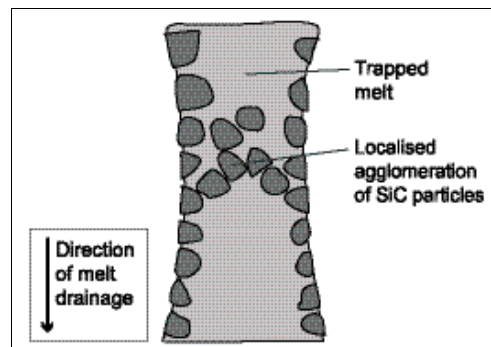
The 10 vol.% concentration of SiC_p in the melt is insufficient to form local networks in bulk melts (§3.4.3). SiC particles of diameter 10 μ m will reach a terminal velocity of ~ 3.5 mm min⁻¹ in pure aluminium at its melting point (§3.6.2). Complete settling of any SiC_p present in the fully dense regions at the base of hydride-based foams would thus be expected in the time the foam remains molten.

The situation within the cell structure is more difficult to predict. The 20-30 vol.% of SiC_p typically observed in hydride foams is probably sufficient to cause significant hindering of

particle settling. In addition, the highly tortuous network of narrow Plateau border channels in a liquid foam means networks of SiC may form at a far lower solid concentration than that required to form a network in a continuous melt, as illustrated in Figure 6.47.

Figure 6.47:

Schematic illustration of how the movement of SiC_p particles in narrow channels at low concentrations of particles will be inhibited by the formation of loosely agglomerated networks.



In the course of melt drainage, particles sometimes flow along near-horizontal channels, where they are likely to settle vertically and cause local blockages by coming into contact with the surface. The protrusion of the inner faces of the surfactant SiC particles may also favour local blockages by further narrowing the open channel width, as illustrated in Figure 6.48.

Figure 6.48:

The effect of solid particles acting as surfactants on the tortuosity of the flow path, and hence the rate of drainage.

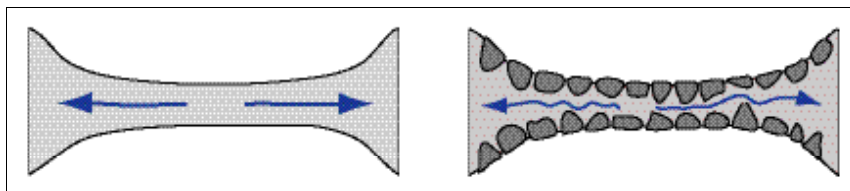


Figure 6.49 shows a cross section of a Plateau border in a hydride-based foam. Although movement of the solid particles could easily be prevented by the formation of a network (Figure 6.47), the large dimension of the cell faces relative to that of the SiC_p particles means that the flow of the liquid metal may be reduced, but is unlikely to completely prevented.

Figure 6.50 shows a vertical cross section of a Plateau border in a carbonate-based foam. Settling of particles is visible within the structure, leading to the blockage of the narrow Plateau borders. Since the cell faces are effectively rigid, and in the process of being pushed out by continued decomposition, a low volume fraction of SiC_p is sufficient to block the already narrow flow paths and further reduce the extent of melt drainage, in addition to the previously mentioned effect of the increased surface viscosity in the finer cell structure.

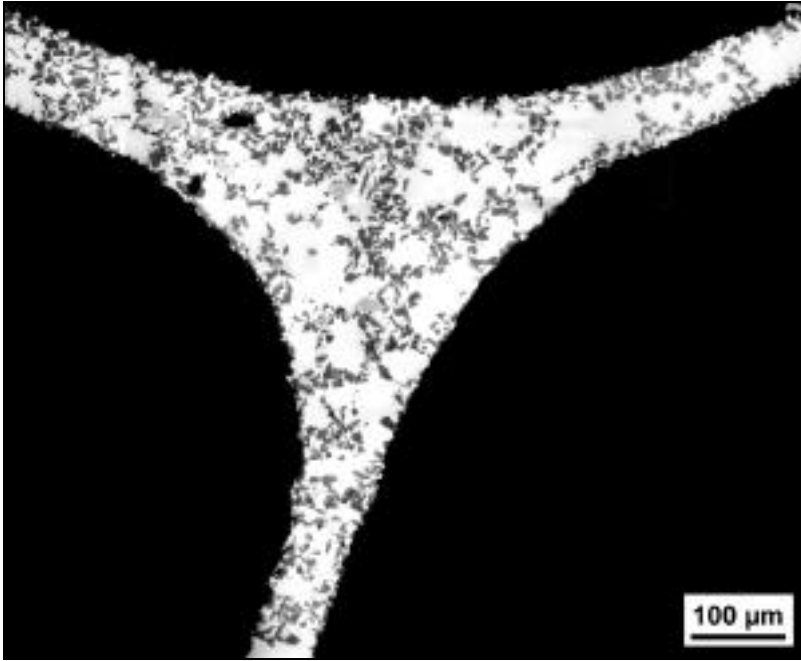


Figure 6.49: Cross section of a typical Plateau border in a hydride based foam with $T_{foam} = 630^{\circ}\text{C}$ and $t_{foam} = 120$ s, cooled in air.



Figure 6.50: Agglomeration of SiC to form a plug at the base of a Plateau border in a carbonate based foam with $T_{foam} = 650^{\circ}\text{C}$ and $t_{foam} = 900$ s, cooled in air.

The presence of a continuous surface film in the carbonate-based foams means the surfactant effects are independent of the particulate content. The effect of the SiC_p content on the melt viscosity can therefore be isolated from its effect on surface stability. This provides a new insight into the relative importance of the two possible effects of SiC on the stability of the foam.

Previous research[180, 181], where foams were produced under microgravity in order to isolate surfactant effects from drainage (and by extension melt viscosity) effects, was reviewed in section 3.4.6. It was demonstrated that non-metallic particles remain a prerequisite for foam stability under microgravity. The instability of foams with a lower particulate content was used to argue that the primary importance of the particles is as a surfactant, which prevents cell coalescence, and hence that the effect of the particles on the melt viscosity is of secondary importance.

In this work, the requirement for a surfactant is removed, in an experiment that complements those of section 3.4.6. The effect of varying the SiC_p content is shown in Figure 6.51. Foams with a reduced SiC_p content show evidence of extensive drainage, with a solid base region similar to that observed in hydride-based foams, and a highly irregular cell structure. It follows that the effect of particles on the surface tension is clearly insufficient to form a stable foam, with the conclusion that the effect of particles on melt viscosity is of equal

importance to the effect of particles on the stabilisation of surfaces in the stabilisation of liquid foams with non-oxidised surfaces. Of course, in carbonate-based foams, the role of the SiC_p is solely as a viscosity-enhancing phase.

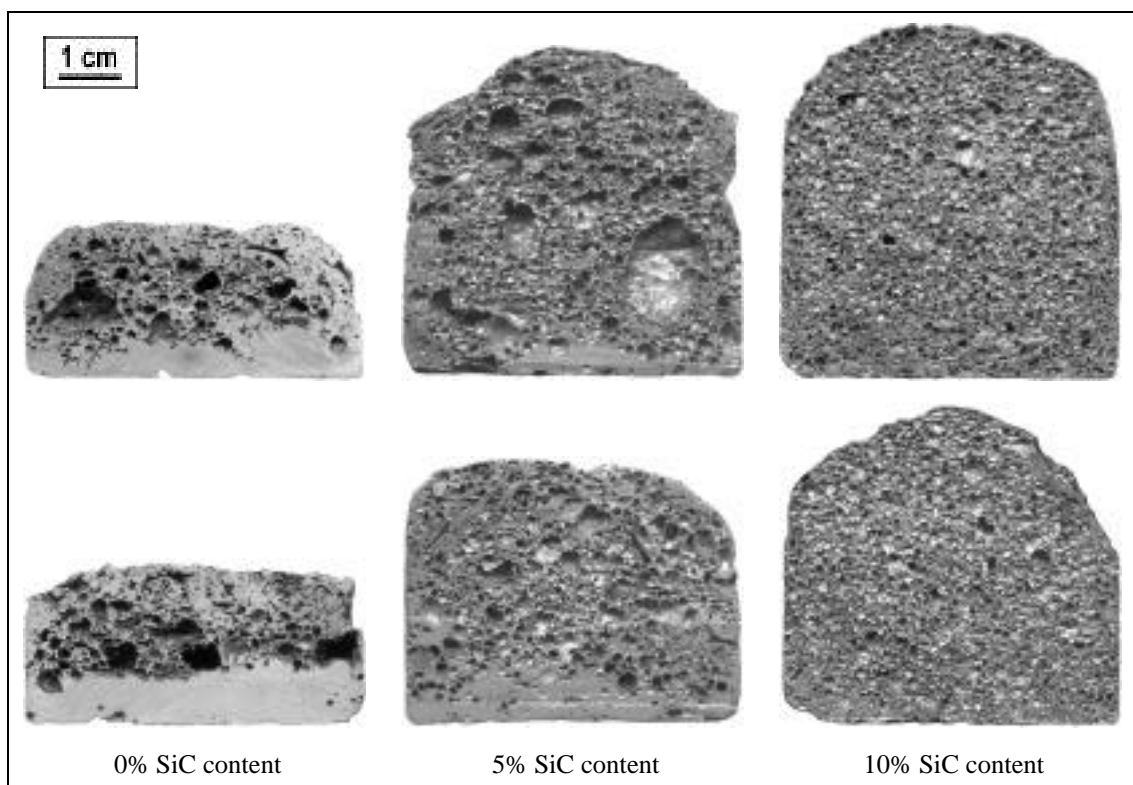
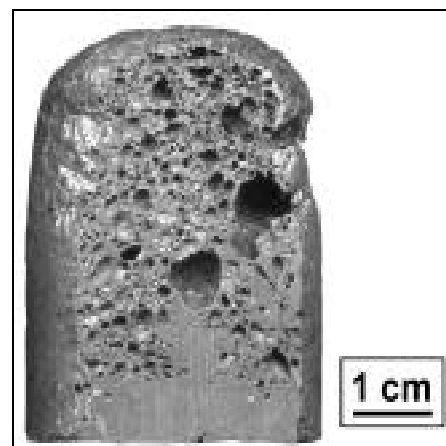


Figure 6.51: The effect of varying the SiC content on the stability of carbonate-based foams. The foams were formed by mixing LM6, 1050 and 6061 melts (§5.1) with the F3S10S alloy to ensure uniform composition while varying the SiC_p content, and dispersing 3.3 wt.% of powdered CaCO_3 to form a foamable precursor material. All the precursor materials were foamed with $T_{\text{foam}} = 650^\circ\text{C}$ and $t_{\text{foam}} = 900$ s.

Tailoring T_{foam} and t_{foam} can produce limited foaming of precursors containing no SiC_p . Figure 6.52 shows the highest porosity foam obtained with the SiC_p -free melt, which was obtained with $T_{\text{foam}} = 700^\circ\text{C}$ and $t_{\text{foam}} = 0$ s. The reduced t_{foam} means the foam does not completely collapse during the foaming time, although drainage is significant, with an irregular cell structure and a fully dense region at the base of the foam.

Figure 6.52:

Cross section of a foam produced by foaming a section of the 0% SiC content precursor in Figure 6.51 with $T_{\text{foam}} = 700^\circ\text{C}$ and $t_{\text{foam}} = 0$ s.

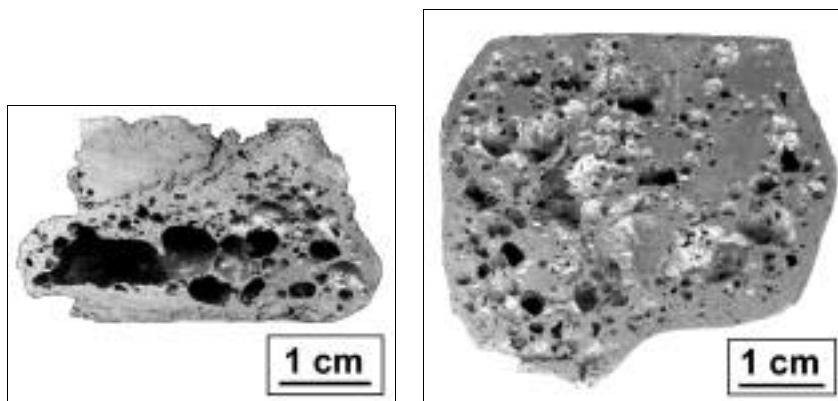


6.7.4 The effect of magnesium content

In view of the high surface activity of Mg (§6.5.2), experiments were carried out to assess whether the high chemical activity of Mg can favour the formation of a stabilising surface film. An Al-10Mg melt (LM10, §5.1) containing no SiC_p was foamed with 3.3 wt.% of CaCO_3 . Typical foams obtained are shown in Figure 6.53.

Figure 6.53:

Vertical and horizontal cross sections through typical foams produced by heating an Al-10Mg foamable precursor material containing 3.3 wt.% of dispersed CaCO_3 , with $T_{\text{foam}} = 650^\circ\text{C}$ and $t_{\text{foam}} = 900$ s.



The foam stability is similar to that of the Al-9Si-0.5Mg foams containing no SiC_p in Figure 6.51, with broadly comparable porosity and melt drainage. The surface of the cells again shows the formation of an apparently continuous oxide film with localised stretch marks, although with additional marked surface roughness on a scale of $\sim 40 \mu\text{m}$ visible, as shown in Figure 6.54.

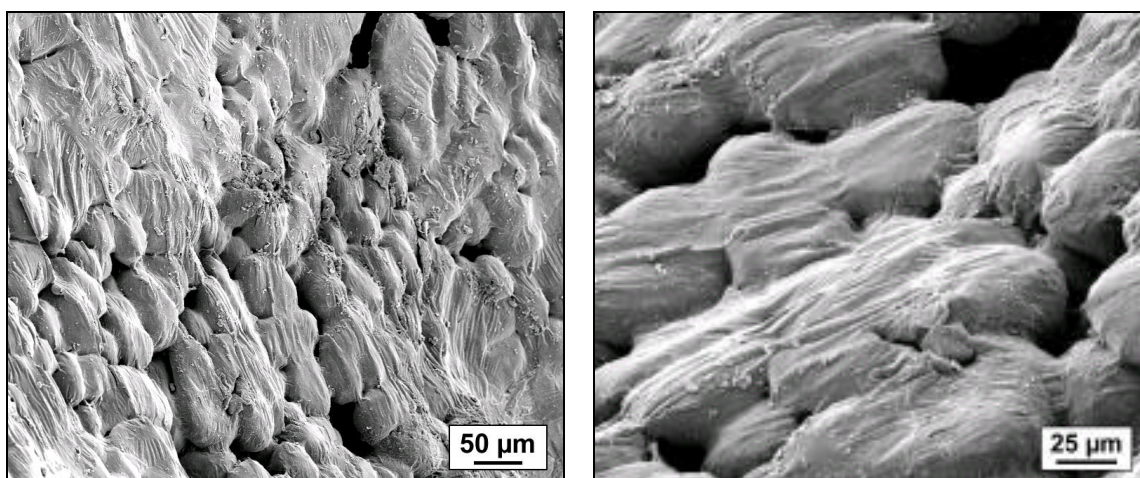
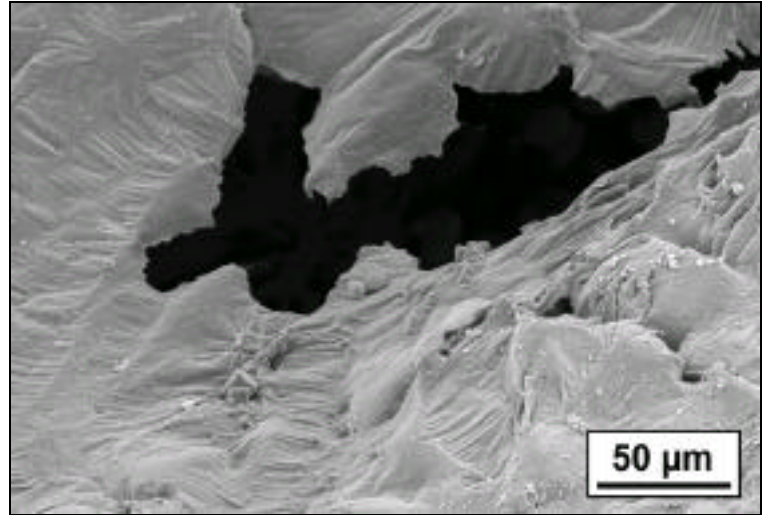


Figure 6.54: SEM micrographs of the surface of an Al-Mg foam, similar to that in Figure 6.53, at two magnifications.

There is a notable difference in cell connectivity, with holes frequently observed between adjacent cells, and hardly any cell faces intact. Tear bands (§6.5.1) are present, as shown in Figure 6.55. These were frequently found in the vicinity of fractured areas of the cell face, apparently compensating for the wide crack opening distance. Fracture is likely to arise when tear bands on both sides of the cell face are formed simultaneously. There is no evidence of significant retraction of the molten cell faces after rupture, with thin, rough fracture edges usually visible.

Figure 6.55:

SEM micrograph of a ruptured cell face in a foam produced with an Al-10Mg melt and a CaCO_3 foaming agent, with several tear bands visible on the adjacent surface.



In contrast to the Al-Si melt, the Al-Mg melt is of a non-eutectic composition. Apparently dendritic structures are visible on the cell surfaces, with an example shown in Figure 6.56. Microstructural analysis confirmed that the surface protrusions were solidification dendrites, often separated by deep shrinkage pores.

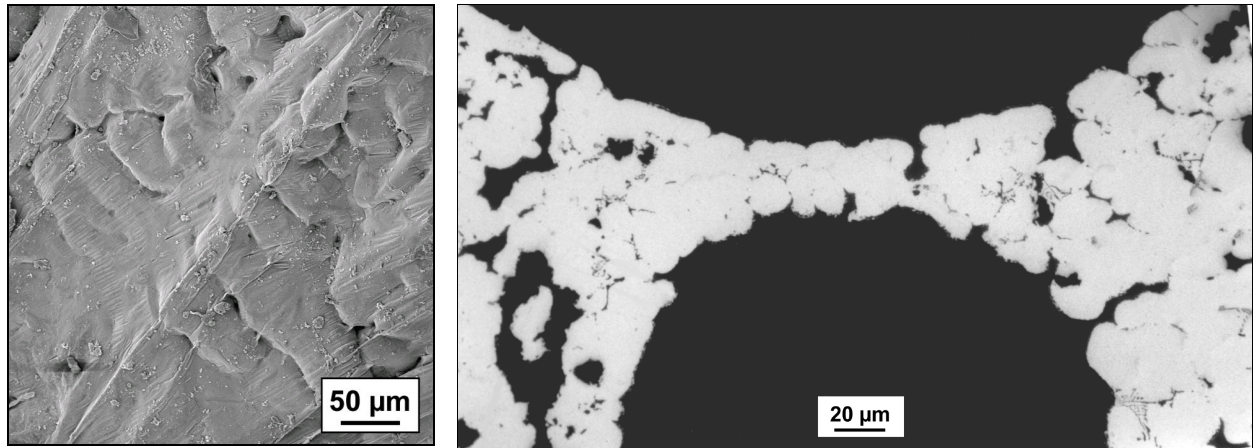


Figure 6.56: SEM micrograph of a cell face in an Al-10Mg foam cooled in air, and corresponding SEM micrograph of a cell face in cross section showing dendrites and deep shrinkage pores.

6.8 Extension to other methods of foaming

The stabilising effects described in this chapter were examined in the context of two other approaches to foaming: direct foaming of melts, and foaming of the foamable precursor by induction heating (§5.1).

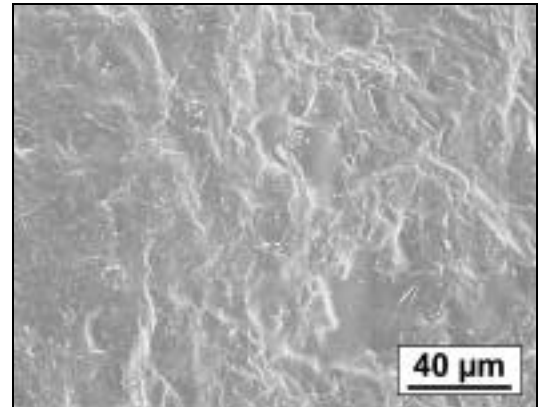
6.8.1 Direct foaming of the melt

Al-9Si-0.5Mg melts with varying SiC_p content were foamed with oxidising (CO_2) and neutral (N_2) gas. The extent of bubbling, and the stability of any foams produced, were compared. Neither gas was able to successfully foam melts containing no SiC_p. The reduced control of the foaming process means that effective foaming is more difficult, although the CO_2 produced limited foaming of melt containing 10 vol.% SiC_p, and extensive foaming of melt containing 20 vol.% SiC_p. The N_2 bubbled through the melt and did not cause any foaming.

Inspection of the cell surface of a foam produced with a melt containing 20 vol.% SiC_p, shown in Figure 6.57, revealed a clear oxide film, similar to that of Figure 6.25 (a), with no SiC_p visible, indicating that the stabilising effect of an oxide film is not particular to the foaming process studied. The absence of tear bands and stretch marks (§6.5.1) is presumably a consequence of the cells reaching their full size immediately as the gas is injected to the melt, rather than gradually expanding as the foaming agent undergoes progressive thermal decomposition.

Figure 6.57:

SEM micrograph of the surface of a cell in a foam produced by the direct injection of CO₂ to an Al-9Si-0.5Mg melt containing 20 vol.% SiC_p at $T_{foam} \sim 650^{\circ}\text{C}$.



6.8.2 Foaming by induction heating

Cross sections of foams produced by induction heating of blocks of various foamable precursor materials are shown in Figure 6.58. The more efficient heating meant that shorter foaming times were used, with T_{foam} typically 120 s. Despite the more rapid heating and cooling, the foams show similar structural features to those produced by the oven-based process. Local stirring of the Si and fluctuation of the melt caused by the induction heating does not appear to adversely affect foam stability or the stability of the oxide films. The carbonate foams still have a far finer cell structure, with reduced melt drainage (although a solid region is visible at the base), while hydride-based foams still show marked drainage early in the foaming process.

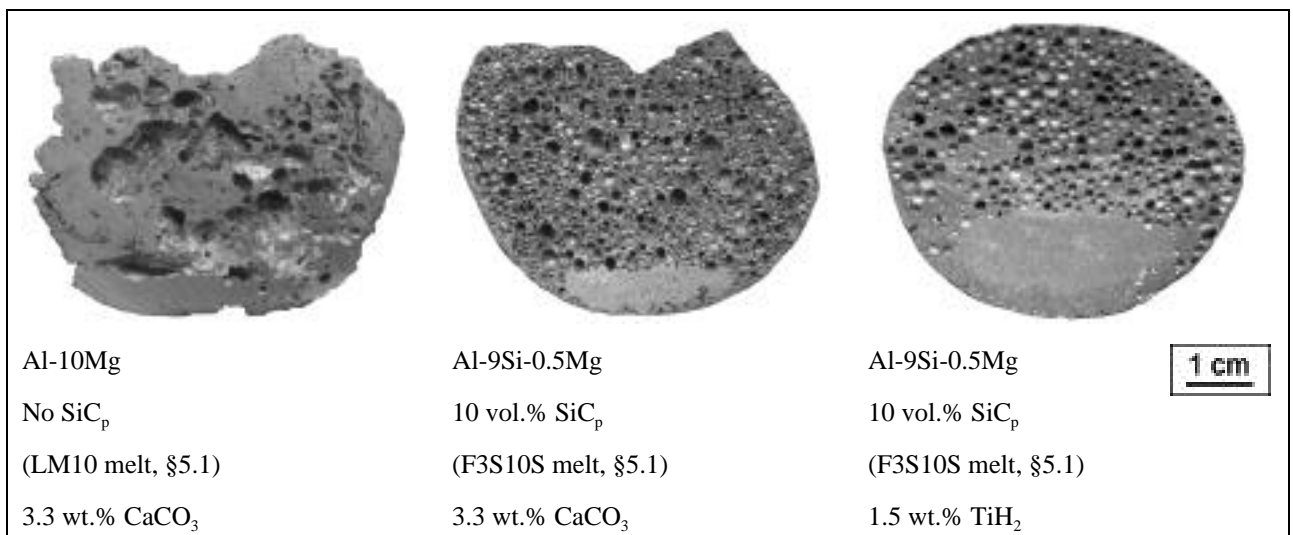


Figure 6.58: Foams produced by rapid induction heating of three foamable precursor materials to $T_{foam} = 650^{\circ}\text{C}$, followed by $t_{foam} \sim 120$ s and cooling in air.

Some processing differences were noted: the ability to heat the carbonate-based foams to elevated temperatures ($T_{foam} \sim 950^{\circ}\text{C}$) in a relatively short time enabled the formation of overbaked carbonate-based foams, with large cells and irregular cell structures, as shown in Figure 6.59. This is presumably the result of rapid gas evolution before the oxide film reaches a thickness sufficient to inhibit further decomposition of the foaming agent.

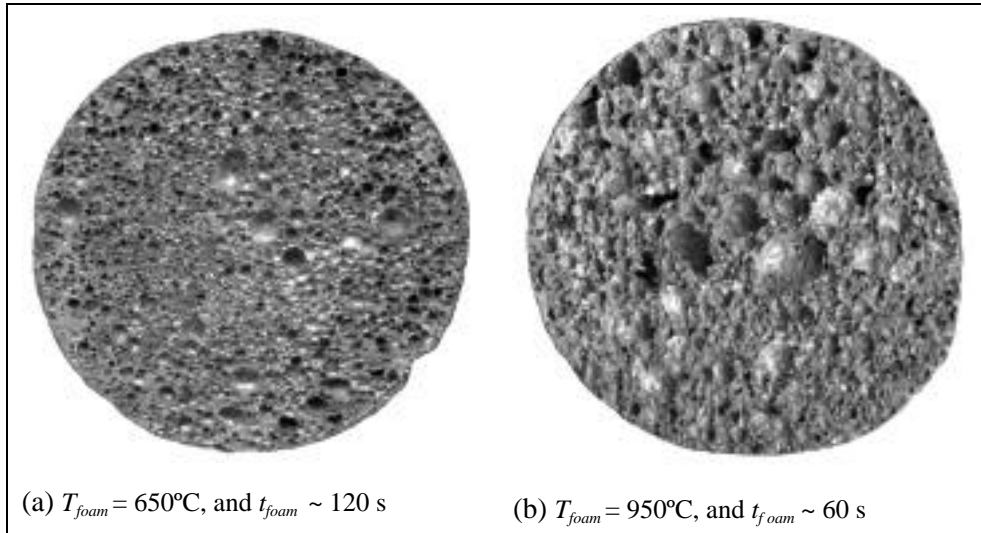


Figure 6.59: Cross section of foams produced by induction heating of an Al-9Si-0.5Mg foamable precursor containing 10 vol.% SiC_p and 3.3 wt.% CaCO₃ with varying T_{foam} and t_{foam} .

1 cm

6.9 Consistency with other work

The presence of an oxide film on the surface of melts has also been noted by Babscán *et al* [286] and Leitmeier *et al* [287], for the case of directly foamed melts containing dispersed refractory particles, in which the effect of foaming with air and nitrogen is compared. The results are entirely consistent with these observations, in that SiC particles are prevented from reaching the surface of the pores foamed with air, but act as surfactants in the nitrogen-foamed melt. Leitmeier *et al* measured the thickness of the oxide films formed by AES, obtaining a half-width of Al₂O₃ concentration of 30 nm when foaming by oxygen, 18 nm with air and 6 nm with nitrogen, and noted an increased stability of the air-blown foams against drainage.

The parallel work of Nakamura *et al* (§3.1.3), concerning foaming with chemically treated particles of CaCO₃, commented on a difference in cell size, although this was attributed to differences in the wettability of the foaming agent rather than a difference in the stability of the molten foams. The results of the current work suggest that the observed difference may be the result of surface oxidation.

7 Mechanisms and Characteristics of Foam Production with Calcium Carbonate

The decomposition of various grades of calcium carbonate is analysed by thermogravimetric analysis. The rate of decomposition is relatively slow, with purity and particle size found to have only a small effect. It is shown experimentally that thermal decomposition is strongly inhibited by an atmosphere of carbon dioxide. Thermodynamic aspects of the decomposition of calcium carbonate in aluminium-magnesium melts are examined. It is confirmed that thermal decomposition of the foaming agent is only thermodynamically favourable if accompanied by subsequent reaction of the foaming gas with the metal melt. Various surface reactions are considered, and the origin of the apparent upper bound of porosity is discussed. The thickness range of the solid film that can be produced is estimated, and the influence of cell size and oxide composition is predicted.

7.1 CaCO₃: Measured properties

7.1.1 Characterisation of the powders

In order to assess the effect of purity and particle size on the kinetics of foaming, CaCO₃ powders with particle size between 5 µm and 70 µm, and varying purity, were analysed. SEM micrographs of various powders are shown in Figure 7.1.

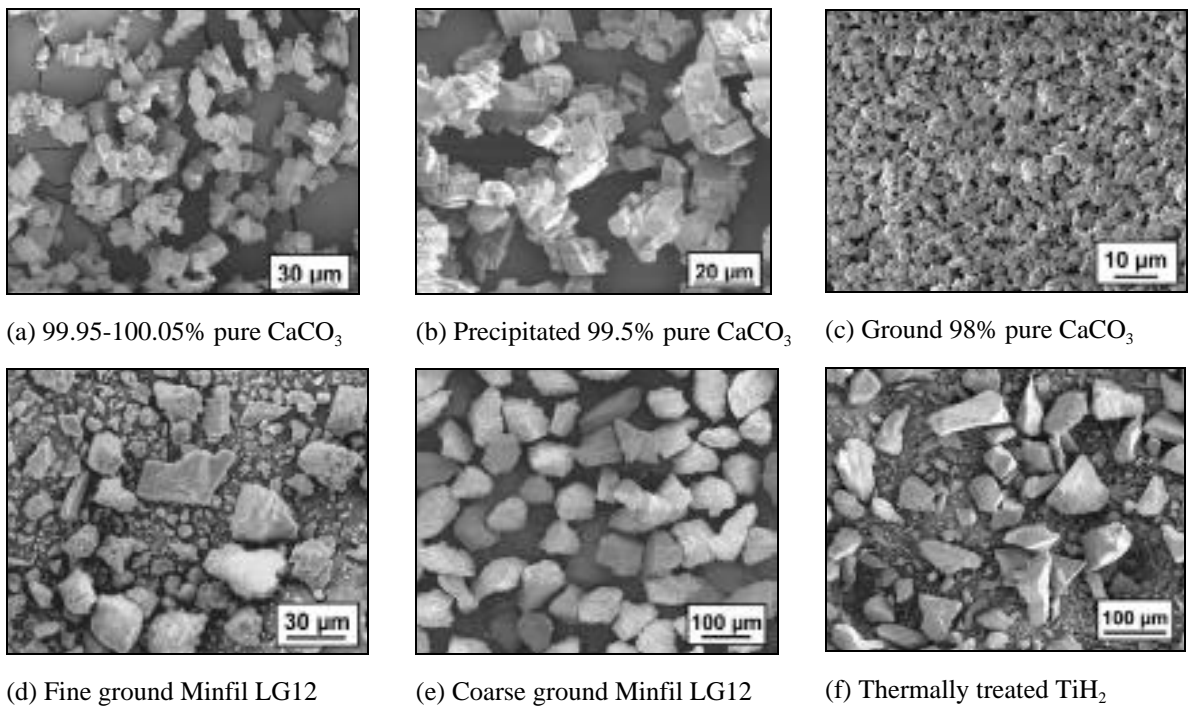


Figure 7.1: SEM micrographs of various powdered calcium carbonate foaming agents used, and the titanium hydride used in the FORMGRIP process.

The measured distribution of powder size (§5.2.1) for three of the powders is shown in Figure 7.2.

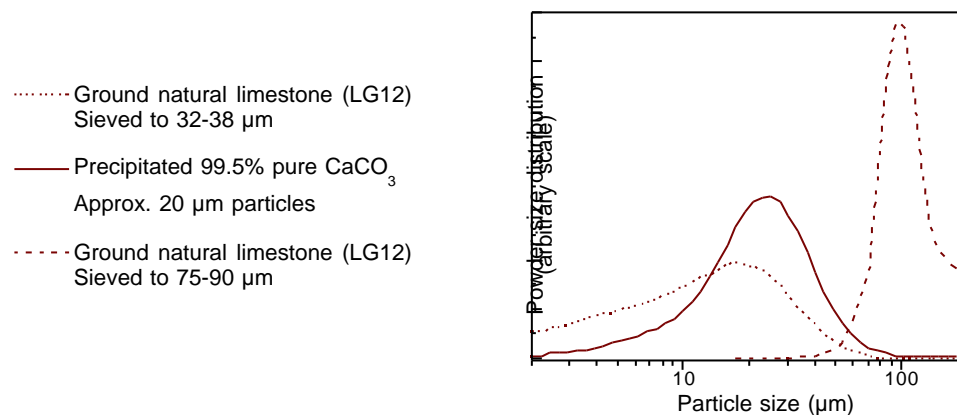


Figure 7.2: Measured size distribution of three of the CaCO_3 powders in Figure 7.1.

X-ray powder diffraction patterns obtained for the powders in Figure 7.1 are shown in Figure 7.3. All the powders are composed of calcite, as expected (§3.1.4). Trace amounts of various crystalline impurities were detected in the lower purity CaCO_3 powders, and traces of SiO_2 (low quartz) were present in the limestone samples. The natural limestone specimens had a slightly brownish colour, possibly due to the presence of inorganic impurities. These observations are consistent with the reported impurity levels in section 5.1.

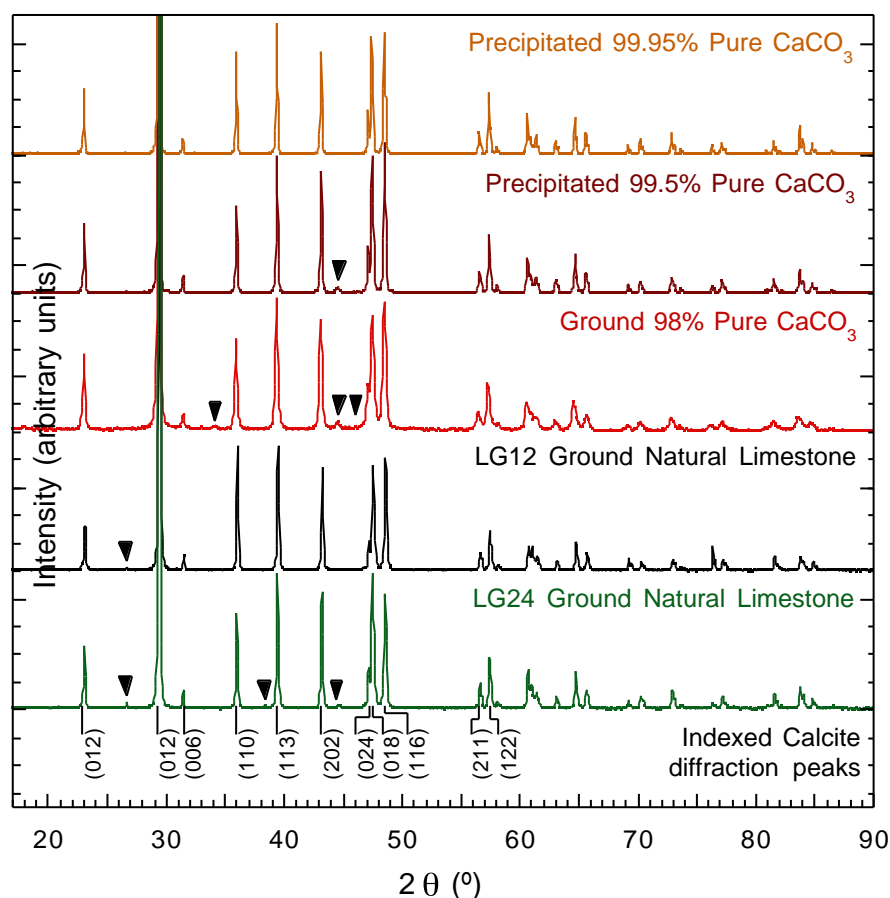
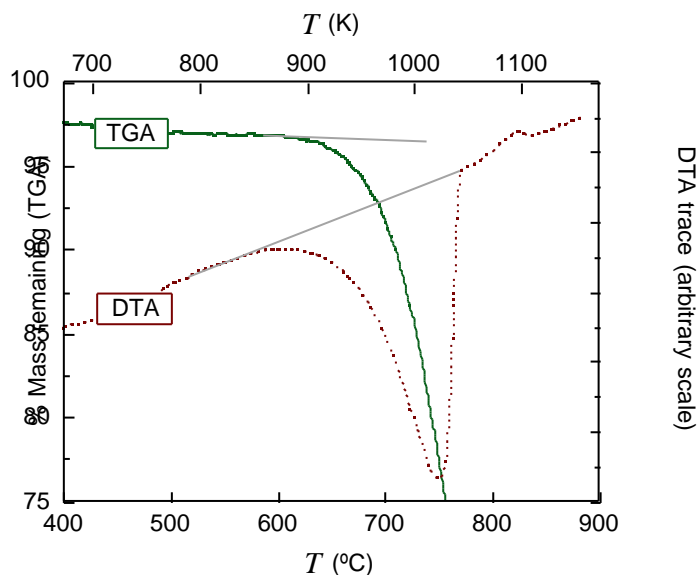


Figure 7.3: X-ray diffraction patterns for the grades of CaCO_3 and natural limestone investigated. Corresponding SEM micrographs of some of the powders are shown in Figure 7.1. The symbol ▼ denotes peaks caused by the presence of impurities; all other peaks were identified as calcite. All the patterns are produced with CuK_α radiation.

Figure 7.4 compares the decomposition of the precipitated 99.5% pure CaCO_3 , as measured by differential thermal analysis (DTA) and thermogravimetric analysis (TGA). Since the decomposition reaction is endothermic and involves a mass loss of 40%, both techniques provide an effective measure of reaction kinetics. TGA was used in preference to DTA, since the lower limit of measured mass provides additional confirmation of the purity of the material.

Figure 7.4:

TGA and DTA traces for the thermal decomposition of precipitated 99.5% purity CaCO_3 , with particle size distribution shown in Figure 7.4 and a heating rate of $20^\circ\text{C min}^{-1}$.



7.1.2 The effect of purity and particle size

The decomposition kinetics of various sizes of CaCO_3 powder were initially analysed by heating samples at a constant rate. The particle diameters studied ranged from $\sim 4 \mu\text{m}$ to $\sim 70 \mu\text{m}$, corresponding to a variation of over an order of magnitude in surface-area-to-volume ratio. As shown in Figure 7.5, the effect of this range of particle size on the kinetics of decomposition is slight, whereas more rapid heating postpones the onset of thermal decomposition to higher temperatures quite significantly.

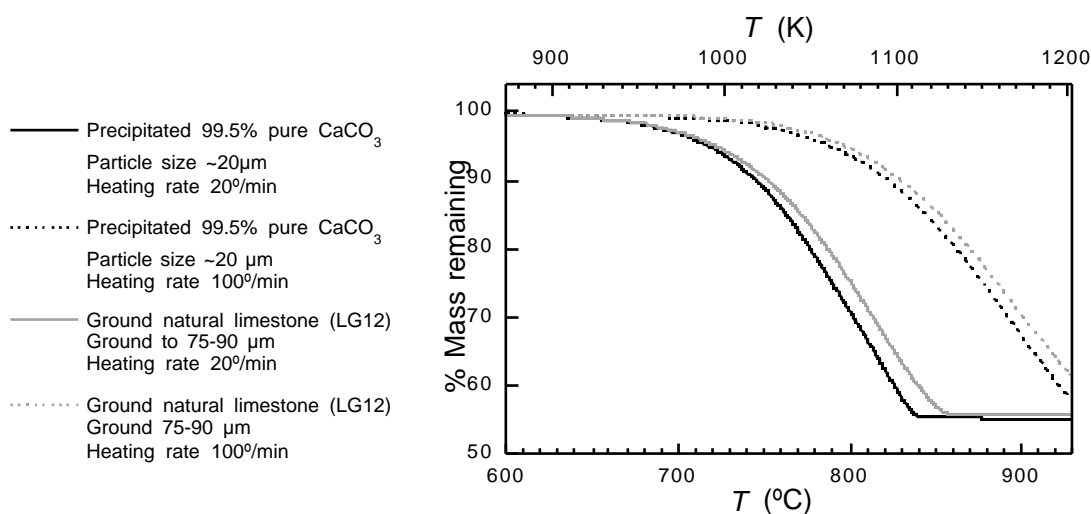


Figure 7.5: TGA data for the direct heating of two sizes of powdered CaCO_3 at two heating rates. The sample size was 16 mg in each case, with measurement made in a nitrogen atmosphere with a flow rate of $20 \text{ cm}^3 \text{ min}^{-1}$.

In order to separate the effect on decomposition temperature of the heating rate from those of particle size and purity, samples were rapidly heated to 650°C or 750°C, followed by an isothermal hold, during which the change in mass was monitored. All samples were subsequently heated to 800°C, where decomposition went to completion. TGA results for thermal decomposition at 650°C and 750°C shown in Figure 7.6. The TGA curves for the ground natural limestone are vertically shifted by 1.5% in order to compensate for a small drop in mass at 500°C, which was apparently caused by an impurity.

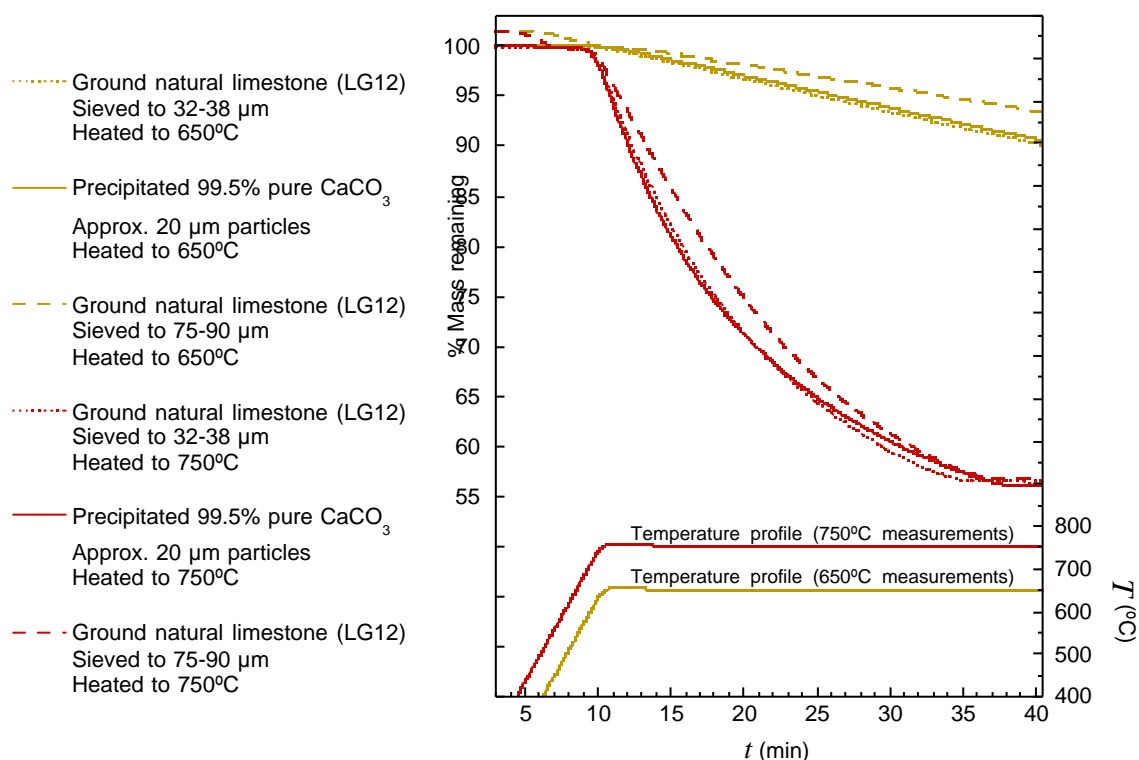
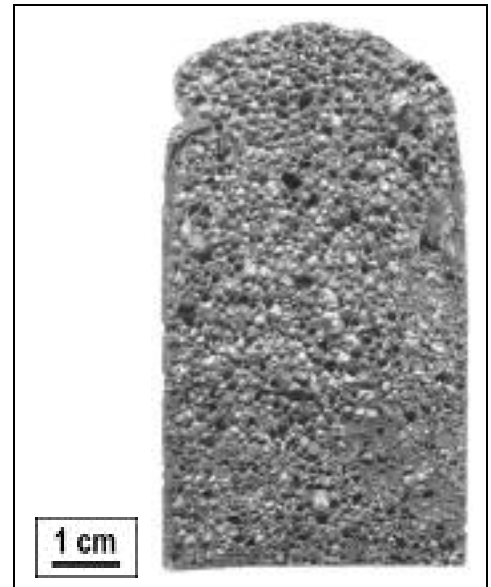


Figure 7.6: TGA data for the thermal decomposition of three grades of powdered CaCO_3 . The sample size was 16 mg, and the gas flow rate of N_2 of $20 \text{ cm}^3 \text{ min}^{-1}$ was maintained throughout the experiment.

It can be seen in Figure 7.6 that all the powders studied had a similar rate of thermal decomposition. The 75-90 μm powder underwent slightly slower thermal decomposition, although the difference was small. Comparison of powders of varying purity and similar particle size showed no discernible difference in decomposition rate. A small reduction in mass of $\sim 1.5\%$ at $\sim 500^\circ\text{C}$ was always observed in the natural limestone samples, which is thought to be the result of the decomposition of an impurity phase. These results, together with the observation that particles had very little effect on the cell structure of the foams produced – as shown by the similarity of the foam shown in section 6.1 to that in Figure 7.7, produced with a far coarser limestone powder – imply that the effect of powder size and purity is small. It follows that the optimum particle size should be selected using other criteria, such as ease of dispersion.

Figure 7.7:

A foam produced with Minfil LG12 natural limestone powder (§5.1), ground and sieved to a coarse 75-90 μm powder size (with a size distribution shown in Figure 7.2).



The rate of thermal decomposition is relatively low, with the fraction of the chemical which has decomposed, f_{dec} , of $\sim 25\%$ after 30 minutes at 650°C . At 750°C decomposition is rapid, although still not complete after 15 minutes. The slow reaction rates is consistent with the experimental findings that control over the foaming process is easier with CaCO_3 as the foaming agent than is the case with TiH_2 (§6.1).

The production of a foam with $\rho^*/\rho_s = 0.20$ at $T_{foam} = 650^\circ\text{C}$ with $t_{foam} = 15$ minutes (900 s) implies f_{dec} of $\sim 7\%$ inside the cells. This compares with an observed f_{dec} of $\sim 12\%$ at the same T_{foam} and t_{foam} , in an atmosphere of flowing nitrogen. The reaction reaches a limit within this time, which is consistent with the observation that ρ^*/ρ_s does not change significantly after $t_{foam} = 10$ minutes. At 750°C , the effect of the limiting of the reaction is more apparent, since f_{dec} of $\sim 80\%$ is observed after 15 minutes (900 s) in flowing nitrogen, compared with f_{dec} of $\sim 15\%$ in the foam.

The recent results of Nakamura *et al*, reviewed in section 3.1.4, suggest that extended surface treatment of CaCO_3 is required for effective foaming, which is reported to aid wettability. The CaCO_3 used by Nakamura *et al* is quoted as having $7.5 \mu\text{m}$ particle size[126]. In the present work a $\sim 5 \mu\text{m}$ powder of 98% pure CaCO_3 was found to be too fine to be readily dispersed in the aluminium melt, while all the coarser powders were found to produce adequate foaming of the melt in the as-received state. In view of the low rate of thermal decomposition of CaCO_3 , and the reduced cell coalescence when using an oxidising foaming gas noted in section 6.7.1, there is no requirement to use such finely powdered foaming agents. The surface treatment applied by Nakamura *et al* is thus demonstrably unnecessary.

7.1.3 Inhibition of thermal decomposition by carbon dioxide

TGA experiments were also carried out in an atmosphere of carbon dioxide. These demonstrated clear inhibition of decomposition for all the powders studied. The initial decomposition rate was similar to that in nitrogen, although decomposition stopped completely once the weight had decreased by ~ 1.5 wt.%. Figure 7.8 compares decomposition of the 99.5% pure precipitated CaCO_3 in carbon dioxide with that in nitrogen (Figure 7.6). Even at 800°C , none of the CaCO_3 powders underwent a weight loss of over 2 wt.%. It is thought that the initial drop is the result of residual nitrogen and oxygen trapped between particles in the powder sample, permitting a degree of thermal decomposition.

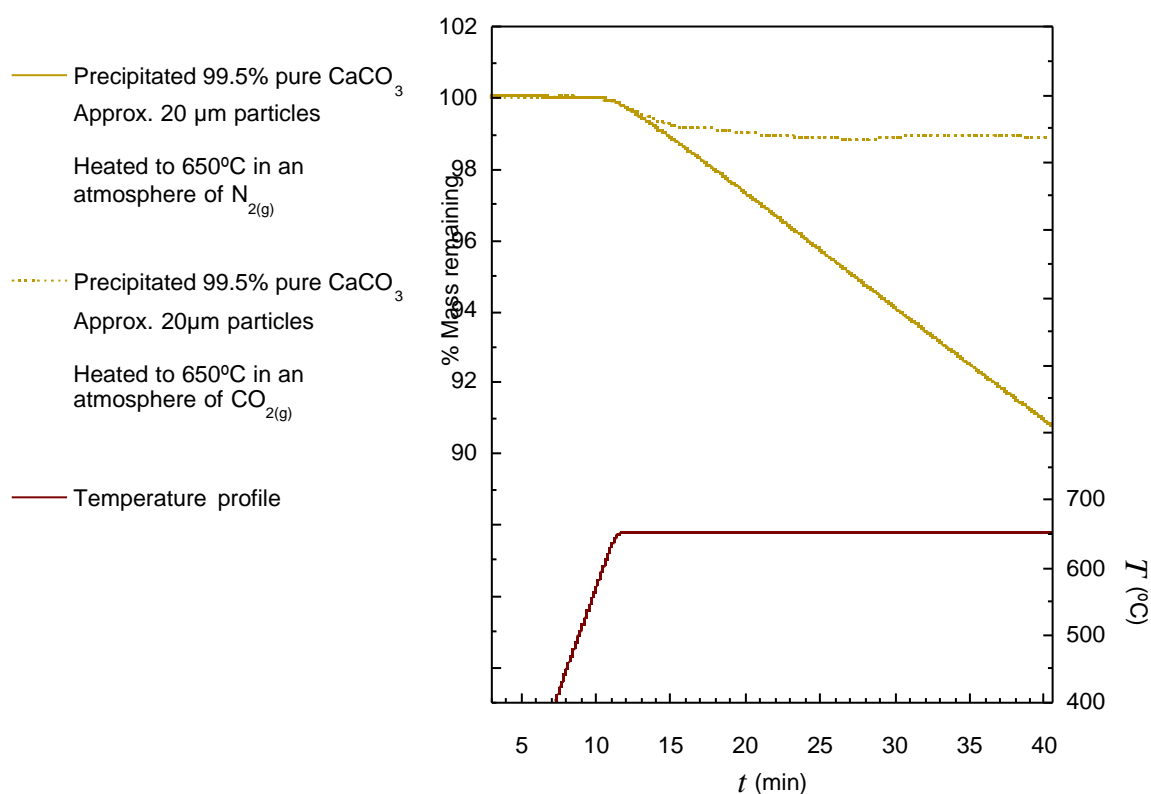


Figure 7.8: TGA curves for the thermal decomposition of powdered CaCO_3 in N_2 , and in commercial purity CO_2 . Sample size was 16 mg, and a gas flow rate of $20 \text{ cm}^3 \text{ min}^{-1}$ was maintained throughout the experiment.

The small fluctuations in the CO_2 atmosphere curve, which were observed in all measurements, are presumably the result of slight variations in the CO_2 flow rate. In the measurements in an inert atmosphere shown in Figure 7.6, decomposition is limited by the kinetics of decomposition. As the N_2 gas flow serving only to remove the reaction product, variations in the flow rate would not be expected to significantly affect the reaction. In contrast the CO_2 is an active reactant and the limiting factor on decomposition, so slight fluctuations in $p\text{CO}_2$ can directly affect the decomposition.

A similar degree of inhibition was observed when samples of the powders were heated in an air furnace for 60 minutes. X-ray diffraction patterns for the 98% pure ground CaCO_3

powder, before and after thermal treatment, are shown in Figure 7.9. There is little evidence of thermal decomposition ($f_{dec} \sim 0.02$). This further demonstrates the strongly inhibiting effect of the carbon dioxide atmosphere, presumably generated in the furnace on thermal decomposition, and the requirement for some mechanism of $p\text{CO}_2$ reduction if foaming of a metal is to be effective.

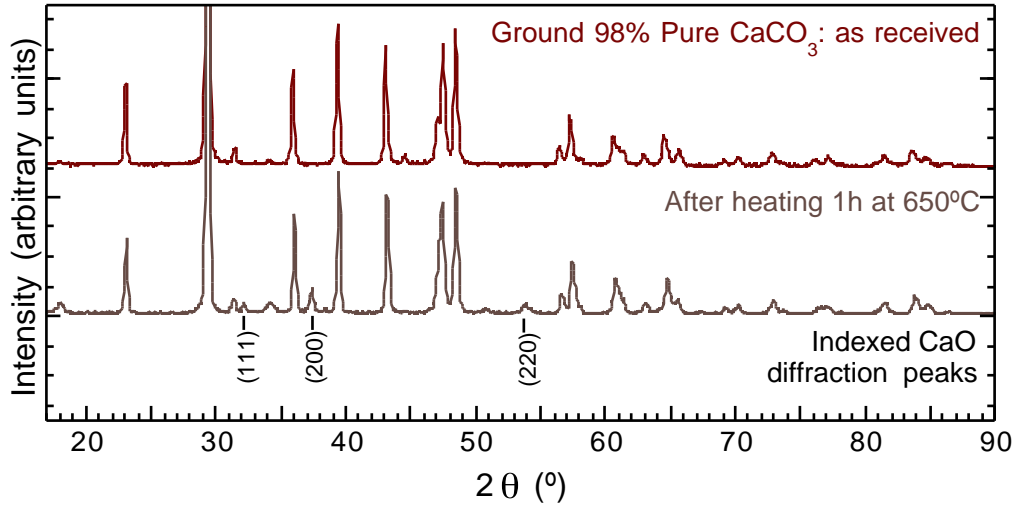


Figure 7.9: X-ray diffraction patterns produced with $\text{CuK}_{\alpha 1}$ radiation showing the effect of heating a sample of 98% pure CaCO_3 in a closed air furnace at 650°C . The labelled peaks are CaO ; all others are CaCO_3 (as indexed in Figure 7.2). Both traces are normalised by the height of the second major Al peak.

7.2 Gas requirements for foaming

An upper bound limit for the gas fraction which can be obtained in a foam, $f_{G,max}$, can be obtained by calculating the volume of gas evolved when the foaming agent undergoes complete thermal decomposition. For the heating of a foamable precursor material of volume V_S containing a volume fraction of CaCO_3 f_{CaCO_3} , complete thermal decomposition at temperature T and pressure P will produce the volume of gas V_G :

$$V_G = V_S \frac{f_{\text{CaCO}_3} \rho_{\text{CaCO}_3}}{M_{\text{CaCO}_3}} \frac{R T}{P} \quad [7.1]$$

The gas fraction is given by:

$$f_{G,max} = \frac{V_G}{V_G + V_S} \quad [7.2]$$

Substituting [7.1] into [7.2] for V_G , rearranging, and eliminating V_S , gives:

$$f_{G,max} = \frac{1}{\frac{M_{\text{CaCO}_3} P}{f_{\text{CaCO}_3} \rho_{\text{CaCO}_3} R T} + 1} \quad [7.3]$$

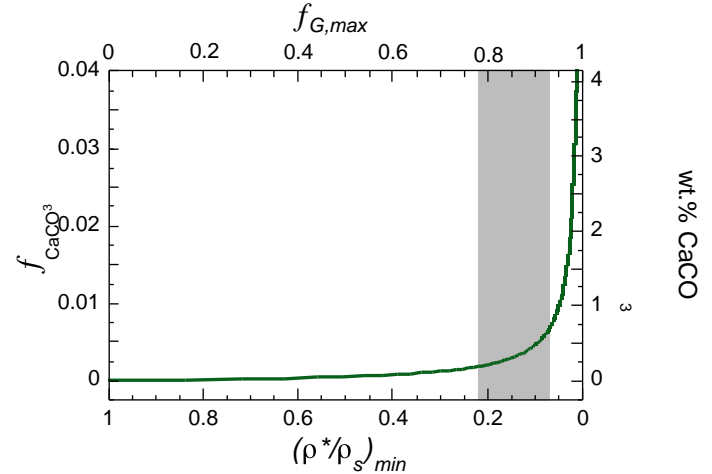
Assuming that the volume of gas produced is not reduced by further reaction, dissolution within the metal, or escape from the foam, $f_{G,max}$ at the metal melting point T_m is directly related to ρ^*/ρ_s :

$$1 - \frac{\rho^*}{\rho_s} \Big|_{\min} = f_{G,\max} \quad (T = T_m) \quad [7.4]$$

Figure 7.10 shows the volume fraction of CaCO_3 thus required to generate a given level of ρ^*/ρ_s in the Al melt, assuming complete decomposition. It is predicted that 0.5 wt.% of added CaCO_3 is sufficient to produce a foam with $\rho^*/\rho_s < 0.1$.

Figure 7.10:

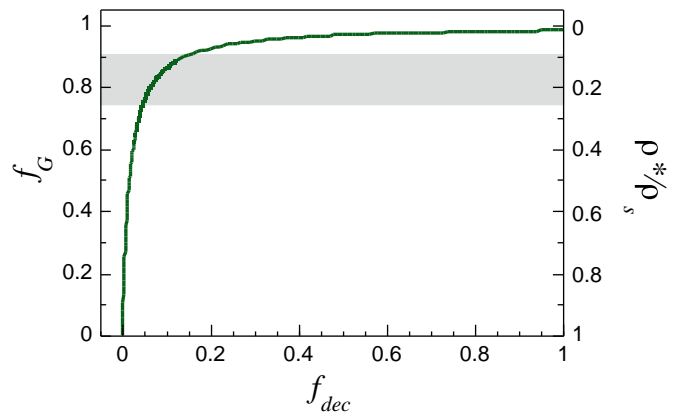
The volume fraction of foaming agent, f_{CaCO_3} , required in the melt to generate a given level of ρ^*/ρ_s in an aluminium foam. Full decomposition is assumed at $T_m = 853 \text{ K}$ (580°C). The shaded region represents ρ^*/ρ_s of typical aluminium foams.



The volume fraction of foaming agent which is needed in order to produce a foamable precursor, f_{CaCO_3} , was determined experimentally. This level was found to be approximately 3.3 wt.% of CaCO_3 ($f_{\text{CaCO}_3} = 0.032$). Figure 7.11 shows the maximum porosity expected with this level of addition, as a function of the fraction of the added powder that undergoes thermal decomposition, f_{dec} .

Figure 7.11:

Estimated ρ^*/ρ_s of an aluminium foam for a foamable precursor containing 3.3 wt.% of CaCO_3 ($f_{\text{CaCO}_3} = 0.032$), as a function of f_{dec} . The shaded region represents ρ^*/ρ_s of typical aluminium foams.



This illustrates a key difference between the foaming of hydride- and carbonate-based foams. When foaming with TiH_2 , 1.5 wt.% of the foaming agent is added. This is in excess of that required for foaming, with corresponding $(\rho^*/\rho_s)_{\min}$ of ~ 0.02 . If heated for extended times ρ^*/ρ_s was observed to approach this minimum, although the thin cell faces became unstable before it was reached, with gas escaping from the foam.

As mentioned in section 6.2, the expansion of carbonate-based foams was observed to reach a limit corresponding to $f_{\text{dec}} < 0.2$. Although openings between cells were observed

(§6.7.1), cells on the outer surface – which is covered with a thick oxide layer formed during heating and melting of the foamable precursor – were always closed.

7.3 Thermodynamics of foaming with calcium carbonate

7.3.1 Inhibition of thermal decomposition

As discussed in section 3.1.3, the thermal decomposition of TiH_2 (§3.1.2), associated with the experimentally observed formation of TiAl_3 intermetallic (§6.3), is thermodynamically favourable at 650°C even in an atmosphere of pure hydrogen. In contrast the direct decomposition of CaCO_3 in to an atmosphere of pure CO_2 is unfavourable, with $\Delta G > 0$ for $T < 900^\circ\text{C}$:



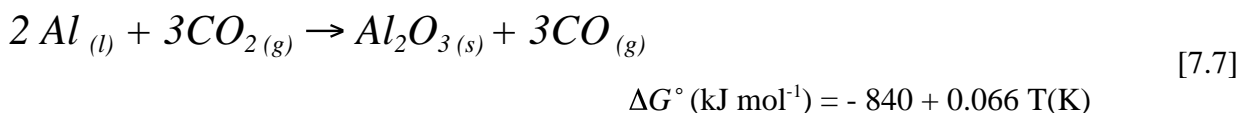
The equilibrium maximum partial pressure of CO_2 under which thermal decomposition of CaCO_3 will continue is given by:

$$\log p\text{CO}_2(\text{atm}) = -\frac{8410}{T} + 7.156 \quad [7.6]$$

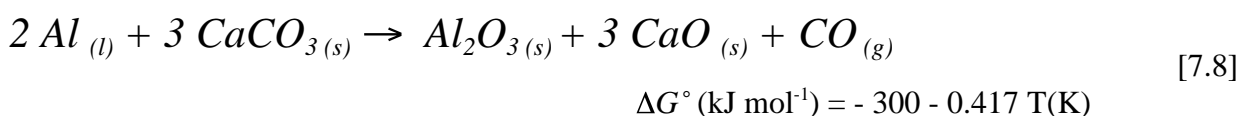
Values of $p\text{CO}_2$ were plotted in section 3.1.4. Continued thermal decomposition is only possible if the production of CO_2 is accompanied by reaction with the metal on the cell surface to reduce its partial pressure inside the cells, $p\text{CO}_{2(g)}$. A partial pressure of CO_2 of under 10^{-2} atm is thus required for thermal decomposition at $T_{\text{foam}} = 650^\circ\text{C}$ to be thermodynamically favourable.

7.3.2 Reactions of the foaming gas

Several such reactions are possible. The $\text{CO}_{2(g)}$ can be reduced by $\text{Al}_{(l)}$ to $\text{CO}_{(g)}$ at the cell surface, forming a film of $\text{Al}_2\text{O}_{3(s)}$. This is thermodynamically favourable at this temperature, with G° of -779 kJ mol^{-1} at 650°C .



[7.5] and [7.7] could be considered in terms of a single-step reaction between CaCO_3 and Al:



The free energy of these reactions is plotted as a function of temperature in Figure 7.12[102, 288].

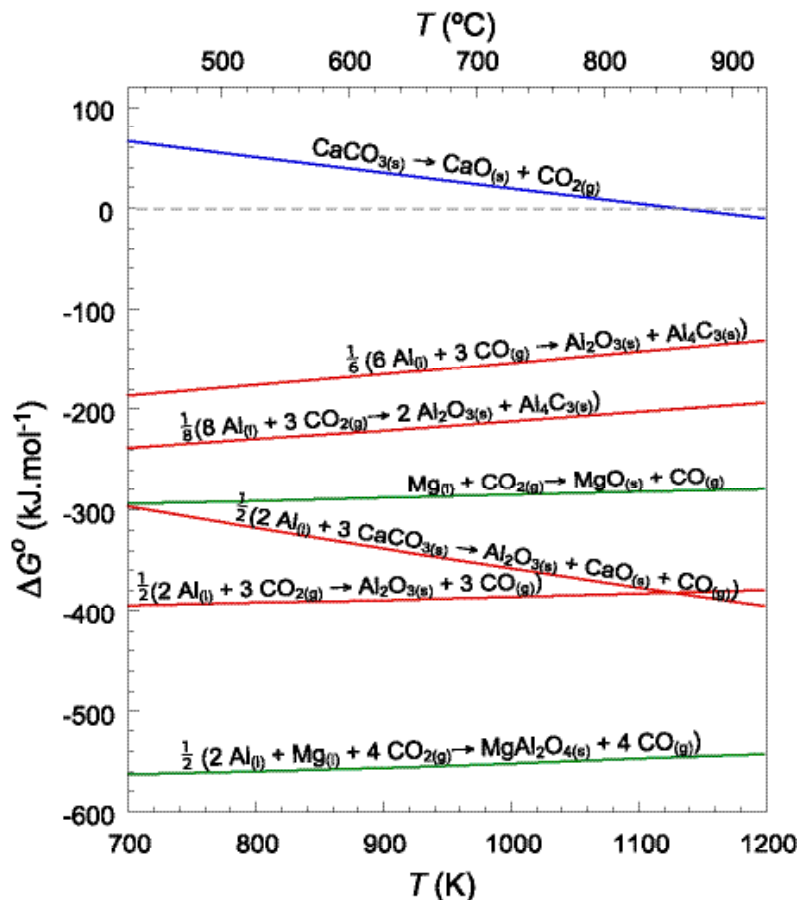


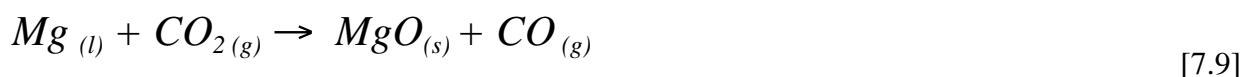
Figure 7.12:

Free energy change, ΔG° , as a function of T for several possible reactions in the molten foams (compiled with data in [102, 288]).

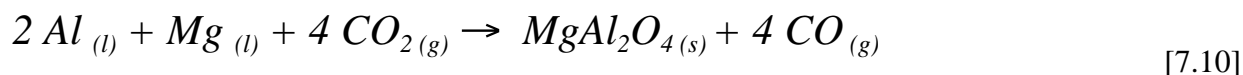
ΔG° is normalised for one mole of Mg or Al, and all elements are assumed to be in their standard state.

The single step reaction [7.8] is unlikely to be significant in practice, since it can only take place at the small region of solid-liquid contact, in contrast to reaction [7.7], which can take place over the entire surface area of the cell. This is confirmed by optical and SEM micrographs of cell surfaces (§6.3) showing that particles of CaCO_3 remain on the surface and retain their original shape. Reaction [7.6] will be rapidly self-limiting, since a layer of $\text{Al}_2\text{O}_{3(s)}$ forms at the interface.

The high surface activity of Mg observed in the carbonate-based foams (§6.5.2) suggests that $\text{CO}_{2(g)}$ may also be reduced by Mg to form magnesium oxide, $\text{MgO}_{(s)}$, or magnesium aluminate spinel, $\text{MgAl}_2\text{O}_{4(s)}$:

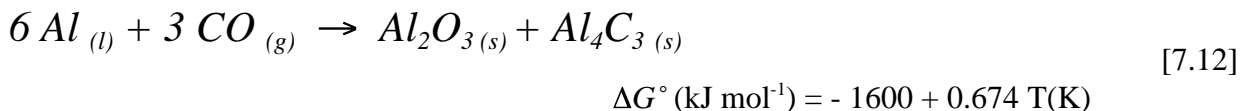
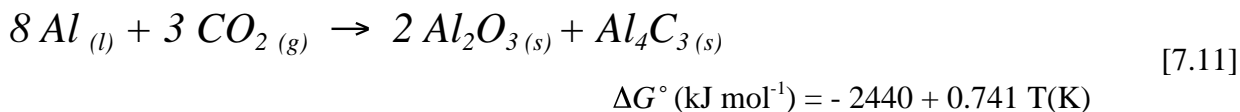


$$\Delta G^\circ (\text{kJ mol}^{-1}) = -321 + 0.037 T(\text{K})$$



$$\Delta G^\circ (\text{kJ mol}^{-1}) = -1181 + 0.077 T(\text{K})$$

It is also possible for the $\text{CO}_{(g)}$ produced to be further reduced in reactions forming $\text{Al}_4\text{C}_{3(s)}$ or $\text{SiC}_{(s)}$:



7.3.3 Formation of the oxide film

The Al_4C_3 -forming reactions [7.11] and [7.12] do not appear to be significant, because no Al_4C_3 has been detected in the current work using X-ray diffraction, and only low concentrations of carbon have been detected by AES depth profiling of the cell surface (§6.5.2). The absence of aluminium carbide is consistent with the slow kinetics of Al_4C_3 formation reported in the literature (§3.6.1), which are in marked contrast to the rapid formation of Al_2O_3 (§3.4.7). The level of Si in the Al-9 wt.% Si alloy studied is sufficient to make SiC more stable than Al_4C_3 , with reaction [7.13] more thermodynamically favourable. Thermodynamic modelling (§3.6.1) of the effect of concentrations of Mg up to $f_{\text{Mg}} = 0.12$ suggests that the presence of Mg favours the formation of Al_4C_3 . The surface activity of Mg in the cells may well be higher than this.

Reactions [7.7], [7.9] and [7.10] are also thermodynamically favourable at 650°C, and the presence of significant amounts of Mg and Al in the oxide film (§6.5.2) suggests that all three reactions take place to some extent. The X-ray diffraction patterns of powdered foams show peaks that can be attributed to all three phases, with the Al_2O_3 peak becoming increasingly dominant relative to the MgO and MgAl_2O_4 peaks as baking time is increased. MgO and MgAl_2O_4 cannot be conclusively distinguished by X-ray powder diffraction. The progression to Al_2O_3 formation as the surface film thickens is consistent with a gradual depletion of Mg in the melt: MgO is initially the most stable oxide, with a transition to MgAl_2O_4 and Al_2O_3 as the surface concentration of Mg is reduced by the formation of surface oxides (§3.4.7).

7.3.4 Limiting of the reaction

The equilibrium $p\text{CO}/p\text{CO}_2$ ratio for reactions [7.7], [7.9] and [7.10] is given by the following relations:

$$\log \frac{p\text{CO}}{p\text{CO}_2} = \frac{14626}{T} - 1.149 \quad (\text{for reaction [7.7])} \quad [7.14]$$

$$\log \frac{p\text{CO}}{p\text{CO}_2} = -\frac{15423}{T} - 1.005 \quad (\text{for reaction [7.9])} \quad [7.15]$$

$$\log \frac{p\text{CO}}{p\text{CO}_2} = \frac{16768}{T} - 1.932 \quad (\text{for reaction [7.10])} \quad [7.16]$$

The $p\text{CO}/p\text{CO}_2$ ratio is extremely high in the presence of molten alloys, as plotted in Figure 7.13 for reactions [7.7] and [7.9]. Virtually all of the $\text{CO}_{2(\text{g})}$ produced will be reduced to $\text{CO}_{(\text{g})}$, even with low metal activities, as can be seen from the curves for a metal activity of 0.0001.

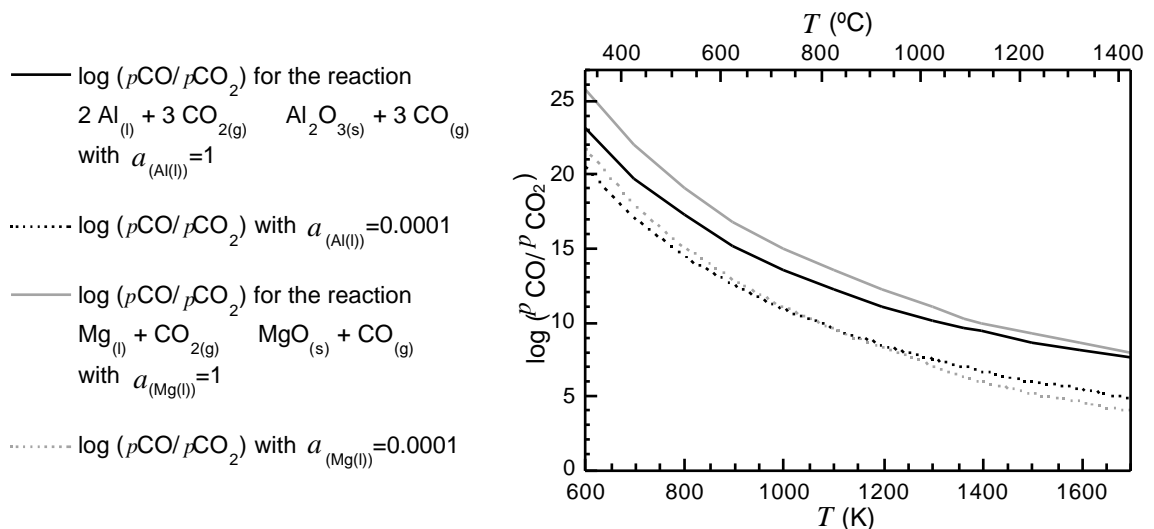


Figure 7.13: Equilibrium $p\text{CO}/p\text{CO}_2$ as a function of temperature, for oxidation of pure $\text{Al}_{(\text{l})}$ and $\text{Mg}_{(\text{l})}$ surfaces by $\text{CO}_{2(\text{g})}$, according to reactions [7.7] and [7.9]. Calculations are shown for Al and Mg in the standard state and for a metal activity of 0.0001.

The formation of a progressively thicker film of metallic oxide will reduce the surface activity of the metal, and cause $p\text{CO}_2$ to increase. The observed tear bands suggest that the decomposition is initially accompanied by expansion of the cells to reveal unoxidised metal surfaces (§6.5.1). However, if the oxide film acquires strength sufficient to inhibit fracture and expansion of the cell, $p\text{CO}_2$ will increase to the point where reaction is inhibited.

The lower limit of ρ^*/ρ_s is thus defined by a combination of the reaction kinetics of the formation of films on liquid metals, and the extent to which these films can resist tension.

Lower values of ρ^*/ρ_s were obtained in foams produced by more rapid induction heating of the foamable precursors, presumably due to the inability of the film to reach a limiting thickness in the short foaming time.

7.4 Estimation of surface oxide thickness

If the maximum extent of decomposition of calcium carbonate is known, and the assumption is made that all of the carbon dioxide produced by thermal decomposition is reduced by the metal surface, an upper-bound estimate of the thickness of the oxide film formed on the cell surface can be obtained. A hollow pentagonal dodecahedron (§3.4.9) of uniform face thickness is used as a geometric approximation of a foam cell. In order to compare the predictions with observed cellular structures, the side length of a pentagonal dodecahedral unit cell can be related to the diameter, d , of a spherical cell of equal volume:

$$L_{PD} = 0.409 \cdot d \quad [7.17]$$

The surface area, S_{PD} , and volume, V_{PD} , in terms of L_{PD} , are given by[284]:

$$V_{PD} = 7.663 \cdot (L_{PD})^3 \quad [7.18]$$

$$S_{PD} = 20.646 \cdot (L_{PD})^2 \quad [7.19]$$

The fraction of gas in the cell is defined as f_G , and the fraction of liquid ($=1-f_G$) as f_L . The inner surface area, $S_{PD,inner}$, of a pentagonal dodecahedron lined with a liquid layer is given by[284]:

$$S_{PD,inner} = 20.646 \cdot (L_{PD})^2 \cdot (f_G)^{2/3} \quad [7.20]$$

The oxide thickness on the internal surface of a single unit cell, w_{oxide} , is given by dividing the total volume of the oxide formed in the cell, V_{oxide} , by $S_{PD,inner}$. The volume of oxide in the cell is in turn equal to the total mass of oxide, m_{oxide} , divided by its bulk density, ρ_{oxide} :

$$w_{oxide} = \frac{V_{oxide}}{S_{PD,inner}} = \frac{m_{oxide}}{\rho_{oxide} S_{PD,inner}} \quad [7.21]$$

The mass of oxide formed in the unit cell, m_{oxide} , is related to the mass of CaCO_3 , which reacts with it to form oxide and $\text{CO}_{(g)}$, contained within the foam, m_{CaCO_3} . Not all of the $\text{CO}_{2(g)}$ in the cell will be reduced to form metal oxides and $\text{CO}_{(g)}$. However, the equilibrium ratio $p\text{CO}/p\text{CO}_2$ in Figure 7.12 is so high in the presence of $\text{Al}_{(l)}$ and $\text{Mg}_{(l)}$ that it is assumed that all of

the $\text{CO}_{2(g)}$ produced is reduced to $\text{CO}_{(g)}$, which will, of course, not be the case in the later stages of foaming. The following equation is obtained:

$$m_{oxide} = \frac{M_{oxide} n_{O(\text{CaCO}_3)}}{M_{\text{CaCO}_3} n_{O(oxide)}} m_{\text{CaCO}_3} f_{dec} \quad [7.22]$$

M_{oxide} and M_{CaCO_3} are the molar mass of oxide formed and CaCO_3 , respectively. The variable $n_{O(oxide)}$ represents the number of oxygen atoms per formula unit in the oxide: 3, 1 and 4 for Al_2O_3 , MgO and MgAl_2O_4 respectively. Similarly, $n_{O(\text{CaCO}_3)}$ is the number of oxygen atoms released for the formation of oxide films for the decomposition of a formula unit of the CaCO_3 .

The f_{dec} term accounts for incomplete decomposition of the CaCO_3 , and is determined experimentally by comparison of the actual f_G with the maximum which could be obtained (defined in [7.3]):

$$f_G = \frac{1}{\frac{M_{\text{CaCO}_3} P}{f_{\text{CaCO}_3} f_{dec} \rho_{\text{CaCO}_3} R T} + 1} \quad [7.23]$$

Experimental measurement of f_G is made by determination of ρ^*/ρ_s after solidification. Contraction of the foaming between T_{foam} and the metal melting point means that this is not directly equivalent to f_G at the foaming temperature: a correction can be made to account for this, although the effect is small for the foaming temperatures used.

The formation of Al_4C_3 by reaction [7.11] or [7.12] would involve further decomposition of the CaCO_3 and growth of the solid surface film, without an associated reduction in ρ^*/ρ_s . The experimental determination of f_{dec} relies on the measured ρ^*/ρ_s , and assumes that neither reaction occurs. The value of $n_{O(\text{CaCO}_3)}$ in [7.22] is thus 1, since one formula unit of CO_2 is released per formula unit of CaCO_3 which decomposes, which in turn releases one unit of O on reduction to CO.

The mass of $\text{CaCO}_{3(s)}$ in the unit cell, m_{CaCO_3} , is obtained by multiplying the volume fraction of $\text{CaCO}_{3(s)}$ dispersed within the liquid phase, f_{CaCO_3} , by the density of the CaCO_3 , ρ_{CaCO_3} , and the volume of liquid in the unit cell, $V_{PD} f_L$:

$$m_{\text{CaCO}_3} = f_{\text{CaCO}_3} \rho_{\text{CaCO}_3} V_{PD} f_L \quad [7.24]$$

Substituting [7.24] for m_{CaCO_3} in [7.22], and [7.22] for m_{oxide} in [7.21], gives:

$$w_{oxide} = \frac{M_{oxide} n_{O(\text{CaCO}_3)} f_{dec} f_{\text{CaCO}_3} \rho_{\text{CaCO}_3} V_{PD} f_L}{\rho_{oxide} S_{PD,inner} M_{\text{CaCO}_3} n_{O(oxide)}} \quad [7.25]$$

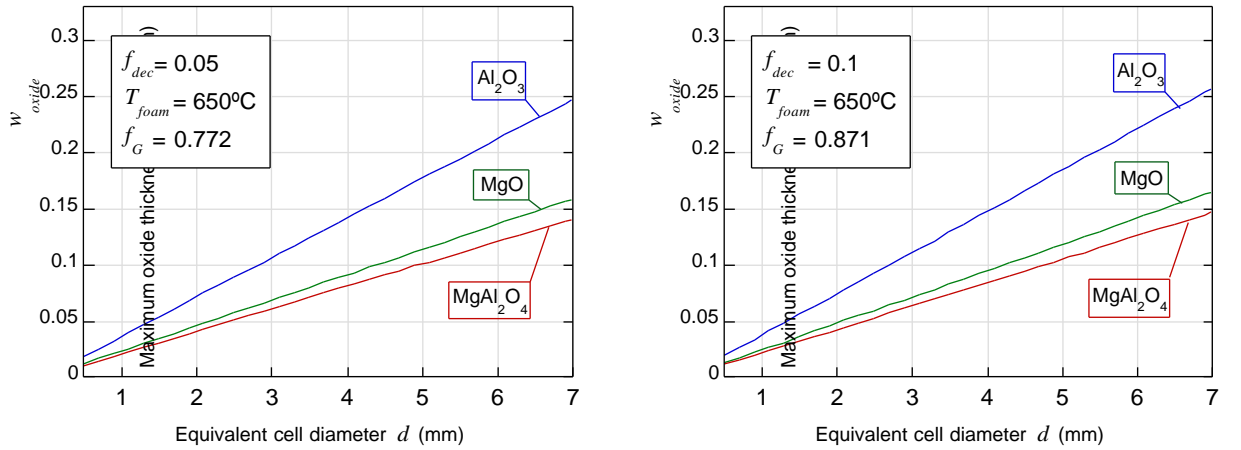
Substituting [7.20] for $S_{PD,inner}$, and rearranging, gives:

$$w_{oxide} = \frac{0.3712 M_{oxide} n_{O(CaCO_3)} f_{dec} f_{CaCO_3} \rho_{CaCO_3} L_{PD} f_L}{\rho_{oxide} (f_G)^{2/3} M_{CaCO_3} n_{O(oxide)}} \quad [7.26]$$

[7.17] can then be used to express L_{PD} in terms of the equivalent cell diameter, d :

$$w_{oxide} = \frac{0.1518 M_{oxide} n_{O(CaCO_3)} f_{dec} f_{CaCO_3} \rho_{CaCO_3} d f_L}{\rho_{oxide} (f_G)^{2/3} M_{CaCO_3} n_{O(oxide)}} \quad [7.27]$$

The effect of varying cell size, d , and fraction of liquid, f_L , can hence be predicted. Figure 7.13 shows the effect of varying d on the oxide thickness in a foam with a given f_{dec} and corresponding f_G , for the oxide forming reactions [7.7], [7.9] and [7.10].

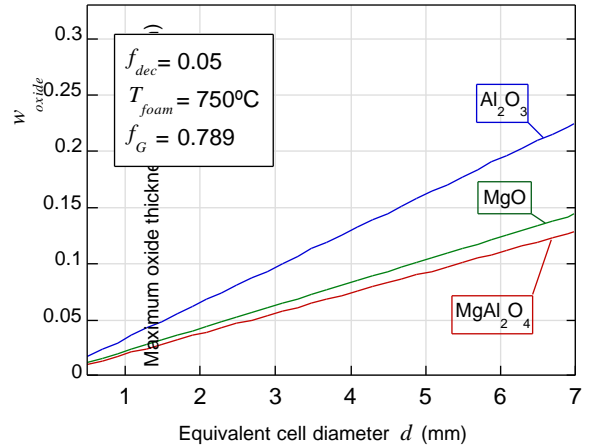


(a)

(b)

Figure 7.13:

Variation of the estimated thickness of films composed of Al_2O_3 , MgO and $MgAl_2O_4$ as a function of cell size, d , according to equation [7.27]. Plots (a) and (b) compare the effect of varying the extent of decomposition at $T_{foam} = 650^\circ C$. Plots (a) and (c) compare the effect of varying f_{dec} at constant foaming temperature. It is assumed in all cases that $P = 1.014 \times 10^5$ Pa inside the cell; f_G is obtained by applying f_{dec} and T_{foam} to equation [7.23].



(c)

Experimental determination of f_{dec} at the observed limiting porosity allows the upper limit of the oxide film thickness to be calculated. At $T_{foam} = 650^\circ C$, f_{dec} was ~ 0.06 and d was ~ 1 mm, corresponding to an oxide film thickness of ~ 20 - 40 nm. At $T_{foam} = 750^\circ C$, f_{dec} of ~ 0.13 and d was ~ 1.5 mm, corresponding to an oxide thickness of ~ 30 - 60 nm. This is consistent with the experimental observations of section 6.5.2. It is worth noting that the foaming temperature will

also affect the rate of film growth, and may influence the homogeneity of the film produced, affecting the ability of a film to restrict thermal decomposition.

8 Mechanical behaviour of Fine, Closed Cell Foams

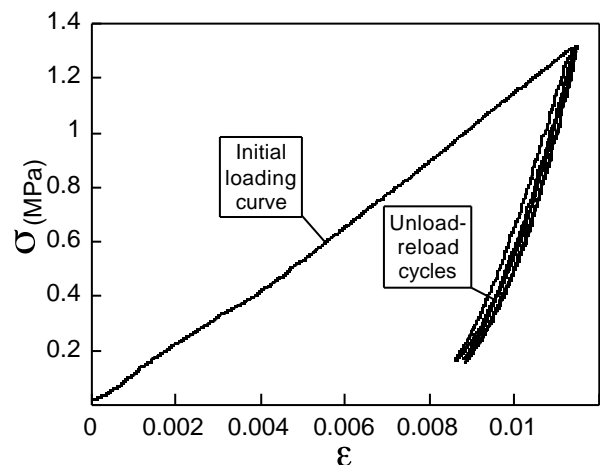
The mechanical properties of foams produced with a calcium carbonate foaming agent in the FOAMCARP process are determined, and compared with those of foams produced using the established titanium hydride-based FORMGRIP process. The smaller cell size of carbonate-based foams is found to give rise to more reproducible mechanical properties, with a reduced sensitivity to point defects, and a close correlation between plastic yield stress and relative density. The foaming agent is found to have a marked effect on the failure mode and the shape of the stress-strain curves, with hydride-based foams having a serrated stress-strain curve characteristic of a brittle foam, and carbonate-based foams having a smooth stress-strain curve characteristic of a ductile foam. This difference is found to be independent of any effect due to cell size. Microstructural analysis of partially yielded specimens suggests that the difference in failure mode is primarily a result of differences in the distribution and volume fraction of stabilising refractory particles.

8.1 Measured elastic properties

In parallel plate compression of cuboid specimens of both carbonate- and hydride-based foams under displacement control, the gradient of the initial stress-strain curve was approximately one third of that measured in subsequent unloading and reloading, with some hysteresis - see Figure 8.1. This is presumably a result of the localised plastic yielding characteristic of the compressive deformation of stochastic foams, reviewed in section 4.3.1.

Figure 8.1:

Low-strain compression testing curve for a specimen of carbonate-based foam consisting of an Al-9Si-0.5Mg melt containing 10 vol.% of SiC_p. The specimen was cubic with a side length of 25 mm, and was subjected to several unload-reload cycles at a strain rate of 0.05 mm min⁻¹.



The elastic modulus of several samples of carbonate- and hydride-based foams, measured by unloading close to σ_{pl} , are plotted as a function of density in Figure 8.2 (a). The same results, normalised by the properties of the bulk metal, are plotted in Figure 8.2 (b), together with the predictions of some of the models reviewed in section 4.6.

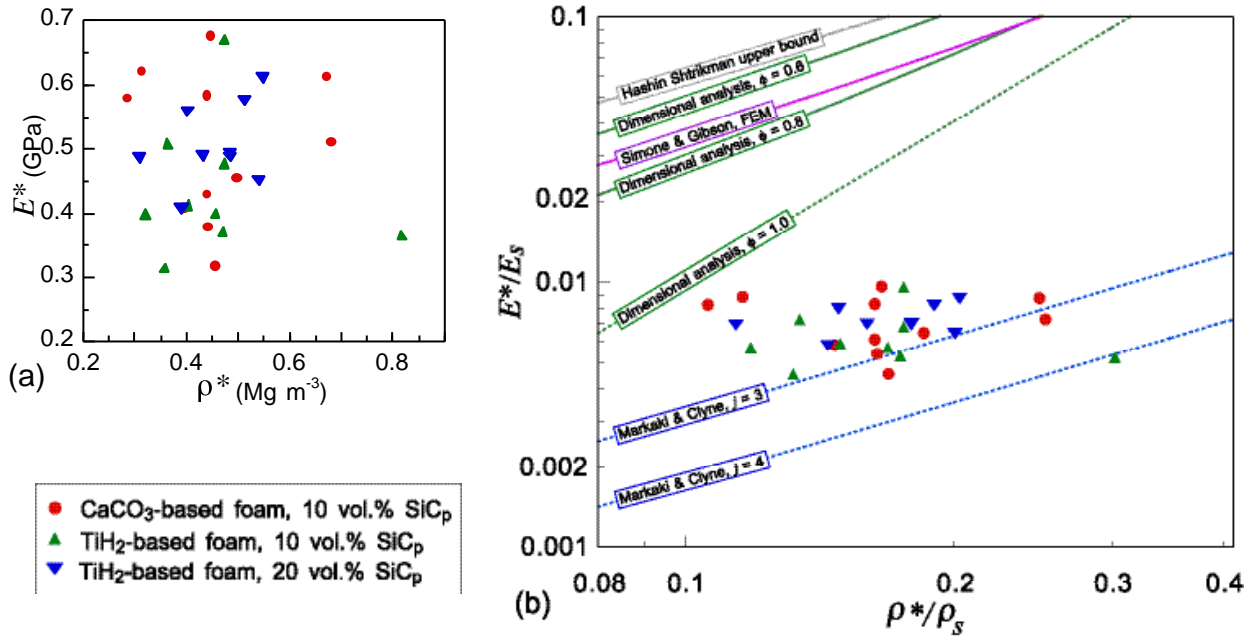


Figure 8.2 (a): Measured elastic modulus, E^* , for the uniaxial compression of cubic specimens of FOAMCARP carbonate-based foams (§5.1), and FORMGRIP hydride-based foams (§2.3.3) with two levels of SiC_p content, as a function of density, ρ^* . The modulus was measured by unloading the specimens prior to the initiation of a plastic band of failed cells. The specimens were all cubic with edge length, D , of 25 mm.

Figure 8.2 (b): The same data, plotted with the elastic modulus of the foam E^* normalised by the stiffness of bulk aluminium E_s (70 GPa), and the density of the foam ρ^* normalised by that of bulk aluminium ρ_s (2.7 Mg m^{-3}). The predictions of some of the models reviewed in section 4.6 are also plotted: The Hashin-Shtrikman upper bound for an isotropic cellular solid[262](§4.6.4), the semi-empirical best-fit analysis of Gibson and Ashby[2](§4.6.1), the FEM modelling of Simone and Gibson[261](§4.6.3), and the fibre-based model of Markaki and Clyne[254, 255](§4.6.2).

Scatter in measured stiffness at a given density for any type of foam is approximately a factor of two, presumably reflecting a degree of batch-to-batch variability. This is similar to the degree of scatter in the reported measurements of the stiffness of commercially available foams (§4.6.1), suggesting that the range in E^* is an inevitable result of the stochastic nature of the cell structures of melt-based foams, in which much of the initial elastic deformation is concentrated at the weakest points in the structure (§4.3.1). As discussed in section 6.2, the principal difference between the cell structure of carbonate- and hydride-based foams is one of scale. The similarity in measured stiffness suggests that varying the cell size by a factor of approximately four has no significant effect on the elastic properties.

Figure 8.2 (b) shows that the measured stiffness of both hydride- and carbonate-based foams at a given density is significantly lower than that predicted by the various modelling approaches for closed-cell foams, and somewhat lower than that reported for other commercially available foams (§4.6.1). The reasons for this difference are unclear. Although density gradients were noted in hydride-based foams (§6.7.1), if their effect was significant the carbonate-based foams – with no gradient in density – would have similar or higher measured stiffness (§4.9.4). This was not the case, although it should be noted that the test specimens were generally cut

from relatively homogenous parts of the hydride-based foams. As mentioned in section 6.2 the cell faces were generally curved, although the FEM modelling of Simone and Gibson reviewed in section 4.9.6[275] suggests that the observed degree of curvature (α/l of 0.07, corresponding to $l/2r$ of 0.14) will have only reduced E^* by $\sim 7\%$.

8.2 Plastic yielding mechanisms

Plastic failure was associated with the formation of a single band of crushed cells, with no visible deformation of cells outside the crushed zone. Compression of the hydride-based foams was sometimes accompanied by the ejection of small fragments of metal. Various degrees of compression of specimens of typical hydride- and carbonate- based foams are shown in Figure 8.3. The propagation of the initial band through the structure is apparently autocatalytic in both types of foam, with multiple failure bands (§4.3.2) not observed.

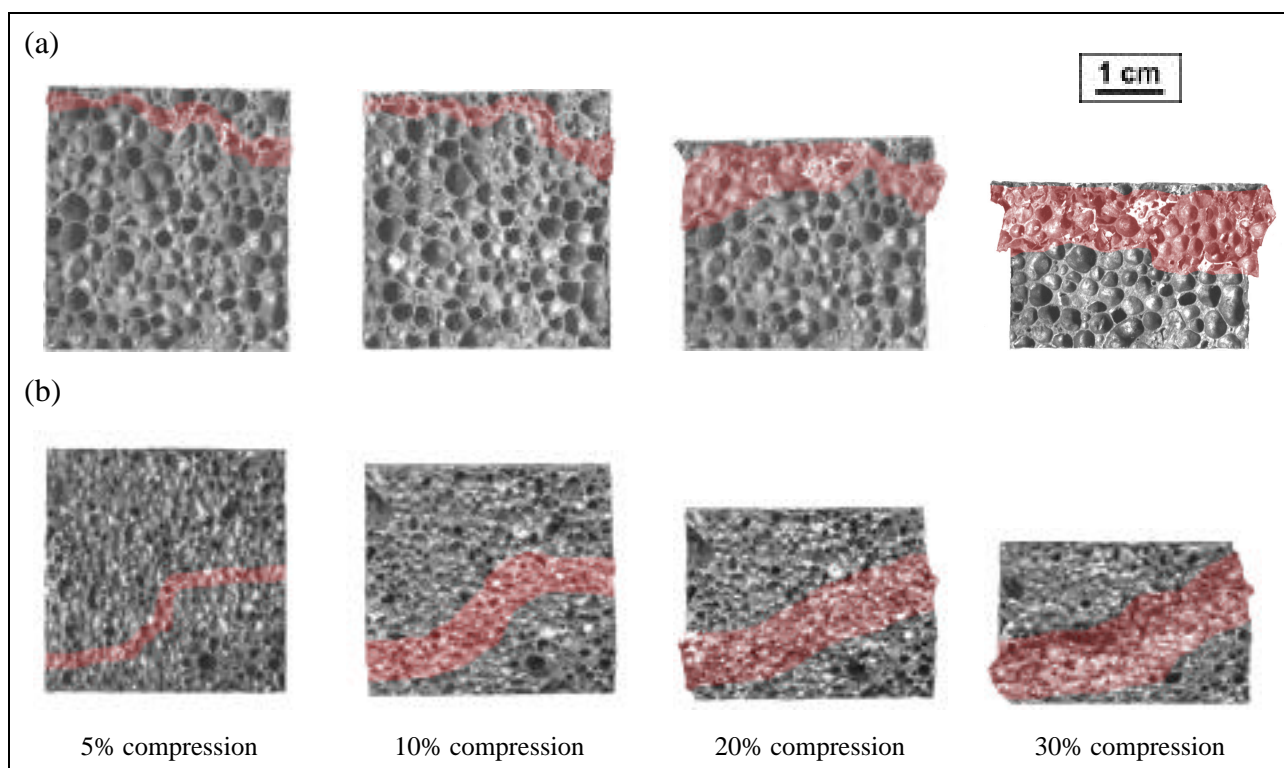


Figure 8.3: Images showing various stages in the uniaxial compression of a specimen of (a) hydride- and (b) carbonate-based foam, with the approximate extent of the bands of collapsed cells highlighted.

The foams were produced by heating of a foamable precursor material consisting of an Al-9Si-0.5Mg melt containing 10vol.% of SiC_p , and (a) 1.5 wt.% of TiH_2 and (b) 3.3 wt.% of CaCO_3 . The relative density, ρ^*/ρ_s , of both specimens was ~ 0.20 .

8.3 Plastic failure of carbonate- and hydride-based foams

The measured plastic yield stress of carbonate- and hydride-based foams with various densities is plotted as a function of density in Figure 8.4 (a). The same results, normalised by the properties of the bulk metal, are plotted in Figure 8.4 (b). The predictions of the dimensional analysis of Gibson & Ashby based on the formation of plastic hinges (§4.8.1), and the finite element modelling of Simone and Gibson (§4.8.2), are also plotted.

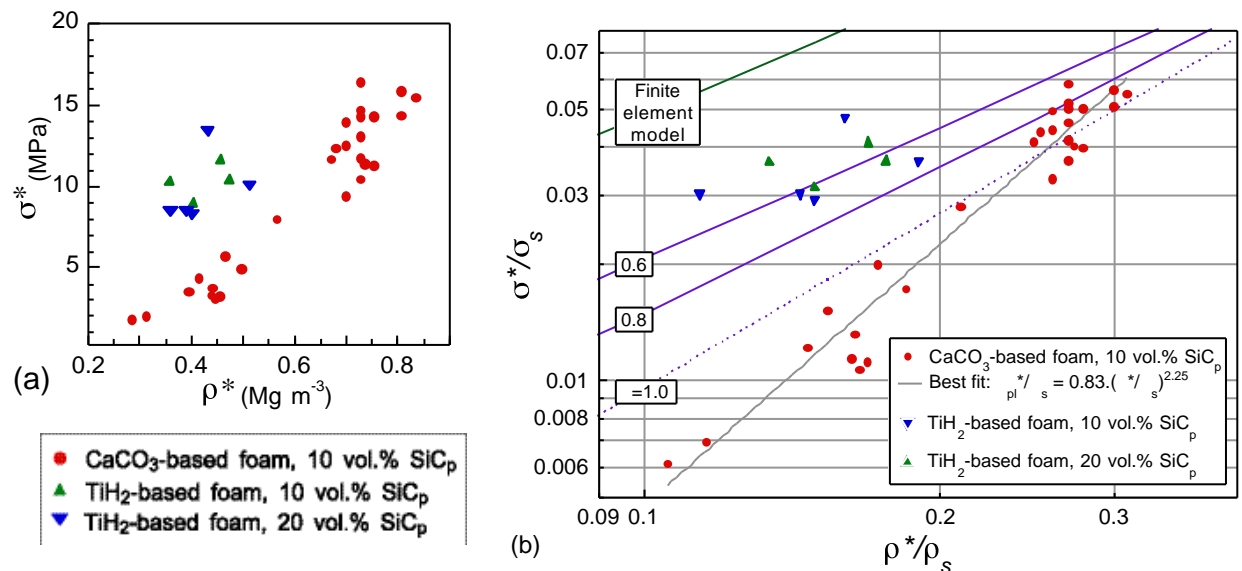


Figure 8.4 (a): Measured plastic yield stress, σ_{pl}^* , for the uniaxial compression of cubic specimens of FOAMCARP carbonate-based foams (§5.1) and FORMGRIP hydride-based foams (§2.3.3) produced with varying SiC_p content, as a function of density ρ^* . The yield stress was defined by applying a horizontal tangent stress to the stress-strain curve immediately after the plastic yield point. The specimens all had $D = 25$ mm.

Figure 8.4 (b): The same data, plotted with the plastic yield stress of the foam σ_{pl}^* normalised by the stiffness of bulk F3S10S metal matrix composite σ_s (283 MPa), and the density of the foam ρ^* normalised by that of bulk aluminium ρ_s (2.7 Mg m^{-3}). The predictions of some of the dimensional analysis results of Gibson and Ashby[2](§4.8.1), and the FEM modelling of Simone and Gibson[261](§4.8.2), are also plotted.

It is worth noting that the metal matrix composite is assumed to preserve its bulk properties in the foam, so that the σ_s value used for normalisation of the yield stress in Figure 8.4 (b) is that of the Al-9Si-0.5Mg-10 vol.%SiC_p F3S10S metal matrix composite (283 MPa), rather than that of an Al-9Si-0.5Mg alloy in the absence of any SiC_p (~ 165 MPa). The cell faces in the carbonate-based foams, which act as a focus for plastic deformation, contain relatively few particles (§6.4), so the appropriate yield stress may be that of the pure alloy, which would give rise to a higher normalised σ_{pl}^*/σ_s .

The immediate conclusion of Figure 8.4 (b) is that carbonate-based foams have a lower yield strength than hydride-based foams of the same ρ^*/ρ_s , as well as a significantly reduced degree of scatter in measured σ_{pl}^* . The reason for this difference becomes more apparent when the shape of the stress-strain curves is compared, as discussed in section 8.4.

Scaling laws for carbonate-based foams

The carbonate-based foams generally had predictable mechanical properties, with plastic yielding scaling with density in a consistent manner. A least squares power law best fit is obtained for $\sigma_{pl}^*/\sigma_s \sim (\rho^*/\rho_s)^{2.25}$, as plotted in Figure 8.4 (b). The yield stress of carbonate-based foams has a more pronounced dependence on ρ^*/ρ_s than would be expected based on the dimensional analysis of Gibson and Ashby (§4.8.1), or the FEM of Simone and Gibson (§4.8.2), both of which predict a power law dependence of $\sigma_{pl}^*/\sigma_s \sim (\rho^*/\rho_s)^{1-2}$.

Although the smaller range of cell sizes in carbonate-based foams means that any point defect – such as a missing cell face – will necessarily have a less marked influence on the mechanical properties of a specimen of a given dimension, it was generally noted that the lower-density foams (which were produced at higher temperatures or for longer foaming times) had a higher concentration of such defects, possibly due to the increased likelihood of rupture of the thinner cell faces by differences in gas pressure between adjacent cells (§6.1-6.2). It is therefore possible that this increased defect concentration accounts for this relative under-performance of lower-density carbonate-based foams.

The presence of small point defects in specimens of carbonate-based foams could not easily be quantified in a non-destructive manner. A qualitative measure of the effect of such point defects on the yield behaviour was therefore made by comparing the yield stress of foam specimens with high concentrations of unusually large defects with that of more homogenous cell specimens. Foams containing such large structural defects were produced by selecting sections of the foamable precursor that contained large pores and internal fold lines, and foaming them at a relatively high T_{foam} . External cross sections, as shown in Figure 8.5, were assumed to be broadly representative of the incidence of large pores inside the specimens.

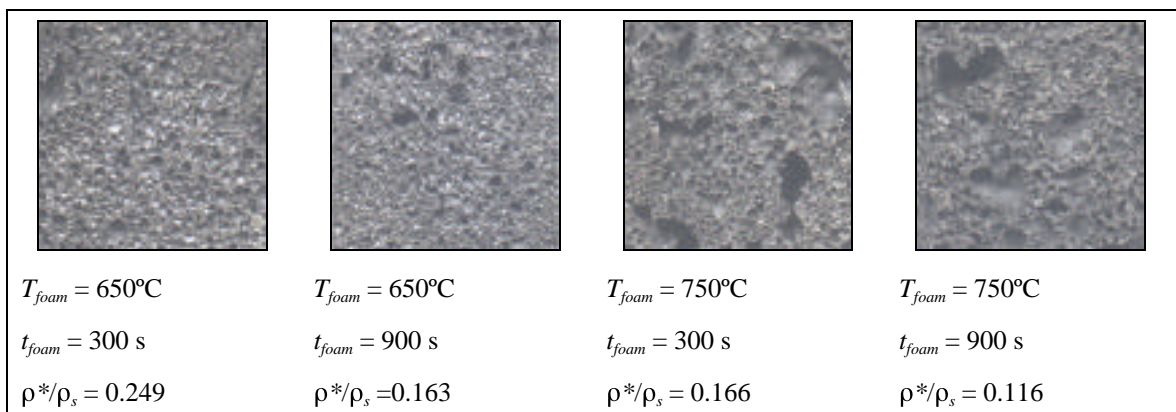


Figure 8.5: Varying degrees of irregularity observed in specimens of carbonate-based foams. The irregular cell structures were produced by selecting specimens of the foamable precursor containing a high concentration of internal fold lines or large pores, and foaming at $T_{foam} = 650\text{-}740^{\circ}\text{C}$. All the foamable precursor materials consist of an Al-9Si-0.5Mg-10 vol.% SiC_p MMC containing 3.3 wt.% of dispersed CaCO₃ powder.



The yield stress of foams with a higher flaw content was significantly lower than that of non-flawed foams of comparable ρ^*/ρ_s , presumably because the defects reduce the effective cross section of the specimens, providing a location for the initiation of a band of plastically collapsed cells. The samples in Figure 8.5 represent extreme examples of irregularity: the presence of defects in specimens with less pronounced flaws could not easily be established in a non-destructive manner. However the observation that defects do reduce the yield stress suggests that the presence of a relatively high concentration of point defects in lower-density carbonate-based foams may account for the difference between the observed dependence of σ_{pl}^*/σ_s on ρ^*/ρ_s and that reviewed in section 4.8.1.

8.4 Plastic collapse of FORMGRIP and FOAMCARP foams

As discussed in section 6.2, the hydride- and carbonate-based foams have a similar cell structure, in terms of the cell face curvature and aspect ratio, with the only significant difference being one of scale. Foams produced with the same MMC alloy might therefore be expected to exhibit broadly similar plastic yielding behaviour. There was, however, a marked difference in plastic collapse behaviour between hydride- and carbonate-based foams.

Typical stress-strain curves for specimens of hydride- and carbonate-based foams of similar density ($\rho^*/\rho_s \sim 0.15$) are shown in Figure 8.6. The onset of large-scale plastic yielding in carbonate-based foams (Figure 8.6 (a)) is accompanied by a slight drop in the load supported by the foam (of under 20%), followed by a smooth plateau stress with gradual work hardening, characteristic of ductile collapse (§4.4). In marked contrast, the onset of large-scale plastic yielding in hydride-based foams (Figure 8.6 (b)) is characterised by a significant drop in the load supported by the foam – generally of over 50% – which is followed by a plateau region with $\sigma_{plateau}^* < \sigma_{pl}^*$ with pronounced serrations. Perhaps surprisingly, there is no discernible difference in mechanical performance between hydride-based foams produced with MMC alloy containing 10 and 20 vol.% of SiC_p (Figures 8.6 (b) and (c))

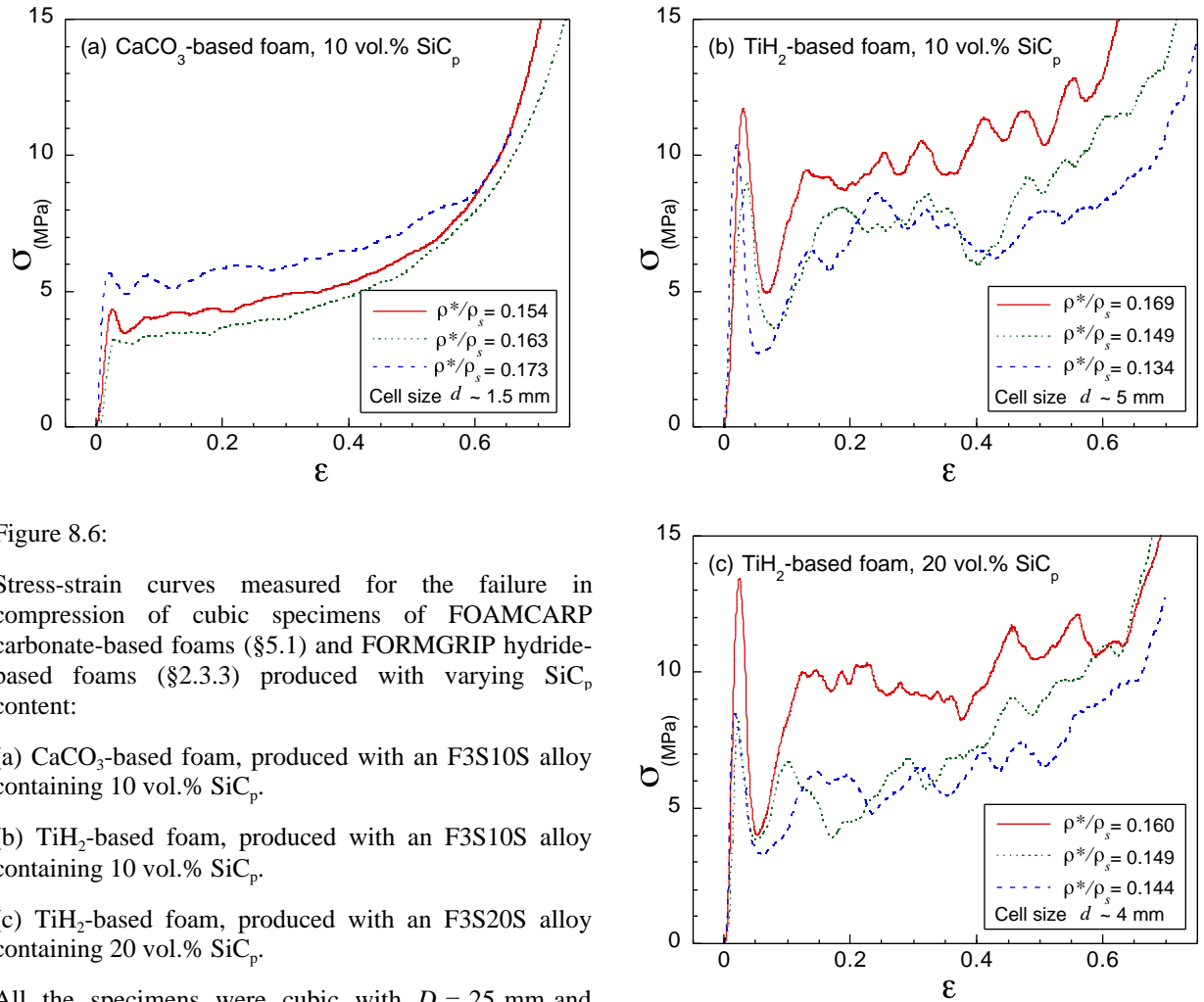


Figure 8.6:

Stress-strain curves measured for the failure in compression of cubic specimens of FOAMCARP carbonate-based foams (§5.1) and FORMGRIP hydride-based foams (§2.3.3) produced with varying SiC_p content:

- (a) CaCO_3 -based foam, produced with an F3S10S alloy containing 10 vol.% SiC_p .
- (b) TiH_2 -based foam, produced with an F3S10S alloy containing 10 vol.% SiC_p .
- (c) TiH_2 -based foam, produced with an F3S20S alloy containing 20 vol.% SiC_p .

All the specimens were cubic with $D = 25$ mm and $\rho^*/\rho_s \sim 0.15$. The measurements were made at a constant strain rate of 0.5 mm min^{-1} . The CaCO_3 -based foams were produced at $T_f = 650^\circ\text{C}$, and the TiH_2 -based foams at $T_f = 630^\circ\text{C}$.

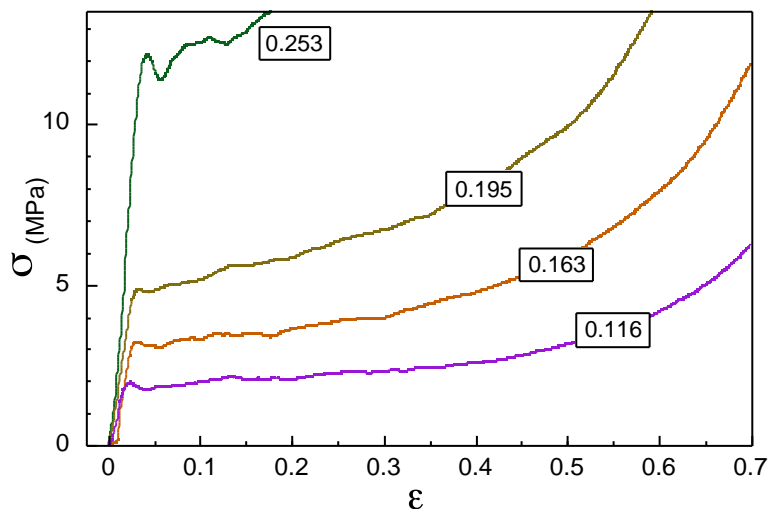
The higher yield stress of the hydride-based foams in Figure 8.4 is mainly a consequence of the large peak in load prior to the onset of plastic failure, although the load supported by the hydride-based foams does remain higher than that of the carbonate-based foams after yielding (the load supported at the lower points of the stress-strain serrations in the hydride-based foams is similar to the average load supported by the carbonate foams). The specific energy absorption of carbonate-based foams is thus lower than that of hydride-based foams. However, the shape of the carbonate-based foams (similar to that shown in Figure 4.4 (a)) means that there is a potential for higher energy absorption before a given critical peak stress is reached than in hydride-based foams (for which the stress-strain curve is similar to that shown in Figure 4.4 (b)). Coupled with the more uniform and predictable behaviour of the carbonate-based foams, the failure behaviour of the carbonate-based foams is clearly advantageous for energy absorption applications (§4.4).

Figure 8.7 shows stress-strain curves for carbonate-based foams with a wide range of ρ^*/ρ_s . As expected, ϵ_d is reduced as ρ^*/ρ_s increases. Varying ρ^*/ρ_s has no discernible effect on the degree of serration of the stress-strain curves of the carbonate-based foams.

Figure 8.7:

Compressive stress-strain curves for cubic specimens of carbonate-based foams with a range of ρ^*/ρ_s (labelled on the curves).

The specimen size, D , was uniform at 25 mm, but values of d (which ranged between 1 and 2 mm) were larger for the lower-density samples. The measurements were made at a constant strain rate of 0.5 mm min^{-1} .



As discussed in section 4.4, brittle eutectic alloys are known to favour brittle failure in foams, and the presence of a dispersed solid phase - such as the SiC_p in these foams - is also thought to favour brittle failure. The marked difference in stress-strain behaviour for foams produced with a nominally similar MMC, shown in Figure 8.6 (a) and (b) suggests that the cell size may also have an influence - for example, a finer cell size might be expected to make the behaviour more consistent and less susceptible to random fluctuations.

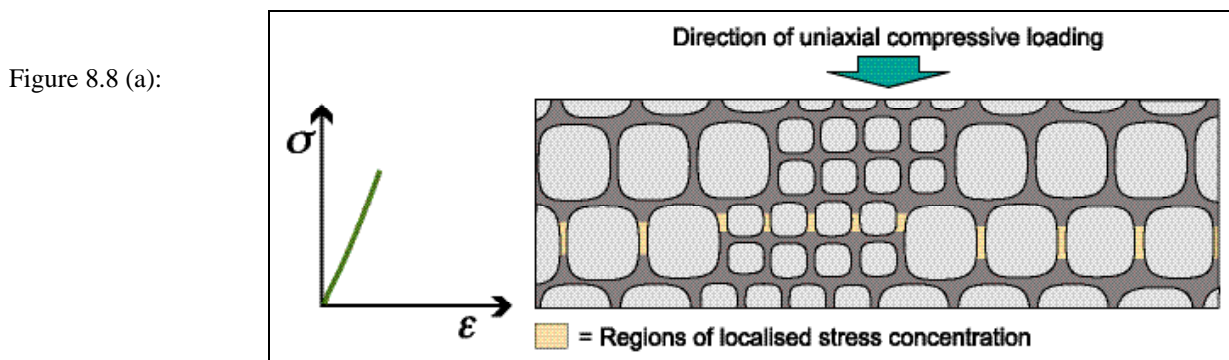
8.5 Serrations in the stress-strain curve

In order to understand the reason for the observed difference in compressive failure properties, it is useful to first examine the possible origin of the serrations in the stress-strain curves of such foams. In this section, the stress-strain curve that would be expected for the uniaxial compression of a schematic melt-based foam is considered, and the possible influence of a reduced cell size on this behaviour is discussed.

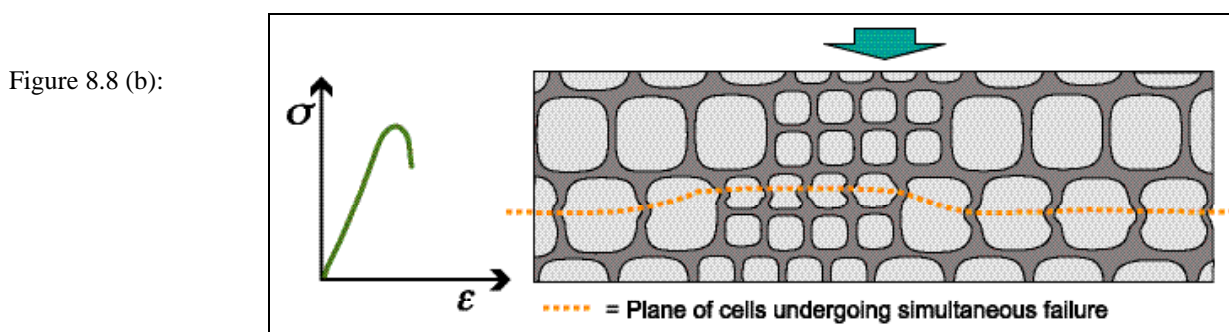
8.5.1 The origin of serrations

A two-dimensional melt-based foam is represented schematically in Figure 8.8 (a). Although reasonably uniform distributions of cells is generally observed on a local scale in melt-based foams, a degree of irregularity in cell size, shape and configuration, as well as local density, is expected. This is represented by a region near the centre of the specimen having smaller cells, and - as the cell face thickness is approximately constant (§4.9.5) - correspondingly higher local density.

In the first stage of compressive loading, where the strain is mostly recoverable, the elastic deformation is usually localised in one or more bands of cells approximately normal to the compression axis (§4.3.1), as illustrated in Figure 8.8 (a).



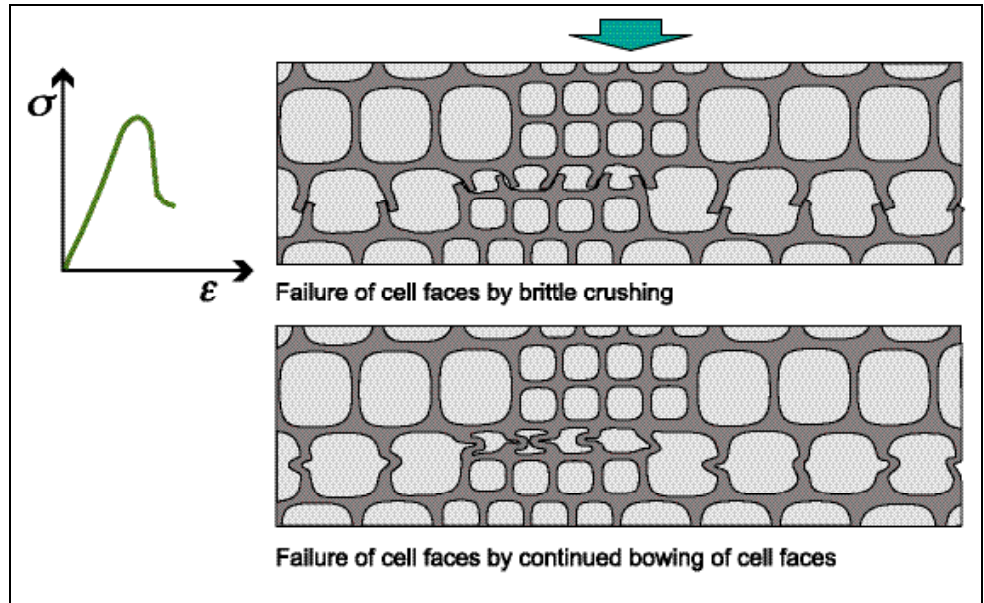
The onset of large-scale plastic yielding in a cell structure subjected to parallel plate compressive loading requires the co-operative collapse of an entire plane of cells across the width of the specimen. Buckling of the cell faces and Plateau borders in a continuous band of cells is shown schematically in Figure 8.8 (b), where the dotted line represents the area over which failure is occurring.



The simultaneous initiation of buckling failure across the entire cross sectional area of the specimen reduces the load supported by the foam. With compression at a constant rate, this corresponds to a sharp dip in the stress-strain curve.

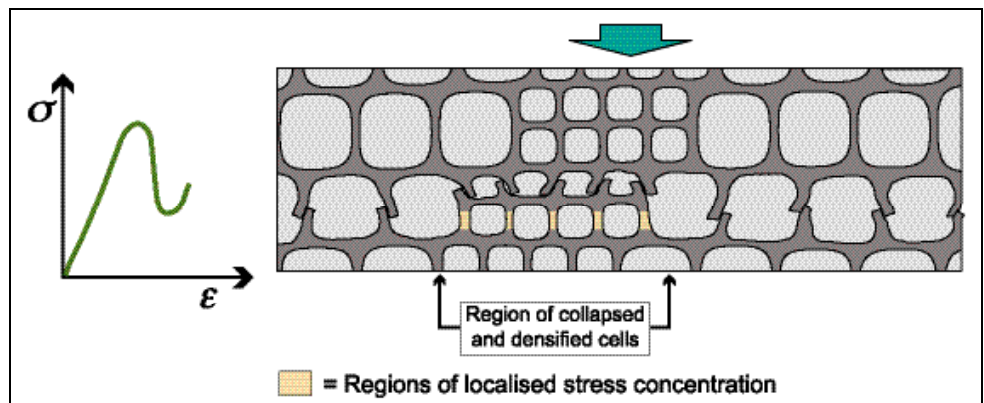
As discussed later in this chapter, continued failure in compression after this stage can proceed by brittle fracture after limited buckling, or by continued buckling. Regardless of the mechanism of failure, opposite sides of the collapse band will at some point come into contact, as illustrated for the two cases in Figure 8.8 (c).

Figure 8.8 (c):



If the cell structure is perfectly uniform, the stress will rise again to the initial stress, and another band of cells will undergo plastic collapse, with a serration in the stress strain curve of similar magnitude and range to the first. The stochastic nature of the cell structure of real melt-based foams, however, gives rise to a range of local density, cell size, and cell configuration. It follows that the band of crushed cells will not undergo simultaneous densification across the entire width of the specimen, with densification instead occurring in some parts of the specimen cross-section before others. This is illustrated in Figure 8.8 (d) where the region of smaller cells at the centre becomes dense before surrounding areas, with stress transferred to neighbouring cells.

Figure 8.8 (d):



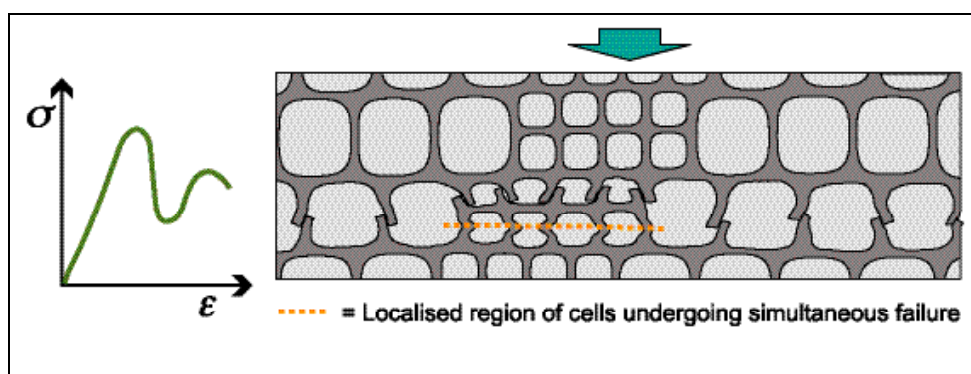
Due to the stochastic nature of typical cell structures, this contact will initially occur only locally. Almost all the external load applied to the specimen is thus supported by a part of the specimen cross section. This causes localised yielding in the region where the stress is concentrated, at a load lower than that which is required to cause simultaneous yielding a band of cells across the entire specimen cross section.

It follows that if only one band of collapsed cells is formed the first serration would be expected to be the most marked, since it is the only point at which an entire band of cells

undergoes simultaneous failure. At all later stages, particularly in specimens with a large number of cells in the cross section, local bands of cells in different parts of the cross sectional area of the foam specimen will collapse at different degrees of strain. The foam specimen will exhibit some residual strength after the first serration, because at any given strain some regions of cells will be at the stress peak prior to collapse.

The initiation of a separate collapse band elsewhere in the specimen would require the compressive stress to rise above the initial σ_{pl}^* , which is unlikely to happen until the onset of densification.

Figure 8.8 (e):



8.5.2 The effect of uniformity in the cell structure on serrations

The presence of serrations is thus to some extent a reflection of the regularity of the cell structure: highly uniform cellular structures, such as the foams produced by tessellation of hollow spheres reviewed in section 2.2.2, would be expected to show a sequence of clear serrations corresponding to the number of possible failure bands. Conversely, highly irregular cell structures that fail by the formation of a single band of crushed cells would show no clear serrations after the initial yield point, as cells fail individually. Most melt-based foams, which possess at least a degree of regularity in cell size, would be expected to fall somewhere in between these two extremes, with a large drop in load followed by smaller serrations as regions of cells fail in parts of the specimen cross section. In structures which fail by the formation of several discrete bands of collapsed cells (§4.3.2) a serration would be expected upon the formation of each band.

8.5.3 The effect of cell size on serrations

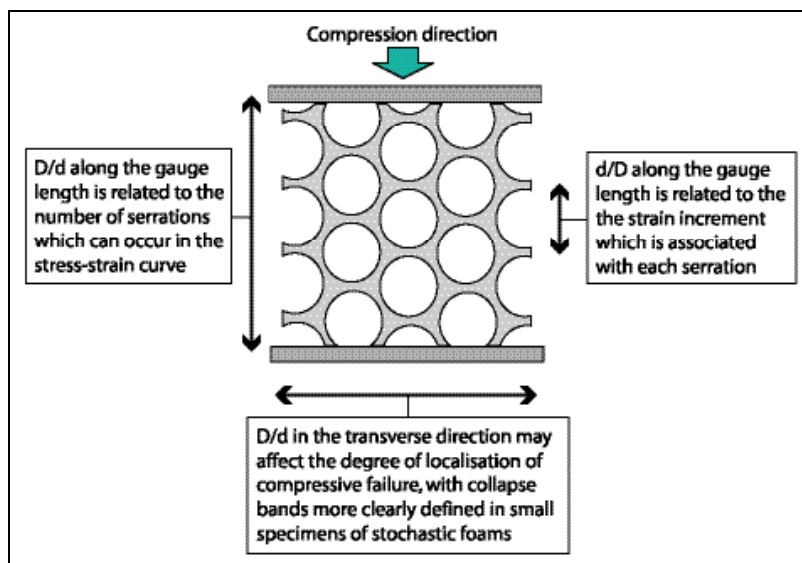
Based on the mechanism depicted in Figure 8.8, and the cell size effects reviewed in section 4.11, varying the cell size, d , relative to the sample size, D , in a given cellular structure can affect the shape of the stress-strain curve. Figure 8.9 illustrates two ways in which the serrations would be expected to relate to the ratio of cell size d to the specimen dimension D :

(1) The number of serrations in the Plateau region should be similar the number of cells along the specimen height, D/d , and the strain associated with each serration will be related to the fraction of the specimen height associated with each band of cells, d/D . The magnitude of the drop in load supported by the foam after each serration may also be less apparent in serrations associated with a narrower collapse band. This may make serrations in the stress-strain curve less apparent as d/D is reduced.

(2) After the large initial drop in load corresponding to the onset of large-scale plastic yielding, the magnitude of the serrations may be smaller in specimens with larger D/d along the specimen width. In a specimen with only 5 cells across, for example, bands of collapsed cells are likely to cover the entire specimen cross section until densification, as there may not be sufficient variation in structure within the cross section to allow for the development of localised collapse regions (as shown in Figure 8.8 (d) and (e)). In a specimen with a larger number of cells in cross section there is more potential for failure to be localised in different parts of the specimen cross section.

Figure 8.9:

Ways in which the ratio of cell size, d , to specimen size, D , could affect the serrations of a compressive stress-strain curve measured at a constant rate of displacement.



8.6 The effect of cell size on plastic collapse

8.6.1 Comparison of hydride- and carbonate-based foams

The cell size effects discussed in section 8.5.3 may explain why the stress-strain curves of small-celled carbonate specimens in Figure 8.6 (a) do not show marked serrations, while that of the larger-celled hydride-based foams in Figure 8.6(b) do. In order to assess the importance of cell size effects on the observed degree of serrations in the stress-strain curve, specimens of hydride- and carbonate-based foams of the same ρ^*/ρ_s were produced with the specimen size adjusted to maintain a constant value of D/d . In order to eliminate the possibility of different specimen aspect ratios giving rise to differing degrees of plastic constraint, or favouring failure by buckling rather than crushing of bands of cells (§4.11), all the specimens studied were cubic.

Figure 8.10 shows stress-strain curves thus obtained for carbonate- and hydride- based foams with D/d along all sides of the specimen equal to 15 in each case. Curves are shown for $\rho^*/\rho_s \sim 0.1$ and $\rho^*/\rho_s \sim 0.165$. At both densities the stress-strain curves for the carbonate-based foams are still markedly smoother from those of hydride-based foams. This demonstrates that the differences in degree of serration after yielding in carbonate- and hydride-based foams are independent of any effect of cell size. The origin of the serrations is discussed further in section 8.7.

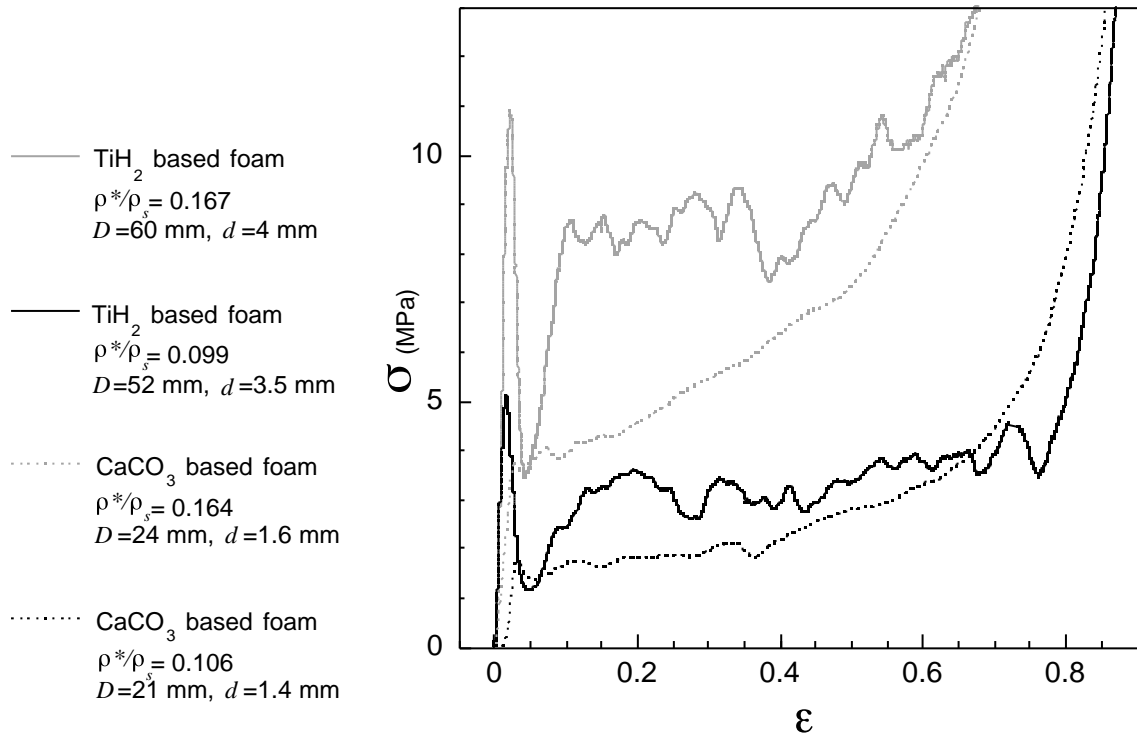


Figure 8.10: Compressive stress-strain curves obtained for cubic foam specimens of carbonate- and hydride-based foams of two densities in which the specimen size, D , was varied in order to ensure a constant ratio of D/d .

All four specimens were produced with an Al-9Si-0.5Mg alloy containing 10 vol.% of dispersed angular $12\mu\text{m}$ SiC particles. The CaCO_3 -based foams were produced by foaming a foamable precursor containing a dispersion of 3.3 wt.% of powdered CaCO_3 at $T_{\text{foam}} = 650^\circ\text{C}$ for $t_{\text{foam}} = 900$ s (for the higher-density specimen), and $T_{\text{foam}} = 750^\circ\text{C}$ for $t_{\text{foam}} = 900$ s (for the lower-density specimen). The TiH_2 -based foams were produced by foaming a foamable precursor containing a dispersion of 1.5 wt.% of powdered TiH_2 at $T_{\text{foam}} = 630^\circ\text{C}$ for $t_{\text{foam}} = 60$ s (for the higher-density specimen), and $T_{\text{foam}} = 630^\circ\text{C}$ for $t_{\text{foam}} = 120$ s (for the lower-density specimen). The measurements were made at a constant strain rate of 0.5 mm min^{-1} .

It is worth noting that although cell size effects do not apparently account for the difference in the shape of the stress-strain curves between hydride- and carbonate-based foams, there is some evidence that cell size effects are significant. The higher D/d for the hydride-based foam specimens in Figure 8.10, relative to that of the specimens in Figure 8.6 (b) and (c), is associated with a slightly smoother stress strain curve with finer serrations, and a more uniform σ_{pl} . This is consistent with the effects of D/d mentioned in section 8.5.3. A small cell size is also expected to enhance the reproducibility of the mechanical properties of a foam, for example

by reducing the influence of point defects such as localised fluctuations in density (4.9.5) and missing cell walls (§4.9.2) on the mechanical properties of a specimen of given dimensions. It may also enable specimens with smaller dimensions to have mechanical properties representative of those of the bulk foam, as discussed in the following section.

8.6.2 Lower limit of specimen size for carbonate-based foams

Measurements on specimens with small external dimensions allow the lower limit of reproducibility – beyond which the properties specimens of carbonate-based foams are not representative of those of bulk foams – to be determined. Relatively high-density foams with $\rho^*/\rho_s \sim 0.25$ were studied in order to reduce the influence of point defects, which are more common in lower-density foams produced at higher T_{foam} (§6.1-6.2), and would be expected to produce an increased scatter at small D/d . The stress-strain curves obtained for three sets of specimens, with different values of D/d , are shown in Figure 8.11.

The bulk σ_{pl}^* of the foam densities studied, according to the best-fit line in Figure 8.4 (b), range from ~ 11.5 to 16 MPa. There is a reduction in measured σ_y for $D/d < 5.3$ (corresponding to specimens with $D < 8$ mm), which is consistent with the analysis of section 4.11. The magnitude of the reduction is not as high as the 33% reduction that would be expected for $D/d = 2.6$, which is possibly due to the increased effect of the constraint of the loading plates on the failure of smaller samples. There is no clear effect of small D/d on the shape or reproducibility of the stress-strain curves.

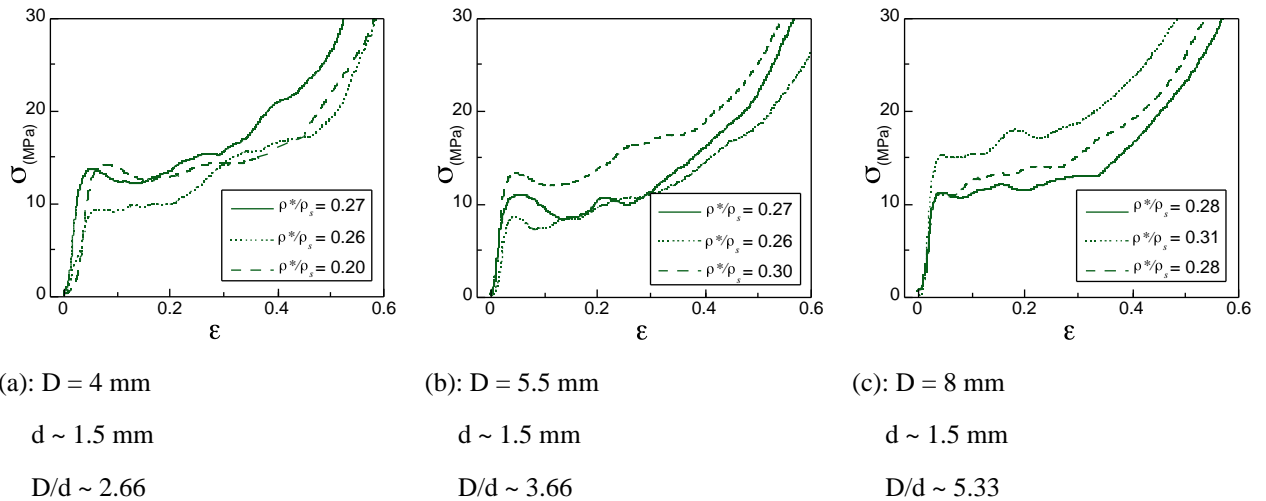


Figure 8.11: Compressive stress-strain curves obtained for small cubic specimens cut from a single carbonate-based foam sample. The cell size, d , was constant at ~ 1.5 mm, and the external dimension of the specimens, D , was varied to obtain D/d of 2.6, 3.7 and 5.3.

All the specimens had $\rho^*/\rho_s \sim 0.25$. The measurements were made at a constant strain rate of 0.05 mm min^{-1} .

8.7 Local yielding mechanisms

8.7.1 Distribution of SiC particulate

As mentioned in section 8.6.1, while a smaller cell size may well reduce the scale of serrations in the compressive stress-strain curves of foam specimens, the effect of cell size is not primarily responsible for the different degree of serration of the stress-strain curves of hydride- and carbonate-based foams.

Aside from the scale of the cell structure, the only significant difference between the two types of foam after solidification is the distribution of the SiC particulate within the cell structure. Gravity drainage of melt during the time the foam is in the liquid state typically leads to the formation of a fully dense region of metal at the base of the foam specimens, which is not incorporated into specimens for mechanical testing. As mentioned in section 6.4, it appears that the formation of local networks of particles within the cell walls means that this melt drainage is not accompanied by drainage of particulate matter. Hydride-based foams, which undergo extensive melt drainage, will thus have a higher concentration of SiC_p in the foamed region than in the MMC materials used in their production.

8.7.2 Stages of plastic yielding

In order to investigate the mechanism of plastic yielding within the cell faces of carbonate- and hydride-based foams, specimens of foams were subjected to interrupted compression tests, with compression tests interrupted at various points shortly after the onset of plastic yielding, sectioned, and prepared for microstructural analysis (§5.3.1).

Figure 8.12 shows cell faces in carbonate- and hydride-based foams immediately after the onset of plastic yielding (i.e. at approximately $\sigma_{yield,upper}$). The mechanism of initial failure in both types of foam is similar, and takes place by highly localised plastic buckling of cell faces at or near their narrowest points. Weakening of the band of cells due to the formation of this band of buckled cell faces is presumably the reason for the drop in load supported by the foam at the yield point. This deformation would be expected to be broadly consistent with the dimensional analysis approach whereby plastic yielding is modelled on the basis of the formation of local plastic hinges (§4.8.1). Given the similarity in the initial failure mechanism between the two types of foam, the higher specific yield stress of the hydride-based foams may be a result of the significantly higher SiC_p content in these foams due to drainage (§6.4.2), although this cannot easily be verified.

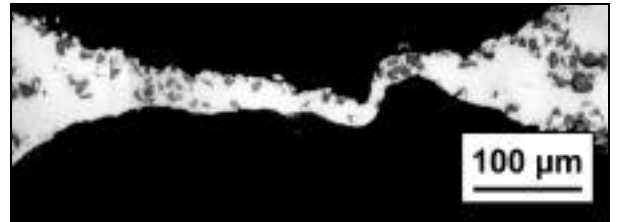
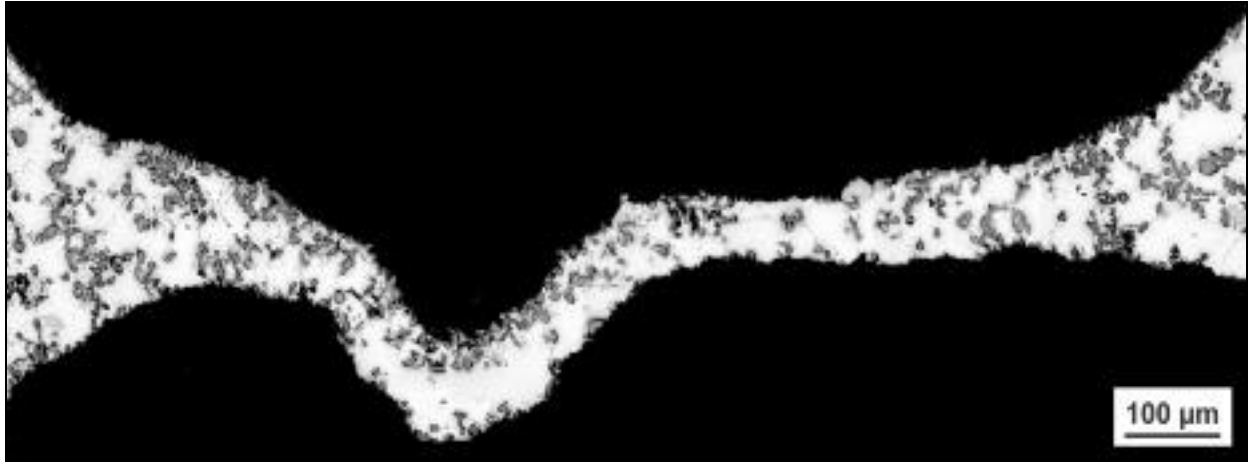


Figure 8.12: Optical micrographs of cell faces within the band of cells undergoing plastic yielding in specimens of (above) hydride- and (right) carbonate-based foams subjected to compressive deformation in which the deformation was interrupted immediately after the onset of plastic yielding.

The hydride-based foam was produced by the dispersion of 1.5 wt.% of powdered TiH_2 in an Al-9Si-0.5Mg alloy containing 10 vol.% of dispersed angular $12\mu\text{m}$ SiC particles. This was subsequently foamed at $T_{\text{foam}} = 630^\circ\text{C}$ for $t_{\text{foam}} = 120$ s. The carbonate-based foam was produced by the dispersion of 3.3 wt.% of powdered CaCO_3 in an Al-9Si-0.5Mg alloy containing 10 vol.% of dispersed angular $12\mu\text{m}$ SiC particles. This was subsequently foamed at $T_{\text{foam}} = 650^\circ\text{C}$ for $t_{\text{foam}} = 900$ s.

Figure 8.13 shows cell faces in carbonate- and hydride-based foams at a strain corresponding to the beginning of the reduction in the load supported by the foam after the onset of plastic yielding (approximately equivalent to the stress-strain curve in Figure 8.8 (b)). At this stage, different mechanisms of failure are observed in hydride- and carbonate-based foams. In hydride-based foams, brittle fracture of the cell faces is visible, whereas in carbonate-based foams the initial buckling of cell faces has simply become more pronounced.

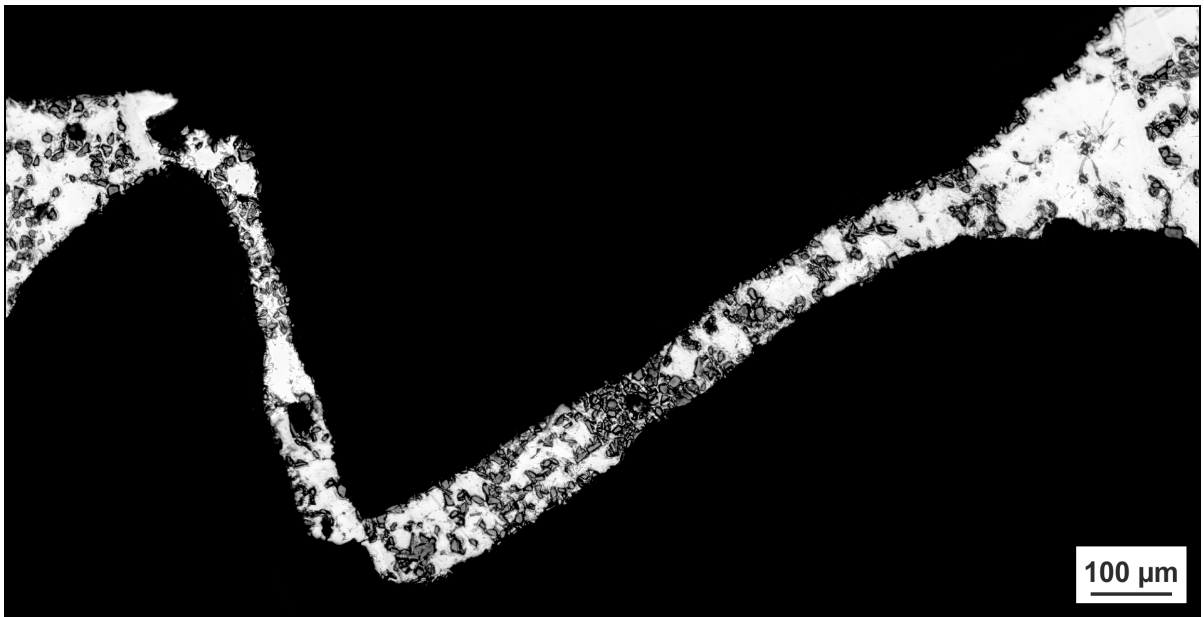


Figure 8.13: Optical micrograph of cell faces in specimens of (above) hydride- and (right) carbonate-based foams, for which compression testing was interrupted after the initial load drop.

The composition and thermal history of the specimens is identical to that of the carbonate- and hydride-based foams in Figure 8.12.



After this point brittle failure of the cell faces in the hydride-based foams means that there is no direct contact between the two sides of the band of collapsed cells. In the carbonate-based foams buckling of the cell faces continues in a uniform manner throughout the deformation process, and a physical connection between the two sides of the band of collapsed cells is always maintained.

This presumably accounts for the more pronounced drop in load after yielding observed for hydride-based foams than for carbonate-based foams. In hydride-based foams, once the band of cells has undergone brittle failure, the only contact between the two sides of the band of collapsed cells is caused by friction. Until the strain reaches a point where the collapsed fragments of cell face are pushed into contact there, will be no effective method for the foam to support the applied load, and a sharp drop in measured load is to be expected. In carbonate-based foams, buckling would also be expected to lower the yield stress. However unlike in the case of hydride-based foams, continued compression of the band of collapsed cells requires continued deformation of material, and the foam would be expected to support some load.

8.7.3 Cell face ductility in compression

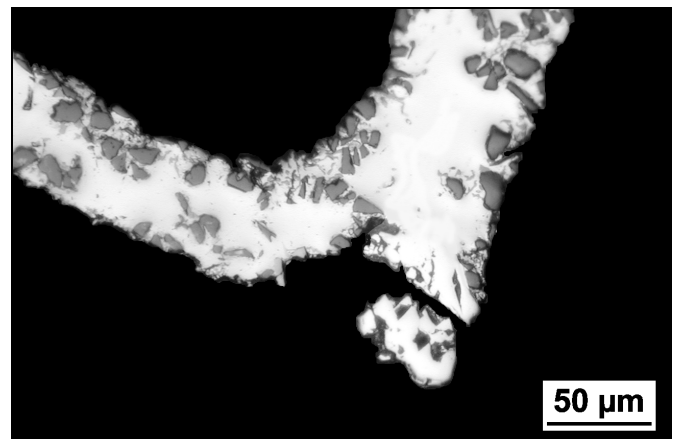
Examination of the failure points suggests that this difference in failure mechanism is a result of the higher level of SiC_p found embedded within the cell faces of the hydride-based foams (§8.7.1), which prevents extended plastic deformation of cell faces by reducing the ductility of the metal matrix composite.

The high concentration of the SiC_p on cell surfaces in the hydride-based foams (§6.4.1) may have a further embrittling effect, by hindering plastic compressibility of the concave side of bowing cell faces, while providing easy initiation sites for cracking by debonding at the smooth Al- SiC_p interface on the convex side. Although SiC_p was frequently observed on fracture surfaces, it was not clear whether the presence of local agglomerations of SiC_p was a prerequisite for failure, with some cross sections of the fracture surfaces encountering very few particles on the surface.

Figure 8.14 shows a partially fractured cell face in a hydride-based foam deformed through $\sim 90^\circ$, with fracture and a detached region visible. Fragmentation of cell faces at several points during plastic yielding was also commonly observed, which is consistent with the observation that pieces of metal are sometimes ejected during the compressive deformation of hydride-based foams (§8.2). This implies that at the level of SiC_p concentration in the hydride-based foams (~ 25 vol.%) the MMC is brittle.

Figure 8.14:

Optical micrograph showing the point of failure of a cell face in a hydride-based foam of composition similar to the hydride-based foam in Figure 8.12, subjected to compressive deformation at 0.05 mm min^{-1} which was interrupted after the drop in load which followed the onset of plastic yielding.



Corresponding micrographs of cell faces in carbonate-based foams subjected to increasing degrees of deformation are shown in Figure 8.15 (a) to (c). Figure 8.15 (a) shows a region of Si that has deformed parallel to the surrounding Al matrix. The concentration of embedded SiC_p particles in the carbonate-based foams (~ 10 vol.%) is lower than that in the hydride-based foams, and does not appear to significantly reduce the ductility of the cell faces. No debonding was observed at the Al- SiC_p interface, as visible in Figure 8.15 (b) and (c).

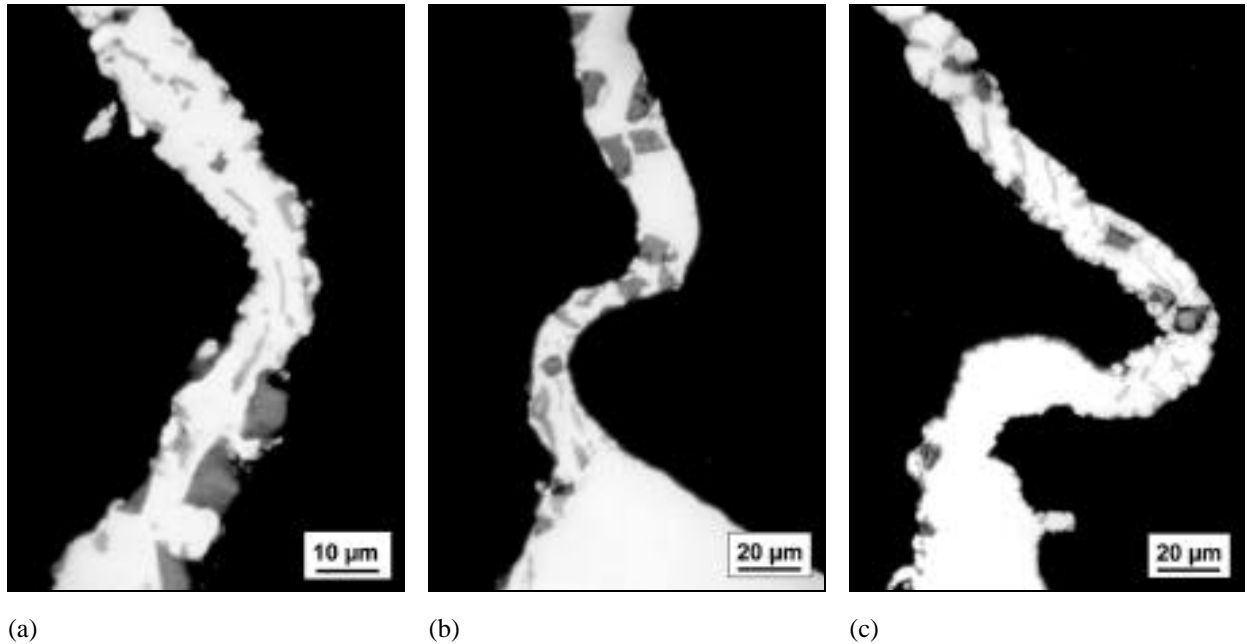


Figure 8.15: Optical micrographs of cell faces in carbonate-based foams in specimens subjected to compressive deformation at 0.05 mm min^{-1} for which testing was interrupted at varying points after the initial load drop, showing successive degrees of deformation during the plastic collapse of a band of cells.

In view of the apparently dominant effect of the SiC_p content on the yield stress and mechanism of failure, the similar level of SiC content measured in hydride-based foams produced with MMC alloys initially containing 10 and 20 vol.% SiC_p in section 6.4.2 may explain the similarity in their measured mechanical properties in Figure 8.6 (b) and (c).

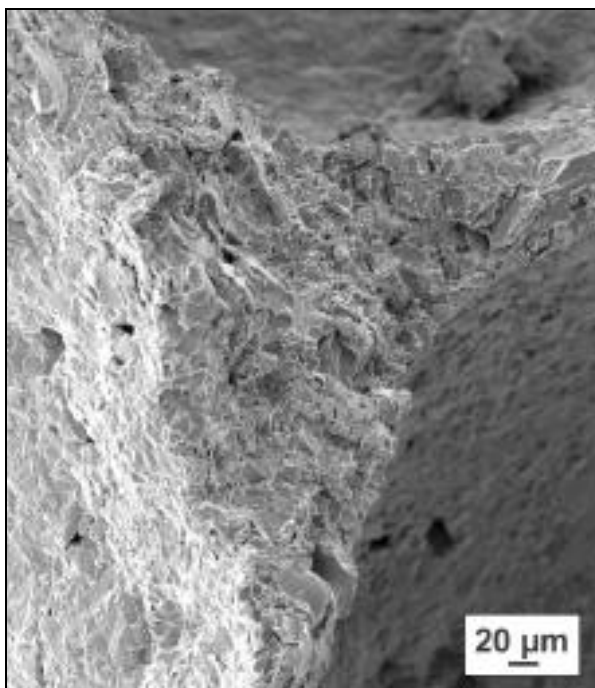
The similarity in the mechanical properties of hydride-based foams containing 10 and 20 vol.% of SiC_p , coupled with the markedly different properties of carbonate- and hydride-based foams produced with identical alloy and SiC_p content (Figure 8.6 (a) and (b)), demonstrate the importance of considering the metallographic microstructure in addition to the cell structure when accounting for the mechanical performance of foams, and the limitations of studies which seek to investigate the effect of particle content by varying the input materials without an accompanying analysis of the foam microstructure.

8.7.4 Cell face ductility in tension

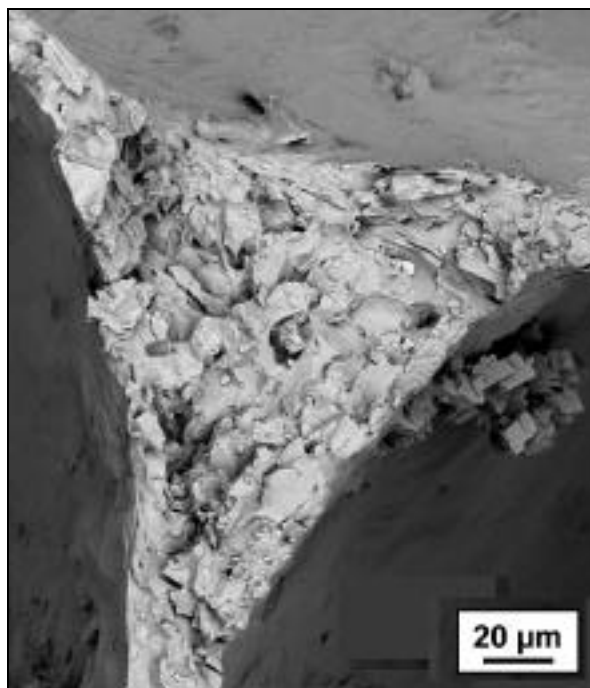
The examination of cross sections of failed cell faces offers only limited information on ductility. A more conclusive comparison of the cell face ductility in hydride- and carbonate-based foams can be obtained by comparing the tensile failure mechanisms of hydride- and carbonate-based foams. Figure 8.16 shows fracture surfaces of Plateau borders in (a) hydride- and (b) carbonate-based foams.

The fracture surface of the hydride-based foam is angular and dominated by evidence of local brittle fracture, with smooth surfaces and particles visible on the surface. In marked

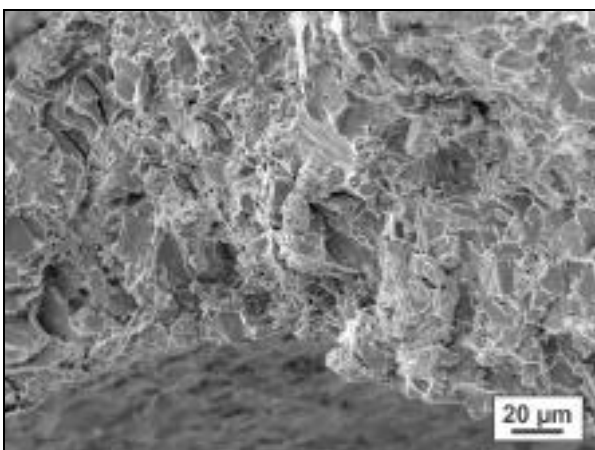
contract, the fracture surface in the carbonate-based foam shows evidence of ductile failure, with extensive ductile dimpling.



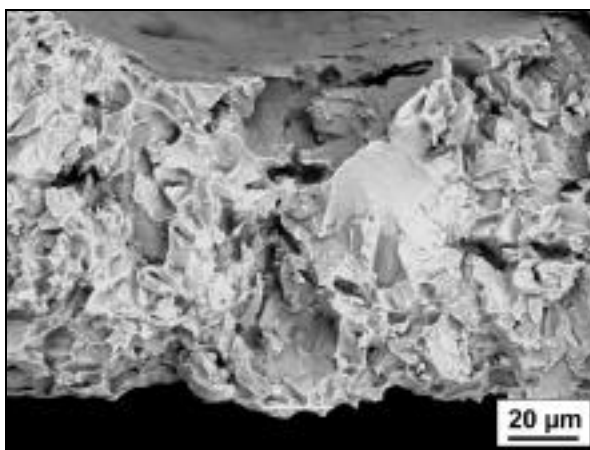
(a)



(c)



(b)



(d)

Figure 8.16 (a) and (b): SEM micrographs showing the tensile failure surface of a Plateau border region in a hydride-based foam, fractured in tension at a strain rate of 0.1 mm min^{-1} , at two magnifications.

The foamable precursor was produced by the dispersion of 1.5 wt.% of powdered TiH_2 in an Al-9Si-0.5Mg alloy containing 10 vol.% of dispersed angular $12\mu\text{m}$ SiC particles. This was subsequently foamed at $T_{\text{foam}} = 630^\circ\text{C}$ for $t_{\text{foam}} = 120 \text{ s}$.

Figure 8.16 (c) and (d): SEM micrographs showing the tensile failure surface of a Plateau border region in a carbonate-based foam, fractured in tension at a strain rate of 0.1 mm min^{-1} , at two magnifications.

The foamable precursor was produced by the dispersion of 3.3 wt.% of powdered CaCO_3 in an Al-9Si-0.5Mg alloy containing 10 vol.% of dispersed angular $12\mu\text{m}$ SiC particles. This was subsequently foamed at $T_{\text{foam}} = 650^\circ\text{C}$ for $t_{\text{foam}} = 900 \text{ s}$.

Figure 8.17 shows cracks found close to tensile failure surfaces in (a) hydride- and (b) carbonate-based foams. The propagation of cracks in hydride-based foams was generally accompanied by fragmentation of the cell face in the vicinity of the crack tip.

In carbonate-based foams, a single failure surface was generally obtained, with apparent stretching of the matrix in the vicinity of the crack tip, and no evidence of crack branching. The opening of small voids and parallel hairline cracks near the failure surface is sometimes visible: these cracks do not appear to join the main crack, which is consistent with ductile tearing failure by the coalescence of individual failure regions.

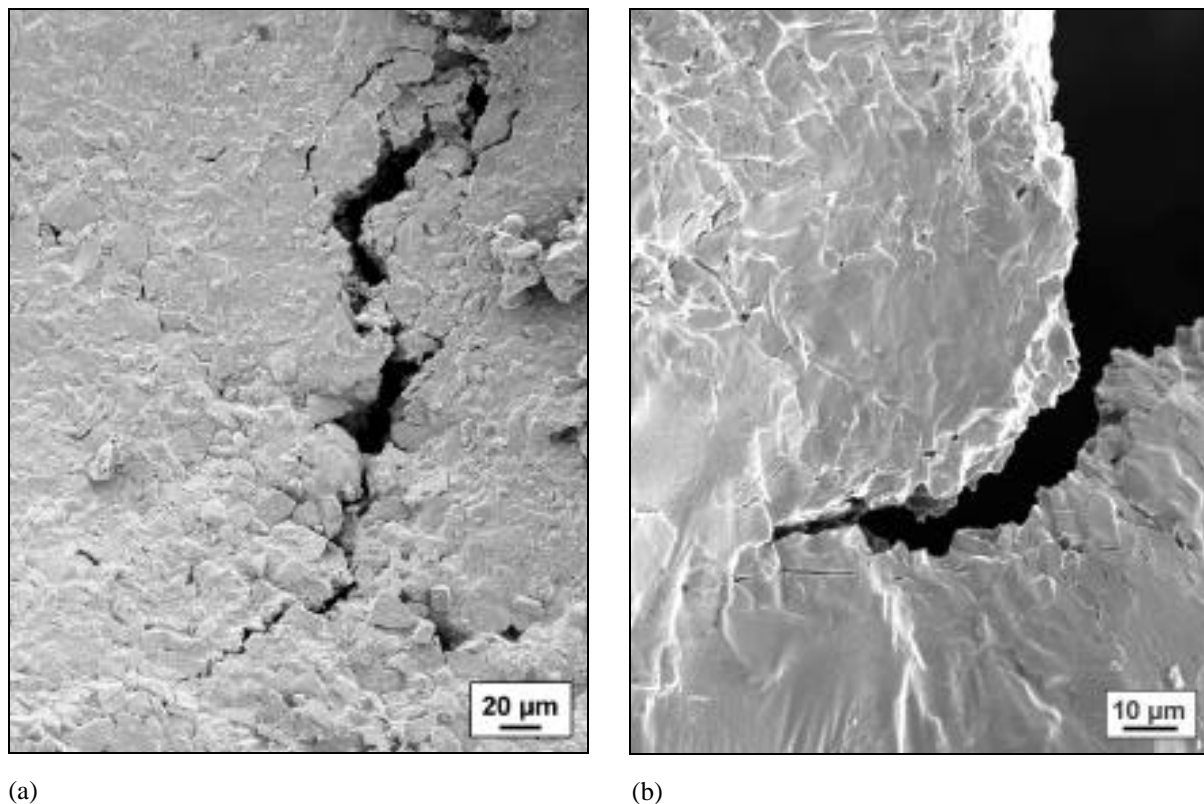


Figure 8.17: SEM micrographs showing the interrupted propagation of cracks across cell faces in the tensile failure of (a) hydride- and (b) carbonate-based foams, fractured in tension at a strain rate of 0.1 mm min^{-1} .

The hydride-based foam was produced by the dispersion of 1.5 wt.% of powdered TiH_2 in an Al-9Si-0.5Mg alloy containing 10 vol.% of dispersed angular $12\mu\text{m}$ SiC particles, to form a foamable precursor material which was subsequently foamed at $T_{\text{foam}} = 630^\circ\text{C}$ for $t_{\text{foam}} = 120 \text{ s}$.

The carbonate-based foam was produced by the dispersion of 3.3 wt.% of powdered CaCO_3 in an Al-9Si-0.5Mg alloy containing 10 vol.% of dispersed angular $12\mu\text{m}$ SiC particles, to form a foamable precursor material which was subsequently foamed at $T_{\text{foam}} = 650^\circ\text{C}$ for $t_{\text{foam}} = 900 \text{ s}$.

8.7.5 The link between foaming agent and stress-strain properties

The observed correlation between the foaming agent and the degree of serration of the compressive stress-strain curves of the foams produced appears to be the result of a number of differences in the processing of the two foams, which are here summarised:

- The use of calcium carbonate rather than titanium hydride as a foaming agent leads to an oxidising atmosphere of carbon dioxide inside the cells (§3.1.4).

- In contrast to the reducing environment inside the cells in hydride-based foams, the oxidising environment inside the cells in carbonate-based foams gives rise to the rapid formation of a solid film of metallic oxide which lines the cell surface (§7.3.3).
- The presence of this solid film prevents particulate SiC from segregating to the melt-gas interface, in contrast to the situation in hydride-based foams where cell surfaces are lined with particles (§6.4.1).
- The presence of the solid film also counteracts the effect of surface tension, and hence significantly reduces the rate of coalescence of cells and coarsening of the cell structure relative to that in hydride-based foams (§6.7.1).
- The retention of a finer cell structure significantly reduces the extent of melt drainage in carbonate-based foams relative to that in hydride-based foams (§6.7.2).
- The fine cell structure, and reduced rate of melt drainage, prevent accumulation of excess particulate SiC in the foamed region due to drainage of the melt (§6.4.2).
- The lower volume fraction of particulate SiC in the carbonate foams increases local ductility of the cell faces, reducing the magnitude of serrations in the stress-strain curve and producing mechanical behaviour characteristic of a ductile foam.

This study suggests that the deleterious effect of high levels of SiC_p (over ~ 20 vol.%) on the ductility of cell faces, and hence the mechanical properties of bulk foams, is significant. Lower concentrations of SiC_p (~ 10 vol.%) do not appear to significantly reduce the ductility of the metal matrix. Although the high SiC_p content of hydride-based foams appears to increase their plastic yield strength, the brittle mode of failure associated with the high particulate content makes the mechanical properties of the foams produced less predictable, and reduces the potential for use of the foams as impact-absorbing materials (§4.4).

9 Conclusions

The use of calcium carbonate

- Calcium carbonate is a viable alternative to the currently-used foaming agents, titanium hydride and zirconium hydride. Its principal advantages are a far lower material cost and a remarkable increase in the stability of metallic foams in the liquid stages of processing. The use of calcium carbonate provides a route to generating finer and more uniform cell structures than can currently be obtained by melt processing.
- Foaming processes using calcium carbonate are relatively insensitive to the particle size of the foaming agent, and the presence of a relatively low level of impurities. The low rate of thermal decomposition of calcium carbonate, relative to that of titanium hydride, gives rise to a more gradual foaming process, enhancing control over the degree of porosity that can be obtained. A temperature-dependent upper limit of porosity exists when foaming with calcium carbonate, apparently due to inhibition of the decomposition reaction by its products, which prevents over-baking.
- The relatively slow decomposition kinetics of calcium carbonate improve the viability of two-step processes, in which a foamable precursor is first generated, by eliminating any requirement for a thermal pre-treatment (of titanium hydride) to delay the onset of thermal decomposition. It also improves the viability of one-stage processes, by allowing more time for the efficient dispersion of the foaming agent.

Foaming mechanisms

- Calcium carbonate acts as a foaming agent by a decomposition reaction at elevated temperatures to form calcium oxide, accompanied by the release of carbon dioxide gas. Experimental observations of the decomposition of calcium carbonate powders show that, at the melting temperature of aluminium, an atmosphere of carbon dioxide inhibits the continued thermal decomposition of the foaming agent. The formation of foams with calcium carbonate is therefore only possible because the carbon dioxide produced inside the cells rapidly reacts with the liquid aluminium on the cell surfaces to form carbon monoxide and solid metallic oxides.
- This reaction of the carbon dioxide with the liquid aluminium leads to the formation of thin films of solid metallic oxides that line the surface of the cells. These films have a thickness of 40-100 nm. The presence of surface features such as stretch bands, and evidence of film rupture,

in solidified foams suggests that these films are initially flexible and become progressively more rigid with time. A temperature-dependent upper limit of porosity is observed when foaming with calcium carbonate, which is thought to be the result of increasingly thick surface films of solid oxide preventing continued reaction of the carbon dioxide with metallic aluminium.

Foams produced with calcium carbonate

- The presence of surface oxide films raises the mechanical stability of cells in liquid aluminium foams, by inhibiting cell coalescence, even when cell walls are ruptured. This preserves a fine cell structure, with thin cell walls, and a reduced rate of gravity drainage of the melt towards the base of the foam. This counterbalances capillarity forces tending to coarsen the cells.
- Surface oxide films also affect the distribution of solid particulate within cell walls, which are commonly added to enhance the melt viscosity, by inhibiting segregation to the gas-metal interface. Local agglomerations of such particles are readily formed within walls, reducing the rate of gravity drainage in the melt. Some dispersed solid particulate is still required during production of carbonate-based foams, but the volume fraction required is significantly lower than is needed for hydride-based processing.
- The formation of local networks of solid particulate means that gravity drainage in the melt, which is usually accompanied by the formation of regions of fully dense metal at the base of the foams, is not generally accompanied by drainage of the solid particles. Foams that undergo significant drainage of metal towards the base of the foam during the foaming process generally have a significantly increased particulate concentration in the porous region of the foam. In foams produced by dispersion of powdered calcium carbonate within a metal matrix composite containing 10 percent by volume, which experience negligible drainage of the melt during the time the foam is molten, the concentration of particulate in the foamed region is equal to that in the metal matrix composite. In foams produced by dispersion of titanium hydride within the same metal matrix composite, where significant drainage of the melt is observed, the concentration of particulate in the foamed region lies between 20 and 30 volume percent, with a solid base region which contains virtually no particulate.

Mechanical properties of carbonate-based foams

- The foams produced using carbonate have a fine cell structure. This enhances the reproducibility of compressive mechanical properties, apparently by reducing the significance of localised defects and sample size effects.

- In hydride-based foams, the onset of plastic failure is accompanied by a marked drop in the load supported by the foam, followed by pronounced serrations in the stress-strain curve. In contrast, the onset of plastic failure in carbonate-based foams is accompanied by a very slight drop in the load supported by the foam, and the stress-strain curve is relatively smooth until densification is reached. This difference in failure mode has been shown to be independent of the difference in cell size between the two types of foam.

- Inspection of the microstructure of foams produced with titanium hydride and calcium carbonate at various stages of plastic failure reveals that the initiation of plastic failure in both types of foam is the result of localised buckling of cell faces. In hydride-based foams, this is followed by brittle fracture of the cell faces and progressive brittle crushing of bands of cells, accompanied by serrations in the stress-strain curve. In carbonate-based foams, continued failure of the specimen occurs by ductile buckling of cell faces. The difference in ductility of the cell faces is attributed to the observed difference in the concentration of particulate in foams produced with titanium hydride and calcium carbonate: cell faces containing 10 percent by volume of particulate SiC fail in a ductile manner, whereas cell faces containing 20-30 percent by volume of particulate SiC fail by localised brittle failure.

10 References

1. Ashby, M.F., *The Mechanical Properties of Cellular Solids*. Metall. Trans. A, 1983. **14A**: p. 1775-1769.
2. Gibson, L.J. and Ashby, M.F., *Cellular Solids*. 2nd ed. 1997, Cambridge: Cambridge University Press. 357.
3. Baumann, G.F., *Thermoplastic-Thermoset Engineering Materials*, in *Engineering Plastics and Their Commercial Development*, R.F. Gould, Editor. 1969, American Chemical Society Publications: Washington. p. 30-45.
4. Kinney, G.F., *Engineering Properties and Applications of Plastics*. 1957, New York: John Wiley & Sons, Inc. 278.
5. Gordon, J.E., *Structures, or Why things don't fall down*. 1979, London: Pitman Publishing Ltd.
6. Rolls-Royce, *The Jet Engine*. 1996, Birmingham: Renault Printing Co Ltd.
7. Gergely, V., Degischer, H.P. and Clyne, T.W., *Recycling of MMCs and Production of Metallic Foams*, in *Comprehensive Composite Materials*, T.W. Clyne, Editor. 2000, Elsevier: Amsterdam. p. 797-820.
8. Ashby, M.F., Evans, A.G., Fleck, N.A., Gibson, L.J., Hutchinson, J.W. and Wadley, H.N.G., *Metal Foams: A Design Guide*. 2000, Boston: Butterworth-Heinemann.
9. Evans, A.G., Hutchinson, J.W. and Ashby, M.F., *Multifunctionality of Cellular Metal Systems*. Progress Mater. Sci., 1999. **43**: p. 171-221.
10. Korner, C. and Singer, R.F. *Processing of Metal Foams - Challenges and Opportunities*. in *Metal Matrix Composites and Metallic Foams - EUROMAT*. 1999: Wiley-VCH.
11. Maine, E. and Ashby, M.F., *Cost Estimation and the Viability of Metal Foams*. Advanced Engineering Materials, 2000. **2**(4): p. 205-209.
12. Dunkley, J.J., *Atomization of Metal Powders*, in *Powder Metallurgy - An Overview*, I.W. Jenkins, J.V and J.V. Wood, Editors. 1991, The Institute of Metals: London. p. 2-21.
13. Williams, H.M. and Boegehold, A.L., *Alloy Structure*, in *US Patent 1,642,348*. 1927.
14. Pashak, J.F., *Cellularized Light Metal*, in *US Patent 2,935,396*. 1960, John F. Pashak.
15. Grubel, R.O. and Busch, L.S., *Composite Metal-Ceramic Body and Method of Producing the Same*, in *US Patent 2,671,955*. 1954.
16. Oh, I.-H., Nomura, N. and Hanada, S., *Microstructures and Mechanical Properties of Porous Titanium Compacts Prepared by Powder Sintering*. Materials Transactions, JIM, 2002. **43**(3): p. 443-446.
17. GKN, *Filter-elements: High porosity sintered materials*. 2003, Addison, Illinois, USA: GKN Sinter Metals Filters. 26.
18. Fedorchenko, I.M., *Progress in Work in the Field of High-Porosity Materials from Metal Powders and Fibres*. Sov. Powder Metall. Met. Cer., 1979. **18**: p. 615-622.
19. Knuwer, M. *Pore Formation During Reactive Sintering of Iron-Aluminium Powder Mixtures*. in *Metal Foams and Porous Metal Structures*. 1999. Bremen (Germany): MIT-Verlag.
20. Li, B.Y., Rong, L.J. and Gjunter, V.E., *A Recent Development in Producing Porous Ni-Ti Shape Memory Alloys*. Intermetallics, 2000. **8**: p. 881-884.
21. Li, B.Y., Rong, L.J., Li, Y.Y. and Gjunter, V.E., *Synthesis of Porous Ni-Ti Shape-Memory Alloys by Self-Propagating High-Temperature Synthesis: Reaction Mechanism and Anisotropy in Pore Structure*. Acta Mater., 2000. **48**: p. 3895-3904.
22. Cochran, J.K., *Ceramic Hollow Spheres and their Applications*. Current Opinion in Solid State & Mat. Sci., 1998. **3**: p. 474-479.
23. Sypeck, D.J., Philip, A.P., Parrish, A. and Wadley, H.N.G. *Novel Hollow Powder Porous Structures*. in *Porous and Cellular Materials for Structural Applications*. 1998. San Francisco: MRS.

24. Torobin, L.B., *Method for Making Hollow Porous Microspheres*, in *US Patent 4 671 909*. 1987.
25. Torobin, L.B., *Hollow Microspheres Made from Dispersed Particle Compositions and Their Production*, in *US Patent 4 777 154*. 1988.
26. Nadler, J.H., Sanders, T.H.J. and Cochran, J.K., *Aluminium Hollow Sphere Processing*. Materials Science Forum, 2000. **331-337**: p. 495-500.
27. Hurysz, K.M., Clark, J.L., Nagel, A.R., Hardwicke, C.U., Lee, K.J., Cochran, J.K. and Sanders, T.H.J. *Steel and Titanium Hollow Sphere Foams*. in *Porous and Cellular Materials for Structural Applications*. 1998. San Francisco: MRS.
28. Andersen, O., Waag, A., Schneider, L., Stephani, G. and Kieback, B. *Novel Metallic Hollow Sphere Structures: Processing and Properties*. in *MetFoam '99*. 1999. Bremen: MIT Verlag.
29. Andersen, O., Waag, U., Schneider, L., Stephani, G. and Kieback, B., *Novel Metallic Hollow Sphere Structures*. *Adv. Eng. Mat.*, 2000. **2**(4): p. 192-195.
30. Clark, J.L., Hurysz, K.M., Lee, K.J., Cochran, J.K. and Sanders, T.H. *Stainless Steel Hollow Sphere Foams - Fabrication, Carburization, and Properties*. in *MetFoam '99*. 1999. Bremen: MIT Verlag.
31. Polonsky, L., Lipson, S. and Markus, H., *Lightweight Cellular Metal*. *Modern Castings*, 1961. **39**: p. 57-71.
32. Cellular Metals, *Cellular Metals: New Concepts Provide Unique Properties*. *The Iron Age*, 1962: p. 119-121.
33. San Marchi, C., Despois, J.F. and Mortensen, A. *Fabrication and Compressive Response of Open-Cell Aluminium Foams with sub-Millimeter Pores*. in *Euromat 99, Symposium on MMCs and Metallic Foams*. 1999. Munich: Willey-VCH Verlag.
34. San Marchi, C. and Mortensen, A., *Deformation of Open-Cell Aluminium Foam*. *Acta. Mat.*, 2001. **49**: p. 3959-3969.
35. Zhao, Y.Y. and Sun, D.X., *A Novel Sintering-Dissolution Process for Manufacturing Al Foams*. *Scripta Mater.*, 2001. **44**: p. 105-110.
36. Ma, L.Q., Song, Z.L. and He, D.P., *Cellular Structure Controllable Aluminium Foams Produced by High Pressure Infiltration Process*. *Script. Mat.*, 1999. **41**(7): p. 785-789.
37. Bram, M., Stiller, C., Buchkremer, H.P., Stover, D. and Bauer, H. *Preparation and Characterization of High-porosity Titanium, Stainless Steel, and Superalloy Parts*. in *Metal Foams and Porous Metal Structures*. 1999. Bremen: MIT Verlag.
38. Bram, M., Stiller, C., Buchkremer, H.P., Stover, D. and Baur, H., *High-Porosity Titanium, Stainless Steel, and Superalloy Parts*. *Adv. Eng. Mater.*, 2000. **2**: p. 196-199.
39. Lanning, B.R., Rawal, S.P. and Misra, M.S. *Interface Structure of a Cast Alumina Microballon Reinforced Titanium Composite*. in *Advanced Metal Matrix Composites for Elevated Temperatures*. 1991. Cincinnati, Ohio.
40. Rawal, S.P., Lanning, B.R. and Misra, M.S. *Design and Mechanical Properties of Microballoon-Aluminum Composite-Core Laminates*. in *9th International Conference on Composite Materials (ICCM-9)*. 1993. Madrid: Woodhead, Cambridge.
41. Hartmann, M., Reindel, K. and Singer, R.F. *Fabrication and Properties of Syntactic Magnesium Foams*. in *Porous and Cellular Materials for Structural Applications*. 1998. San Francisco: MRS.
42. Nadler, J.H., Hurysz, K.M., Clark, J.L., Cochran, J.K., Lee, K.J. and Sanders, T.H. *Fabrication and Microstructure of Metal-Metal Syntactic Foams*. in *MetFoam '99*. 1999. Bremen: MIT Verlag.
43. Hartmann, M., Reindel, K., Singer, R.F. and Crossmann, I. *Microstructure and Mechanical Properties of Cellular Magnesium Matrix Composites*. in *MetFoam '99*. 1999. Bremen: MIT Verlag.
44. Kiser, M., He, M.Y. and Zok, F.W., *The Mechanical Response of Ceramic Microballon Reinforced Aluminum Matrix Composites under Compressive Loading*. *Acta Mat.*, 1999. **47**(9): p. 2685-2694.

45. Davies, G.J. and Zhen, S., *Metallic Foams: their Production, Properties and Applications*. J. Mat. Sci., 1983. **18**: p. 1899-1911.
46. Wagner, I., Hintz, C. and Sahm, P.R. *Precision Cast Near Net Shape Components Based on Cellular Metal Materials*. in *Metal Matrix Composites and Metallic Foams*. 1999: Wiley-VCH.
47. Yamada, Y., Shimojima, K., Sakaguchi, Y., Mabuchi, M., Nakamura, M. and Asahina, T., *Processing of an Open-Cell AZ91 Magnesium Alloy with a Low Density of 0.05 g/cm³*. J. Mater. Sci. Letts., 1999. **18**: p. 1477-1480.
48. Duocel, *Duocel® aluminum foam brochure*. 1998, ERG, INC., Oakland, CA.
49. Hintz, C., Wagner, I., Sahm, P.R. and Stoyanov, P. *Investment Cast Near-Net-Shape Components Based on Cellular Metal Materials*. in *Metal Foams and Porous Metal Structures*. 1999. Bremen, Germany: MIT Verlag.
50. Babjak, J., Ettel, V.A. and Paserin, V., *Method of Forming Nickel Foam*, in *US Patent 4,957,543*. 1990.
51. Matsumoto, I., Iwaki, T. and Yanagihara, N., *Battery Electrode*, in *US Patent 4,251,603*. 1981.
52. Banhart, J. and Baumeister, J. *Production Methods for Metallic Foams*. in *Porous and Cellular Materials for Structural Applications*. 1998. San Francisco: MRS.
53. Yan, X.Y. and Fray, D.J., *Using electro-deoxidation to synthesize niobium sponge from solid Nb₂O₅ in alkali-alkaline-earth metal chloride melts*. Journal of Materials Research, 2003. **18**(2): p. 346-356.
54. Chen, G.Z., Fray, D.J. and Farthing, T.W., *Direct electrochemical reduction of titanium dioxide to titanium in molten calcium chloride*. Nature, 2000. **407**(6802): p. 361-364.
55. Shapovalov, V.I., *Method for Manufacturing Porous Articles*, in *US Patent 5,181,549*. 1993.
56. Shapovalov, V.I. *Formation of Ordered Gas-Solid Structures via Solidification in Metal-Hydride Systems*. in *Porous and Cellular Materials for Structural Applications*. 1998. San Francisco: MRS.
57. Apprill, J.M., Poirier, J.R., Maguire, M.C. and Gutsch, T.C. *Gasar Porous Metals Process Control*. in *Porous and Cellular Materials for Structural Applications*. 1998. San Francisco, CA.: Materials Research Society.
58. Paradies, C.J., Tobin, A. and Wolla, J. *The Effect of Gasar Processing Parameters on Porosity and Properties in Aluminium Alloy*. in *Porous and Cellular Materials for Structural Applications*. 1998. San Francisco, CA: Materials Research Society.
59. Park, C. and Nutt, S.R. *Metallographic Study of Gasar Porous Magnesium*. in *Porous and Cellular Materials for Structural Applications*. 1998. San Francisco, CA.: Materials Research Society.
60. Hyun, S.K. and Nakajima, H., *Fabrication of Porous Iron by Unidirectional Solidification in Nitrogen Atmosphere*. Materials Transactions, JIM, 2002. **43**(3): p. 526-531.
61. Sosnick, B., *Process for Making Foamlike Mass of Metal*, in *US Patent 2,434,775*. 1948.
62. Sosnick, B., *Foamlike Metal*, in *US Patent 2,553,016*. 1951.
63. Ridgway, J.J., *Cellularized Metal and Method of Producing Same*, in *US Patent 3,297,431*. 1967.
64. Kotera, S., *A New or Improved Electrode or Pole for use in Electric Cells*, in *UK Patent 206,797*. 1923.
65. Wang, N., Starke, E.A. and Wadley, H.N.G. *Porous Al Alloys by Local Melting and Diffusion of Metal Powders*. in *Porous and Cellular Materials for Structural Applications*. 1998. San Francisco, California, U.S.A.: Materials Research Society.
66. Masson, B.L. and Cizeron, G., *Influence of Kirkendall effect on sintering of copper-nickel powder mixtures*. Powder Metallurgy, 1991. **34**(4): p. 285-288.
67. Jin, I., Kenny, L.D. and Sang, H., *Method of Producing Lightweight Foamed Metal*, in *U.S. Patent 4,973,358*. 1990, Alcan International Limited: United States. p. 1-5.
68. Jin, I., Kenny, L.D. and Sang, H., *US Patent 5,112,697: Stabilized Metal Foam Body*. 1992.

69. Sang, H., Kenny, L.D. and Jin, O., *Process for Producing Shaped Slabs of Particle Stabilized Foamed Metal*. U.S. Patent 5,334,236, 1994.
70. Simone, A.E. and Gibson, L.J., *Aluminum Foams Produced by Liquid-State Processes*. Acta Mater., 1998. **46**: p. 3109-3123.
71. Niebylski, L.M., Jarema, C.P. and Lee, T.E., *Reinforced Foamed Metal*, in U.S. Patent 3,940,262. 1976.
72. Elliott, J.C., *Method of Producing Metal Foam*, in US Patent 2,751,289. 1956, Elliot, J.C.
73. Elliott, J.C., *Metal Foam and Method for Making*, in US Patent 2,983,597. 1961.
74. Hardy, P.W. and Peisker, G.W., *Method of Producing a Lightweight Foamed Metal*, in US Patent 3,300,296. 1967.
75. Akiyama, S., Ueno, H., Imagawa, K., Kitahara, A., Nagata, S., Morimoto, K., Nishikawa, T. and Itoh, M., *US Patent 4,713,277: Foamed Metal and Method of Producing Same*. 1987.
76. Aoyagi, N. and Kojima, Y. *Production Process and Microstructure of Aluminium Alloy Foams by Semi-Solid Stirring Method*. in *5th International Conference on Semi-Solid Processing of Alloys and Composites*. 1998. Colorado, USA.
77. ALPORAS, *ALPORAS® brochure*. 1998, Shinko Wire Co., Ltd., Amagasaki-shi, Japan.
78. Miyoshi, T., Itoh, M., Akiyama, S. and Kitahara, A., *ALPORAS Aluminium Foam: Production Process, Properties, and Applications*. Advanced Engineering Materials, 2000. **2**(4): p. 179-183.
79. Miyoshi, T., Hara, S., Mukai, T. and Higashi, K., *Development of a Closed Cell Aluminium Alloy Foam with Enhancement of the Compressive Strength*. Materials Transactions, JIM, 2001. **42**(10): p. 2118-2123.
80. Simancik, F. and Kovacic, J. *Porosity in Complex 3D-Parts Prepared from Aluminium Foam*. in *Metal Foams*. 1997. Bremen, Germany: MIT-Verlag Publishing, Bremen.
81. Schorghuber, F., Simancik, F. and Hartl, E., *Method of Producing Molded Bodies of a Metal Foam*, in US Patent 5,865,237. 1999.
82. Baumgärtner, F., Duarte, I. and Banhart, J., *Industrialization of Powder Compact Foaming Process*. Advanced Engineering Materials, 2000. **2**(4): p. 168-174.
83. Baumgärtner, F. and Gers, H. *The Production of Aluminium Foam by PM and Examples for Application*. in *Metal Matrix Composites and Metallic Foams, EUROMAT*. 1999: Wiley-VCH.
84. Baumeister, J. and Schrader, H., *Methods for Manufacturing Foamable Metal Bodies*, in U.S. Patent 5,151,246. 1992.
85. Banhart, J., Baumeister, J. and Weber, M. *Powder Metallurgical Technology for the Production of Metallic Foams*. in *Euro Powder Metallurgy 1995: Light Alloys*. 1995.
86. Duarte, I. and Banhart, J., *A study of aluminium foam formation - kinetics and microstructure*. Acta Materialia, 2000. **48**: p. 2349-2362.
87. Yu, C.J., Eifert, H.H., Knuewer, M., Weber, M. and Baumeister, J. *Investigation for the Selection of Foaming Agents to Produce Steel Foams*. in *Porous and Cellular Materials for Structural Applications*. 1998. San Francisco, Ca.: Materials Research Society.
88. Mukai, T., Kanahashi, H., Yamada, Y., Shimojima, K., Mabuchi, M., Nieh, T.G. and Higashi, K., *Dynamic Compressive Behavior of an Ultra-Lightweight Magnesium Foam*. Scripta Mater., 1999. **41**(4): p. 365-371.
89. Park, C. and Nutt, S.R., *PM synthesis and properties of steel foams*. Mater. Sci. Eng. A-Struct. Mater. Prop. Microstruct. Process., 2000. **288**(1): p. 111-118.
90. MEPURA, *Alulight® brochure*. 1996, MEPURA-Metallpulver GmbH, Ranshofen, Austria.
91. Gergely, V. and Clyne, T.W., *The FORMGRIP Process: Foaming of Reinforced Metals by Gas Release In Precursors*. Adv. Engng. Mater., 2000. **2**: p. 175-178.
92. Gergely, V., *Melt Route Processing for Production of Metallic Foams*, in *Materials Science and Metallurgy*. 2000, University of Cambridge: Cambridge.

93. Gergely, V. and Clyne, T.W. *The Effect of Oxide Layers on Gas-generating Hydride Particles During Production of Aluminium Foams*. in *Porous and Cellular Materials for Structural Applications*. 1998. San Francisco: MRS.
94. Gergely, V. and Clyne, T.W. *A Novel Melt-Based Route to Aluminium Foam Production*. in *International Conference on Metal Foams and Porous Metal Structures (MetFoam '99)*. 1999. Bremen, Germany: Verlag MIT.
95. Goetzl, C.G., *Manufacture of Aluminium Alloys*, in *US Patent 2,155,651*. 1939.
96. Fiedler, W.S., *Method for Preparing a Catalytic Metal Foam and Use Thereof*, in *US Patent 2,895,819*. 1959.
97. Fiedler, S.O., Bjorksten, J. and Fiedler, W.S., *Production of Metal Foam*, in *US Patent 2,937,938*. 1960.
98. Fiedler, S.O., Bjorksten, J. and Fiedler, W.S., *Foaming of Granulated Metal*, in *US Patent 2,979,392*. 1961.
99. Markaki, A.E. and Clyne, T.W., *The Effect of Cell Wall Microstructure on the Deformation and Fracture of Aluminium-Based Foams*. *Acta Mater.*, 2001. **49**(9): p. 1677-1686.
100. Frei, J., Gergely, V., Mortensen, A. and Clyne, T.W., *The Effect of Prior Deformation on the Foaming Behavior of "FORMGRIP" Precursor Material*. *Adv. Eng. Mater.*, 2002. **4**(10): p. 749-752.
101. Barin, I., Knacke, O. and Kubaschewski, O., *Thermochemical properties of inorganic substances*. 1973, Berlin: Springer-Verlag.
102. Barin, I., Knacke, O. and Kubaschewski, O., *Thermodynamic properties of inorganic substances*. 1977, Berlin: Springer-Verlag.
103. Speed, S.E., *Foaming of Metal by the Catalyzed and Controlled Decomposition of Zirconium Hydride and Titanium Hydride*, in *US Patent 3,981,720*. 1976.
104. Barin, I., *Thermochemical data of pure substances*. 1989, Weinheim: VCH Verlagsgesellschaft.
105. Barin, I., *Thermochemical data of pure substances*. 1993, Weinheim: VCH Verlagsgesellschaft.
106. Chase, M.W.J., Davis, C.A. and al, e., *NIST-JANAF Thermochemical Tables*. Fourth Edition ed. 1998, Gaithersburg, Maryland: American Chemical Society and American Institute of Physics.
107. Knacke, O., Kubaschewski, O. and Hesselman, K., *Thermodynamic Properties of Inorganic Substances*. 1991, Berlin: Springer Verlag.
108. Stern, K.H., *High Temperature Properties and Thermal Decomposition of Inorganic Salts with Oxyanions*. 2001: CRC Press.
109. Biswas, A.K. and Bashforth, G.R., *The Physical Chemistry of Metallurgical Processes*. 1962, London: Chapman & Hall.
110. Haux, E.H., *Method of Preparing Cellular Materials*, in *US Patent 2,191,658*. 1940.
111. Salvador, A.R., Calvo, E.G. and Aparicio, C.B., *Effects of Sample Weight, Particle Size, Purge Gas and Crystalline Structure on the Observed Kinetic Parameters of Calcium Carbonate Decomposition*. *Thermochimica Acta*, 1989. **143**: p. 339-345.
112. Rao, T.R., Gunn, D.J. and Bowen, J.H., *Kinetics of Calcium Carbonate Decomposition*. *Chemical Engineering Research and Design*, 1989. **67**: p. 38-47.
113. Wilburn, F.W., Sharp, J.H., Tinsley, D.M. and McIntosh, R.M., *The effect of procedural variables on TG, DTG and DTA curves of calcium carbonate*. *Journal of Thermal Analysis*, 1991. **37**: p. 2003-2019.
114. Wang, Y. and Thomson, W.J., *The Effect of Sample Preparation on the Thermal Decomposition of CaCO₃*. *Thermochimica Acta*, 1995. **255**: p. 383-390.
115. Rao, T.R., *Kinetics of Calcium Carbonate Decomposition*. *Chemical Engineering Technology*, 1996. **19**: p. 373-377.
116. Xiao, X., Sichen, D., Sohn, H.Y. and Seetharaman, S., *Determination of the Kinetic Parameters Using Differential Thermal Analysis – Application to the Decomposition of CaCO₃*. *Metallurgical and Materials Transactions B*, 1997. **28B**: p. 1157-1164.

117. Criado, J.M., González, M., Málek, J. and Ortega, A., *The Effect of CO₂ Pressure on the Thermal Decomposition of Calcium Carbonate*. *Thermochimica Acta*, 1995. **254**: p. 121-127.
118. Bouineau, V., Pijolat, M. and Soustelle, M., *Characterisation of the Chemical Reactivity of a CaCO₃ Powder for Its Decomposition*. *J. Am. Cer. Soc.*, 1998. **18**: p. 1319-1324.
119. Khinast, J., Krammer, G.F., Brunner, C. and Staudinger, G., *Decomposition of Limestone: The Influence of CO₂ and Particle Size on the Reaction Rate*. *Chem. Eng. Sci.*, 1996. **51**: p. 623-634.
120. L'vov, B.V., *Review: Mechanism and kinetics of thermal decomposition of carbonates*. *Thermochimica Acta*, 2002. **386**: p. 1-16.
121. Zakharov, V.Y., *The Study of the Influence of Particle Sizes on the Thermal Decomposition of Minerals Present in Solid Fuel*. *Thermochimica Acta*, 1989. **146**: p. 63-73.
122. Ar, İ. and Dogu, G., *Calcination Kinetics of High Purity Limestones*. *Chemical Engineering Journal*, 2001. **83**: p. 131-137.
123. Gallagher, P.K. and Johnson, D.W.J., *The Effects of Sample Size and Heating Rate on the Kinetics of the Thermal Decomposition of CaCO₃*. *Thermochimica Acta*, 1973. **6**: p. 67-83.
124. Beruto, D. and Searcy, A.W., *Use of the Langmuir Method for Kinetic Studies of Decomposition Reactions: Calcite (CaCO₃)*. *Journal of the Chemical Society: Faraday Transactions 1*, 1974. **7**: p. 2145-2153.
125. Gallagher, P.K. and Johnson, D.W.J., *Kinetics of the Thermal Decomposition of CaCO₃ in CO₂ and some Observations on the Kinetic Compensation Effect*. *Thermochimica Acta*, 1976. **14**: p. 255-261.
126. Nakamura, T., Gnyloskurenko, S.V., Sakamoto, K., Byakova, A.V. and Ishikawa, R., *Development of New Foaming Agent for Metal Foam*. *Mater. Transactions*, 2002. **43**: p. 1191-1996.
127. Long, X. and Khanna, S.K., *Numerical Simulation of Residual Stresses in a Spot Welded Joint*. *Trans A.S.M.E.*, 2003. **125**: p. 222-226.
128. Körner, C., Arnold, M., Thies, M. and Singer, R.F., *The Physics of Foaming: Structure Formation and Stability*, in *Handbook of Cellular Metals: Production, Processing, Applications*, H.P. Degischer and B. Krizst, Editors. 2002, Wiley-VCH: Weinheim. p. 33-43.
129. Stanzick, H., Klenke, J., Danilkin, S. and Banhart, J., *Material flow in metal foams studied by neutron radiography*. *Applied Physics A: Materials Science & Processing [supplement]*, 2002. **74**: p. S1118-S1120.
130. Banhart, J., Stanzick, H., Helfen, L. and Baumbach, T., *Metal foam evolution studied by synchrotron radiography*. *Applied Physics Letters*, 2001. **78**(8): p. 1152-1154.
131. Stanzick, H., Wichmann, M., Weise, J., Helfen, L., Baumbach, T. and Banhart, J., *Process Control in Aluminium Foam Using Real-Time X-ray Radiography*. *Advanced Engineering Materials*, 2002. **4**(10): p. 814-823.
132. Körner, C., Thies, M., Arnold, M. and Singer, R.F. *Modelling of Metal Foaming by in-situ Gas Formation*. in *Cellular Metals and Metal Foaming Technology*. 2001. Bremen: MIT Verlag.
133. Körner, C. and Singer, R.F. *Numerical Simulation of Foam Formation and Evolution with Modified Cellular Automata*. in *Metal Foams and Porous Metal Structures*. 1999. Bremen: MIT Verlag.
134. Gergely, V., Jones, R.L. and Clyne, T.W., *The Effect of Capillarity-Driven Melt Flow and Size of Particles in Cell Faces on Metal Foam Structure Evolution*. *Trans. JWRI (Special Issue)*, 2001. **30**: p. 371-376.
135. Magrabi, S.A., Dlugogorski, B.Z. and Jameson, G.J. *Osawatwald Ripening in Aqueous Foams*. in *International Workshop on Foams and Films*. 1999. Bremen: MIT Verlag.
136. Clark, N.O. and Blackman, M., *The Degree of Dispersion of the Gas Phase in Foam*. *Trans. Faraday Soc.*, 1948. **44**: p. 1-7.

137. Lin, R.Y. and Hoch, M., *The Solubility of Hydrogen in Molten Aluminum Alloys*. Metall. Trans. A, 1989. **20 A**: p. 1785-1791.
138. Brandes, E. and Brook, G., eds. *Smithells' Metals Reference Book*. 7th Ed. ed. 1992, Butterworth Heinemann: Oxford.
139. Hatch, J.E., ed. *Aluminum: Properties and Physical Metallurgy*. 1990, American Society for Metals.
140. Thomas, D.G., *Transport Characteristics of Suspension: VIII. A Note on the Viscosity of Newtonian Suspensions of Uniform Spherical Particles*. J. Colloid Sci., 1965. **20**: p. 267-277.
141. Surappa, M.K. and Rohatgi, P.K., *Fluidity of Aluminium-Silicon-Alumina Composites*. Met. Trans. B., 1981. **12B**: p. 327-332.
142. Lloyd, D.J. *Factors influencing the Properties of Particulate Reinforced Composites Produced by Molten Metal Mixing*. in *Metal Matrix Composites - Processing, Microstructure and Properties*. 1991. Riso, Denmark: Riso National Laboratory, Denmark.
143. Mortensen, A. and Jin, I., *Solidification Processing of Metal Matrix Composites*. Int. Mat. Rev., 1992. **37**: p. 101-128.
144. Kolsgaard, A. and Brusethaug, S., *Fluidity of Aluminium Alloy AlSi7Mg-SiC particulate composite melts*. Mater. Sci. Technol., 1994. **10**: p. 545-551.
145. Flemings, M.C., Riek, R.G. and Young, K.P., *Rheocasting*. Mat. Sci. Eng., 1976. **25**: p. 103-117.
146. Rohatgi, P.K., Asthana, R. and Das, S., *Solidification, Structures and Properties of Cast Metal-Ceramic Particle Composites*. International Metals Reviews, 1986. **31**(3): p. 115-139.
147. Kirkwood, D.H., *Semisolid Metal Processing*. Intern. Mater. Rev., 1994. **39**: p. 173-189.
148. Fan, Z., *Semisolid Metal Processing*. International Materials Reviews, 2002. **47**(2): p. 49-85.
149. Mehrabian, R., Riek, R.G. and Flemings, M.C., *Preparation and Casting of Metal-Particulate Non-Metal Composites*. Metall. Trans., 1974. **5**: p. 1899-1905.
150. Moon, H.K., Cornie, J.A. and Flemings, M.C., *Rheological Behaviour of SiC Particulate-(Al-6.5wt.%Si) Composite Slurries at Temperatures Above the Liquidus and Within the Liquid + Solid Region of the Matrix*. Materials Science and Engineering, 1991. **A144**: p. 253-265.
151. Mada, M. and Ajersch, F., *Rheological Model of Semi-Solid A356-SiC composite alloys. Part I: Dissociation of Agglomerate Structures during Shear*. Mater. Sci. Eng., 1996. **A212**: p. 157-170.
152. Geiger, G.H. and Poirier, D.R., *Transport Phenomena in Metallurgy*. 1973, Reading, Massachusetts: Addison-Wesley Publishing Company.
153. Dahle, A.K. and St John, D.H., *Rheological Behaviour of the Mushy Zone and its Effect on the Formation of Casting Defects During Solidification*. Acta Mater, 1999. **47**(1): p. 31-41.
154. Loue, W.R., Landkron, S. and Kool, W.H., *Rheology of Partly Solidified AlSi7Mg0.3 and the Influence of SiC Additions*. Mater. Sci. Eng., 1992. **A151**: p. 255-262.
155. Flemings, M.C., *Solidification Processing*. 1974, New York: McGraw-Hill, Inc.
156. Kurz, W. and Fisher, D.J., *Fundamentals of Solidification*. 1986: Trans Tech Publications.
157. Haferkamp, H., Bormann, D., Niemeyer, M. and W., B. *Casting Process for the Production of Foamed Magnesium Structural Parts*. in *EuroMat '99*. 1999: Wiley-VCH.
158. Ma, L. and Song, Z., *Cellular Structure Control of Aluminium Foams During Foaming Process of Aluminium Melt*. Scripta Mater., 1998. **39**: p. 1532-1528.
159. Fusheng, H. and Zhengang, Z., *The Mechanical Behavior of Foamed Aluminium*. J. Mater. Sci., 1999. **34**: p. 291-299.
160. Arnold, M., Körner, C. and Singer, R.F., *Influence of the Oxide on the Stability of PM Aluminium Foam*, T.W. Clyne, Editor. 2001: Materials Week 2001, Munich.

161. Kenny, L.D., *Mechanical Properties of Particle Stabilized Aluminum Foam*. Mater. Sci. Forum, 1996. **217-222**: p. 1883-1890.
162. Prakash, O., Sang, H. and Embury, J.D., *Structure and Properties of Al-SiC Foam*. Mater. Sci. Eng., 1995. **A199**: p. 195-203.
163. Bjorksten, J., *Method for Foaming Metals*, in *US Patent 3,707,367*. 1972.
164. Niebylski, L.M., Jarema, C.P. and Immethun, P.A., *Metal Foams and Process Therefore*, in *U.S. Patent 3,794,481*. 1974.
165. Rock, E.J., *Method of Static Mixing to Produce Metal Foam*, in *US Patent 3,773,098*. 1973.
166. Wilde, P.J., Mackie, A.R., Husband, F.A., Gunning, A.P., Morris, V.J. and Fillery-Travis, A. *The Role of Interfacial Structure and Composition upon Foam Drainage and Fluid Dynamics*. in *International Workshop on Foams and Films*. 1999. Bremen: MIT Verlag.
167. Goicoechea, J., Garcia-Cordovilla, C., Louis, E. and Pamies, A., *Surface Tension of Binary and Ternary Aluminum-Alloys of the Systems Al-Si-Mg and Al-Zn-Mg*. Journal of Materials Science, 1992. **27**: p. 5247-5252.
168. Maruyama, B., Barrera, E.V. and Rabenberg, L., *Characterization and Modification of Composite Interfaces*, in *Metal Matrix Composites: Processing and Interfaces*, R.K. Everett and R.J. Arsenault, Editors. 1991, Academic Press: Boston. p. 181-216.
169. Aveyard, R., Binks, B.P., Fletcher, P.D.I. and Rutherford, C.E., *Contact Angles in Relation to the Effects of Solids on Film and Foam Stability*. J. Dispersion Sci. Technology, 1994. **15**: p. 251-271.
170. Frye, G.C. and Berg, J.C., *Antifoam Action by Solid Particles*. J. Colloid Interface Sci., 1989. **127**: p. 222-238.
171. Aveyard, R., Cooper, P., Fletcher, P.D.I. and Rutherford, C.E., *Foam Breakdown by Hydrophobic Particles and Nonpolar Oil*. Langmuir, 1993. **9**: p. 604-613.
172. Garrett, P.R., *The Mode of Action of Antifoams*, in *Defoaming, Theory and Industrial Applications*, P.R. Garrett, Editor. 1993, Marcel Dekker, Inc.: New York. p. 1-117.
173. Bergeron, V. *PDMS Based Antifoams*. in *International Workshop on Foams and Films*. 1999. Leuven, Belgium: Verlag MIT Publishing, Bremen.
174. Dippenaar, A., *The Destabilization of Froth by Solids: I. The Mechanism of Film Rupture*. Int. J. Mineral Processing, 1982. **9**: p. 1-14.
175. Kumagai, H., Torikata, Y., Yoshimura, H., Kato, M. and Yano, T., *Estimation of the Stability of Foam Containing Hydrophobic Particles by Parameters in the Capillary Model*. Agric. Biol. Chem., 1991. **55**: p. 1823-1829.
176. Binks, B.P., *Particles as surfactants - similarities and differences*. Current Opinion in Colloid & Interface Science, 2002. **7**: p. 21-41.
177. Naidich, J.V., *The Wettability of Solids in Liquid Metals*. Progress in Surface and Membrane Science, 1981. **14**: p. 353-385.
178. Delannay, F., Froyen, L. and Deruyttere, A., *The wetting of solids by molten metals and its relation to the preparation of Metal-Matrix Composites*. J. Mat. Sci., 1987. **22**: p. 1-16.
179. Ip, S.W., Wang, Y. and Toguri, J.M., *Aluminum Foam Stabilization by Solid Particles*. Canadian Metall. Quarterly, 1999. **38**: p. 81-92.
180. Wuebben, T., Odenbach, S. and Banhart, J. *Study of lead foams under microgravity*. in *Met Foam 2001*. 2001. Bremen: MIT Verlag.
181. Wübben, T., Stanzick, H., Banhart, J. and Odenbach, S., *Stability of metallic foams studied under microgravity*. Journal of Physics: Condensed Matter, 2003. **15**: p. S427-S433.
182. Goumiri, I. and Joud, J.C., *Auger Electron Spectroscopy Study of Aluminium-Tin Liquid System*. Acta Metallurgica, 1982. **30**: p. 1397-1405.
183. John, H. and Hausner, H., *Influence of Oxygen Partial Pressure on the Wetting Behaviour in the System Al/Al₂O₃*. Journal of Material Science Letters, 1986. **5**: p. 549-551.
184. Anson, J.P., Drew, R.A.L. and Gruzleski, J.E., *The Surface Tension of Molten Aluminium and Al-Mg-Si Alloy under Vacuum and Hydrogen Atmospheres*. Metallurgical and Materials Transactions B, 1999. **30B**: p. 1027-1032.

185. Pamies, A., Garcia Cordovilla, C. and Louis, E., *The Measurement of Surface Tension of Liquid Aluminium by Means of the Maximum Bubble Pressure Method; The Effect of Surface Oxidation*. Scripta Metallurgica, 1984. **18**: p. 869-872.
186. Garcia-Cordovilla, C., Louis, E. and Pamies, A., *The Surface Tension of Liquid Pure Aluminium and Aluminium-Magnesium Alloy*. Journal of Materials Science, 1986. **21**: p. 2787-2792.
187. Goicoechea, J., Garcia-Cordovilla, C., Louis, E. and Pamies, A., *Effects of Wetting and Surface Oxidation on the Measurement of the Surface Tension of Al by the Maximum Bubble Pressure Method*. Scripta Metallurgica et Materialia, 1991. **25**: p. 479-484.
188. Russell, K.C., Oh, S.-Y. and Figueredo, A., *Theoretical and Experimental Studies of Ceramic-Metal Wetting*. MRS Bull., 1991: p. 46-52.
189. Keene, B.J., *Review of Data for the Surface Tension of Pure Metals*. International Materials Reviews, 1993. **38**(4): p. 157-192.
190. Laurent, V., Chatain, D., Chatillion, C. and Eustathopoulos, N., *Wettability of Monocrystalline Alumina Between its Melting Point and 1273 K*. Acta Met. Mater., 1988. **36**(7): p. 1797-1803.
191. Kaptay, G., *On Surface Properties of Molten Aluminium Alloys of Oxidized Surface*. Materials Science Forum, 1991. **77**: p. 315-330.
192. Eustathopoulos, N., Joud, J.C. and Desre, P., *The Wetting of Carbon by Aluminium and Aluminium Alloys*. Journal of Materials Science, 1974. **9**: p. 1233-1242.
193. Saravanan, R.A., Molina, J.M., Narciso, J., García-Cordovilla, C. and Louis, E., *Surface Tension of Pure Aluminium in Argon/Hydrogen and Nitrogen/Hydrogen Atmospheres at High Temperatures*. Journal of Materials Science Letters, 2002. **21**: p. 309-311.
194. Jörgensen, C. and Thorngren, I., *Thermodynamic tables for process metallurgists*. 1969, Stockholm: Almqvist & Wiksell.
195. Rault, L., M., A. and Dubus, A., *In-situ Study of Liquid Al-Mg Alloys Oxidation*. Materials Science Forum, 1996. **217-222**: p. 165-170.
196. Kacar, A.S., Rana, F. and Stefanescu, D.M., *Kinetics of Gas-to-liquid Transfer of Particles in Metal Matrix Composites*. Materials Science and Engineering, 1991. **A135**: p. 95-100.
197. Hondros, E.D., *Rule for Surface Enrichment in Solutions*. Scripta Metallurgica, 1980. **14**: p. 345-348.
198. Zayan, M.H., Jamjoom, O.M. and Razik, N.A., *High-Temperature Oxidation of Al-Mg Alloys*. Oxidation of Metals, 1990. **34**(3/4): p. 323-333.
199. Raveh, A., Tsameret, Z.K. and Grossman, E., *Surface characterization of thin layers of aluminium oxide*. Surface & Coatings Technology, 1996. **88**: p. 103-111.
200. Nylund, A., Mizuno, K. and Olefjord, I., *Influence of Mg and Si on the Oxidation of Aluminum*. Oxidation of Metals, 1998. **50**(3/4): p. 309-325.
201. Carney, T.J., Tsakiroopoulos, P., Watts, J.F. and Castle, J.E., *Oxidation and Surface Segregation in Rapidly Solidified Al Alloy Powders*. International Journal of Rapid Solidification, 1990. **5**: p. 189-217.
202. Talbot, D.E.J. and Silva, M.P., *Oxidation of Aluminium-Magnesium Alloys in the Liquid and Semiliquid States Physical Metallurgy of Oxidation*. Journal of Metals, 1987: p. 47-48.
203. Surla, K., Valdivieso, F., Pijolat, M., Soustelle, M. and Prin, M., *Kinetic Study of the Oxidation by Oxygen of Liquid Al-Mg5% Alloys*. Solid State Ionics, 2001. **143**: p. 355-365.
204. Surla, K., Valsivieso, F., Pijolat, M., Soustelle, M. and Prin-Lamaze, M., *Application d'un Modele de Reaction en Phase Gazeuse à l'oxidation d'un Alliage Liquide Al-Mg5% sous Faible Pression d'Oxygène*. Annales de Chimie et Science des Matériaux, 2002. **27**(4): p. 83-91.
205. McLeod, A.D. and Gabryel, C.M., *Kinetics of the Growth of Spinel, MgAl₂O₄, on Alumina Particulate in Aluminium Alloys Containing Magnesium*. Metallurgical Transactions A, 1992. **23A**: p. 1279-1283.

206. Salvo, L., L'Espérance, G., Suéry, M. and Legoux, J.G., *Interfacial Reactions and Age Hardening in Al-Mg-Si Metal Matrix Composites Reinforced with SiC Particles*. Materials Science and Engineering, 1994. **A177**: p. 173-183.
207. Cabrera, N. and Mott, N.F., *Theory of the Oxidation of Metals*. Reports on Progress in Physics, 1948/1949. **12**: p. 163-184.
208. Cabrera, N. and Hamon, J., *Sur l'oxydation de l'aluminium à haute température*. Comptes Rendus de l'Académie des Sciences, Paris, 1947. **224**: p. 1713-1715.
209. Krizst, B., Cekan, P. and Faure, K. *Foamability of the Al-Si system*. in *MetFoam 2001*. 2001. Bremen: MIT Verlag.
210. Gergely, V. and Clyne, T.W. *Modelling of Material Redistribution During Melt Route Processing of Metallic Foams*. in *Euromat 99, Symposium on MMCs and Metallic Foams*. 1999. Munich: Wiley-VCH.
211. Gergely, V., Curran, D.C. and Clyne, T.W. *Drainage of Metallic Foams: Modelling and Experimental Observations*. in *2nd Int. Conf. Cellular Metals and Metal Foaming Technology (MetFoam 2001)*. 2001. Bremen, Germany: Verlag MIT Publishing Bremen.
212. Gergely, V. and Clyne, T.W., *Drainage in Standing Liquid Metal Foams: Modelling and Experimental Observations*. Acta materialia, 2003. **In press**.
213. Pai, B.C., Ramani, G., Pillai, R.M. and Satyanarayana, K.G., *Review: Role of Magnesium in Cast Aluminium Alloy Matrix Composites*. Journal of Materials Science, 1995. **30**: p. 1903-1911.
214. Petzow, G. and Effenberg, G., *Ternary Alloys: a comprehensive compendium of evaluated constitutional data and phase diagrams*. Vol. 7. 1990-, New York: VCH.
215. Polmear, I.J., *Light Alloys*. 1st ed. Metallurgy and Materials Science Series, ed. R.W.K. Honeycombe and P. Hancock. 1981, London: Edward Arnold.
216. Yaghmaee, M.S. and Kaptay, G., *On the Stability Range of SiC in Ternary Liquid Al-Si-Mg Alloy*. In press.
217. Surappa, M.K. and Rohatgi, P.K., *Preparation and Properties of Cast Aluminium-Ceramic Particle Composites*. J. Mat. Sci., 1981. **16**: p. 983-993.
218. Urena, A., Gomez de Salazar, J.M., Gil, L., Escalera, M.D. and Baldonedo, J.L., *Scanning and Transmission Electron Microscopy Study of the Microstructural Changes Occurring in Aluminium Matrix Composites Reinforced With SiC Particles During Cutting and Welding: Interface Reactions*. J. Microscopy, 1998. **196**(2): p. 124-136.
219. Iseki, T., Kameda, T. and Maruyama, T., *Interfacial Reactions Between SiC and Aluminium during Joining*. Journal of Materials Science, 1984. **19**: p. 1692-1698.
220. Viala, J.C., Bosselet, F., Laurent, V. and Lepetitcorps, Y., *Mechanism and Kinetics of the Chemical Interaction Between Liquid Aluminium and Silicon-Carbide Single Crystals*. J. Mat. Sci., 1993. **28**: p. 5301-5312.
221. Lloyd, D.J., Lagace, H., McLeod, A. and Morris, P.L., *Microstructural Aspects of Aluminium-Silicon Carbide Particulate Composites Produced by a Casting Method*. Mater. Sci. Eng., 1989. **A107**: p. 73-80.
222. Lloyd, D.J., *The Solidification Microstructures of Particulate Reinforced Al/SiC Composites*. Comp. Sci. & Tech., 1989. **35**: p. 159-180.
223. Janghorban, K., *Investigation of the Effects of Silicon and Carbon on the Phase Composition of SiC/Al Composites*. Composites Science and Technology, 1994. **50**: p. 299-303.
224. Kumar, S., Jayaram, V., Mani, T. and Warriar, K.G.K., *Degradation of Al₂O₃-SiC-Al Composites Prepared by the Oxidative Growth of Al-Alloys Into SiC Particulate*. J. Mat. Sci., 1997. **32**: p. 4719-4722.
225. Andrews, E., Sanders, W. and Gibson, L.J., *Compressive and Tensile Behaviour of Aluminium Foams*. Mater. Sci. Eng., 1999. **A270**: p. 113-124.
226. Irons, G.A. and Owusu-Boahen, K., *Settling and Clustering of Silicon Carbide Particles in Aluminium Metal Matrix Composites*. Metall. Trans., 1995. **26B**: p. 981-989.

227. Tian, C., Irons, G.A. and Wilkinson, D.S., *Settling of Multisized Clusters of Alumina Particles in Liquid Aluminium*. Metallurgical and Materials Transactions B, 1999. **30B**: p. 241-247.
228. Jin, I. and Lloyd, D.J. *Solidification of SiC Particulate Reinforced Al-Si Alloy Composites. in Fabrication of Particulate Reinforced MMCs*. 1990. Montreal: ASM International.
229. Rohatgi, P.K., Yarandi, F.M., Liu, Y. and Asthana, R., *Segregation of Silicon Carbide by Settling and Particle Pushing in Cast Aluminium-Silicon Carbide Particulate Composites*. Mat. Sci. Eng., 1991. **A147**: p. L1-L6.
230. Kennedy, A.R., *The Redistribution of Reinforcements during the Solidification Processing of MMC's*. 1993, University of Cambridge.
231. Thornton, P.H. and Magee, C.L., *The Deformation of Aluminum Foams*. Metall. Trans. A, 1975. **6A**: p. 1253-1263.
232. Sugimura, Y., Meyer, J., He, M.Y., Bart-Smith, H., Grenestedt, J. and Evans, A.G., *On the Mechanical Performance of Closed Cell Al Alloy Foams*. Acta Mater., 1997. **45**(12): p. 5245-5259.
233. Motz, C. and Pippin, R., *Fracture behaviour and fracture toughness of ductile closed-cell metallic foams*. Acta Materialia, 2002. **50**: p. 2013-2033.
234. Von Hagen, H. and Bleck, W., *Compressive, Tensile and Shear Testing of Melt-Foamed Aluminium*, in *Porous and Cellular Materials for Structural Applications*, D.S. Schwartz, et al., Editors. 1998, MRS: San Francisco, California. p. 59-64.
235. McCullough, K.Y.G., Fleck, N.A. and Ashby, M.F., *Uniaxial Stress-Strain Behaviour of Aluminium Alloy Foams*. Acta mater., 1999. **47**(8): p. 2323-2330.
236. Otsuka, M., Houjo, N., Kojima, A., Itoh, M. and Ishii, E., *Mechanical Properties of Aluminum Foam*, in *Light Materials for Transportation Systems*, N.J. Kim, Editor. 1993. p. 435-444.
237. Deshpande, V.S. and Fleck, N.A., *Isotropic Constitutive Models for Metallic Foams*. Journal of the Mechanics and Physics of Solids, 2000. **48**(6-7): p. 1253-1283.
238. Gibson, L.J., *Mechanical Behaviour of Metallic Foams*. Annual Review of Materials Science, 2000. **30**: p. 191-227.
239. Bart-Smith, H., Bastawros, A.-F., Mumm, D.R., Evans, A.G., Sypeck, D.J. and Wadley, H.N.G., *Compressive Deformation and Yielding Mechanisms in Cellular Al Alloys Determined Using X-Ray Tomography and Surface Strain Mapping*. Acta mater., 1998. **46**(10): p. 3583-3592.
240. Bastawros, A.-F., Bart-Smith, H. and Evans, A.G., *Experimental analysis of deformation mechanisms in a closed-cell aluminium alloy foam*. Journal of the Mechanics and Physics of Solids, 2000. **48**: p. 301-322.
241. Bastawros, A.-F. and Evans, A.G., *Deformation Heterogeneity in Cellular Al Alloys*. Advanced Engineering Materials, 2000. **2**(4): p. 210-214.
242. Simancik, F., Jerz, J. and Kovacik, J. *Deformation Behaviour of the Foamed Aluminium During Compressive and Bending Loading*. in *Deformation and Fracture in Structural PM Materials*. 1996. Kosice: IMR-SAS.
243. Gibson, L.J., *Modelling the Mechanical Behavior of Cellular Materials*. Mater. Sci. & Eng., 1989. **A110**: p. 1-36.
244. Krizst, B., Foroughi, B., Faure, K. and Degischer, H.P. *Deformation Behaviour of Aluminium Foam Under Uniaxial Compression (A Case Study)*. in *MetFoam '99: Metal Foams and Porous Metal Structures*. 1999. Bremen: MIT Verlag.
245. McCullough, K.Y.G., *The Mechanical Properties of Metallic Foams*. 1997, University of Cambridge: Cambridge.
246. Deshpande, V.S. and Fleck, N.A., *High Strain Rate Compressive Behaviour of Aluminium Alloy Foams*. Int. J. Impact Engng, 2000. **24**(3): p. 277-298.
247. Maiti, S.K., Ashby, M.F. and Gibson, L.J., *Fracture Toughness of Brittle Cellular Solids*. Scripta Metall., 1984. **18**: p. 213-217.

248. Otsuka, M., Akojima, A., Itoh, M. and Ishi, E. *Structure and Mechanical Properties of Cellular Aluminium*. in *International Conference on Recent Advances in Science and Engineering of Light Metals (RASELM 91)*. 1991.
249. Ashby, M.F., Evans, A.G., Hutchinson, J.W. and Fleck, N.A., *Metal Foams: A Design Guide*. 1998, Cambridge University, Engineering Department: Cambridge.
250. Shaw, M.C. and Sata, T., *The Plastic Behavior of Cellular Materials*. Int. J. Mech. Sci., 1966. **8**: p. 469-478.
251. Fusheng, H., Zhengang, Z. and Junchang, G., *Compressive Deformation and Energy Absorbing Characteristic of Foamed Aluminium*. Metall. Trans., 1998. **A29**: p. 2497-2502.
252. Lloyd, D.J. *Properties of Shape Cast Al-SiC Metal Matrix Composites*. in *Cast Reinforced Metal Composites*. 1988. Chicago: ASM.
253. Gibson, L.J. and Ashby, M.F., *The Mechanics of Three-Dimensional Cellular Materials*. Proc. R. Soc. Lond., 1982. **A382**: p. 43-59.
254. Markaki, A.E. and Clyne, T.W., *Mechanical and Electrical Properties of Stainless Steel Sandwich Sheets with Fibrous Metal Cores, Designed for Automotive Applications*, in *Submitted to 'Metal and Ceramic Composites: Automotive Applications'*, B. Cantor, Editor. 2003.
255. Markaki, A.E. and Clyne, T.W., *Mechanics of Thin Ultra-Light Stainless Steel Sandwich Sheet Material: Part I - Stiffness*. Acta Mater., 2003. **51**(5): p. 1341-1350.
256. Warren, W.E. and Kraynik, A.M., *The Linear Elastic Properties of Open-Cell Foams*. Journal of Applied Mechanics, 1988. **55**: p. 341-346.
257. Weaire, D. and Hutzler, S., *The Physics of Foams*. 1999, Oxford: Oxford University Press. 246.
258. Kraynik, A.M., Neilsen, M.K., Reinelt, D.A. and Warren, W.E., *Foam Micromechanics*, in *Foams and Emulsions*, J.F. Sadoc and N. Rivier, Editors. 1999, Kluwer Academic Publishers: Amsterdam. p. 259-286.
259. Zhu, H.X., Knott, J.F. and Mills, N.J., *Analysis of the Elastic Properties of Open-Cell Foams with Tetraikaidcahedral Cells*. J. Mech. Phys. Solids, 1997. **45**(3): p. 319-343.
260. Warren, W.E. and Kraynik, A.M., *Linear Elastic Behavior of a Low-Density Kelvin Foam with Open Cells*. Journal of Applied Mechanics, 1997. **64**: p. 787-794.
261. Simone, A.E. and Gibson, L.J., *Effects of Solid Distribution on the Stiffness and Strength of Metallic Foams*. Acta Mater., 1998. **46**: p. 2139-2150.
262. Grenestedt, J.L., *Effective elastic behaviour of some models for 'perfect' cellular solids*. International Journal of Solids and Structures, 1999. **36**: p. 1471-1501.
263. Hashin, Z. and Shtrikman, S., *A Variational Approach to the Theory of the Elastic Behaviour of Multiphase Materials*. J. Mech. Phys. Sol., 1963. **11**: p. 127-140.
264. Gibson, L. and Ashby, M.F., *Cellular Solids: Structure and Properties*. Vol. 1. 1988, Oxford: Pergamon Press. 357.
265. Grenestedt, J.L. and Tanaka, K., *Influence of Cell Shape Variations on Elastic Stiffness of Closed Cell Cellular Solids*. Scripta Mater., 1999. **40**(1): p. 71-77.
266. Silva, M.J. and Gibson, L.J., *The Effects of Non-Periodic Microstructure and Defects on the Compressive Strength of Two-Dimensional Cellular Solids*. Int. J. Mech. Sci., 1997. **39**(5): p. 549-563.
267. Olurin, O.B., Arnold, M., Körner, C. and Singer, R.F., *The investigation of morphometric parameters of aluminium foam using computed micro-tomography*. Materials Science and Engineering A, 2002. **328**: p. 334-343.
268. Huber, A.T. and Gibson, L.J., *Anisotropy of Foams*. J. Mater. Sci., 1988. **23**: p. 3031-3040.
269. Nieh, T.G., Higashi, K. and Wadsworth, J., *Effect of cell morphology on the compressive properties of open-cell aluminium foams*. Materials Science and Engineering A, 2000. **283**: p. 105-110.
270. Beals, J.T. and Thompson, M.S., *Density Gradient Effects on Aluminium Foam Compression Behaviour*. J. Mater. Sci., 1997. **32**: p. 3595-3600.

271. Gradinger, R. and Rammerstorfer, F.G., *On The Influence of Meso-Inhomogeneities on the Crush Worthiness of Metal Foams*. Acta Mater., 1999. **47**(1): p. 143-148.
272. Miyoshi, T., Itoh, M., Mukai, T., Kanahashi, H., Kohzu, H., Tanabe, S. and Higashi, K., *Enhancement of Energy Absorption in a Closed-Cell Aluminum by the Modification of Cellular Structures*. Scripta Mater., 1999. **41**: p. 1055-1060.
273. Ashby, M.F., *The Effect of Non-Uniformity on the Properties of Cellular Solids*. 1996, Engineering Design Centre: Cambridge.
274. Grenestedt, J.L., *Influence of Wavy Imperfections in Cell Walls on The Elastic Stiffness of Cellular Solids*. J. Mech. Phys. Solids, 1998. **46**(1): p. 29-50.
275. Simone, A.E. and Gibson, L.J., *The Effects of Cell Face Curvature and Corrugations on the Stiffness and Strength of Metallic Foams*. Acta Mater., 1998. **46**(11): p. 3929-3935.
276. Park, C. and Nutt, S.R., *Strain rate sensitivity and defects in a steel foam*. Materials Science and Engineering A, 2002. **323**: p. 358-366.
277. Lankford, J. and Dannemann, K.A. *Strain Rate Effects in Porous Materials*. in *Porous and Cellular Materials for Structural Applications*. 1998. San Francisco: MRS.
278. Dannemann, K.A. and Lankford, J., *High strain rate compression of closed-cell aluminium foams*. Materials Science and Engineering, 2000. **A293**: p. 157-164.
279. Mukai, T., Kanahashi, H., Miyoshi, T., Mabuchi, M., Nieh, T.G. and Higashi, K., *Experimental Study of Energy Absorption in a Close-Celled Aluminum Foam Under Dynamic Loading*. Scripta Mater., 1999. **40**(8): p. 921-927.
280. Paul, A. and Ramamurty, U., *Strain rate sensitivity of a closed-cell aluminium foam*. Materials Science and Engineering A, 2000. **281**(1-7).
281. Onck, P.R., Andrews, E.W. and Gibson, L.J., *Size effects in ductile cellular solids. Part 1: Modeling*. Int. Journal of Mechanical Sciences, 2001. **43**: p. 681-699.
282. Andrews, E.W., Gioux, G., Onck, P. and Gibson, L.J., *Size Effects in Ductile Cellular Solids Part II: Experimental Results*. Int. J. Mech. Sci., 2001. **48**: p. 701-713.
283. Rawle, A., *Basic Principles of Particle Analysis*. 2000, Malvern instruments: Malvern.
284. Underwood, E.E., *Quantitative Stereology*. 1970, Reading: Addison-Wesley Publishing Company.
285. DeHoff, R.T., *Engineering of Microstructures*. Materials Research, 1999. **2**(3): p. 111-126.
286. Babscán, N., Leitmeyer, D. and Degischer, H.P., *Foamability of Particle Reinforced Aluminium Melt*. Materialwissenschaft und Werkstofftechnik, 2003. **34**: p. 22-29.
287. Leitmeyer, D., Degischer, H.P. and Flankl, H.J., *Development of a Foaming Process for Particulate Reinforced Aluminium Melts*. Adv. Eng. Mater., 2002. **4**: p. 735-739.
288. JANAF, *Thermochemical tables*, ed. M.W.C.e. al. Vol. 14. 1985: Journal of Physical and Chemical Reference Data. 1-1856.